12-2010

Size and composition dependent electrochemical oxidation and deposition of metal nanostructures.

Olga S. Ivanova
University of Louisville

Follow this and additional works at: https://ir.library.louisville.edu/etd

SIZE AND COMPOSITION DEPENDENT ELECTROCHEMICAL OXIDATION

AND DEPOSITION OF METAL NANOSTRUCTURES

By

Olga S. Ivanova

A Dissertation
Submitted to the Faculty of the
Graduate School of the University of Louisville
in Partial Fulfillment of the Requirements
for the Degree of

Doctor of Philosophy

Department of Chemistry
University of Louisville
Louisville, Kentucky

December 2010

SIZE AND COMPOSITION DEPENDENT ELECTROCHEMICAL OXIDATION

AND DEPOSITION OF METAL NANOSTRUCTURES

By

Olga S. Ivanova

A Dissertation Approved on

December 8, 2010

by the following Dissertation Committee:

_____
Dissertation Director Dr. Francis P. Zamborini

_____
Dr. Marta C. Yappert

_____
Dr. Richard P. Baldwin

_____
Dr. Christopher T. Burns

_____
Dr. Gerold A. Willing

DEDICATION

"If you raise your children to feel that they can accomplish any goal or task they decide upon, you

will have succeeded as a parent and you will have given your children the greatest of all

blessings."

Brian Tracy

This Dissertation is dedicated to my parents

Natalya and Sergey Ivanov

ACKNOWLEDGEMENTS

patience. I am honored to have you as my parents. A special thanks to my fiancé, Grzegorz, who supported me throughout these years in graduate school, patiently assisting with words of assurance and not letting me procrastinate.

ABSTRACT

SIZE AND COMPOSITION DEPENDENT ELECTROCHEMICAL OXIDATION AND DEPOSITION OF METAL NANOSTRUCTURES

Olga S. Ivanova

December 8, 2010

This dissertation describes 1) size-dependent electrochemical oxidation/stripping of gold and silver nanoparticles (NPs), 2) alloying of copper with gold nanoparticles at underpotential deposition potentials, 3) electrochemical characterization of Au/Ag core-shell structures, 4) characterization of metal nanoparticle alloys by stripping voltammetry, and 5) layer-by-layer assembly of metal nanoparticle/polymer structures. The motivation of this work is to better understand fundamental properties of metal nanostructures as a function of size, shape, and composition.

We synthesized Au and Ag NPs with different size by electrochemical reduction of the metal salt directly on the electrode surface and by seed-mediated growth in solution followed by chemisorption on a silane functionalized electrode surface, respectively. Linear sweep voltammetry results demonstrated a negative shift in peak potential for oxidation with decrease in size. For Ag NPs, the oxidation potential is 275 mV and 382 mV for 8 and 50 nm particles, respectively. In the case of Au NPs, the peak potentials are 734 and 913 mV for 4 and 250 nm particles, respectively. This shift in

oxidation potential with change in size of metal nanoparticles is consistent with Plieth theory.

Underpotential deposition of copper on Au NPs of different size led to alloying of Au and Cu. Several peaks were observed on linear sweep voltammograms. We assigned these peaks to different copper locations in the alloy structure: 1) Cu UPD on the surface of Au NP, 2) outer-shell Cu-Au alloy, and 3) core of Cu-Au NP alloy.

Au/Ag core-shell nanostructures were synthesized by seed-mediated growth directly on the electrode surface and characterized with electrochemical techniques. During electrochemical characterization, dealloying of Au from Au/Ag alloy structures occurred by cycling in bromide containing electrolyte solution. Composition analysis based on LSV showed that less than 3% of Au remained on the electrode surface. SEM images showed that the morphology of Au/Ag nanostructures changes after electrochemical oxidation. Particles become bigger and form hollow "bulbs", porous structures, and networks.

We also synthesized Au/Ag alloy nanoparticles through a high temperature seed-mediated growth procedure and characterized them by UV-Vis and LSV at different stages of synthesis. LSV results provided information about the composition and atomic arrangements of alloy nanoparticles synthesized using 1:1 Au:Ag ratio, but a different synthesis method. After a 24-hour heating time, the $(Au_{4nm})Ag$ NPs did not show the oxidation peak for Ag, indicating that it stabilized during the alloy formation. In the case of $(Ag_{8nm})Au$ NPs, Ag oxidation peak appeared on LSVs regardless the heating time.

Electrochemical characterization and UV-vis spectroscopy results for metal nanoparticle-polymer multilayer films showed that, with increase in the number of metal-

polymer layers, absorbance and coverage increases due to an increase of the amount of metal assembled on the surface. A red shift in peak wavelength indicates an increase in size and aggregation of NPs on the electrode surface. SEM analysis shows that the morphology of the film depends on the nature of the metal deposited and the size of NPs. Films of Ag NPs consisted of large aggregated structures on the electrode surface, while films of Au NPs were uniform and porous. Experiments on the electron transfer through the polymer film to the metal NPs, demonstrated that electron transport depends on the number of polymer bilayers and the nature of the NPs. After deposition of 5 polymer bilayers, Au oxidation peak disappeared, while Ag oxidation peak was lower compared to 1 layer, but still observable.

This dissertation describes a few sets of experiments on fundamental electrochemical properties of metal nanostructures. The results of these experiments are crucial for the application areas such as catalysis and sensing. It is important to study the stability of these nanoparticles, and also their recycling potential, since it can be affected by changes in the shape and size of the nanoparticles during the course of a reaction. This will not only provide information about electrochemical stability but may also prove useful as a method for analyzing nanoparticles and using them as labels for analytical applications by electrochemical stripping voltammetry.

TABLE OF CONTENTS

LIST OF TABLES

LIST OF FIGURES

CHAPTER I

INTRODUCTION

1.1 MAIN GOAL AND SUMMARY

The mail goal of this research was to study stability towards electrochemical oxidation of metal nanoparticles as a function of their size and composition directly by linear sweep voltammetry. Chapter I provides background information on the research findings in the area of nanoparticle stability. Two different theories of size-dependent electrochemical oxidation of metal nanoparticles are described. Chapter II describes experimental procedures and instrumentation used in this study. Chapter III and IV are focused on our research on size-dependent oxidation of silver and gold nanoparticles. Chapter V describes our research on size-dependent alloying of copper with gold nanoparticles at underpotential deposition (UPD) potentials. Chapter VI describes our attempt to electrochemically characterize core-shell nanostructures. Chapter VII shows our preliminary data on electrochemical characterization of gold-silver alloy nanoparticles. Chapter VIII focused on layer-by-layer deposition of metal nanoparticle films and their characterization. Chapter IX summarizes the results of this research and provides future directions.

1.2 MOTIVATION/OBJECTIVE

The motivation behind this research was to better understand the properties of gold and silver nanoparticles and various alloys. Our findings will not only provide useful information about electrochemical stability but may also prove useful as a method for analyzing nanoparticle samples for size and composition, and using them as labels for analytical applications by electrochemical stripping voltammetry. This is critical information for designing highly active catalysts and using nanostructures in electrochemical sensing devices.

1.3 IMPORTANCE OF METAL NANOPARTICLES RESEARCH

Due to their unique optical,[1,2] magnetic,[3,4] thermal,[5] and electrochemical[6-8] properties metal nanoparticles (NPs) have been an object of intensive studies during the past decade. Their properties are very different from the bulk forms of the same material and strongly related to their size and shape. Over the years researches have developed various methods to synthesize metal nanostructures with controlled size and shape.[9] This led to fundamental research on their size, shape and composition dependent properties. Of special interest is the relationship between the particle size, shape and structure with chemical or electrochemical reactivity.[10-14]

The use of metal nanostructures in electrochemical sensing devices is a promising prospect.[15] Mono- or multilayer arrays of conductive nanoparticles assembled on electrode surface may be considered as assemblies of nanoelectrodes.[16] Their high surface area, reactivity, and ability to facilitate electron transfer make arrays of metal nanoparticles useful as electrochemical sensors for vapors.[17-19]

2

Nanoparticle-based materials also offer excellent prospects for biological sensing. Silver deposition on gold nanoparticles was used to amplify optical signal for DNA-conjugated gold particles. Mirkin and co-workers developed DNA sensors using hybridization-induced changes in distance-dependent optical properties of gold-particle-modified oligonucleotides[20] and scanometric DNA array based on silver amplification of hybridization events.[21] Silver enhancement was also used for detecting single viral copies using in situ hybridization, providing an alternative for in situ polymerase chain reaction.[22]

Transition metal nanoparticles are very attractive to use as catalysts due to their high surface-to-volume ratio and high surface energy, which makes their surface very active. However, active surface atoms can result in nanoparticle instability during the course of its catalytic function. There have been numerous types of reactions that have been catalyzed using supported metal nanocatalysts such as oxidations,[23] cross-coupling reactions,[24-33] electron-transfer reactions,[34-38] hydrogenations,[39,40] and fuel cell reactions.[41,42]

Researches have also used metal nanoparticles in areas such as separations,[43] plasmonics,[44-46] nanoelectronics,[47] therapeutics,[48-50] biological imaging and diagnostics.[51-54]

One issue of importance for these applications that is often ignored is the metal nanoparticle stability. Not only is stability important in terms of their resistance against aggregation and size and shape transformations, but it is also essential for these metal nanostructures to be inert toward oxidation and dissolution.

1.4 ELECTROCHEMICAL STUDIES OF METAL NANOPARTICLES

1.4.1 Oxidation of metal NPs.

Since metal oxidation is an electrochemical process, previous electrochemical studies of metal NPs are relevant to our work, which include studies of electrochemical sensing,[55-61] electrocatalysis,[62-65] electron transport,[8,66-72] and metal nanoparticle oxidation.[6,7,73-76]

Murray and co-workers studied the electrochemistry of monolayer-protected gold NPs dissolved in solution or attached to the surface. Au NPs were synthesized using different thiolate ligands. Electrochemical measurements were performed in 0.1 M tetrabutylammonium perchlorate in dichloromethane solution. In their work, the entire NP core becomes oxidized and reduced by single electron events known as quantized double layer (QDL) charging for metallic NPs greater than about 1.5 nm in diameter.[8,71] It was shown that QDL charging of monolayer protected cluster is temperature-dependent.[70] Smaller NPs, including those as small as Au_{13},[69] develop a highest occupied molecular orbital (HOMO) – lowest unoccupied molecular orbital (LUMO) gap, indicative of a metal-to-molecule transition.[68,69,71] This metal-to-molecule transition can be detected optically or electrochemically. The electrochemical energy gap is a difference between potentials for the first oxidation and first reduction peaks. HOMO-LUMO energy gaps were studied on Au NPs with different core sizes.[71]

A second type of study involves the oxidation and dissolution of the individual metal atoms within a NP. This process has been probed mainly by stripping voltammetry and microscopy. Voltammetry studies include use of metal NPs as labels in an

4

electrochemical immunoassay, where the stripping voltammogram of the metal NPs identifies and quantifies the analyte of interest, usually DNA[77,78] or proteins.[79,80] Alegret et. al. demonstrated direct voltammetric method of detection of DNA hybridization event based on Au_{67} NPs and paramagnetic beads.[78] Hsing and co-workers introduced electrochemical DNA hybridization detection method using silver enhanced gold NPs labels.[77] Merkoci et. al. constructed sandwich-like silver-enhanced immunoassay based on Au NPs and magnetic beads for detection of proteins.[79] Silver enhancement was achieved by direct electrochemical reduction of Ag ions on the surface of Ag NPs. Detection limits of such assay were reported to be up to 23 fg/mL that are 1000 times lower in comparison with direct detection of Au NPs.

Other researchers used scanning tunneling microscopy (STM) to directly image metal NPs of various sizes during oxidation under potential control.[73-75,81] Some observe unusual electrochemical stability of metal clusters on the electrode surface,[74,75] while others demonstrated the negative shift in oxidation potential with a decrease in cluster size.[73] For example, Kolb examined the stability of copper particles on Au (111) surfaces.[74] Copper cluster were arranged on gold surfaces by using the tip of a STM. They found that these copper clusters were stable to potentials ~200 mV greater than the Cu^{2+}/Cu^0 equilibrium potential of a bulk Cu electrode. Penner's group used electrodeposition to produce Ag NPs on the surface of a highly oriented pyrolytic graphite (HOPG) electrode and also reported an unusual stability of 0.4 to 1.0 nm diameter Ag clusters at potentials corresponding to +500 mV larger than the reversible potential of bulk silver.[75] In contrast with work of Kolb and Penner, Stimming using an approach similar to Kolb for nanoparticle formation, investigated the stability of

palladium clusters on the Au (111) surfaces.[73] They reported the dissolution process of Pd clusters of ~5 nm in diameter at potentials ~330 mV, which shifts negative from the standard electrode potential for bulk Pd by 370 mV. Their simulations suggest that the larger clusters consist of a palladium-gold alloy, which is more stable that pure palladium. Ceder et. al. studied electrochemical stability of platinum particles as a function of size using electrochemical scanning tunneling microscopy (ECSTM), deposited on Au (111) substrate and showed that smaller particles have less stability to dissolution in comparison to larger ones.[81] There is some debate on whether the metastability of metal clusters is due to particle size or interactions with the electrode surface such as mechanical alloying.[82-84] Microscopy studies raised interesting questions about the electronic, structural, and chemical effect of the electrode-metal interaction on metal NP oxidation potential and kinetics. These studies lacked direct electrochemical measurements.

Considering the above studies of metal NP oxidation and previous theoretical studies, there are two reasons to believe that the oxidation of metal NPs should be size-dependent. First, theoretical calculations and experimental studies showed that the standard redox potential of metal NPs decreases with decreasing size.[85,86] Plieth[86] derived an equation that predicts the shift in oxidation potential of metal NPs as a function of size as follows:

$$E^0_p = (E^0_{bulk} - \frac{2\gamma V_m}{zFr}) \qquad \text{(Eq. 1.1)}$$

where γ is the surface tension, V_m is the molar volume, z is the number of electrons, F is Faraday's constant, and r is the radius. This equation is based on calculations of Gibbs free energies associated with the change in surface area; bulk metal becomes dispersed

into smaller nanoparticles. Figure 1.1 shows the plot of shift in the standard reduction potential of silver particles as a function of their radius. Shifts in potential are more dramatic at small sizes and then begin to level off as approaches larger diameters. Small particles more easily lose electrons and dissolve in solution compare to big particles due to their higher surface energy and fewer Ag-Ag bonds.

Henglein[85] also predicted a decrease in the metal/metal-ion oxidation potential with decreasing particle size by calculating the equilibrium potentials from sublimation energies and showed that small metal clusters can reduce organics. For example, he calculated that the standard reduction potential for a single Ag^+/Ag atom is shifted to -1.8 V vs. NHE, and the silver trimer Ag_3 is predicted to have a standard potential of -1.0 V vs. NHE, compared to the standard reduction potential Ag macroelectrode, which occurs at +0.799 V vs. NHE.

Experimentally, Brus and co-workers examined the stability of arrays of Ag nanoparticles on HOPG and indium tin oxide (ITO) surfaces and reported the operation of electrochemical Ostwald ripening associated with particle-size differences.[76] Because of different reduction potentials for different sized Ag particles, larger Ag NPs grew larger at the expense of smaller Ag NPs.

The work of Compton and co-workers offers a second explanation for size-dependent electrochemical oxidation of metal NPs.[87-90] Their work addresses the oxidation of an array of metal NPs attached to a conductive electrode surface and based on models of electrode arrays and the concentration profile of the oxidized metal ions diffusing away from the dissolving NPs.[89] Under the assumption that standard electrode potential does not shift with particle size, theory, based on diffusion only, predicts that

7
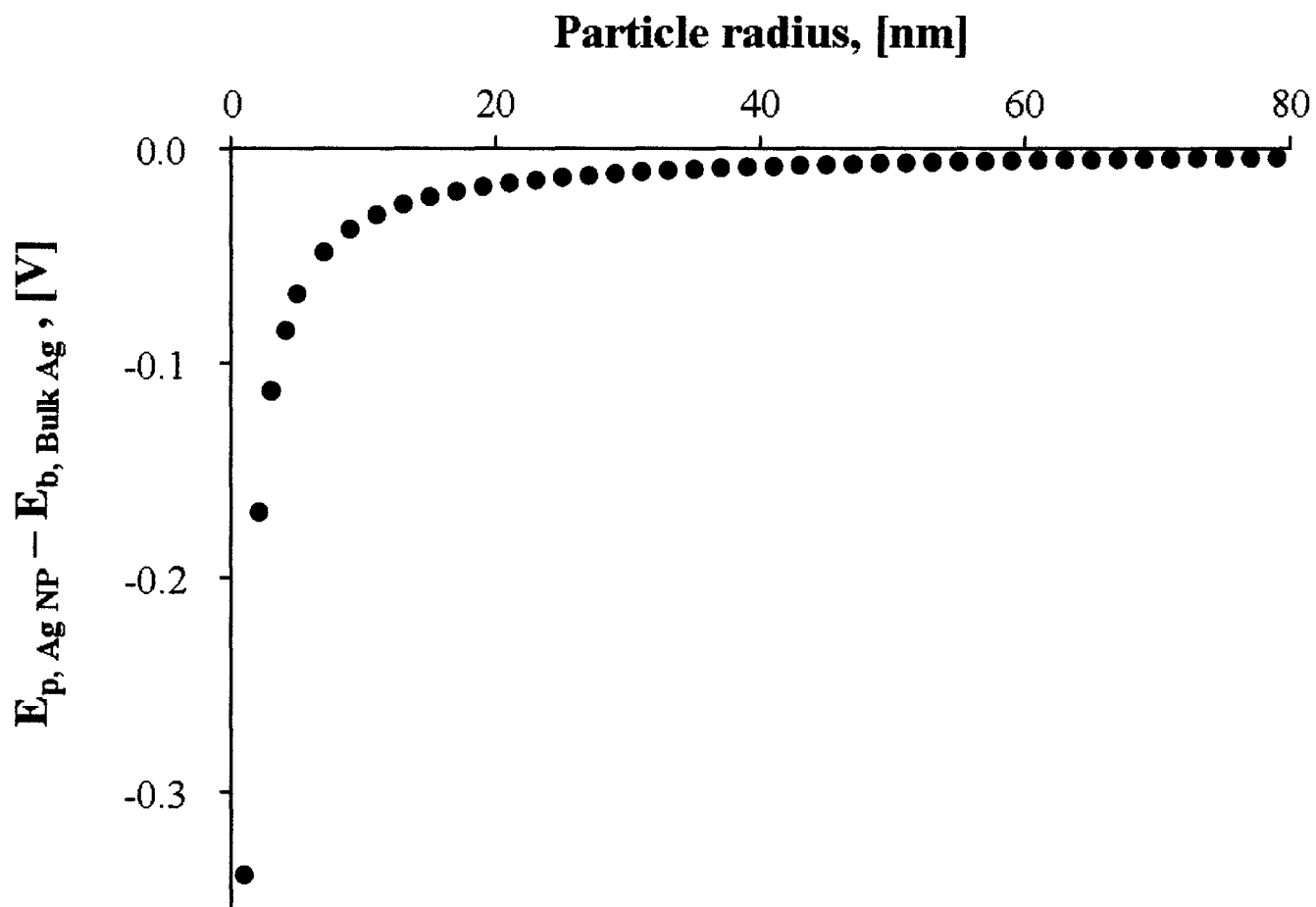
Figure 1.1 Graph of shift from bulk in standard electrode potential of small silver particles as a function of radius.

the peak potential (E_p) in a stripping voltammogram does not depend on NP size, but shifts positive with increasing coverage of metal atoms provided that the system is electrochemically reversible and the diffusion layers of the NPs overlap. When the diffusion layers do not overlap, E_p shifts with particle size and is independent of the coverage. Under conditions of planar diffusion, the oxidation of Ag NPs with diameters in the range from 25 to 100 nm on a basal-plane pyrolytic graphite electrode did not exhibit a size-dependent E_p experimentally.[87] For irreversible systems, theory predicts that E_p shifts negative with decreasing NP size and is independent of metal atom surface coverage.

1.4.2 Electrochemical alloying and dealloying.

Electrodeposition of alloys is an important area of research due to the differences in properties of alloy versus single metal electrodeposits. The properties of the electrodeposited alloys can be varied by changing the deposition conditions, such as composition of plating solution, current density, potential, temperature, and deposition time. While electrochemical deposition on macroscale is well known, the formation of bimetallic alloys by electrodeposition on nanometer scale is not well explored. There are two reports on the formation of Cu-Au alloy nanostructures by electrodeposition by Tanaka group.[91,92] They electrodeposited Cu-Au alloy nanoparticles on an amorphous carbon film in the underpotential deposition region of Cu^{2+}. Under conditions of the experiment they were able to synthesize decahedral and icosahedral Cu-Au nanoparticles when the Cu content was below 30%. With increase of Cu content particles were smaller and had a spherical shape. The formation of Au-Cu alloy particles was proposed to be a

layer-by-layer growth. The region of Cu UPD is in the region of overpotential deposition of Au, therefore the alloy nanoparticle growth is initiated by the formation of Au nuclei. When Au nuclei are formed, the underpotential deposition of Cu may occur on the surface of Au. Only one layer of Cu can be deposited at UPD potentials. Then Au ions cover this surface and so forth and so on. Pt-Cu alloy nanoparticles were fabricated by simultaneous reduction of two metal salts with hydrazine hydrate.[93] Coreduction of two metals led to formation of poorly crystalline Pt, Cu and Pt-Cu alloy NPs. Annealing of these particles alloyed the metals and increased particles size and crystallinity. Using this method three different particle size distributions were achieved, > 25 nm, 12 – 25 nm and <12 nm.

Dealloying of one or more elements from the alloy attracted the attention of various research groups because of formation of porous films with high surface area and reactivity. Chemical and electrochemical dealloying is usually used to produce porous films. Chemical dealloying or etching involves the dissolution of one metal from alloy in a suitable solution. The formation of monolithic nanoporous silver by chemical dealloying in hydrochloric acid of Ag-Al alloys was demonstrated by Zhang group.[94] Nanoporous Au nanowires were synthesized by chemical etching with nitric acid of Ag-Au alloy nanowires by Searson group.[95] It was shown that dealloying of Cu from Cu-Pt nanoparticles in nitric acid, led to the formation of porous "Swiss-cheese" structure with high surface area, which increased the activity of these nanoparticles toward oxygen reduction reaction.[93]

In the case of electrochemical dealloying, potential is applied to the sample in order to electrochemically remove usually the less noble metal from the alloy. Recent

report from Erlebacher group demonstrates that the formation of nanoporous gold film by chemical dealloying of Ag from Ag-Au alloy occurs in neutral (pH=7) silver nitrate solution under potential control.[96] It was shown that the morphology of resulting nanoporous films are similar to those obtained by etching in nitric acid, but the pore size is much smaller which led to threefold increase in surface area. Corcoran[97] et. al. studied the electrochemical dealloying of Ag from Ag-Au alloys in halide-containing electrolytes. They showed that addition of halides affects the critical overpotential for dealloying. The critical overpotential decreases with the addition of halides in the order of I⁻ > Br⁻ > Cl⁻ > no halides. Addition of halides also affected the porosity of the film and it was found that the porosity of the film produced in iodine-containing electrolyte was nine times greater than the films prepared without addition of halide ions. The formation of porous Ag by electrochemical alloying/dealloying in zinc chloride-1-ethyl-3-methyl imidazolium chloride ionic liquid was studied.[98] The influence of such factors as quantity of zinc, applied potential, current, and temperature on the morphology of the final Ag structure was investigated. There are no reports on formation of porous metal nanoparticles by electrochemical dealloying.

1.4.3 Electrochemical characterization of metal NP films.

It is common now to modify electrodes with nanoparticles in order to fabricate the electrode with enhanced properties. Much of the recent work is driven by application of such electrodes in the areas of microelectronics, catalysis, sensing and other fields. There are numerous reports on formation of monolayer and multilayer metal nanoparticle films. Formation of monolayer films starts with modification of the electrode surface with self-

assembled monolayer, which contains the functional groups that can be attached to the metal nanostructures. Multilayer films usually composed of charged polyelectrolytes and functionalized metal nanoparticles in a layer-by-layer fashion. The properties of such films can be tuned by changing the linker molecules, size of metal nanoparticles deposited, and number of deposition cycles used. For example, Claus group studied the change in resistance of Au/linker molecule multilayer films fabricated by layer-by-layer method.[99] Three linker molecules were used: 2-mercaptoethanol, 1,6-hexanedithiol, and 1,10-decanedithiol. The initial resistance of the films varied as a function of length of linker molecule (longer molecule led to higher resistance). By applying different temperatures for the different periods of time to the films, resistance changes were monitored and it was shown that resistance decreases with increase in temperature and time of heating. The decrease in resistance was a result of desorption of linker molecules and aggregation of Au particles. Chirea et. al. fabricated the polyelectrolyte/Au NP multilayers using poly(L-lysine) and characterized films electrochemically using $[Fe(CN)_6]^{3-/4-}$ and $[Ru(NH_3)_6]^{3+/2+}$.[100] It was shown that permeability of studied ions highly depends on the charge of the last layer deposited. For the films terminated with Au NPs permeability of negatively charged ions was low and decreased with increase of number of deposition layers. In contrast, permeability of positively charged ions was high and increased with increase of number of layers. When films were terminated with poly(L-lysine), permeability was high for negatively charged, and low for positively charged ions. Crespilho et. al. studied charge transport and incorporation of redox mediators in LBL film containing dendrimer encapsulated Au NPs[101] and considered

12

electron hopping as a charge transport mechanism between Au NPs and polymer in LBL film.

1.5 SUMMARY AND ACCOMPLISHMENTS

In the main part of this dissertation (Chapter III and Chapter IV) I will present the work on oxidation/stripping of silver and gold NPs as a function of NP size. Chapter III will be focused on Ag NPs. Their synthesis by seed-mediated growth method, assembly on the surface, and size-dependent electrochemical oxidation in sulfuric acid will be described. The main accomplishments of this work are:

- Demonstration for the first time of size-dependent stripping of Ag NPs directly by linear sweep voltammetry.

- Under our experimental conditions of planar diffusion, constant coverage, and electrochemical reversibility, Compton theory based on diffusion only predicts a constant E_p with size. This fact suggests that the experimental shift in E_p is due to a size-dependent change in E^0 for Ag/Ag^+

- Constant potential experiments show the fast dissolution rates for small particles and slow dissolution rate for big Ag NPs, which is consistent with a negative shift in standard potential (E^0) for the smaller Ag NPs.

- Stirring experiments showed approximately the same shift in oxidation potentials for 8 and 35 nm Ag NPs, suggesting that diffusion is not the reason for the size-dependent shift in oxidation potential.

Chapter IV describes size-dependent electrochemical oxidation of Au NPs. We synthesize Au NP by electrodeposition. The main findings of this project are:

- For the first time, we synthesized Au NPs with different size directly on the electrode surface by electrochemical reduction of Au salt at different potentials. This method of synthesis provided us with control of the coverage of metal on the electrode surface. In addition, it is fast and simple method to synthesize Au NPs with controlled size.

- The oxidation potential for Au NPs shift negative with decrease in size.

- Two well resolved oxidation peaks can be seen on LSV of Au NPs of two different sizes deposited on the electrode surface at the same time. These results demonstrate that the LSV can be used as a tool for metal NP size analysis.

Chapter V describes size dependent alloying of Cu with Au NPs at underpotential deposition potentials. By using cycling voltammetry we observed for the first time process of alloying of Cu with Au NP of 8 and 60 nm. This alloying behavior happens with less extent on bigger particles and does not occur on Au NPs of 250 nm and Au film.

Chapter VI focuses on attempt to characterize Au/Ag core/shell structures electrochemically. We synthesized Au/Ag core/shell structures by seed-mediated growth directly on the surface of the electrode. Results of electrochemical oxidation in bromide electrolyte solution of such synthesized nanostructures led to formation of bulb-like and porous nanostructures. It is first time observation of formation of porous Ag nanoparticles by electrochemical dealloying of Au from Au-Ag alloy.

Chapter VII describes synthesis of Au/Ag alloys by seed-mediated growth in solution and their electrochemical characterization. Optical and electrochemical properties of these alloys strongly depend on the synthesis conditions.

Chapter VIII focuses on fabrication of metal NP/polymer multilayer films by electrostatic attachment of Au and Ag NPs through positively charged polymer using layer-by-layer procedure. We characterized these films by UV-Vis spectroscopy, Scanning Electron Microscopy (SEM), and LSV. The morphology of films was different for different metal NPs deposited on the surface.

Chapter IX summarizes and provides future directions of this research.

The work presented in this dissertation may inspire future fundamental and applied studies in the area of electrochemistry of nanomaterials.

CHAPTER II

EXPERIMENTAL

Figure 2.1 shows the general scheme of experiments used in this work. The experimental route includes the following steps: substrate preparation, synthesis of metal NPs, assembly of metal NPs on the electrode surface and their characterization with various techniques. All these steps will be described in details in this chapter.

2.1 SUBSTRATES

Indium Tin Oxide (ITO) coated glass slides. Indium tin oxide (ITO or tin-doped indium oxide) is a solid solution of indium (III) oxide (In_2O_3) and tin (IV) oxide (SnO_2), typically 90% In_2O_3, 10% SnO_2 by weight. It is widely used because of its two main properties: electrical conductivity and optical transparency. The unpolished float (soda – lime) glass coated ITO slides (Delta Technologies, LTD) were used in experiments as an electrode material for electrochemical experiments and for UV-Vis measurements. These slides have a typical surface roughness of <0.2 μm/20 mm, peak-to-peak. The ITO coating is applied over the SiO_2, with the coating on both or just one surface of the glass with a resistance of 8-12 ohms. Slides were cut with a diamond pen into 25×7 mm slices, and then cleaned by sonication for 20 min each in acetone, ethanol, and 2-propanol before drying under a stream of N_2 and used in experiments.

16
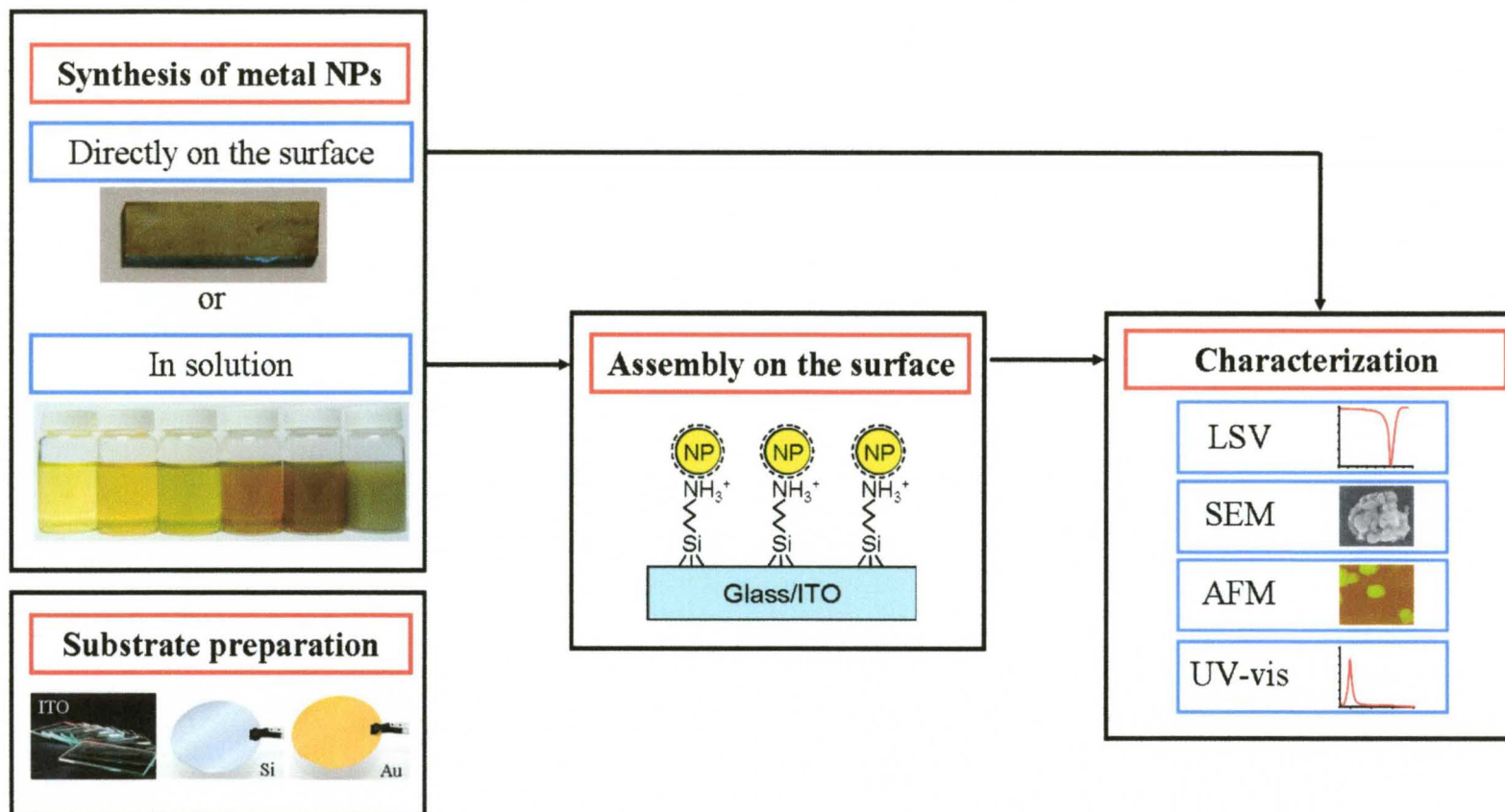
Figure 2.1 General scheme of experiments used in the work.

Silicon. Silicon substrates were used for characterization of nanostructures with Atomic Force Microscopy (AFM). A p-type <100> silicon wafer (purchased from Silicon Quest International, CA) was cut with a diamond pen into smaller, approximately 5×5 mm pieces. Next, every piece was cleaned with piranha solution, rinsed with nanopure water, and dried under a stream of N_2. The clean silicon slides were then used as substrates for NP assembly and for their AFM characterization.

Gold film. The gold film was a silicon substrate sputter-coated with 250 Å Ti/W and 2000 Å of Au (Lance Goddard Assoc., Foster City, CA). It was used for as an electrode material in cyclic voltammetry measurements.

2.2 SOLUTIONS

Piranha solution. Piranha solution is a mixture of sulfuric acid (H_2SO_4) and hydrogen peroxide (H_2O_2) in a ratio of 3:1, respectively. It is commonly used to clean organic residues off substrates. The solution may be prepared before application or directly applied to the material by adding hydrogen peroxide first, following by sulfuric acid. The piranha solution was used to clean silicon and gold substrates. All operations were performed under a hood. Substrates were kept in piranha for 20 min, then rinsed with nanopure water several times, rinsed with isopropyl alcohol (IPA) and dried under a stream of N_2.

Au nanoparticle (Au NP) seed. We used the procedure described by Murphy[102] and co-workers to chemically synthesize Au NPs of 4 nm average diameter. In order to prepare the Au NPs seed solution, the following solutions are required: 0.01 M trisodium citrate salt, 0.01 M $HAuCl_4$, and 0.1 M sodium borohydride ($NaBH_4$). Hydrogen

tetrachloroaureate trihydrate ($HAuCl_4 \times 3H_2O$) was synthesized in the lab according to a literature procedure.[103] Trisodium citrate and sodium borohydride were used as received from Bio-Rad Laboratories and Sigma-Aldrich respectively. A 20 mL aqueous solution of 0.25 mM $HAuCl_4$ and 0.25 mL trisodium citrate was prepared. Next, 0.6 mL of ice-cold 10 mM $NaBH_4$ was added at once into the solution with rapid stirring for 2h. The solution turned red immediately after $NaBH_4$ addition, indicating Au NP formation. In this procedure $NaBH_4$ serves as a reducing agent, citrate as a capping agent to stabilize the particles by electrostatic repulsion, which prevents aggregation. The average particle size was 3-5 nm according to literature[102] and our previous work. These particles were attached to an electrode surface and served as an object in the study of the oxidation properties of metal nanoparticles as a function of size and also as a nucleation sites for the growth of Au and Ag nanostructures directly on the electrode surface.

Ag nanoparticle (Ag NP) seed. Ag NP seeds were prepared using a similar approach that described for Au NP seeds. In this case, a 20 mM of aqueous solution of 0.25 mM silver nitrate ($AgNO_3$) and 0.25 mM trisodium citrate was prepared. Ice-cold 10 mM $NaBH_4$ (0.6 mL) was injected at once into the solution and stirred for 2h. The solution went from colorless to yellow immediately after the addition of $NaBH_4$. The average particle size was 8-12 nm according to AFM and SEM measurements. The particles in this solution were used as a seed solution for chemical synthesis of Ag NP with different size, as described in Chapter III.

Au growth solution. Gold growth solution was used for synthesis of Au nanostructures directly on the electrode surface. It contains 4.5×10^{-4} M $HAuCl_4$, 0.1 M CTAB (cetyltrimethylammonium bromide), and 5.0×10^{-4} M ascorbic acid. Appropriately

functionalized with organic linker molecule and Au NP seeds Glass/ITO slides were immersed in Au growth solution for 1 hour at 25 °C. This led to the seed-mediated growth of Au nanoparticles (Au NPs), nanorods (NRs) and other shape nanostructures.

Ag growth solution. Ag growth solution was used for the synthesis of Ag nanostructures on the surface of Glass/ITO, 0.29 g (8×10^{-4} mol) of CTAB was first dissolved by sonication (Branson, Connecticut, Model 8510) in 10 mL of pH 10.6 phosphate buffer leading to a ~0.08 M CTAB solution. Next, 0.25 mL of 0.01 M AgNO$_3$, and 0.50 mL of freshly prepared 0.1 M ascorbic acid solutions were added in that order. Au seed-coated Glass/ITO slides were placed in this solution to grow Ag nanostructures. The substrate was immersed in growth solution and kept in it for 30 min at 28 °C.

2.3 PROCEDURES

Functionalization of Glass/ITO and Si/SiO$_x$ with organic silane linker. In order to attach metal NPs to the electrode surfaces, substrates were functionalized with aminopropyltriethoxysilane (APTES) or mercaptopropyltrimethoxysilane (MPTMS) by heating for 30 min in a solution containing 10 mL of 2-propanol, 100 μL of APTES or MPTMS and 4 to 5 drops of nanopure water. In this step, the surface hydroxyl groups (-OH) of the glass or silicon react with the methoxy (-O-CH$_3$) group of MPTMS or ethoxy (-O-CH$_2$-CH$_3$) group of APTES covalently to form a monolayer. The substrate surface modified with MPTMS produces a thiol (-SH) terminated surface. In the case of APTES, the substrate surface is amine terminated. Structures of APTES and MPTMS

molecules and the chemically functionalized Glass/ITO or Si/SiO$_x$ substrates are schematically illustrated on Figure 2.2.

Attachment of metal NPs to the surface of substrate. Au and Ag nanoparticles were attached to the functionalized Glass/ITO or Si/SiO$_x$ surfaces by simple immersion of the substrate in a colloidal solution of nanoparticles as shown in figure 2.3. Au and Ag NPs strongly attach to the –SH group of MPTMS through a covalent bond. Metal NPs attach to the APTES – functionalized surface through electrostatic interactions between negatively charged particles and positively charged amine – terminated surface of the substrate. In this case, one is able to control the coverage of NPs on the surface by varying the soaking time in the colloidal NPs solution.

Chemical growth of metal nanostructures directly on the electrode surface. The functionalized Glass/ITO/MPTMS/Au NPs slide was placed in the Au or Ag growth solution described above for 1 hour or 30 min, respectively. The growth solutions remained colorless throughout the entire time indicating that reduction of Au^{3+} to Au^0 and Ag$^+$ to Ag^0 did not occur in solution. The scheme of the entire growth procedure starting from functionalization of substrate is shown in Figure 2.3. The attached Au NPs seeds act as nucleation sites for growth of gold and silver nanostructures, leading to formation of variety of shapes. Most of the nanostructures growth directly on the surface had a spherical/near spherical shape (~90%), also growth of some rods, triangle and hexagons were observed.

Construction of multilayer polymer and metal nanoparticle films using layer-by-layer procedure. A layer-by-layer procedure was used in order to construct multilayer films of polymers and mixed films of polymer and metal nanoparticles.

21

MPTMS

$$HS - CH_2CH_2CH_2 - \overset{\displaystyle OCH_3}{\underset{\displaystyle OCH_3}{|}} Si - OCH_3$$

APTES

$$H_2N - CH_2CH_2CH_2 - \overset{\displaystyle OCH_2CH_3}{\underset{\displaystyle OCH_2CH_3}{|}} Si - OCH_2CH_3$$

OH   OH   OH   OH

Glass/ITO or Si/SiO$_x$

MPTMS   APTES

SH SH SH SH

Si   Si   Si   Si

Glass/ITO or Si/SiO$_x$

$NH_3^+ NH_3^+ NH_3^+ NH_3^+$

Si   Si   Si   Si
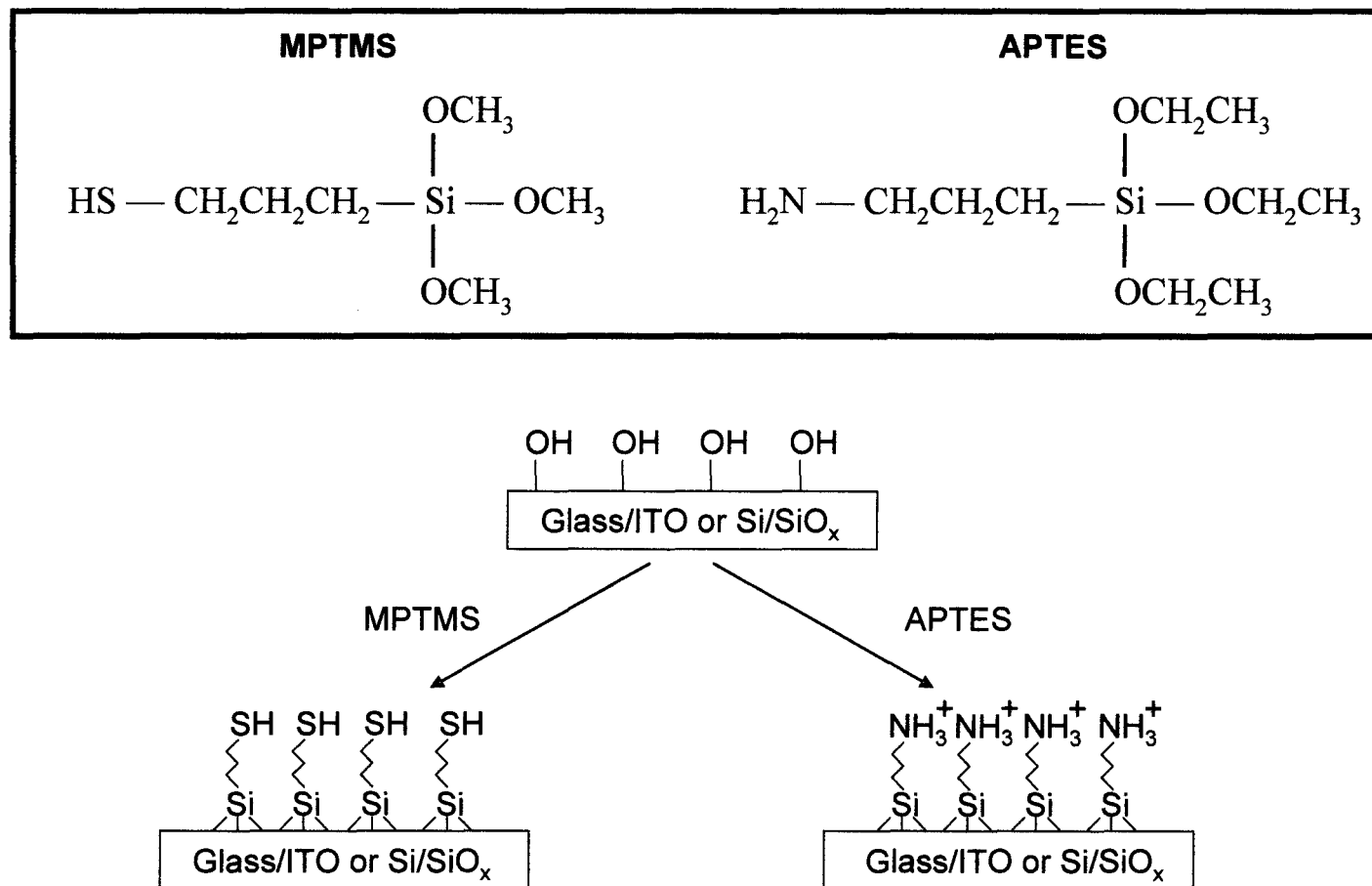
Glass/ITO or Si/SiO$_x$

Figure 2.2 Structures of MPTMS and APTES molecules and schematics of chemically functionalized surfaces of Glass/ITO and Si/SiO$_x$.
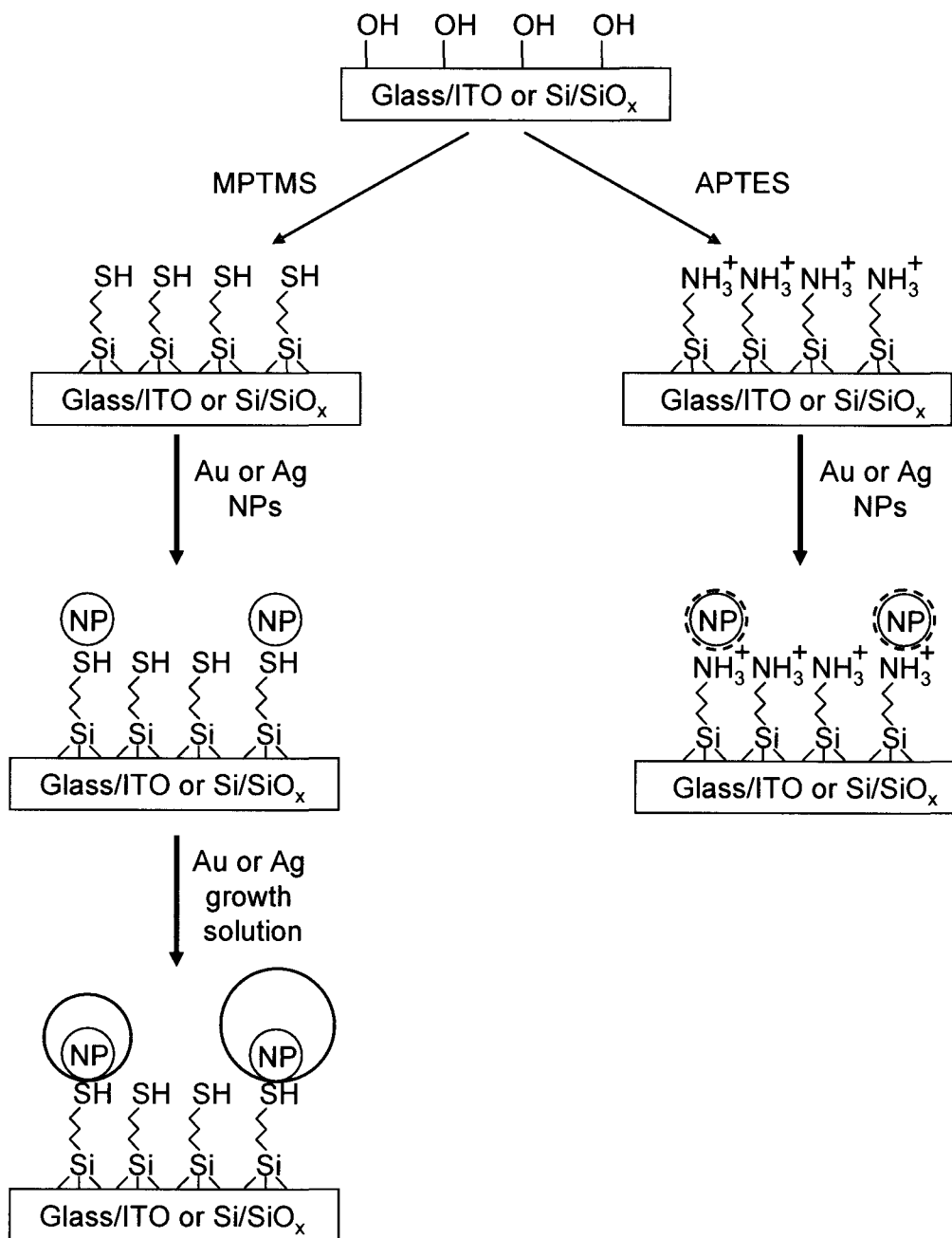
Figure 2.3 Attachment of metal nanoparticles to the functionalized substrate surface and the direct chemical growth of metal nanostructures.

Figure 2.4 (A) shows the steps for the preparation of multilayer polymer films. First, the surface of the Glass/ITO was functionalized with APTES as described above in this section. Then, the Glass/ITO/APTES slide was immersed in an aqueous solution of 5% wt. polystyrene sulfonate (PSS), which is a negatively charged polymer. Adsorption of PSS is possible due to electrostatic interactions between the positively charged amine – terminated surface of Glass/ITO and the negatively charged polymer. In step 3, the Glass/ITO/APTES/PSS substrate was immersed in a 5% wt. aqueous solution of Poly-(diallyldimethylammonium) (PDDA), which is positively charged. Adsorption in this step occurs between the negatively charged PSS and the positively charged PDDA molecules. Each deposition cycle reverses the surface charge leaving the surface primed for the next oppositely-charged polymer. The immersion time for both polymers was 20 min in all experiments. The same approach was used to assemble metal nanoparticle/polymer multilayer films. Here we substitute PSS with negatively charged metal nanoparticles (see Figure 2.4 (B)). Immersion time for metal nanoparticles was 20 min. It is theoretically possible to build an infinite number of layers.

2.4 CHARACTERIZATION AND INSTRUMENTATION

2.4.1 Electrochemical Methods

Electrochemical techniques are experimental methods developed to study the chemical phenomena associated with electron transfer at the interface of an electrode and
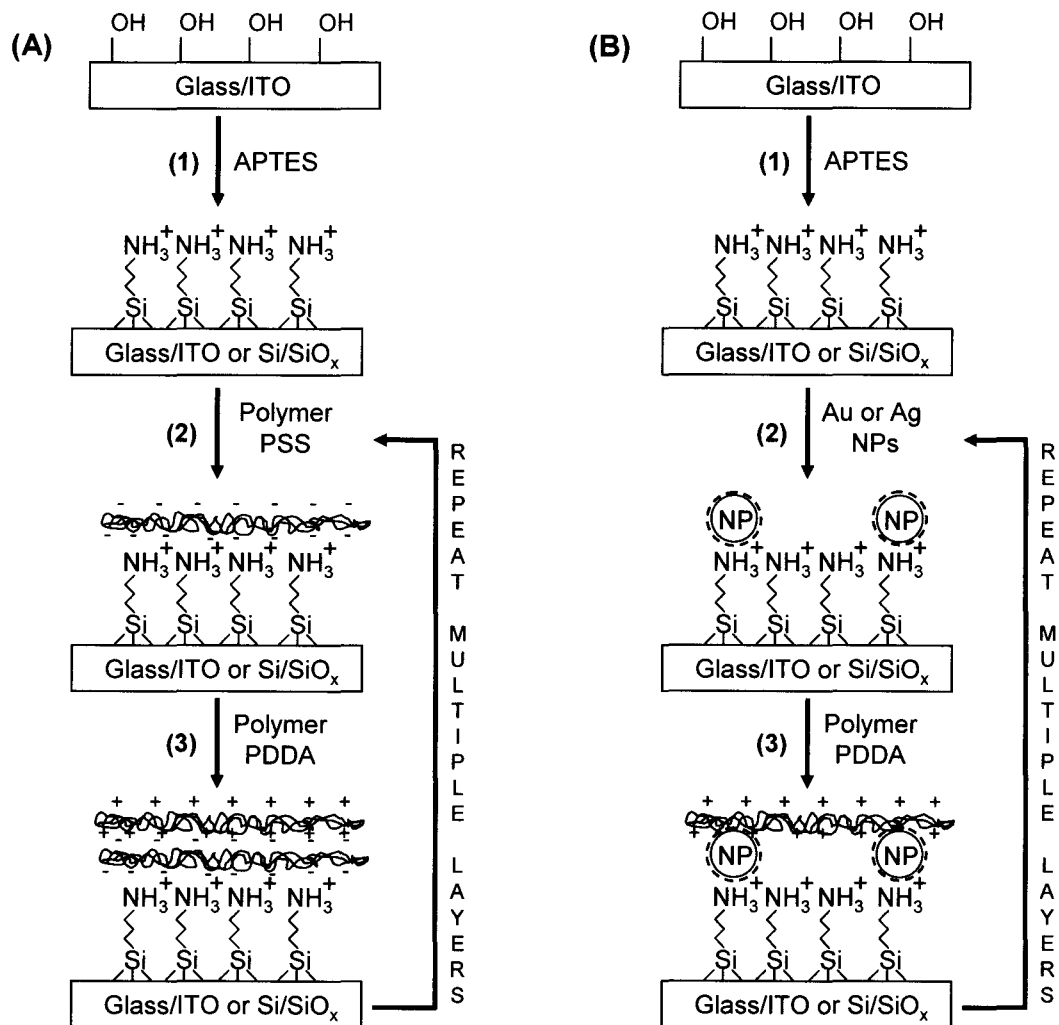
Figure 2.4 Layer-by-layer procedures (A) for multilayer polymer films (B) for multilayer polymer/metal nanoparticle films.

solution. This section will describe the electrochemical cell set-up, and techniques that were used in the studies. Figure 2.5 shows the basic electrochemical set-up that was used in this research. The main components of the system are: the electrochemical cell, which consists of three electrodes and a beaker with electrolyte, a potentiostat, and a computer for data acquisition and analysis.

Electrochemical cell. The electrochemical cell consists of three electrodes:

1) Working electrode – an electrode on which the electrochemical reaction occurs.

2) Reference electrode – is a half cell with a known reduction potential. Its role is to act as a reference in measuring and to control the working electrode potential. It does not pass any current.

3) Counter electrode – an electrode used to close the circuit. It passes all the current needed to balance the current observed at the working electrode.

In this work, Glass/ITO/linker/Metal NPs served as a working electrode, Ag/AgCl (3M KCl) was the reference electrode and a Pt wire was the counter electrode. The main requirement for the reference electrode is that its potential must be stable. The Ag/AgCl electrode is usually in the form of silver wire coated with AgCl. The coating is done by making silver the anode in an electrolytic cell containing hydrochloric acid (HCl). The electrolyte solutions used in electrochemical measurements were varied depending on the goal of the experiment and will be specified for each particular experiment in the following chapters.

Potentiostat. The potentiostat is an electronic instrument required to run most of the electroanalytical experiments. The system measures and controls the voltage
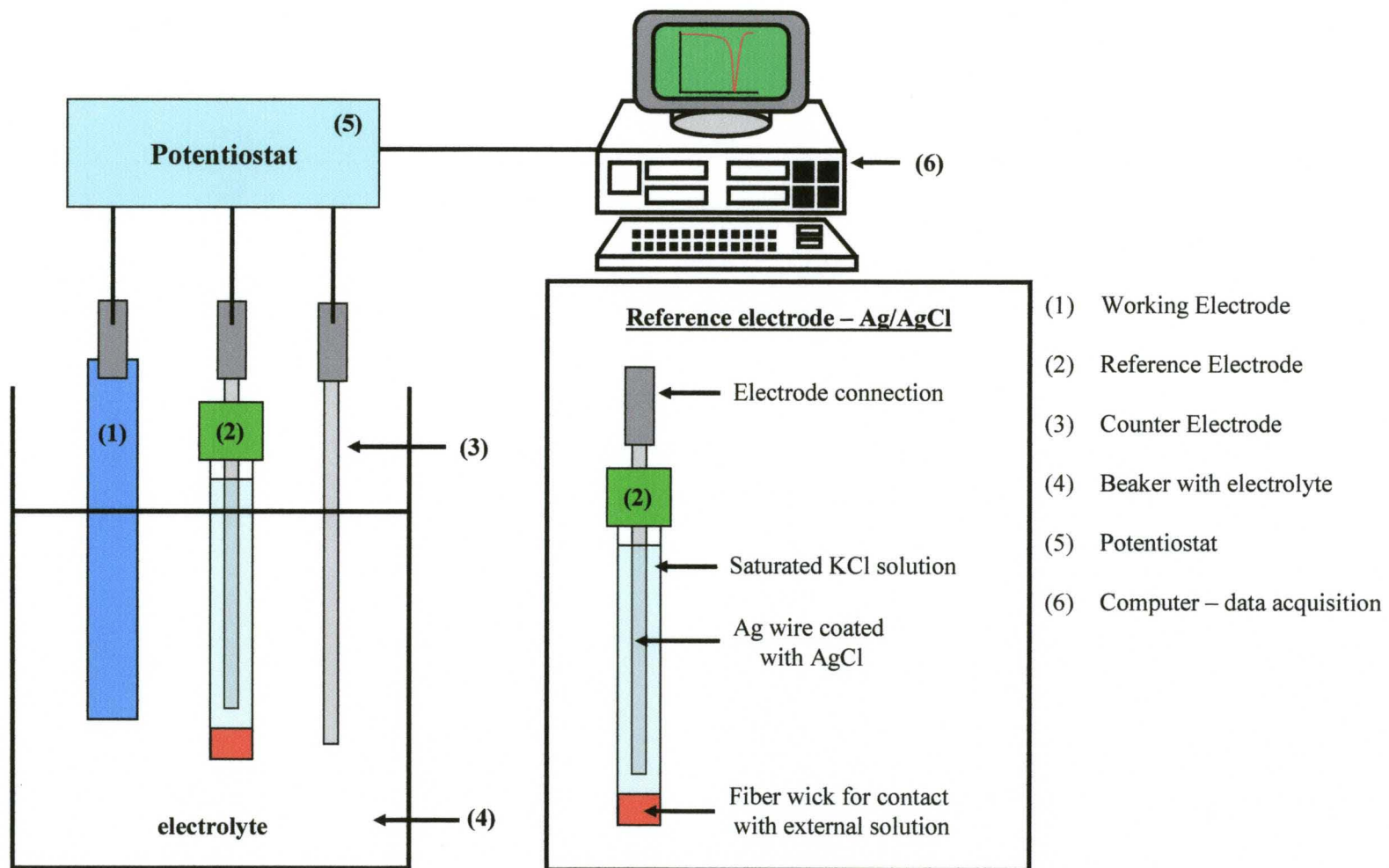
Figure 2.5 Electrochemical set-up

difference between the working electrode and reference electrode and also measures the current flow between the working electrode and counter electrode. CH Instruments (Austin, TX) 630C electrochemical workstation was used in all experiments.

Linear sweep voltammetry (LSV) – stripping voltammetry. Stripping voltametry is a widely used electroanalytical tool that is applied to determine the composition and amount of species present on the electrode surface. LSV is a method in which the current at a working electrode is measured while the potential between the working electrode and a reference electrode is swept linearly in time. The excitation potential-time waveform and current-potential response in LSV are shown on Figure 2.6. The slope of excitation wave is equal to:

$$slope = \frac{\Delta E}{\Delta time} \qquad \text{(Eq. 2.1)}$$

and has units of volts per unit of time, and is generally called the scan rate of the experiment. Oxidation or reduction of species is registered as a peak in the current signal at the potential at which the species begins to be oxidized or reduced. Figure 2.7 shows the typical stripping voltammogram of Glass/ITO/APTES/Ag NPs (~8nm). The scan begins at 0.1 V, potential at which silver is stable. Then, the potential is swept in the positive direction and the current measured. The negative flow of current with a maximum at ~280 mV corresponds to the oxidation of Ag according to the reaction:

$$Ag^0_s - e^- \rightarrow Ag^+_{aq} \qquad \text{(Rxn. 2.1)}$$

During the scan the current reaches the maximum and then drops back to the baseline once all of the Ag is oxidized to Ag^+. The resulting i-V curve can be used to determine the amount of Ag oxidized. The area under the oxidation peak is the charge passed during the oxidation reaction. The SI unit of charge is Coulomb (C). According to

Excitation

Applied Potential, [V]

E_2

E^0

E_1

Time, [sec]

Response

Current, [A]

E_1

E^0

E_2

Applied Potential, [V]
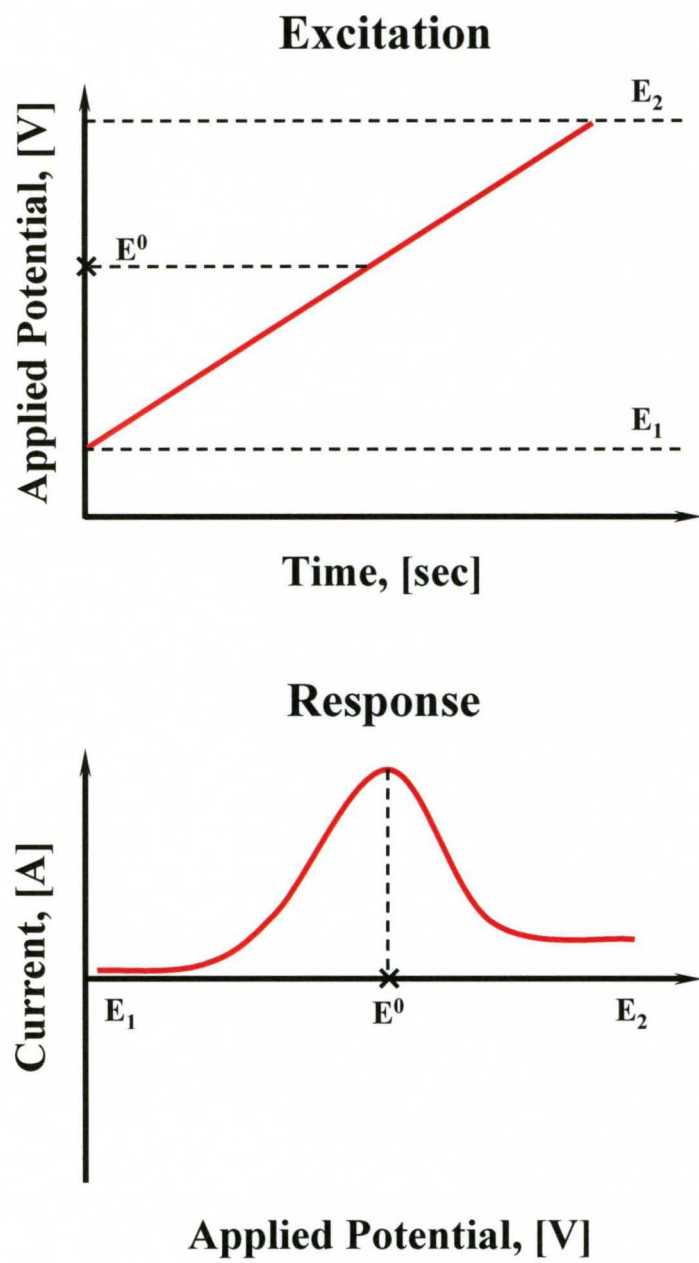
Figure 2.6 The excitation waveform and current-potential response in a LSV experiment.
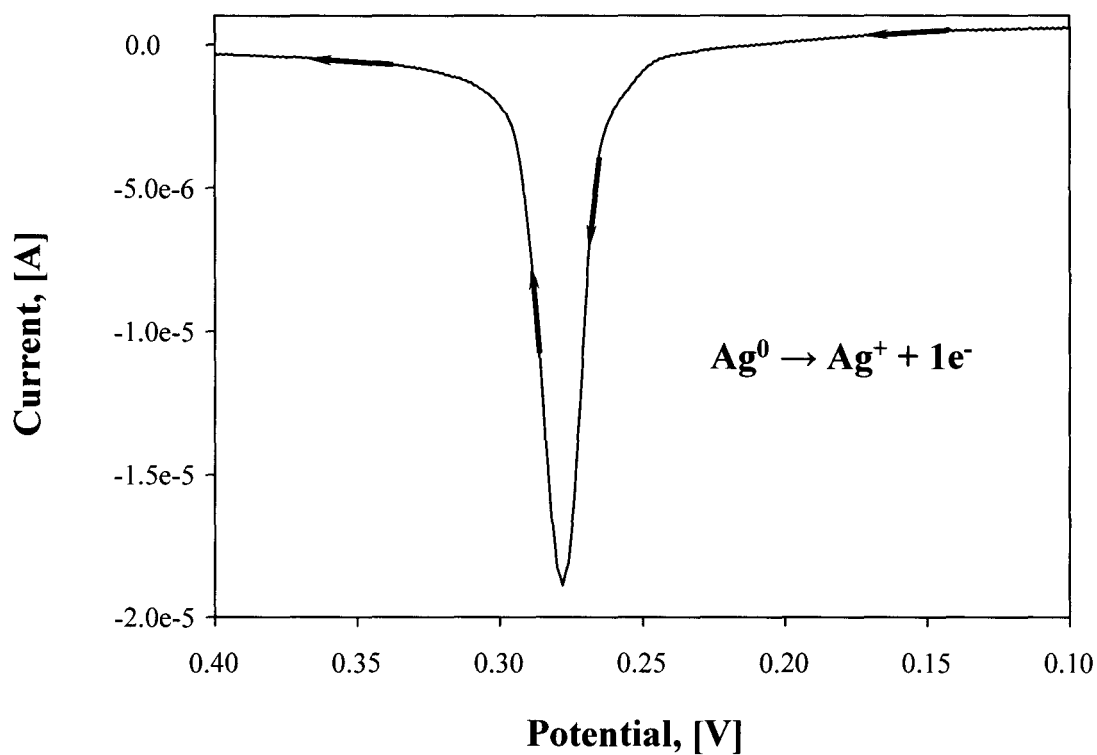
Figure 2.7 LSV of Glass/ITO/APTES/Ag NPs in 0.5 M H_2SO_4, scan rate 1 mV/s.

The arrows indicate the direction of the scan.

Faraday's first law, the mass of a substance changed at an electrode during the reaction is directly proportional to the quantity of electricity transferred at that electrode. Faraday's law is expressed by the following equation:

$$mol = \frac{Q}{nF}$$ (Eq. 2.2)

where *mol* is the number of moles of oxidized or reduced species, Q is the electric charge passed through the working electrode during the reaction (area under the peak), n is the number of electrons involved in the reaction, F is the Faraday's constant ($96,485$ C×mol^{-1}). LSV was used in this work to study the electrochemical oxidation of metal nanoparticles, and also for underpotential deposition (UPD) of copper.

Cyclic voltammetry (CV). Cyclic voltammetry is very similar to LSV. In this method, the voltage is swept between two values at a fixed rate. However, when the voltage reaches E_2 (Figure 2.8 – Excitation wave), the scan is reversed and the voltage is swept back to E_1. A typical expected response of a reversible redox couple during a single scan is shown in Figure 2.8. It is assumed that only the oxidized form O is initially present. The forward sweep produces an identical response to that seen for the LSV experiment. During the reverse scan, equilibrium moved back and R molecules (produced in the forward scan) are reoxidized back to O. For a reversible electrochemical reaction, the CV recorded has certain well defined characteristics:

1. The voltage separation between the current peaks is

$$\Delta E = E_p^a - E_p^c = \frac{59}{n} mV$$ (Eq. 2.3)

2. The positions of the peak voltages are not affected by the voltage scan rate

3. The ratio of the peak currents is equal to one

31

Excitation
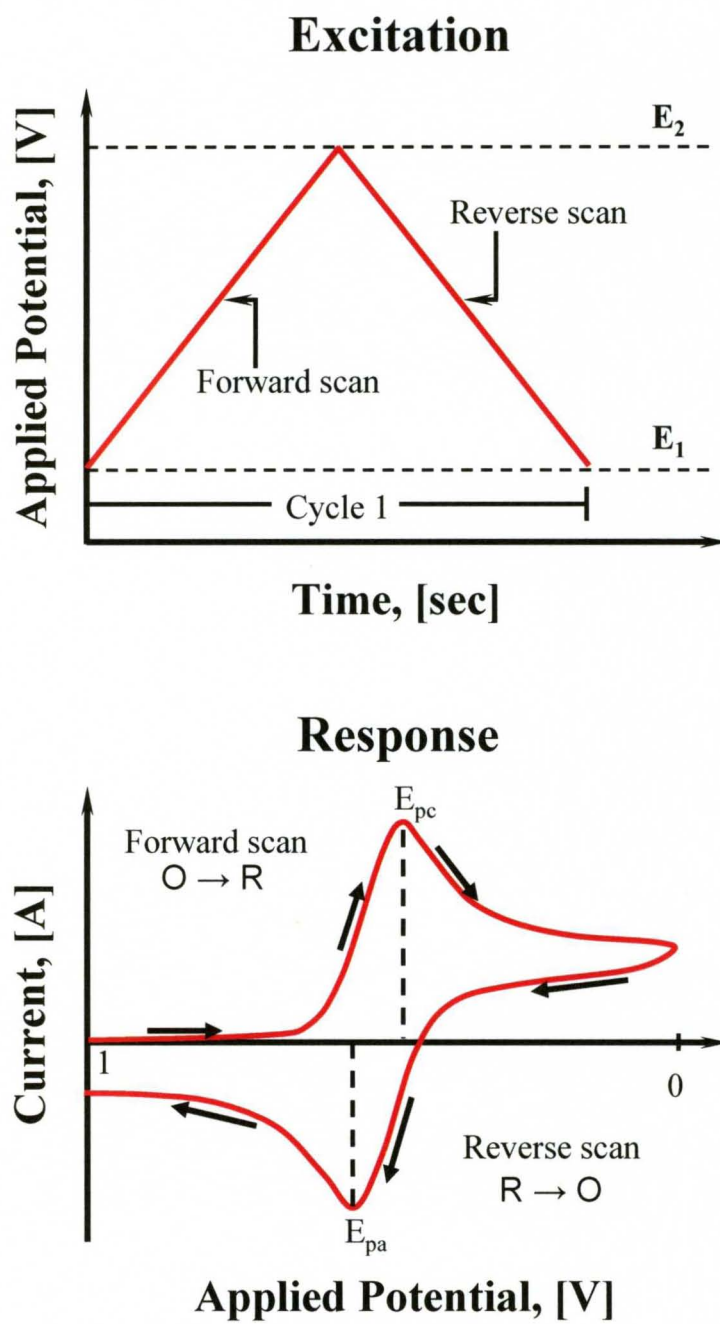
Response

Figure 2.8 The excitation waveform and current-potential response in a CV experiment.

$$\left| \frac{i_p^a}{i_p^c} \right| = 1 \qquad\qquad \text{(Eq. 2.4)}$$

4. The peak currents are proportional to the square root of the scan rate υ

$$i_p^a \text{ and } \quad i_p^c \quad \propto \quad \sqrt{v}$$

CV was used to study the electrochemical oxidation – reduction of Au^{3+} for the electrochemical deposition of Au nanostructures and Cu^{2+} for the UPD studies.

Chronocoulometry (CC). Chronocoulometry involves the measurement of the charge – versus – time response to an applied potential step waveform. A potential step waveform and the response for a CC experiment are shown in Figure 2.9. The experiment typically starts at a potential E_1 at which there is no electrolysis. The potential is then changed instantaneously (stepped) to a value that leads to oxidation or reduction of species in solution and is held at that potential for the desired time period (τ). In a single potential step experiment, the experiment is complete at the end of this step. In a double potential step experiment, the potential is then stepped to a third potential at which the species formed on the first step is reelectrolyzed. The single step potential method was used in this work. The equation for the charge (Q) versus time (τ) is obtained by integrating the Cottrell equation:

$$Q = \frac{2nFACD^{1/2}\tau^{1/2}}{\pi^{1/2}} + Q_{dl} + Q_i \qquad\qquad \text{(Eq. 2.5)}$$

were n is the number of electrons, F is the Faraday's constant, A is the surface area, C is the concentration, D is the diffusion coefficient, τ is the time, Q_{dl} is the charge due to double layer charging, and Q_i is the charge due to reaction of adsorbed species.
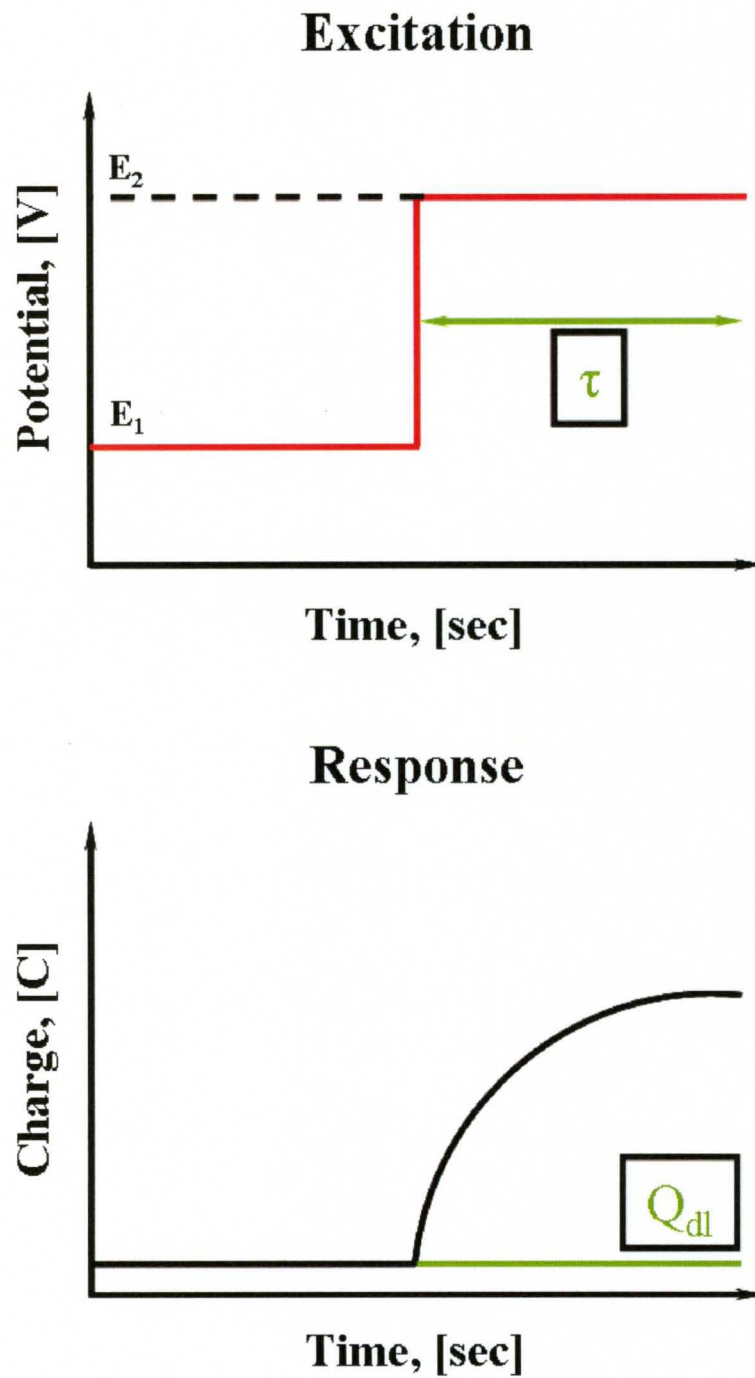
Figure 2.9 The excitation waveform and current-potential response in a CC experiment.

Applications of CC include the measurement of electrode surface areas, diffusion coefficients, concentrations, kinetics of heterogeneous electron transfer reactions and chemical reactions coupled to electron transfer, adsorption, and the effective time window of an electrochemical cell. In this work CC was used to electrochemically deposit Au NPs of different size, by varying the deposition potential and keeping the amount of Au deposited constant.

2.4.2 Ultraviolet – Visible Spectroscopy (UV-vis) and Localized Surface Plasmon Resonance (LSPR)

UV-Vis spectroscopy data were obtained using a Varian Cary 50 Bio UV-Visible Spectrophotometer. It measures the intensity of light (I) passing through a sample, and compares it to the intensity of light before it passes through the sample (I_0). The ratio I/I_0 is called the transmittance (T), and is usually expressed as a percentage (%T). The absorbance, A, is based on the transmittance:

$$A = -\log(\%T / 100\%) \qquad \text{(Eq. 2.6)}$$

The basic parts of a spectrophotometer are a light source (UV and visible), a monochromator to separate the different wavelengths of light, a sample holder, a detector, and a signal processor and readout. For molecules, the absorption of light in the UV-vis region occurs when the light energy matches the energy required for a possible electronic transition within the molecule. Some of the light intensity will be absorbed as the electron is promoted to a higher energy orbital. A spectrophotometer records the wavelength at which the absorption occurs, and the degree of absorption at each wavelength.

Au or Ag nanostructures absorb strongly in the visible region due to the well-known localized surface plasmon absorption. The excitation of conducting electrons of a metal by light is referred to surface plasmon resonance (SPR) for planar surfaces or localized surface plasmon resonance (LSPR) for nanometer-sized metallic structures. For the case of LSPR, light interacts with particles much smaller than the incident wavelength and leads to a plasmon that oscillates locally around the nanoparticle. Surface plasmon absorption bands are characteristic of the type of material and are highly sensitive to the size, and shape of nanostructures. In the case of nanostructures for which one dimension is greater than the other, such as high aspect ratio nanorods (NRs) and nanowires (NWs), the LSPR band splits into two peaks. The shorter wavelength band is called transverse plasmon absorption band while the longer wavelength one is called the longitudinal band. The transverse band is produced by the oscillation of the electrons perpendicular to the major axis of the rods while the longitudinal band is caused by the oscillation of the electrons along the major axis of the NRs or NWs. The greater the aspect ratio (length divided by width) of the nanostructure, the greater the λ_{max} of the longitudinal band.

UV-vis spectroscopy was used to characterize the solutions of different size silver NPs, Au/Ag alloy NPs solutions, and Au or Ag NPs or alloy NPs attached to the electrode surface.

2.4.3   Scanning Electron Microscopy (SEM).

Conventional light microscopes use a series of glass lenses to bend light waves and create a magnified image. The SEM creates the magnified image by using electrons instead of light waves. Schematic drawing of the SEM is shown in Figure 2.10.
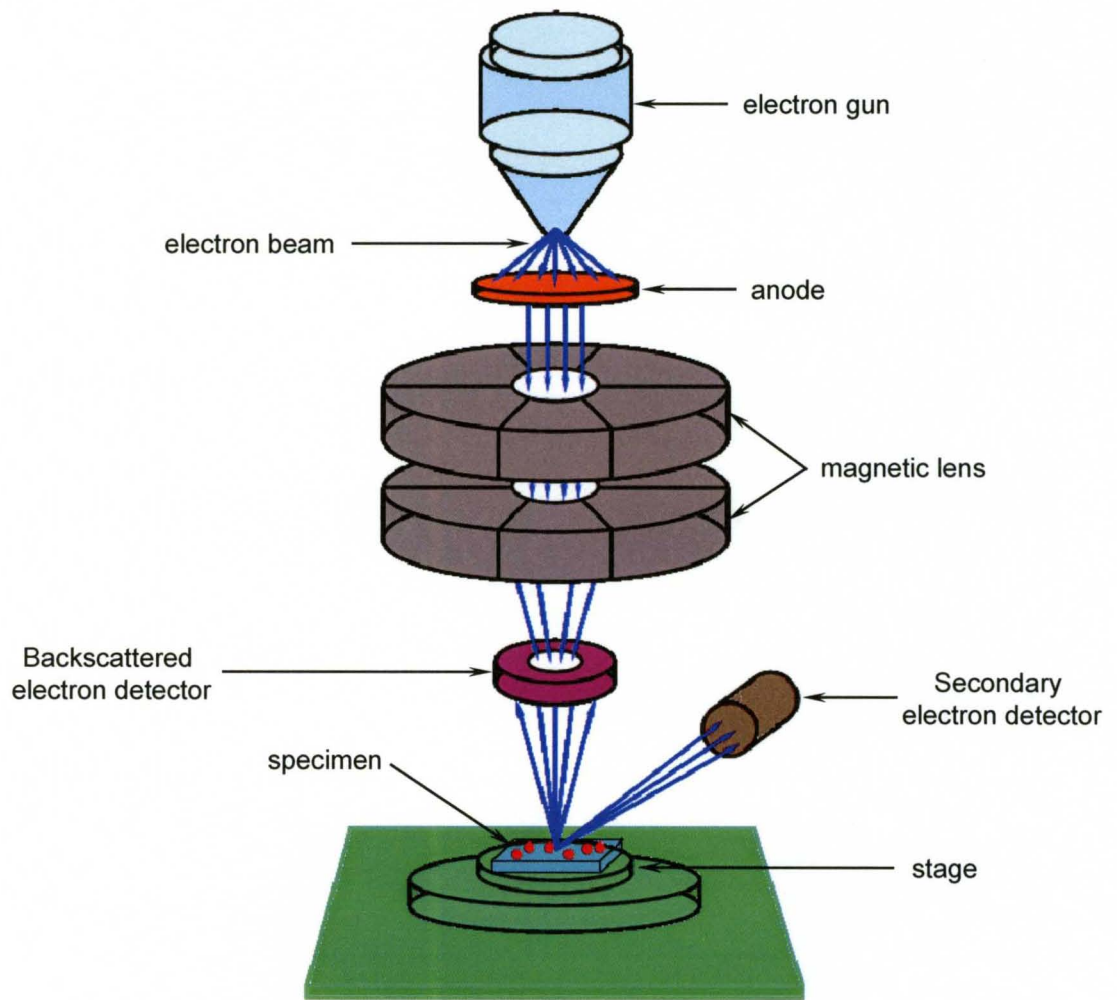
Figure 2.10 Schematic drawing of SEM.

Essential components of all SEMs include the following: electron source (gun), electron lenses, sample stage, detectors for all signals of interest, display and data output devices. A beam of electrons is produced at the top of the microscope by heating of a metallic filament, most commonly made of tungsten and lanthanum hexaboride. This beam travels downward through a series of magnetic lenses designed to focus the electrons to a very fine spot. Near the bottom, a set of scanning coils (not shown) moves the focused beam back and forth across the specimen, row by row. As the electron beam hits each spot on the sample, other electrons (backscattered or secondary) are ejected from the sample. Detectors collect the secondary (SE) or backscattered (BSE) electrons, and convert them to a signal that is sent to a viewing screen, producing an image. As shown in Figure 2.11, these are the most common type of electrons used to obtain topographical information about the sample.

Detection of secondary electrons is the most common imaging mode. Secondary electrons produced when the energy from the primary beam electrons causes the atoms of the specimen to ionize. As a result of this ionization, electrons are emitted from the sample. These electrons are called secondary electrons and have energies which are typically less than 50 eV. Due to their low energy, these electrons originate within a few nanometers from the surface (50 to 500 Å) and it is necessary to collect them with a positively biased collector in order to form an image. Bright areas on the image correspond to areas of the sample where large quantities of secondary electrons were emitted relatively to other areas of the sample.

Backscattered electrons have energies comparable to those of the incident beam. Because these electrons move fast, they travel in straight lines. The negatively charged

SEM Setup

Electron/Specimen Interactions
When the electron beam strikes the sample, both **photon** and **electron** signals are emitted
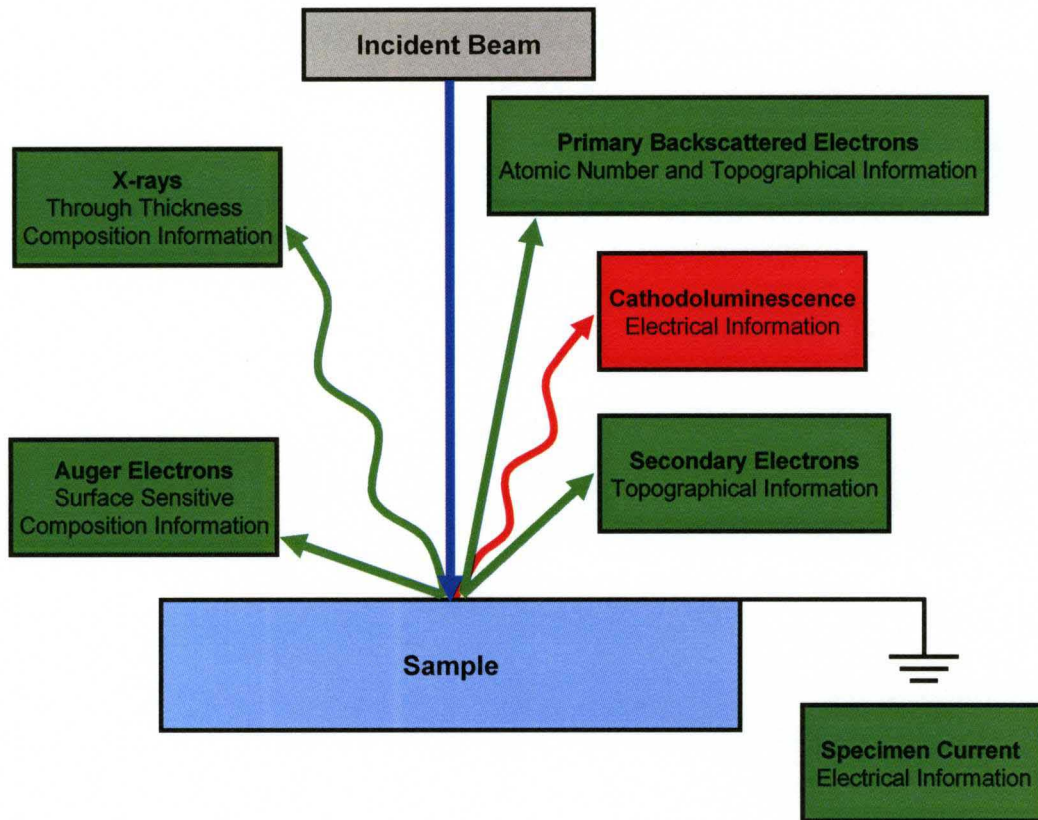
Figure 2.11 Electron beam/specimen interactions.

electrons are attracted by positively charged nuclei, when the angle at which the electrons hit the sample is correct, then, instead of being captured by nuclei, they will circle around the nuclei and come back out of the sample without slowing down. The number of backscattered electrons increases with increase of the size of the nuclei, which can be used to obtain an image that represents the sample composed of different elements.

SEM can provide topographic, morphological, compositional and crystallographic information about the sample. The strengths of SEM are: easy operation, rapid data acquisition, and minimal sample preparation. The drawbacks of SEM are: it is limited to conductive or semiconductive samples, it requires vacuum to operate, and it damages the sample.

In this work, a Carl Zeiss SMT AG SUPRA 35VP field emission scanning electron microscope (FESEM) operating at an accelerating voltage of 20.00 kV and using an in-lens ion annular secondary electron detector was used.

2.4.4 Atomic Force Microscopy (AFM).

AFM images were collected with a Veeco Metrology Multimode Nanoscope IIIA atomic force microscope operating in the tapping mode. This technique, unlike SEM, allows imaging of the samples with atomic resolution. A typical AFM setup is shown in Figure 2.12. The main components of AFM are a microscale cantilever with a nanosharp tip, a piezoelectric scanner, a laser source, and a photodiode detector. AFM tips and cantilevers are microfabricated from Si or Si_3N_4 and typically, the tip radius varies from a few to 10s of nm. The tip is scanned over the surface with feedback mechanisms that
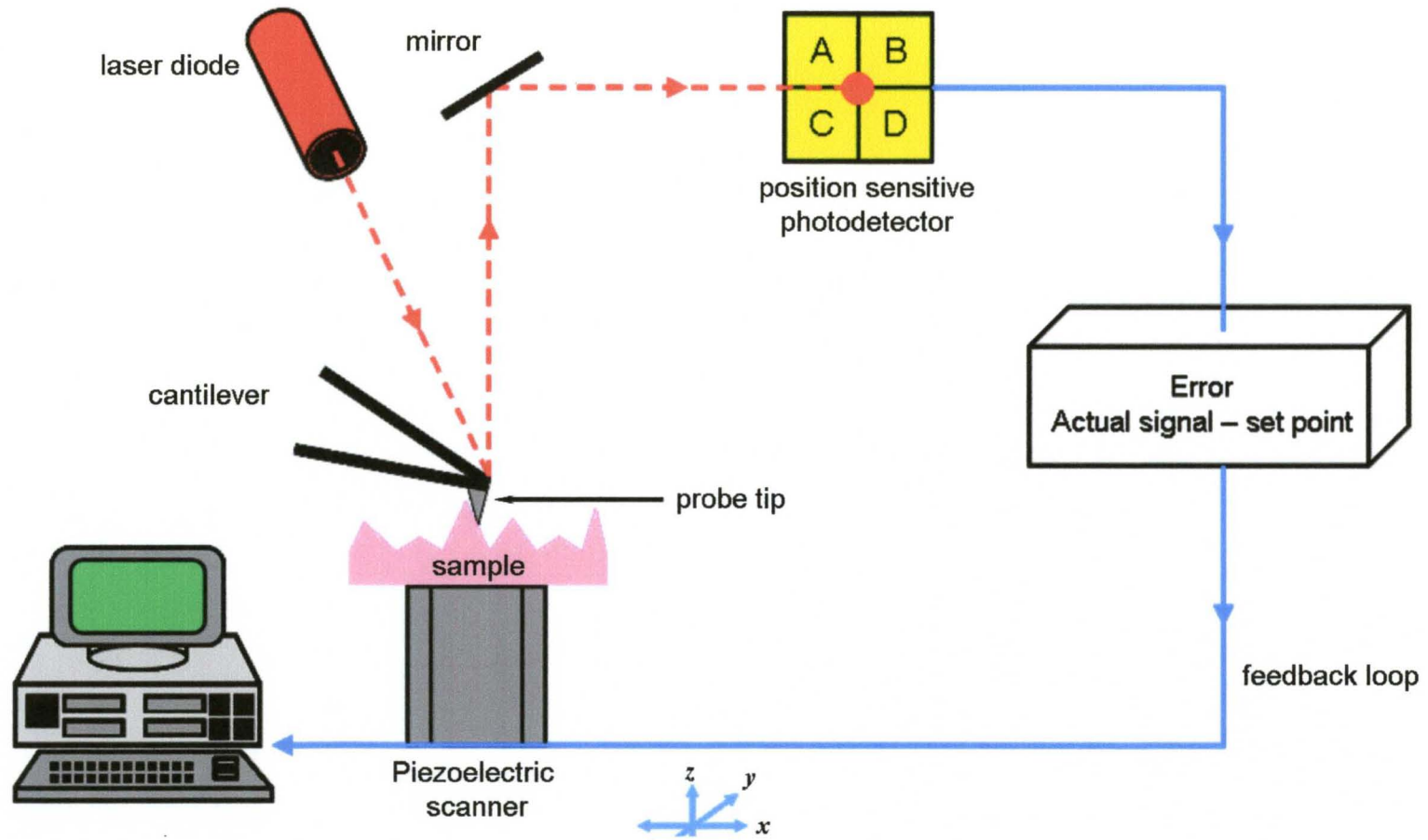
Figure 2.12 Typical AFM setup.

enable the piezoelectric scanners to maintain it at a constant force or height above the sample surface. The laser is focused onto the back of a reflective cantilever. The interactions between the tip and the surface are detected as deflections of a cantilever during scanning, measured by deflections of a laser beam reflected off the metal coating on a cantilever. The laser beam is reflected on to the photocell and recorded as differential electrical signal. The tip movement during scanning changes the amount of reflected beam to the photocell thus producing different electrical signals that are translated further to topographical images. The tip-to-sample distance is controlled by the feedback mechanism and the piezoelectric tube capable of moving the sample in the z direction in sub – angstrom resolution. The sample is scanned in the x and y direction.

The most common modes of operation are contact and tapping. In the contact mode, the tip scans the sample in contact with the surface. In contact mode AFM, the force between the tip and the surface is held constant at a desired value called the setpoint, causing static cantilever deflection during scanning. If the measured deflection varies from the setpoint, the feedback loop changes the voltage applied to the piezoelectric scanner which raises or lowers the surface appropriately to restore the desired deflection. The topography of the surface is measured by plotting the distance the surface raised or lowered as a function of x-y tip position while maintaining constant deflection.

Tapping mode AFM relies on oscillating the cantilever at its resonant frequency by a piezoelectric crystal, and maintaining the amplitude of this oscillation constant by a feedback loop. The vibrating tip is brought close to the surface to a distance of about 10 Å, and the intermittent contact with a sample surface changes the oscillating amplitude.

The taller features on the surface decrease the amplitude of the oscillation while depressions cause an increase in the amplitude. This change is detected and the tip position is modulated to return to the previous amplitude by a feedback loop.

AFM provides a three – dimensional map of the sample surface. In contrast to SEM, one can use conductive and insulator samples and the experiments can be performed under ambient conditions or in solutions. One disadvantage of AFM versus SEM is that it is much slower. It takes a few minutes to scan a 10 μm × 10 μm image.

CHAPTER III

SIZE-DEPENDENT ELECTROCHEMICAL OXIDATION OF SILVER

NANOPARTICLES

Here we quantify the electrochemical oxidation of Ag nanoparticles (NPs) as a function of size by electrostatically attaching Ag NPs synthesized by seed-mediated growth in the presence of citrate (dia. = 8 to 50 nm) to amine-functionalized Glass/ITO electrodes and obtaining a linear sweep voltammogram from 0.1 V, where Ag^0 is stable, up to 1.0 V and observing the peak potential (E_p) for oxidation of Ag^0 to Ag^+. Electrostatic attachment to the organic linker presumably removes direct interactions between Ag and ITO and allows control over the total Ag coverage by altering the soaking time. This is important as both metal-electrode interactions and overall Ag coverage can affect E_p. E_p shifts positive from an average of 275 to 382 mV as the Ag NP diameter increases for a constant Ag coverage and under conditions of planar diffusion, suggesting a shift in E_p due to a thermodynamic shift in E^0 for the Ag/Ag^+ redox couple with size. The negative shift in E_p with decreasing Ag NP radius follows the general trend predicted by theory and demonstrated by previous qualitative experimental observations.

3.1 INTRODUCTION

There are two main reasons to expect size-dependent electrochemical oxidation of metal nanoparticles. First, theoretical and experimental studies showed that the standard redox potential of metal nanoparticles decreases with decreasing size.[85,86] For example, Henglein predicted large negative shifts in the redox potential for small Ag_n clusters (n=1 to 15) as the number of atoms in the cluster decreases.[85] Plieth similarly predicted a negative shift in the redox potential proportional to (1/radius) for small nanoparticles relative to the bulk metal based on the difference in surface free energy between bulk metal and the same number of atoms dispersed into smaller NPs.[86] According to Plieth, the standard electrode potential E^0_p of a small metal particle shifts negatively via Equation 3.1

$$E^0_p = (E^0_{bulk} - \frac{2\gamma V_m}{zFr})$$ (Eq. 3.1)

where γ is the surface tension, V_m is the molar volume, z is the lowest valence state, F is Faraday's constant (96,485 $C \times mol^{-1}$), and r is the radius. Experimentally, Brus and co-workers showed that large Ag NPs grow at the expense of small NPs on a conductive surface (Ostwald ripening) due to the predicted negative shift in oxidation potential for smaller sizes.[76] The work of Compton and co-workers offers a second explanation for size-dependent electrochemical oxidation of metal nanoparticles.[87-90] Their work addresses the oxidation (stripping) of an array of metal nanoparticles attached to a conductive electrode surface. The different electrochemical behavior is based on the size-dependent diffusion profiles of the metal ions that emanate from the oxidizing array of nanoparticles. Under the assumption that E^0 does not shift with particle size, theory

predicts that in electrochemical reversible systems the peak potential (E_p) depends on the metal coverage, but not the NP radius under conditions where the diffusion layers of the nanoparticles overlap (planar diffusion) and vice versa when they do not overlap.[89] Under conditions of planar diffusion, the oxidation of Ag NPs (diameter = 25 to 100 nm) on a basal-plane pyrolytic graphite electrode did not exhibit a size-dependent E_p experimentally.[87] In irreversible systems, theory predicts that E_p is independent of metal coverage but shifts negative as the NP radius decreases.

A number of microscopy studies have shown that tiny clusters of Cu on Au[74] and Ag on graphite[75] (<1.0 nm) exhibit greater stability against electrochemical oxidation (+200 to +500 mV) compared to the bulk metal, contrasting the predictions of Plieth[86] and Henglein.[85] These results raise interesting questions about the electronic, structural, and chemical effects of the electrode – metal interaction on metal NP oxidation potential and kinetics.[74,75,104] These studies lacked direct quantitative measurements of the shift in oxidation potential of a metal as a function of size that could be compared to Eq 3.1.

3.2 EXPERIMENTAL DETAILS

General scheme of experiments used in this study is shown in Figure 3.1 Main steps include: 1) chemical synthesis of Ag NPs of different size by seed-mediated citrate reduction method, 2) attachment of Ag NPs to the electrode surface, 3) characterization of these NPs by UV-vis, SEM and LSV.

Synthesis of AgNPs of different size. We used the procedure described by Pyatenko et al. to synthesize citrate-capped spherical AgNPs with controlled size.[105] A solution containing x mL of 0.01 M $AgNO_3$ and 100-x mL of water was brought to boiling followed by the addition of 2 mL of 1% trisodium citrate solution by weight and 4 mL of Ag NP seed solution (described in Chapter II) for a total volume of approximately 106 mL. After boiling with intense stirring, the solution was cooled to room temperature, analyzed by UV-vis spectroscopy and used. The amount of $AgNO_3$ (Ag^+) in the solution controlled the eventual size of the Ag NPs by altering the Ag^+/Ag Seed (n_+/n_s) mole ration in solution, where n_+ is the mol Ag^+ and n_s is the total mol of Ag in the Ag NPs. As the ration of Ag^+/Ag seed increased, the size of Ag NPs increased. The ratios studied included 0:0 (Ag seed only), 5:1, 10:1, 20:1, 40:1, 60:1 and 100:1. This required x = 0, 0.5, 1.0, 2.0, 4.0, 6.0 and 10.0 mL of $AgNO_3$ in the solution, respectively, as shown in Table 3.1. The mechanism of NP growth was described by Henglein in 1999[106] and schematically shown in Figure 3.2. According to this mechanism the growth of Ag NPs is conducted via the reduction of silver ions on their surface.
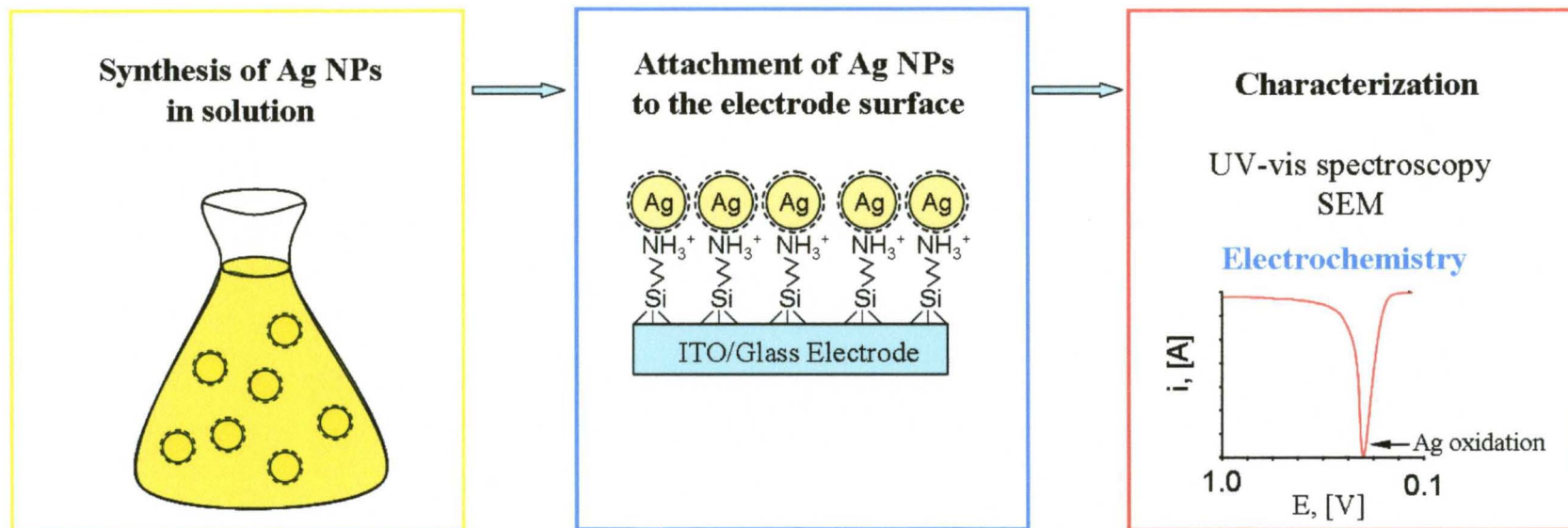
Figure 3.1 General scheme of experiment for measuring the oxidation potential of Ag NP as a function of size.

Ag$^+$/Ag seed (n_+/n_s) Ratio	Vol H$_2$O (mL)	Vol 0.01 M AgNO$_3$ (mL)	Vol 2.5x10^{-4} M Ag Seed (mL)	Vol 1% Trisodium citrate (mL)
5	99.5	0.5	4.0	2.0
10	99.0	1.0	4.0	2.0
20	98.0	2.0	4.0	2.0
40	96.0	4.0	4.0	2.0
60	94.0	6.0	4.0	2.0
100	90.0	10.0	4.0	2.0

Table 3.1 Compositions used for seed-mediated synthesis of various – sized Ag NPs
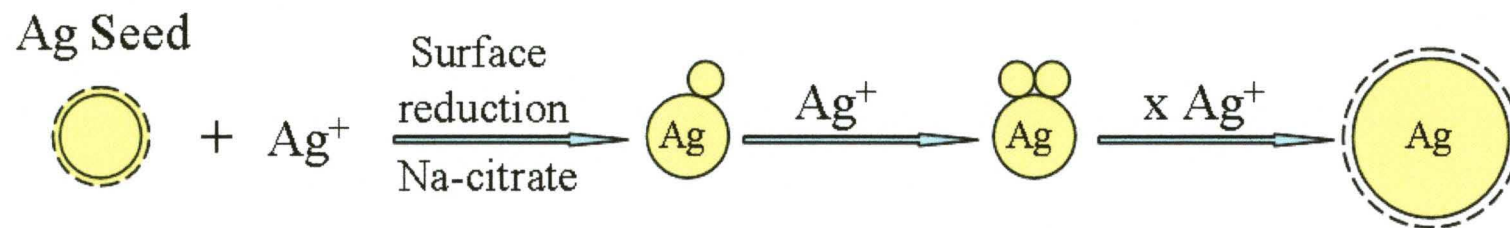
Figure 3.2 Schematic of Ag NP growth by citrate reduction.

Attachment of Ag NPs to the Glass/ITO electrode surface. Glass/ITO slides were cleaned and functionalized with APTES as described previously in Chapter II. Then the Glass/ITO/NH$_2$ substrate was directly immersed into an aqueous solution of the negatively – charged citrate – capped Ag NPs for 10 to 60 minutes, leading to electrostatic attachment to surface NH$_3^+$ groups. The time was varied to keep the constant Ag coverage for different particle sizes. The time was generally shorter as the particle size increased. The functionalized Glass/ITO/NH$_3^+$/Ag NP electrodes were removed from solution, rinsed with nanopure water, and dried under N$_2$ before electrochemical analysis.

Linear sweep voltammetry measurements. The electrochemical cell consisted of three electrode with Glass/ITO/NH$_3^+$/Ag NP as the working electrode, a Pt wire as an auxiliary electrode and an Ag/AgCl (3 M KCl) reference electrode. All of the electrochemical measurements were performed in 0.1 M H$_2$SO$_4$ electrolyte solution at a scan rate of 1 mV/s with a potential range of 0.1 to 1.0 V.

3.3 RESULTS AND DISCUSSION

Figure 3.3 shows a photograph of solutions of Ag NPs synthesized with the different Ag^+/Ag seed ratios. The color of the solution changed from light yellow to a cloudy greenish with increasing n_+/n_s, which is consistent with an increasing size of the Ag NPs as the n_+/n_s ratio increases. Immediately after the synthesis, all Ag NP solutions were characterized by UV-visible spectroscopy. Samples were diluted in order to keep the amount of silver constant in each solution. Figure 3.4 shows the UV-vis absorbance spectra of solutions of Ag NPs with different n_+/n_s ratios. The dashed vertical line in all spectra corresponds to the λ_{max} for the surface Plasmon band of the Ag seed NPs (394 nm). The solid horizontal line corresponds tot eh absorbance maximum of the surface Plasmon band for the Ag seed NPs (Abs~1.1). The position of the plasmon peak was ~400 nm for n_+/n_s from 5 to 40, however, the intensity increased slightly as the ratio increased. This is consistent with Mie theory for absorbance/scattering of spherical NPs as a function of size. The UV-vis spectra show that with increasing n_+/n_s ratio, the position of the surface Plasmon band also red shifts, especially for ratios higher than 40. This is also consistent with an increase in Ag NP size. The surface Plasmon band in the spectra for n_+/n_s from 40 to 100 broadens significantly and is more red-shifted. This is consistent with larger NP sizes, the possible formation of more complex shapes, and some possible NP aggregation. Overall, the optical pictures and the UV-vis data are consistent with the controlled synthesis of Ag NPs of increasing average NP size as the n_+/n_s ratio increases.
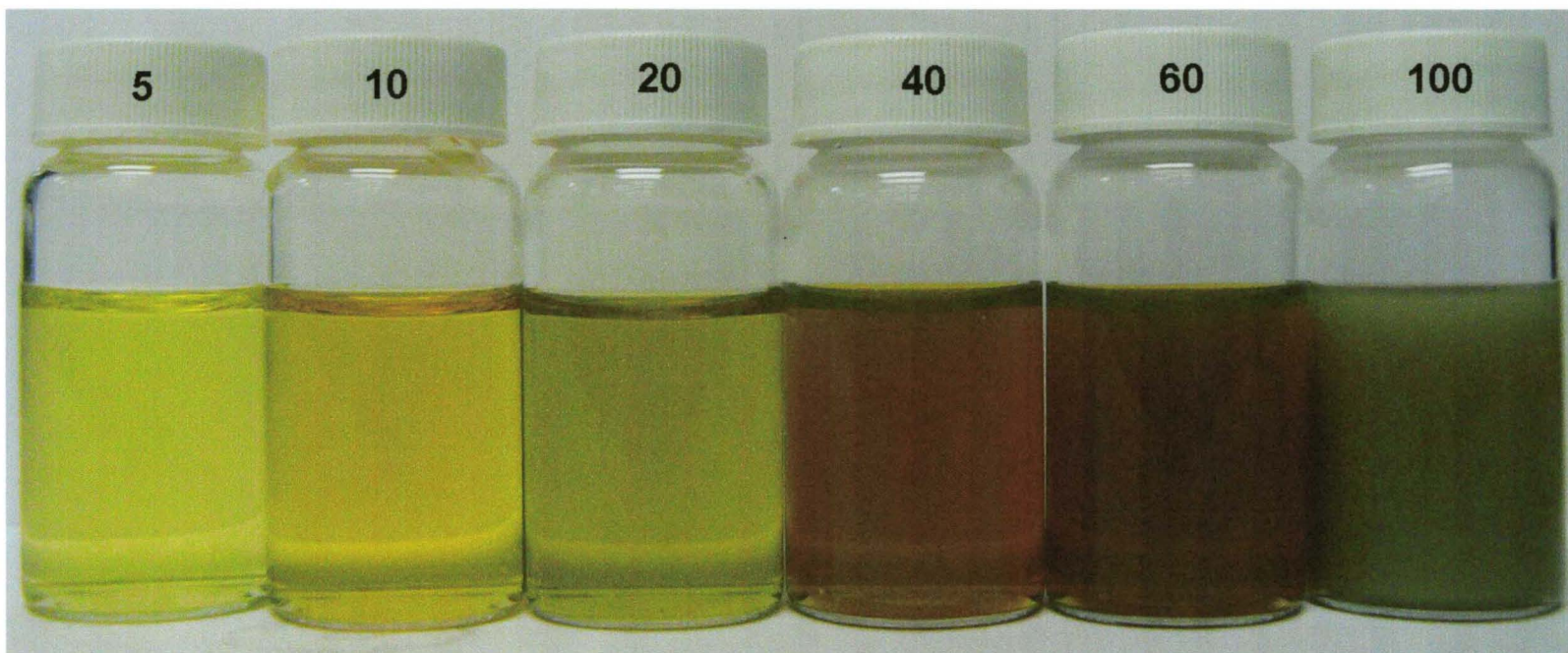
Figure 3.3 Optical pictures of Ag NP solutions synthesized with different Ag⁺/Ag seed ratios.
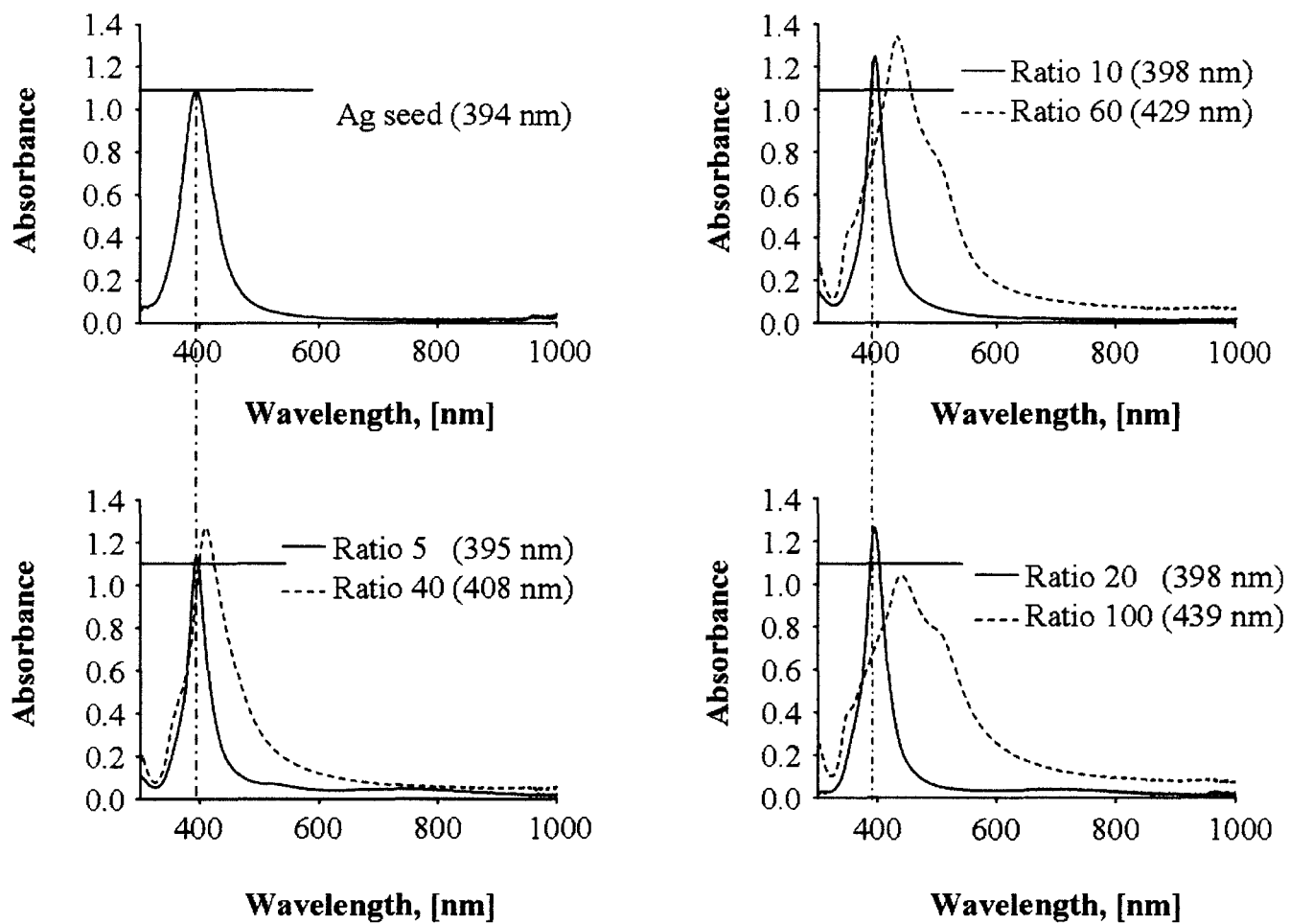
Figure 3.4 UV-vis spectra of Ag Seed and Ag NPs synthesized with an n_+/n_s ratio from 5 to 100 as indicated.

Average size of synthesized Ag NPs was determined by AFM and SEM after electrostatic attachment to Si/SiO$_x$/NH$_2$ and Glass/ITO/NH$_3$ surfaces, respectively. Figure 3.5 shows typical SEM images of Glass/ITO/NH$_2$ electrodes containing Ag seed NPs and those synthesized with various Ag$^+$/Ag seed ratios. Figure 3.6 shows the AFM images and cross section of Si/SiO$_x$/NH$_2$ substrates after electrostatic attachment of Ag NPs synthesized with various Ag$^+$/Ag seed ratios. Ag NP seeds are 8-12 nm in diameter, ratio 5, 10, 20, 40, 60 and 100 with average diameters of 16.7, 21.4, 25.0, 30.9, 35.1, 42.9 nm respectively according to AFM measurements. Average size determined by SEM was in agreement with AFM results. The Ag NPs were fairly well-spaced and isolated on the surface. We obtained LSVs from 0.1 to 1.0 V in 0.1 M H$_2$SO$_4$ at 1.0 mV/s of Glass/ITO/NH$_2$ electrodes coated with Ag NPs of different sizes. Figure 3.7 shows LSVs in the range of 0.2 to 0.45 V for all range of Ag NPs studied. No electrochemistry was observed outside of this range for all LSVs and it therefore not shown. The negative anodic current corresponds to the reaction of:

$$Ag^0 \rightarrow Ag^+ + 1e^- \qquad \text{(Rxn 3.1)}$$

E$_p$ shifts positive with increasing Ag$^+$/Ag seed ratio (or increasing size). We also observed experimentally that for constant NP size, E$_p$ was directly proportional to ln(Ag coverage), which is expected for reversible Ag oxidation kinetics.[89] Figure 3.8 shows the LSVs of Glass/ITO/NH$_2$ electrodes coated with 8-12 nm diameter Ag seed NPs as a function of the coverage of Ag controlled by soaking time in Ag seed solution. The times were 15 min, 1h and 3h and corresponding Ag coverages were 2.2, 8.8 and 20.5 × 10^{-4} C respectively. The inset of the Figure 3.8 shows a plot of E$_p$ versus ln(coverage).
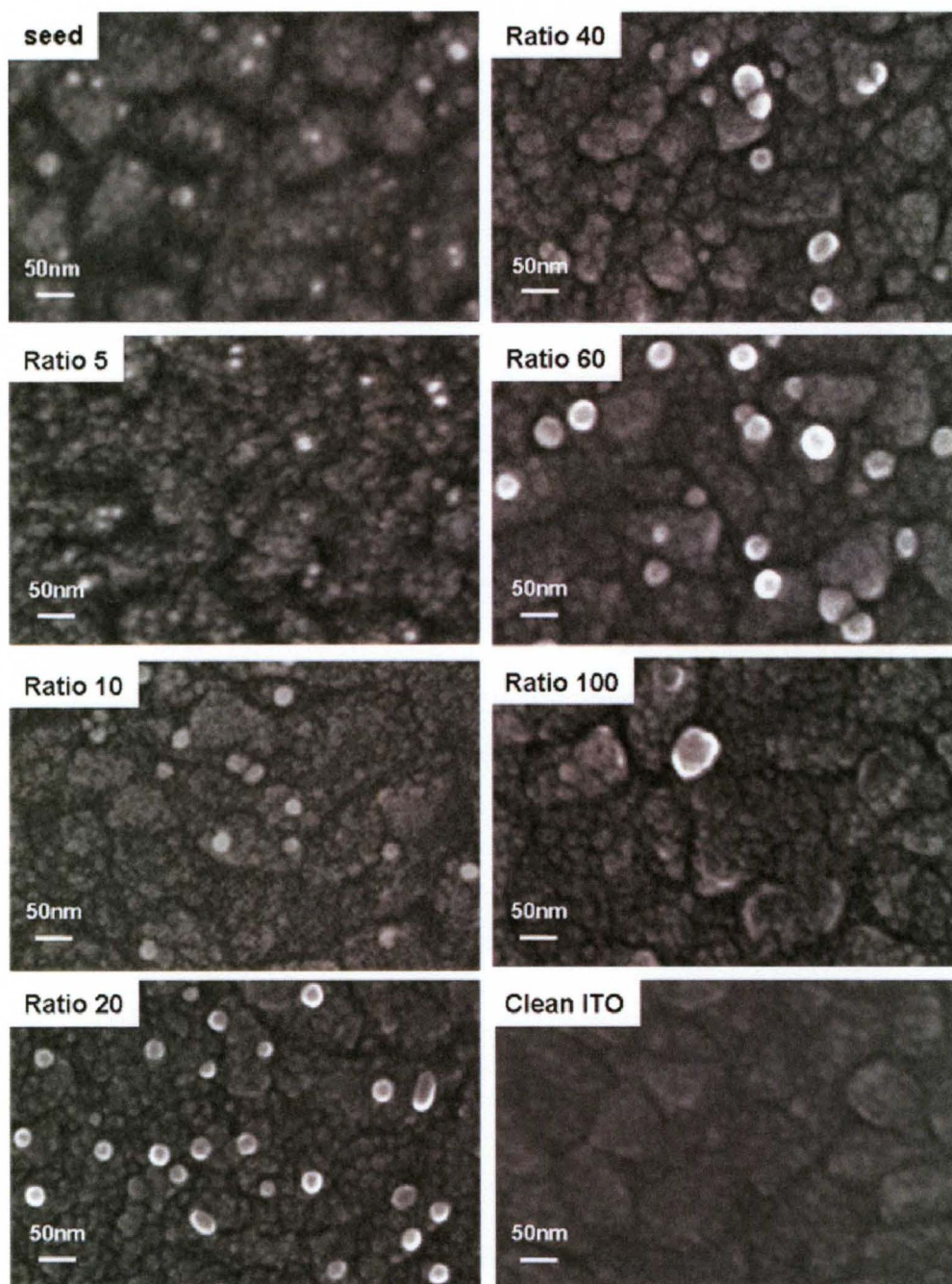
Figure 3.5 SEM images of Glass/ITO/NH$_2$ electrodes containing Ag seed NPs and those synthesized with various Ag$^+$/Ag seed ratios as labeled.
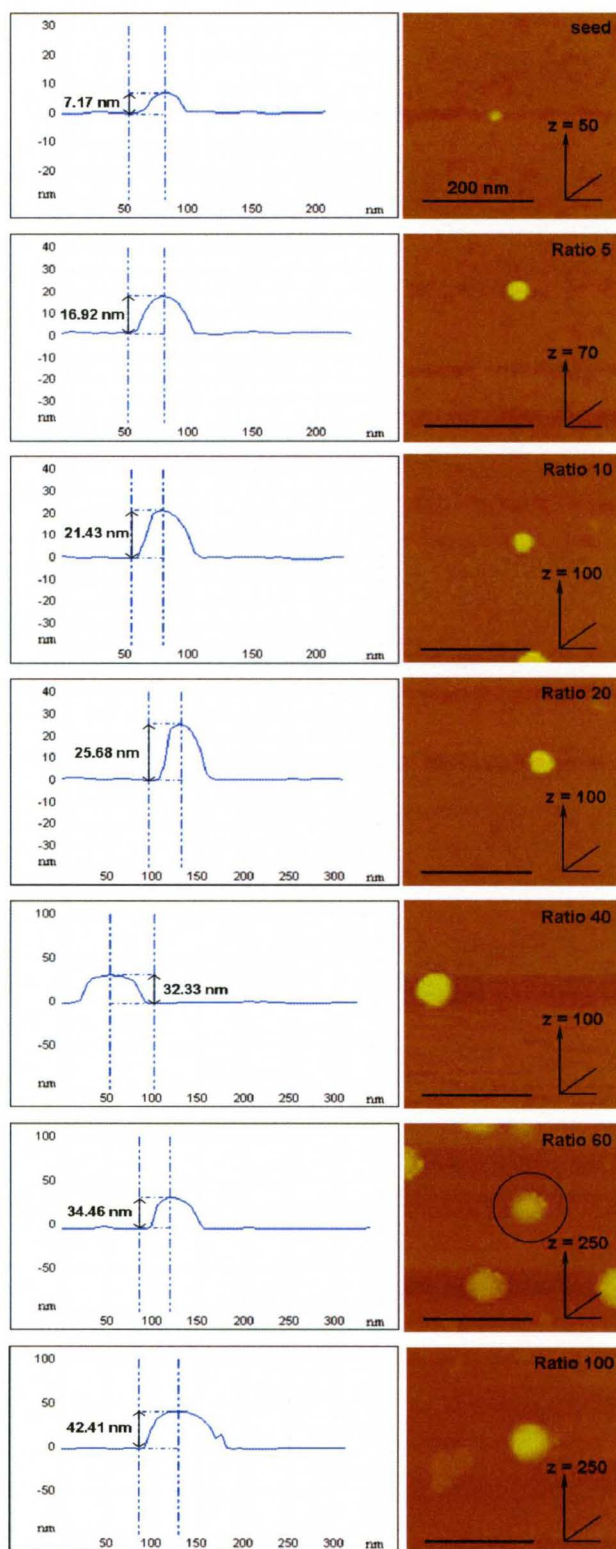
Figure 3.6 AFM images and cross section of Si/SiOx/NH2 substrates after electrostatic attachment of Ag NPs with various Ag+/Ag0 ratios as labeled.

57
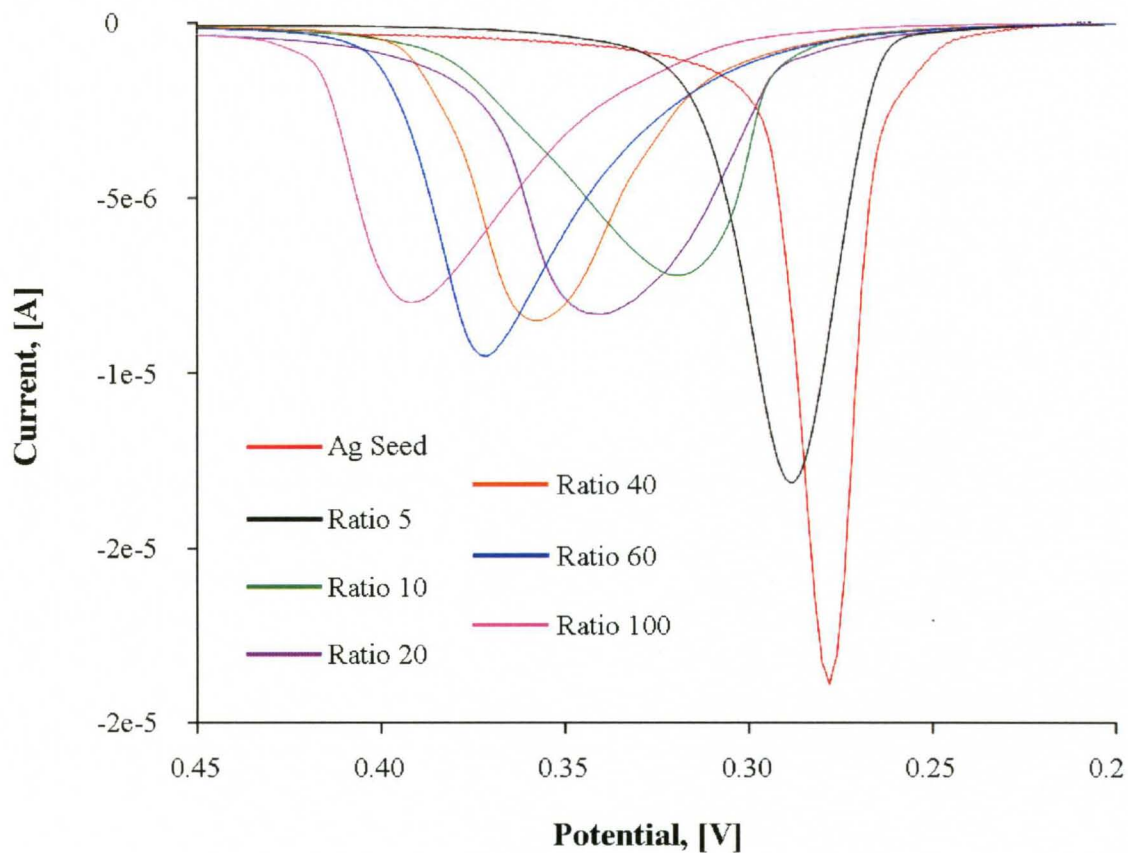
Figure 3.7 LSVs obtained in 0.1 M H$_2$SO$_4$ electrolyte at 1.0 mV/s from 0.1 to 1.0 V (0.20 to 0.45 shown) of Glass/ITO/NH$_2$ electrodes coated with Ag seed NPs and Ag NPs synthesized by seed-mediated growth using Ag$^+$/Ag seed ratios of 5, 10, 20, 40, 60, and 100 as indicated.
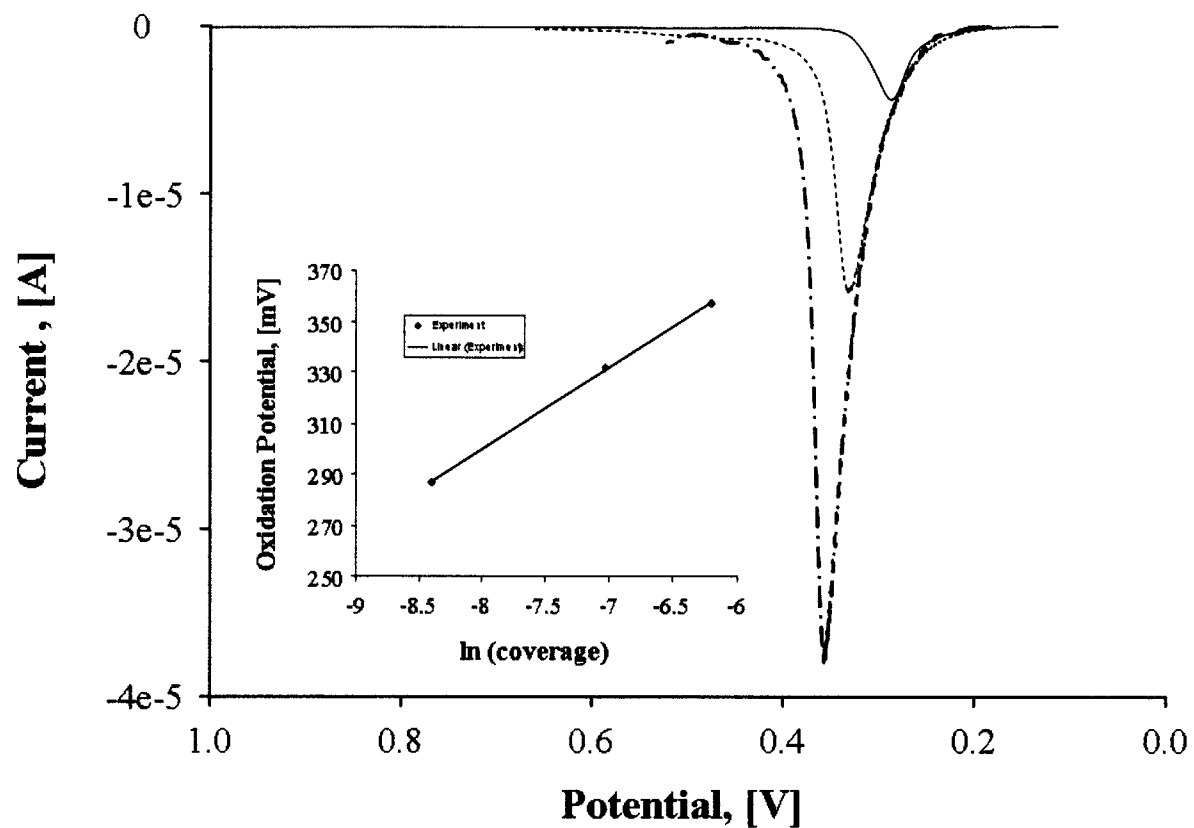
Figure 3.8 LSVs in 0.1 M H₂SO₄ at 1 mV/s from 0.1 to 1.0 V of Glass/ITO/NH₂ electrodes coated with Ag seed NPs

by soaking in solution for 15 min (—), 60 min (---), and 180 min (— · —). Inset shows the plot of E_p versus ln(coverage), which is

expected to be linear.

This experimental plot is linear as expected.[89] To rule out the effect of coverage we kept

coverage, we kept the total coverage of Ag on the electrode surface constant within (3-5)

× 10^{-4} coulomb (C). We also observed that E_p shifts positive with increasing scan rate.

Figure 3.9 shows the LSVs of Glass/ITO/NH$_2$ functionalized with Ag seed NPs recorded

in 0.1 M H$_2$SO$_4$ at different scan rates. Table 3.2 displays the relevant data. Figure 3.10

(A) shows the exponential dependence of E_p on the scan rate and Figure 3.10 (B) shows

that E_p is directly proportional to ln(scan rate). Previous literature predicts that E_p is

proportional to ln(scan rate), which is in good agreement with our results.[89] We chose a

slow scan rate of 1 mV/s to ensure electrochemical reversibility and conditions of planar

diffusion in which case diffusion profiles overlap. At 1 mV/s, the diffusion layer

thickness (δ) is ~0.04 cm over the ~45 sec, time that it takes to oxidize the Ag (peak

width 30-60 mV). The diffusion layer thickness was calculated using the following

equation:

$$\delta = 2(Dt)^{\frac{1}{2}} \qquad \text{(Eq. 3.2)}$$

The δ is much larger than the average calculated Ag NP spacing of 50 nm for seed and

370 nm for ratio 100 Ag NPs, ensuring planar diffusion.

Table 3.3 shows the average diameter measured by AFM and SEM for the Ag

Seed NP and different Ag$^+$/Ag seed ratio Ag NPs along with average E_p, full width at

half-maximum, and charge under the peak determined from LSVs. At least 5 samples

were analyzed. The Ag NP diameter is in good agreement with the theoretical values at

different ratios of Ag$^+$/Ag seed based on the equation:

$$d_p = d_{p0}(1+\frac{n_+}{n_s})^{\frac{1}{3}} \qquad \text{(Eq. 3.3)}$$
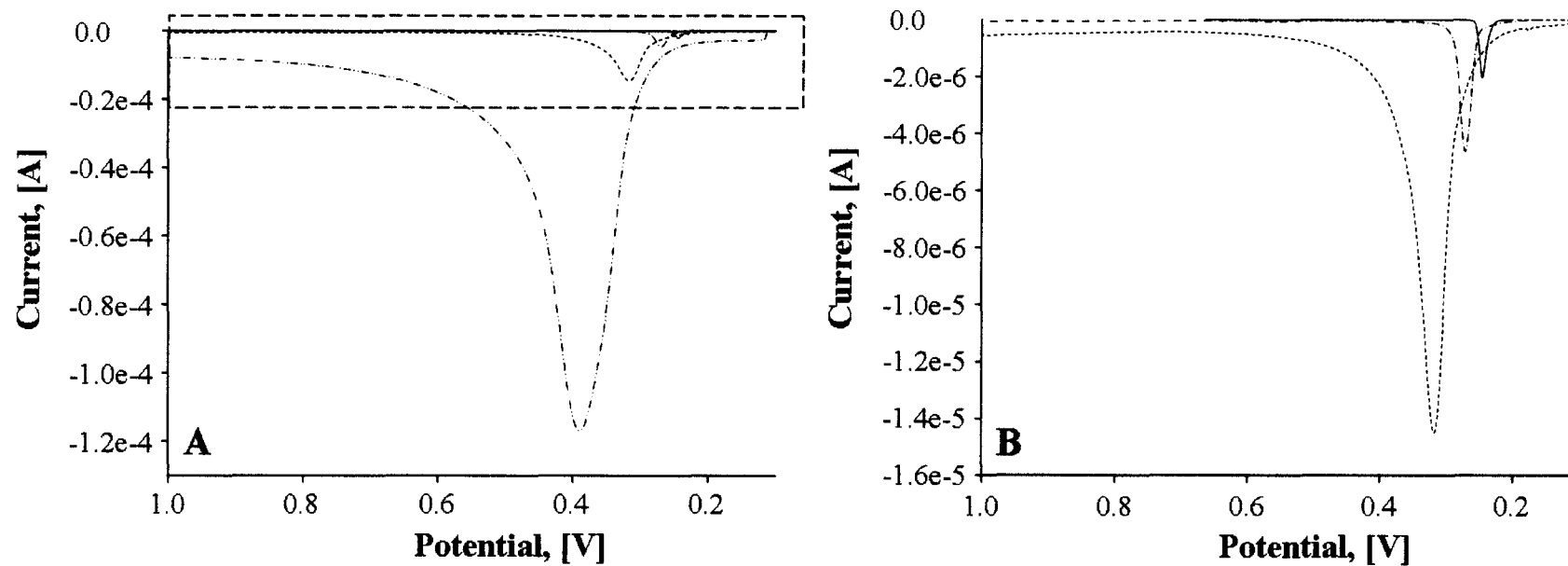
Figure 3.9 LSVs in 0.1 M H₂SO₄ from 0.1 V to 1.0 V of Glass/ITO/NH₂ electrodes coated with Ag Seed NPs (soaking time 15 min) obtained at a scan rate of 0.1 (—). 1.0 (— · —), 10 (- - -), and 100 (— · · —) mV/s. Figure B is the zoomed in area from Figure A showing the LSVs at 0.1, 1.0 and 10 mV/s.

Scan rate, mV/s	ln(scan rate)	E_p, [mV]	Charge, [C]
0.1	-2.3	245	2.528×10^{-4}
1.0	0	270	1.435×10^{-4}
10	2.3	317	1.368×10^{-4}
100	4.6	389	2.096×10^{-4}

Table 3.2 E_p for Ag seed NPs as a function of scan rate
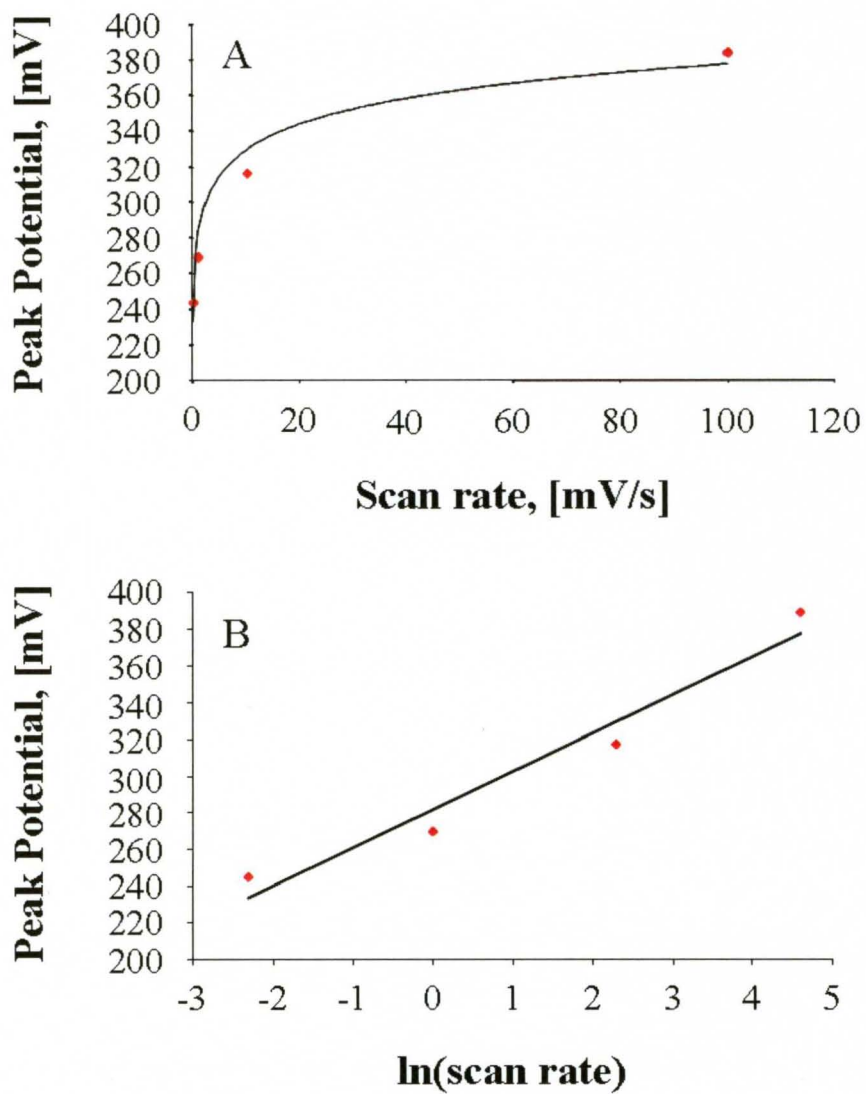
Figure 3.10 Plot of peak potential versus (A) scan rate and (B) ln(scan rate) for Glass/ITO/NH$_2$ electrodes covered with Ag seed NPs.

Synthesis Ratio (n_+/n_s)	Diameter AFM (nm)	Diameter SEM (nm)	Theoretical diameter (nm)	Peak Potential E_p (mV)	Width at half maximum (mV)	Charge under the peak $(\times 10^{-4}$ C$)$
0:0 (seed)	8.5 (±3.3)	12.3 (±3.5)	8.5	275 (±25)	33 (±10)	-4.3 (±1.7)
5:1	16.7 (±6.9)	16.8 (±5.4)	15.5	291 (±11)	33 (±13)	-3.5 (±0.9)
10:1	21.4 (±6.3)	20.5 (±4.3)	18.9	318 (±6)	48 (±11)	-3.9 (±0.5)
20:1	25.0 (±6.5)	26.6 (±5.1)	23.6	340 (±4)	55 (±8)	-3.0 (±0.2)
40:1	30.9 (±8.9)	27.9 (±8.7)	29.5	354 (±7)	54 (±15)	-3.8 (±1.0)
60:1	35.1 (±12..3)	37.9 ((±11.0)	33.6	371 (±10)	66 (±19)	-4.1 (±0.8)
100:1	42.9 (±13.2)	45.5 (±15.1)	39.8	382 (±9)	65 (±20)	-3.3 (±0.7)

Table 3.3 Statistical size and electrochemical data for Glass/ITO/NH_3^+/Ag NP electrodes.

were d_p is the final diameter of the NP, d_{p0} is the diameter of the Ag seed, and n_+/n_s is the Ag$^+$/Ag seed mole ratio used in the synthesis.[105] The average E_p values shift positive with increasing Ag NP diameter and are all statistically different from each other except for the ratio 60 and 100 Ag NPs. E_p shifts ~107 mV from the smallest seed particles to largest ratio 100 Ag NPs. Under the conditions of experiment such as reversible system, constant coverage and planar diffusion, previous theory based on diffusion alone predicts that E_p should not shift as a function of size.[87] For this reason, we believe that observed negative shift in E_p with size is not due to diffusion, but rather due to a negative shift in the standard redox potential (E^0) as the size decreases as predicted by Plieth[86] and Henglein[85] and shown qualitatively by Brus.[76] This was the first direct measurement of this phenomenon by voltammetry. The graph in Figure 3.11 plots the difference between $E_{p, AgNP}$ and $E_{p, bulk Ag}$ (ΔE_p) as a function of Ag NP radius (based on AFM measurements) as compared to the predictions by Plieth.[86] We used E_p of the ratio 100 Ag NP as $E_{p, bulk Ag}$ (382 mV). Our experimental ΔE_p is larger than the theoretical prediction for all NP sizes except the two largest sizes, and they do not follow the theoretical trend, other than general negative shift in potential with decreasing radius. The reasons for the discrepancy are not clear at this time. Clearly more work is needed to explain the data theoretically. Note that we used the surface stress (γ) of Ag in vacuum for the theoretical plot. The actual value for γ would be different in electrolyte solution due to adsorbate – induced stress, and it also depends on the electrode potential, which would affect the theoretical values of ΔE_p. Compton and co-workers previously showed no change in E_p for Ag NPs with diameters ranging from 25 to 100 nm.[87]
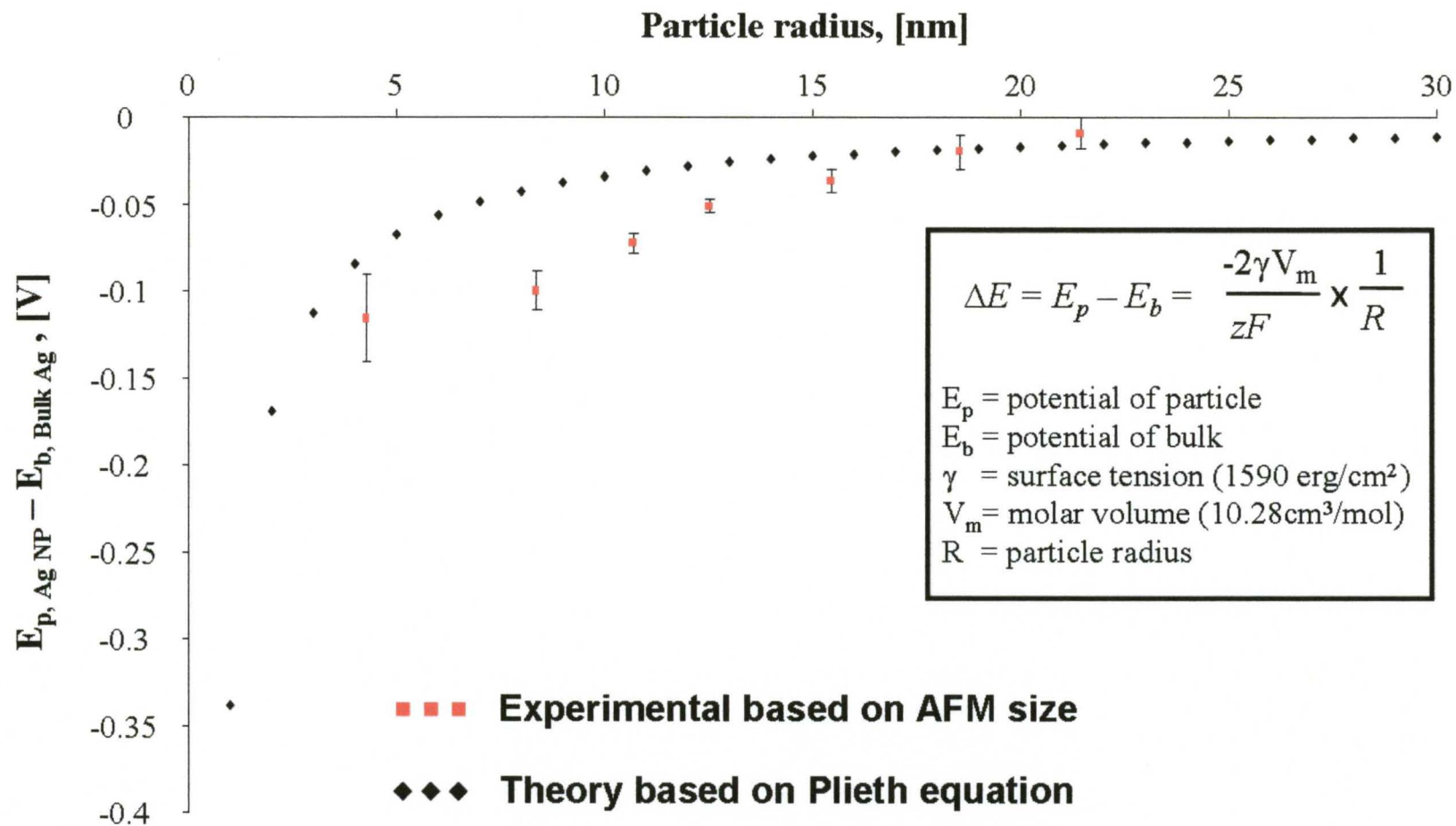
Figure 3.11 Experimentally measured shift in potential (■) for Ag NPs versus bulk Ag as a function of NP radius compared to theory (♦)

Our results show a ~40 mV shift for 25 nm diameter Ag NPs versus bulk Ag and no significant difference in E_p above 35 nm diameter NPs. The difference at 25 nm may be due to the aggregated state of the Ag NPs in the Compton work.[87]

We constructed three theoretical LSVs for the oxidation of ~5×10^{-4} C of Ag from the electrode surface and compared them to experimental data. In order to create a theoretical LSV (i-E plot), we needed to determine the number of mol of Ag oxidized at each 1 mV change in potential. The scan rate was 1 mV/s. The mol of Ag oxidized at each 1 mV was then converted into charge Q (in Coulombs) using Faraday's constant (96485.34 C/mol) and then converted to current (C/s).

We assumed a linear concentration gradient and used the Nernst equation in order to determine the concentration of Ag^+ at the electrode surface at each applied potential. The Nernst equation is as follows:

$$E = E^0 - 0.592 \log(\frac{1}{[Ag^+]_{x=0}}) \qquad \text{(Eq. 3.4)}$$

where E is the applied voltage (0 mV, 1 mV, 2 mV,...1000 mV), E^0 is the standard redox potential, and $[Ag^+]_{x=0}$ is the concentration of Ag^+ ions at the electrode surface (x = 0). Figure 3.12 shows the situation, where the $[Ag^+]$ is given by Nernst equation at the electrode surface. We then assume a linear decrease in the $[Ag^+]$ as a function of distance away from the electrode until the $[Ag^+]$ reaches 0 in the bulk solution at a distance father away than the diffusion layer thickness (δ). From the $[Ag^+]_{x=0}$ and knowing δ and the area of the electrode (A = 1.4 cm^2), we calculated the total mol of Ag oxidized at a given potential as follows:

$$mol \text{ } of \text{ } Ag \text{ } oxidized = (\frac{[Ag^+]_{x=0}}{2}) \times \delta \times A \qquad \text{(Eq. 3.5)}$$
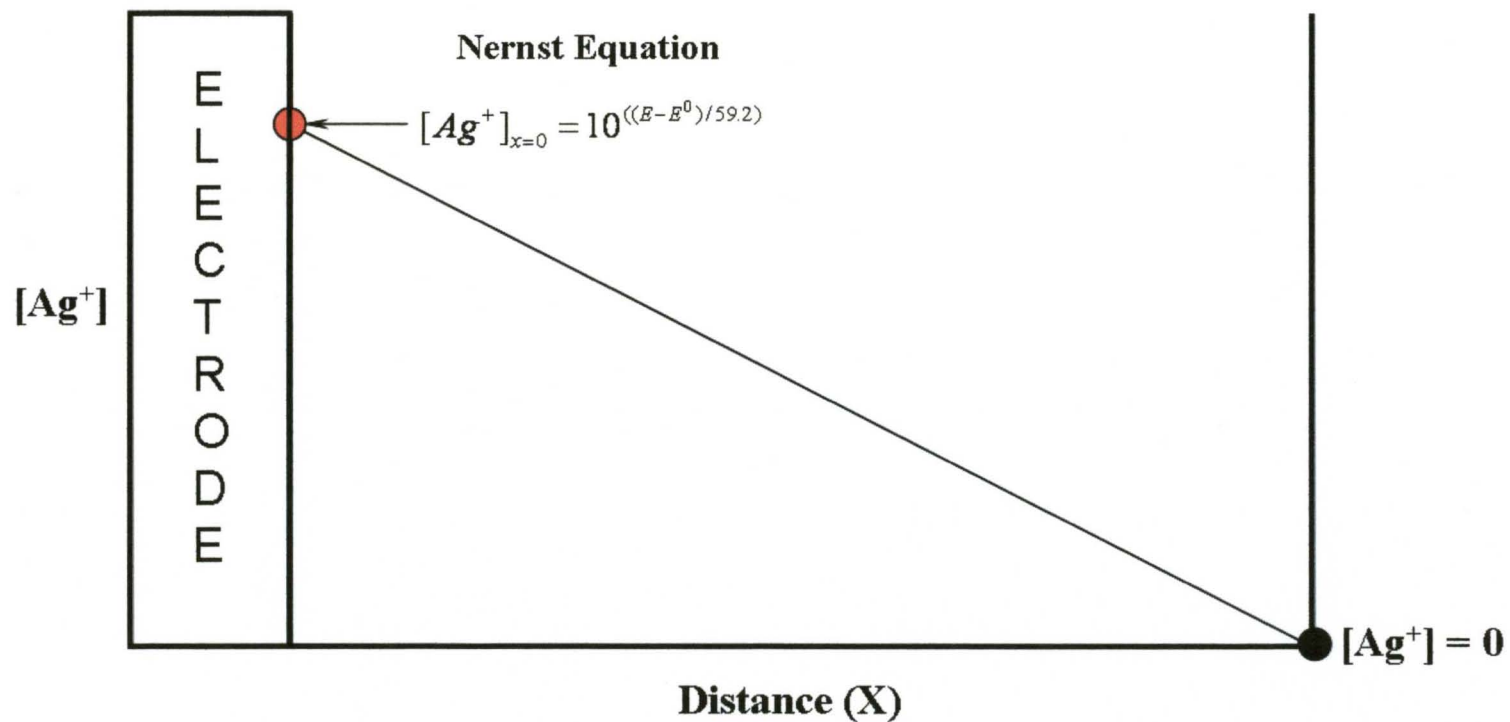
Figure 3.12 Illustration of the linear concentration gradient of Ag$^+$ as a function of distance from the electrode surface.

The diffusion layer thickness, δ, is a function of time (t) and the diffusion coefficient (D_{Ag+}) of Ag^+ as shown in Equation 3.2. Equation 3.2 in case of Ag^+ will be:

$$\delta = 2(D_{Ag^+}t)^{\frac{1}{2}} \qquad \text{(Eq. 3.6)}$$

where D_{Ag+} is 1.2×10^{-5}, cm^2/s and time is determined by the applied potential and the scan rate as follows:

$$t = \Delta E \,/\, scan\ rate \qquad \text{(Eq. 3.7)}$$

For the theoretical plot, we started from 0 mV and scanned to 1000 mV at 1.0 mV/s. At 5 mV, for example the time would then be:

$$t = 5mV \,/\, 1.0mV \,/\, s \ \text{ or 5 sec.}$$

Once we determined the number of mol Ag oxidized, we determined the Coulombs of charge from Faraday's constant, where:

$$Q = (mol\ Ag\ oxidized) \times (96485.34\ C/mol) \qquad \text{(Eq. 3.8)}$$

We calculated the current by determining the total charge at one potential (E_1) and then determining the total charge at the next potential (E_2), which is 1.0 mV larger after 1 sec. The difference between the total charges at the two potentials is equal to the Coulombs of Charge passed in that 1.0 second, or the current. The following equation was used:

$$i = (Q_{E_2} - Q_{E_1})/1.0s \qquad \text{(Eq. 3.9)}$$

Table 3.4 shows the example calculations for the different parameters for the LSV from 0 to 10 mV. Once the calculated mol Ag oxidized exceeds the amount of Ag on the surface ($3\text{-}5 \times 10^{-4}$ C), we then made the current zero, since there is no more Ag to oxidize. The theoretical plots are shown in figure 3.13. We adjusted the E^0 value to match the experimental data and then compared that to what is expected for bulk Ag. Ratio 60 and 100 Ag NPs are consistent with the E^0 of bulk Ag while the E^0 values for smaller Ag NPs

E $_{applied,}$ [V]	Ag$^+$ Concentration from Nernst (M) $[Ag^+] = 10^{[(E-E_0)/59.2]}$	Charge Q (C) $Q = \dfrac{[Ag^+]_{x=0}* \delta * A}{2000}$	Current [C/s] $i = (Q_{E+1}-Q_E)/1.0s$
0	0	0	0
1	1.46e-9	6.85e-10	6.85e-10
2	1.52e-9	1.01e-9	3.22e-10
3	1.58e-9	1.28e-9	2.75e-10
4	1.65e-9	1.54e-9	2.57e-10
5	1.71e-9	1.79e-9	2.50e-10
6	1.78e-9	2.04e-9	2.49e-10
7	1.85e-9	2.29e-9	2.51e-10
8	1.92e-9	2.54e-9	2.55e-10
9	2.00e-9	2.81e-9	2.61e-10
10	2.08e-9	3.07e-9	2.69e-10

Table 3.4 Example calculations for theoretical LSV plots.
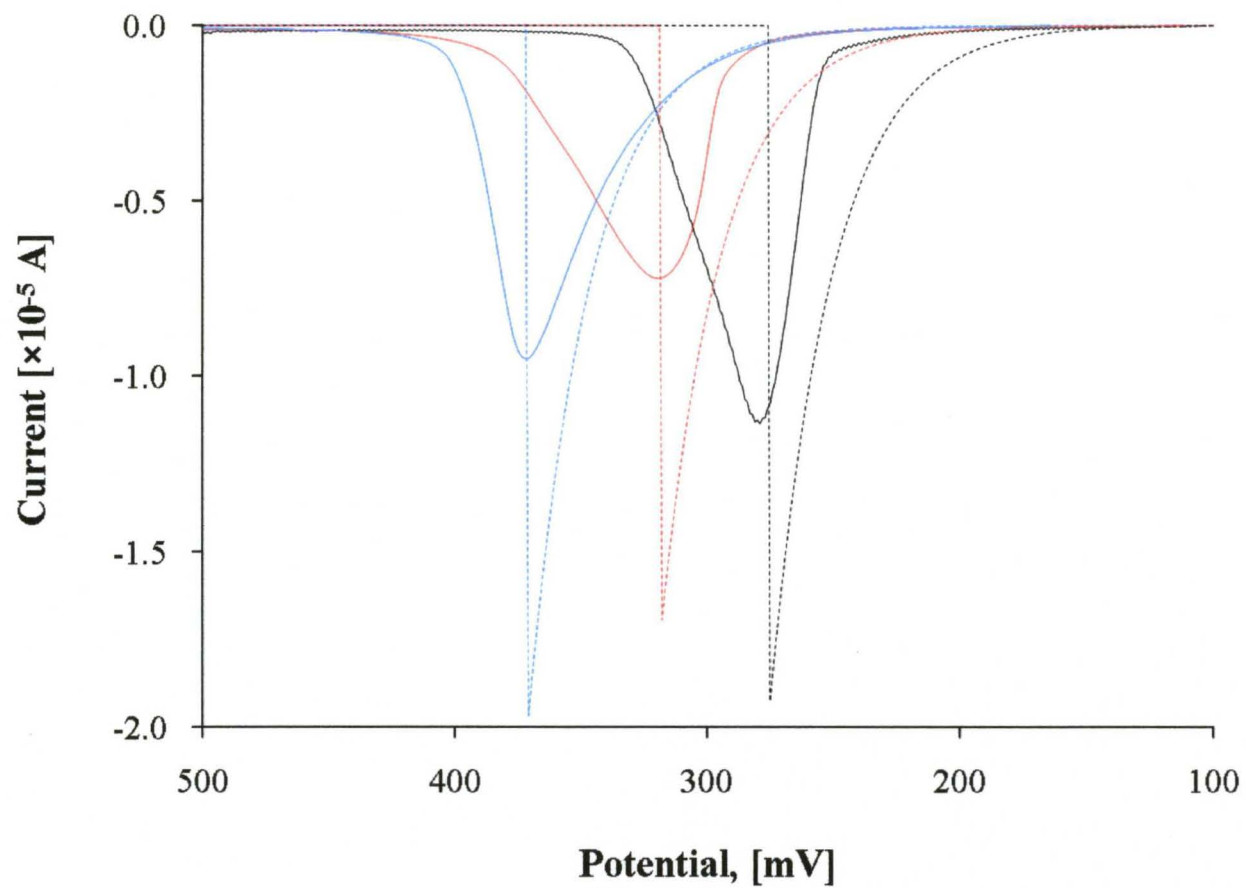
Figure 3.13 Theoretical LSVs (dotted lines) based on E^0 values of 623 mV (blue), 575 mV (red), and 524 mV (black). Experimental LSVs (solid lines) for ratio 60 (blue), ratio 10 (red), and seed (black) Ag NPs. The coverages of the theoretical plots match the coverages of the experimental plots in the figure.

are consistent with a negative shift in E^0. The theory predicts that when $E^0 = 623$ mV, the Ag NPs fully oxidize by 371 mV. This agrees well with the experimental E_p for ratio 60 Ag NPs. Theoretical E^0 values of 575 and 523 mV fit the E_p for ratio 10 and Ag seed NPs, where the Ag fully oxidized by 318 and 275 mV, respectively. The standard redox potential for Ag/Ag^+ is 0.799 V vs NHE. We found our Ag/AgCl reference electrode was ~172 mV vs NHE based on a cyclic voltammogram of $Fe(CN)_6^{3-/4-}$, giving a bulk E^0 value of 0.627 V for Ag/Ag^+. This value agrees well with the E^0 of 0.623 V that best fits the ratio 60 Ag NP LSV. Ratio 60 and 100 Ag NPs (d=35-45 nm) were not statistically different; both behave electrochemically as a bulk Ag. The analysis is consistent with our conclusion that the smaller Ag NPs exhibit a lower E_p value due to a negative shift in E^0 for the Ag/Ag^+ redox couple.

We also performed constant potential experiments and stirring experiments suggesting that diffusion is not responsible for the change in E_p with size. As was mentioned before interparticle spacing, slow scan rate should be able to provide the conditions of planar diffusion in our experiments. We performed the following experiments in order to demonstrate experimentally, that diffusion is not responsible for the shift in oxidation potential. We studied the rate of Ag oxidation for two different sizes of 8-12 nm (Ag Seed NPs) and 35 nm (ratio 60 Ag NPs) by holding the potential at different values of 100 mV, 50 mV and 0 mV for different periods of time from 0 to 20 h. Table 3.5 A and B displays the data from these experiments and Figure 3.14 shows the plots of remaining Ag coverage as a function of pausing time. We determined the coverage remaining on the surface after holding the potential at particular value for a desired time by running the LSV after the potential was held and determining the charge

(A) Ag Seed NPs

Pausing Potential (mV)	*Coverage (C) at Different Pausing Times (min)*				
	30 min	*60 min*	*180 min*	*420 min*	*1200 min*
0	*3.94e-4*	*2.25e-4*	*1.69e-4*	*1.02e-4*	*0.72e-4*
50	*2.06e-4*	*1.55e-4*	*1.44e-4*	*0.89e-4*	*0*
100	*1.77e-4*	*1.45e-4*	*1.19e-4*	*0.72e-4*	*0*

(B) Ratio 60 Ag NPs

Pausing Potential (mV)	*Coverage (C) at Different Pausing Times (min)*				
	30 min	*60 min*	*180 min*	*420 min*	*1200 min*
0	*3.94e-4*	*2.25e-4*	*1.69e-4*	*1.02e-4*	*0.72e-4*
50	*2.06e-4*	*1.55e-4*	*1.44e-4*	*0.89e-4*	*0*
100	*1.77e-4*	*1.45e-4*	*1.19e-4*	*0.72e-4*	*0*

Table 3.5 Coverage (Charge) of Ag left on the surface as a function of time when holding the potential at 0, 50 or 100 mV for (A) Ag Seed NPs, and (B) ratio 60 Ag NPs. The initial coverage was $\sim5\times10^{-4}$ C.

73
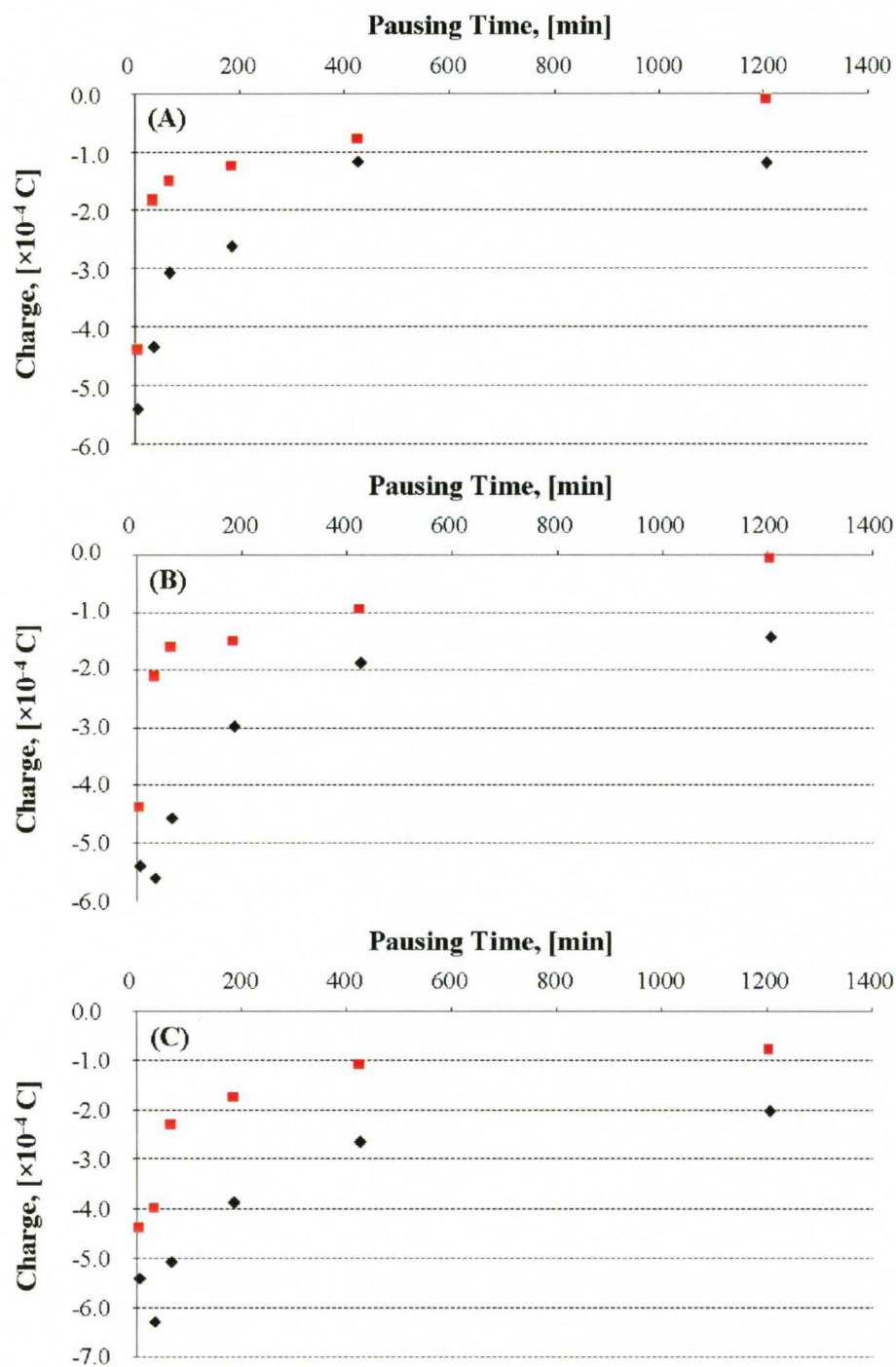
Figure 3.14 Plots of charge remaining on the surface versus time after pausing the potential at (A) 100 mV, (B) 50 mV, and (C) 0 mV for Glass/ITO/NH$_2$ electrodes coated with Ag Seed NPs (■) and ratio 60 Ag NPs (♦).

under the remaining Ag oxidation peak. For example, we held the potential at 100 mV for 30 min and then continued the LSV scan at 1.0 mV/s to observe the Ag stripping peak. The charge under the peak decreased with increasing time, but E_p also decreased due to a combination of a lower Ag coverage and a smaller size Ag NP with time. The important conclusion from this work is that the Ag seed NPs oxidize at a faster rate compared to the ratio 60 Ag NPs at all potentials. This is consistent with a smaller E^0 value for smaller Ag NPs since there will be a larger $[Ag^+]$ at the electrode surface for a given applied E and therefore a faster rate of Ag oxidation. Importantly, at 50 and 100 mV, the Ag seed nanoparticle was completely oxidized after 20 h while the ratio 60 seed still had a significant amount of Ag on the surface. This shows that the ratio 60 Ag NP is stable after very long times, suggesting that the larger Ag NPs are thermodynamically more stable compared to the smaller Ag seed. This is consistent with a negative shift in E^0 for the smaller Ag seed. Additionally, this data shows that we can reduce the Ag NP size by controlled electrochemical oxidation over long time scales.

Additionally we obtained the LSVs of Glass/ITO/NH$_2$ electrodes coated with Ag Seed NPs and ratio 60 Ag NPs while stirring the solution (Figure 3.15). We observed that stirring the electrolyte solution affects the smaller seed NPs and larger ratio 60 Ag NPs in a similar way. E_p shifted negative by 26 and 36 mV, respectively for the two samples shown. Stirring the solution leads to faster transport of Ag^+ away from the electrode surface. This in effect increases the diffusion layer thickness and more mole of Ag oxidized at each E value during scanning. With more mol Ag oxidized at each E during
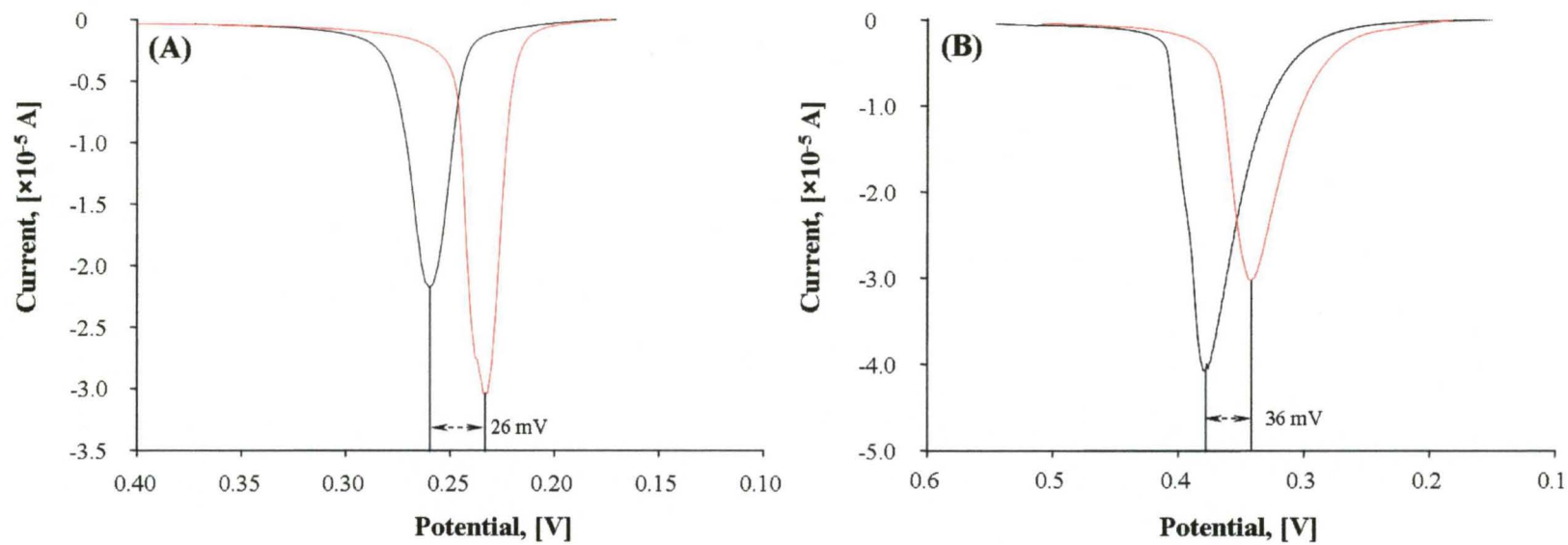
Figure 3.15 LSV of Ag seed NPs (A) and ratio 60 Ag NPs (B) performed without (black) and with (red) stirring of the electrolyte solution.

the LSV, the Ag will be completely oxidized and removed from the surface at an earlier time and more negative E_p. Since stirring affects both sizes in a similar manner, we do not believe diffusion is a major reason for the size-dependent shift in E_p when there is no stirring. This supports our conclusion that E_p shifts due to a shift in E^0.

3.3 CONCLUSIONS

We described the direct voltammetric measurement of oxidation potential (E_p) for Ag oxidation as a function of Ag NP size. Under the experimental conditions of planar diffusion, constant Ag coverage, and electrochemical reversibility, previous theory based on diffusion only predicts a constant E_p with size. This fact and our theoretical LSVs suggest that the experimental shift in E_p is due to a size – dependent change in E^0 for the Ag/Ag$^+$ redox couple. Constant potential experiments show the fast dissolution rates for small particles and slow dissolution rate for big Ag NPs, which is consistent with a negative shift in E^0 for the smaller Ag NPs. Ag NPs with average size of 35 nm were stable for 20 h during the pausing experiment while Ag NPs with average diameter of 8 nm were dissolved completely at pausing potentials of 50 mV and 100 mV over the 20 h period. Stirring experiments showed approximately the same shift in oxidation potentials for both sizes (8 and 35 nm). All these experiments suggest that diffusion is not the reason for the size-dependent shift in E_p.

CHAPTER IV

ELECTROCHEMICAL SIZE DISCRIMINATION OF GOLD NANOPARTICLES ATTACHED TO GLASS/INDIUM-TIN-OXIDE ELECTRODES BY OXIDATION IN BROMIDE-CONTAINING ELECTROLYTE

Here we describe the electrochemical oxidation of an assembly of gold nanoparticles (Au NPs) attached to glass/indium-tin-oxide (ITO) electrodes as a function of particle size. We synthesized Au NP arrays with NP diameters ranging from 8 to 250 nm by electrodeposition of Au from $HAuCl_4$ in H_2SO_4 at potentials of -0.2 to 0.8 V versus Ag/AgCl using chronocoulometry to keep the amount of Au deposited constant. The average Au NP size increased with increasing deposition potential. The chemical reduction of $HAuCl_4$ by $NaBH_4$ in trisodium citrate solution led to 4 nm average diameter Au NPs, which we chemisorbed to the glass/ITO electrode. Linear sweep voltammograms (LSVs) obtained on the glass/ITO/Au NP (4 to 250 nm) electrodes from 0.5 V to 1.1 V in 0.01 M potassium bromide plus 0.1 M $HClO_4$ showed a positive shift in oxidation potential from 734 ± 1 mV to 913 ± 19 mV with increasing diameter and constant coverage of Au atoms on the electrode surface. The shift agrees qualitatively with that predicted by a shift in the redox potential based on a difference in free energy associated with a change in surface energy as a function of particle size. Based on the charge during Au deposition versus the charge during oxidation, the oxidation process produces a mixture of $Au^{III}Br_4^-$ (25%) and $Au^IBr_2^-$ (75%). A glass/ITO electrode coated

79

with a mixture of 4 nm and 250 nm Au NPs revealed 2 oxidation peaks, consistent with the two Au NP size populations present on the surface.

4.1 INTRODUCTION

As was mentioned before there are two reasons to believe that oxidation of metal NPs should depend on size. First, is theoretical predictions based on calculations of Gibbs free energy change associated with metal surface area.[86] According to these calculations oxidation potential is proportional to $1/r$ (r is the radius of NP). The second theory is based on concentration profiles of metal ions diffusing away from the dissolving NPs.[89] Theory based on diffusion only predicts that the peak potential in a stripping voltammogram does not depend on NP size, but shifts positive with increase in coverage of metal atoms when the system is electrochemically reversible and diffusion layers of NPs overlap. When the diffusion layers do not overlap, peak potential shifts with particles size and independent of the coverage. For irreversible systems, theory predicts that oxidation peak potential shifts negative with decrease in NPs size and is independent of metal atom surface coverage. In Chapter III we attributed the experimentally observed negative shift in peak potential with decreasing NP radius to a shift in standard potential for the Ag/Ag^+ redox couple based on the fact that our system was reversible and operating under conditions of planar diffusion. Here we extend our work to the study of the size-dependent electrochemical oxidation of Au NPs. There are several different aspects compared to our previous report on Ag NPs.[6] First, this work involves a different metal. Second, we electrodeposit Au directly on Glass/ITO electrodes with size control from about 8 to 250 nm in diameter. This contrasts our previous method of chemically synthesized Ag NPs and depositing them chemically onto Glass/ITO through a silane linker. This removes the effect of the linker or stabilizer molecule on NP oxidation.

Third, the oxidation process involves complex ion formation ($AuBr_2^-$ or $AuBr_4^-$)[107] as opposed to the formation of a simple ion (Ag^+). Finally, we demonstrated the discrimination of two different sizes electrochemically on the same electrode, which is a step toward electrochemical multinanoparticle size analysis for characterization or multianalyte sensing applications.

4.2 EXPERIMENTAL DETAILES

Figure 4.1 shows the general scheme of experiment. There are two main steps: 1) synthesis of Au NPs of different size directly on Glass/ITO electrode surface by Chronocoulometry and 2) electrochemical oxidation of Au NPs as a function of size by LSV.

Electrochemical deposition of Au NPs. Au nanoparticles (NPs) were electrochemically deposited onto the clean Glass/ITO working electrode using a CH Instruments (Austin, TX) 630C electrochemical workstation in chronocoulometry mode with an Ag/AgCl (3M KCl) reference electrode and a Pt counter electrode to complete the cell. The potential was stepped from 1.0 V to a final deposition potential ranging between -0.2 V and 0.8 V for an appropriate time until 6×10^{-4} Coulombs (C) of charge passed during deposition. After the desired charge was achieved, the Glass/ITO/Au NPs electrode was removed from the cell. The electrodes were gently rinsed further with water and dried under N_2. The deposition time ranged between 2 and 5 min and the average Au NP diameter ranged from 8 to 250 nm.

Electrochemical Oxidation Measurements. The electrochemical cell consisted of three electrodes with a 1.4 cm^2 Glass/ITO/Au NP as the working electrode, a Pt wire counter electrode and an Ag/AgCl reference electrode. All of the electrochemical measurements were performed in 10 mM KBr in 0.1 M $HClO_4$ electrolyte solution at a scan rate of 1 mV/s with a potential range of 0.5 to 1.1 V in linear sweep voltammetry (LSV) mode.

Electrochemical Deposition
Chronocoulometry

Electrochemical Stripping
Linear Sweep Voltammery

$[AuCl_4]^- + 3\ e^- \rightarrow Au^0 + 4\ Cl^-$

$E^0 = +0.93\ V$

Advantage:
Control of the coverage by controlling #
of Coulombs deposited

$[AuBr_4]^- + 3\ e^- \rightarrow Au^0 + 4\ Br^-$

$E^0 = +0.85\ V$

$[AuBr_2]^- + 1\ e^- \rightarrow Au^0 + 2\ Br^-$

$E^0 = +\ 0.96\ V$
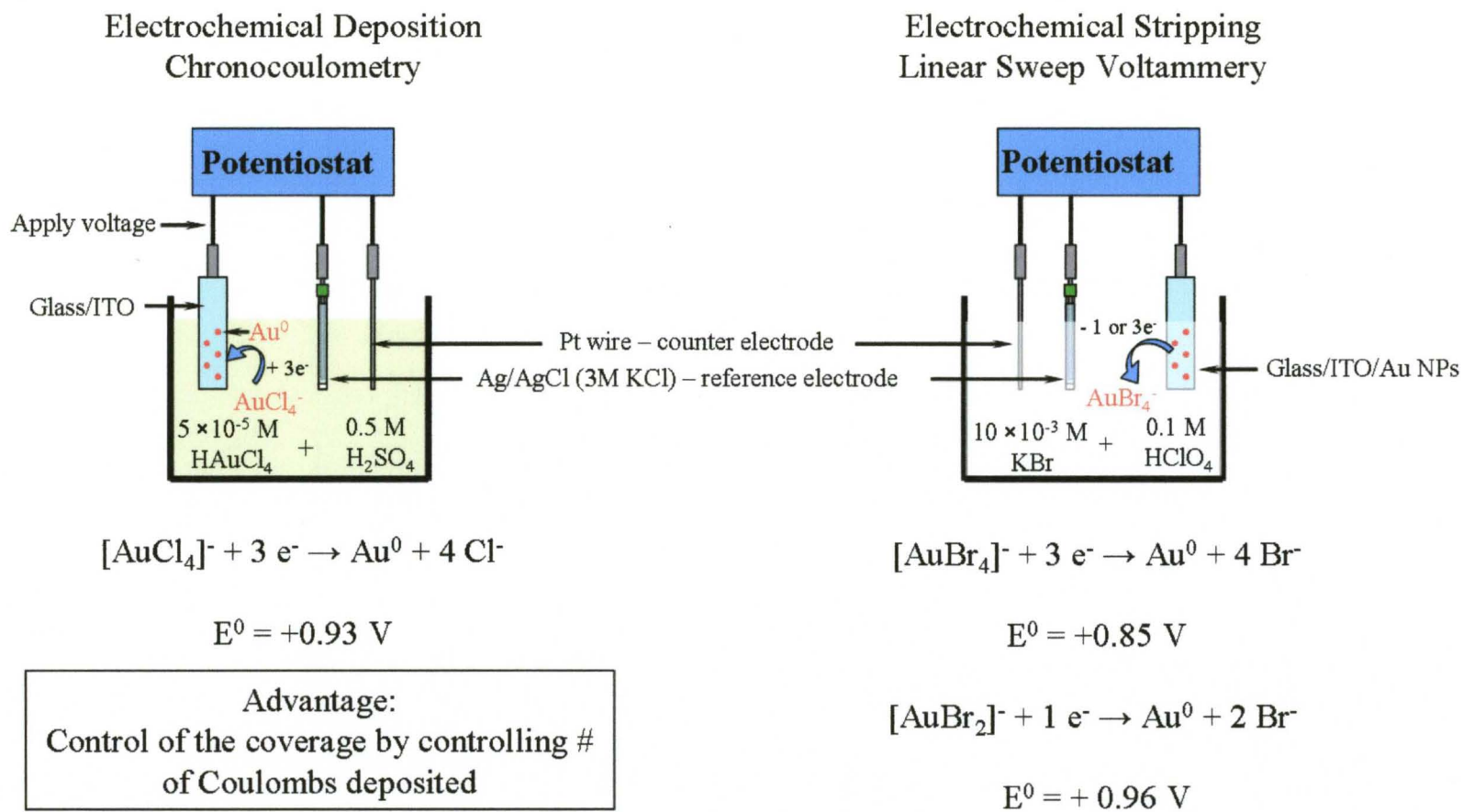
Figure 4.1 General set-ups for Au NPs deposition and Au NP oxidation experiments

4.3 RESULTS AND DISCUSSION

Electrochemical deposition of Au NPs of different size on Glass/ITO. Figure 4.2 shows a cyclic voltammogram (CV) of a clean Glass/ITO electrode measured from 1.5 V to -1.0 V at 100 mV/s in a solution of 5×10^{-5} M HAuCl$_4$ in 0.5 M H$_2$SO$_4$. There is a cathodic peak at ~290 mV on the forward scan attributed to the reduction of AuCl$_4^-$ to metallic Au^0 at the electrode surface according to the following reaction:

$$AuCl_4^- + 3e^- \rightarrow Au^0 + 4Cl^- \qquad E^0 = 0.994V \text{ vs. NHE} \qquad \text{(Rxn 4.1)}$$
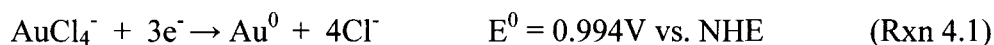
There is a second cathodic peak starting at ~-0.6V due to the hydrogen evolution reaction. During the reverse scan, a cathodic current flowed until about 0.85 V, which is the onset for the Au oxidation peak centered at about 1.3 V. The cathodic current flowing up until 0.85 V is due to the reduction of Au by reaction (4.1) above. The fact that the onset of Au reduction occurs at about 0.5 V on the forward scan, but remains up until 0.85 V on the reverse scan is due to the well known nucleation and growth phenomenon. Within the timescale of the forward scan, a significant amount of current is due to reduction of AuCl$_4^-$ does not flow until a potential below 0.5 V even though it is thermodynamically possible at more positive potentials. This is because an activation barrier must be overcome to initially reduce the AuCl$_4^-$ to form Au nucleation sites. Once these sites form below 0.5 V, the reduction of AuCl$_4^-$ is possible up until potentials of 0.85 V as shown by the crossover in the CV and presence of cathodic current up until 0.85 V on the reverse scan. The Au formed below 0.5 V on the forward scan catalyzed
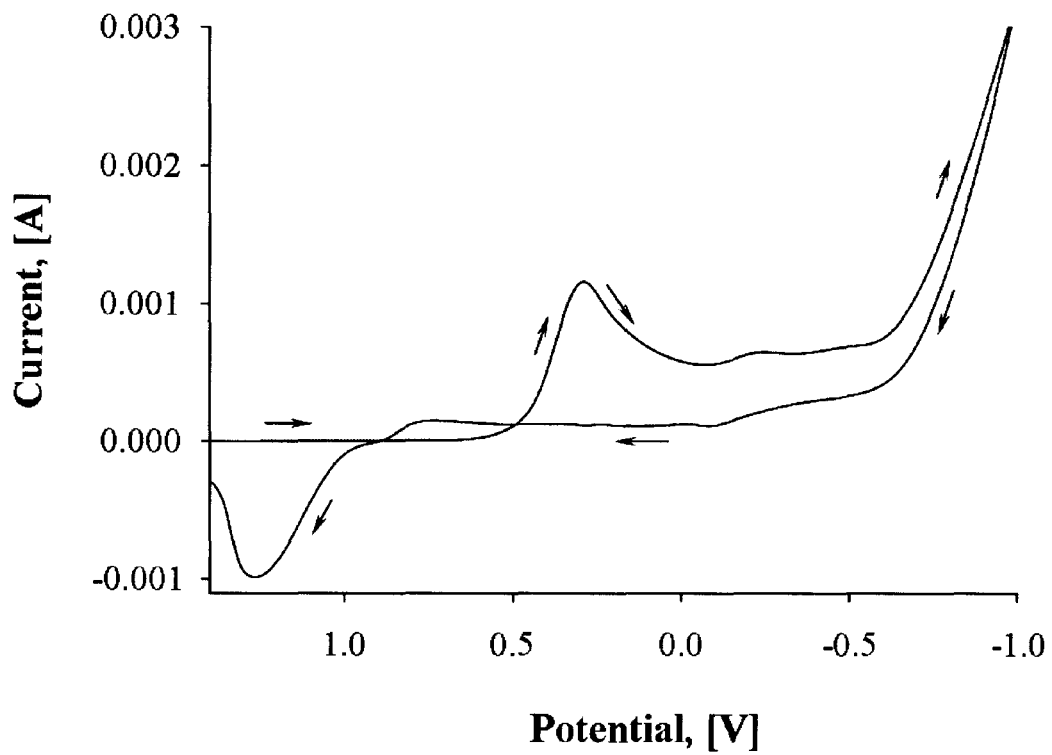
Figure 4.2 A cyclic voltammogram (CV) of a Glass/ITO electrode obtained in

5×10^{-5} M HAuCl$_4$ plus 0.5 M H$_2$SO$_4$ at a scan rate of 100 mV/s. The arrows show the

direction of the forward and reverse scan beginning at 1.5 V and ending at -1.0 V.

the reduction of $AuCl_4^-$ so that it can proceed at more positive potentials on the reverse scan. This is a well-known phenomenon that has been described previously.[108]

Figure 4.3 shows scanning electron microscopy (SEM) images of Glass/ITO electrodes before (inset on Figure 4.3 F) and after Au electrodeposition at different potentials for the required time needed to deposit 6 x 10^{-4} C of charge. The dark, grainy background corresponds to the Glass/ITO electrode and the bright, somewhat rough and spherical features correspond to the Au NP deposits. It is clear from the images that the size of the Au NPs increases and the density of the Au NPs decreases with increasing electrode potential from -0.2 to 0.8 V while keeping the total coverage in terms of Au atoms constant on the surface by controlling the amount of charge deposited. It is crucial to keep the coverage in terms of Au atoms constant on the surface and only vary the NP size and density in order to properly study the size-dependent oxidation properties. Based on SEM analysis, the average diameters of the Au NPs on the Glass/ITO electrodes were 8 ± 6, 10 ± 7 nm, 13 ± 7, 23 ± 9, 61 ± 20 and 249 ± 52, respectively, for electrode deposition potentials of -0.2 V, 0.0 V, 0.2 V, 0.4 V, 0.6 V, and 0.8 V. The average diameter of the Au NPs formed at -0.2 and 0.0 V are statistically the same according to a t-test for comparison of two means at a 95% confidence level. Most of the Au NPs have a spherical or irregular shape and the larger particles formed at 0.6 and 0.8 V have a noticeably rough, flower-like morphology that has been observed by others for Au deposition on Glass/ITO.[109,110] The density of Au NPs ranged from 85 to less than 1 NP per $1\mu m^2$ at -0.2 and 0.8 V, respectively.
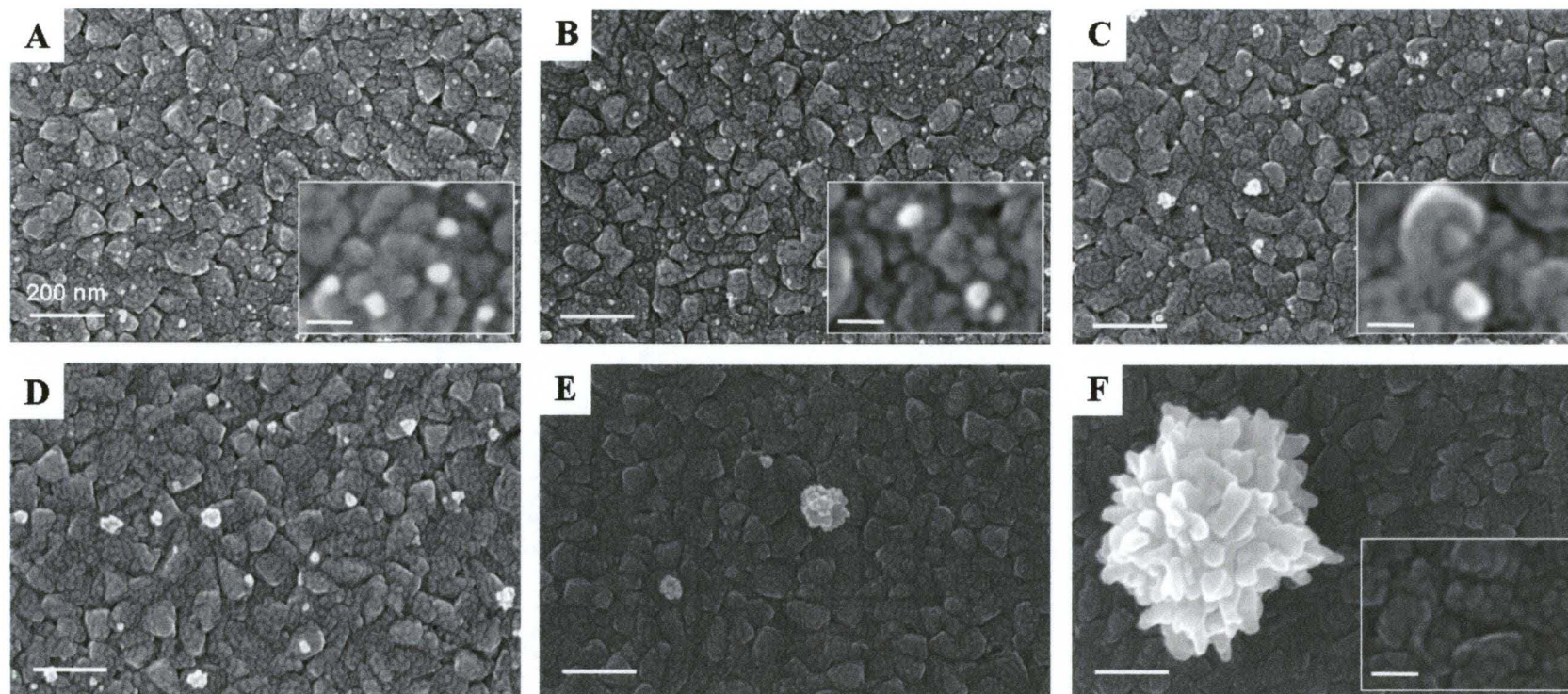
Figure 4.3 SEM images of Glass/ITO/AuNPs deposited at different potentials: A) -0.2V, B) 0.0V, C) 0.2V, D) 0.4V, E) 0.6V, and F) 0.8 V. The inset of F is a bare Glass/ITO electrode. The scale bars in the insets are 50 nm.

The electrochemical deposition of metal proceeds through the nucleation of metal clusters and subsequent growth.[111] Small Au NPs deposit on the surface at high overpotentials (-0.2 V), because the formation of small Au nucleation sites is energetically favorable all over the electrode surface. This leads to a large number of nucleation sites and, given the same total amount of Au deposited, a smaller average diameter of each Au NP deposited. At small overpotentials (or the very onset of the thermodynamically favored potential for Au deposition), the energy is not sufficient for rapid Au nucleation all over the surface. The energy barrier is significant relative to the electron energy (governed by potential), so that there is a lower probability of an Au nucleation event. As soon as a nucleation event occurs, though, that nucleation site catalyzes further Au reduction, leading to the preferential growth of that particle over the formation of new nucleation events. This leads to a low density of Au NPs that are larger relative to Au NPs formed at more negative potentials, given that the total amount of Au deposited is constant.

The relative standard deviation of the average NP diameter was larger for small particles (73, 69, 56% for deposition potentials of -0.2, 0.0, 0.2 V respectively) compared to that for the larger particles (38, 32, 21% for deposition potentials of 0.4, 0.6, 0.8 V, respectively). The larger relative standard deviation at negative deposition potentials could be due to 1) interparticle diffusional coupling[112] that occurs with a higher density of Au NPs and 2) the fact that new nucleation sites can form throughout the deposition process, which leads to some nanoparticles that nucleate and grow at a later time. In contrast, the lower density of nucleation sites at larger deposition potentials prevents interparticle diffusional coupling and the continued growth of the initial Au nucleation

sites formed is favored over the formation of new nucleation sites, preventing a significant amount of nucleation and growth at a later time. The fact that smaller particles grow faster than larger particles helps to reduce size dispersity if some particles nucleate and grow at a later time and do not experience interparticle diffusional coupling.[112]

Electrochemical oxidation of Au NPs as a function of size. Figure 4.4 shows linear sweep voltammograms (LSVs) of Glass/ITO electrodes with Au NPs electrodeposited at different potentials as shown in the SEM images in Figure 4.3. We obtained the LSVs from 0.5 V to 1.1 V in 10 mM KBr plus 0.1 M $HClO_4$ at 1.0 mV/s in order to determine the peak oxidation potential (E_p) for the different-sized Au NPs. The E_p shifts positive with increasing NP diameter as predicted by Plieth[86] and shown by our group previously for chemically-synthesized Ag NPs attached electrostatically to Glass/ITO.[6] We found that we could only electrodeposit Au NPs as small as 8 ± 6 nm on Glass/ITO with our procedure. In order to study the oxidation of smaller Au NPs, we chemically synthesized 4 nm average diameter Au NPs using a literature procedure[102] (as described in Chapter II) and attached the NPs to Glass/ITO electrostatically as described in Experimental chapter. Figure 4.4 shows the LSV of a Glass/ITO electrode coated with the 4 nm average diameter Au NPs, where the E_p value was 733 mV, which is in line with the trend that the oxidation potential decreases with decreasing NP diameter. The 4 nm average diameter Au NPs remarkably oxidized at a potential ~200 mV more negative than the ~250 nm diameter Au NPs deposited electrochemically at 0.8 V. The larger current in the LSV for the 4 nm Au NPs is due to a slightly higher coverage of Au on that
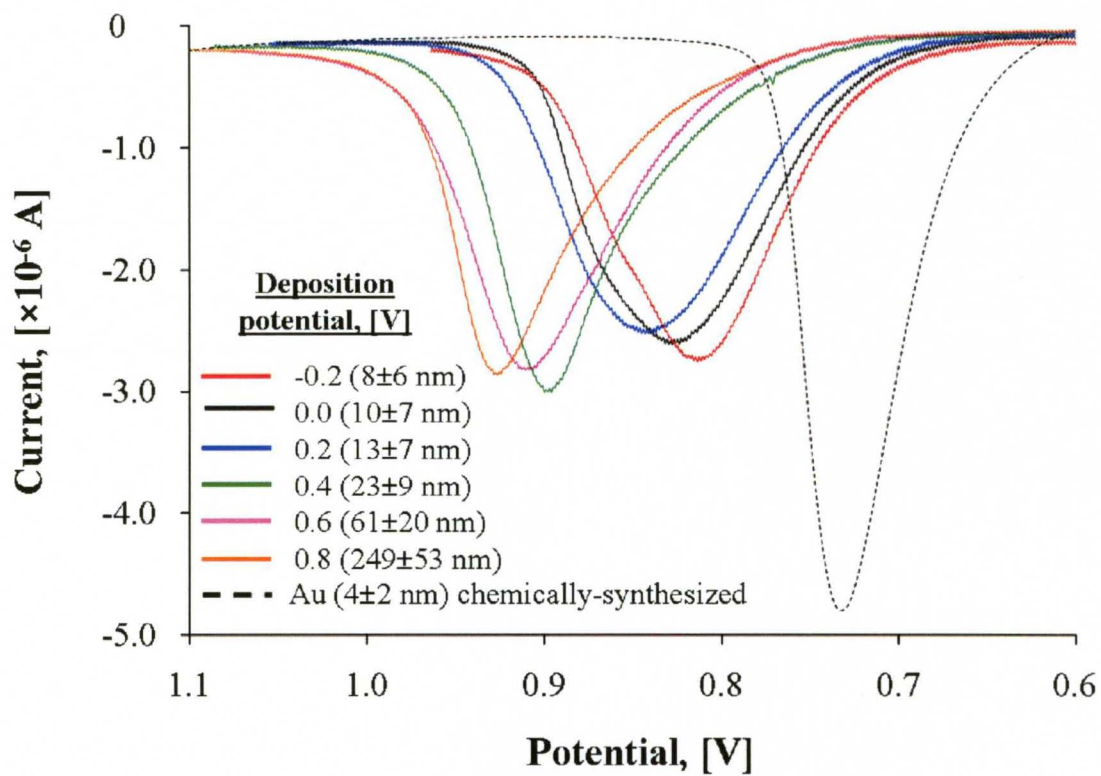
Figure 4.4 Linear Sweep Voltammograms obtained in 10 mM KBr plus 0.1 M HClO₄ electrolyte at 1 mV/s of Glass/ITO electrodes coated with electrochemically- and chemically-synthesized Au NPs as indicated.

particular sample and a narrower oxidation peak compare to those of the electrochemically-deposited Au NPs.

Previously, Compton and co-workers described a theory for the oxidation of an array of Ag NPs on an electrode surface.[89] Based on models of the dissolved ions diffusing away from the array of NPs during metal oxidation, they reported that under conditions of planar diffusion (where the diffusion layers of the NPs significantly overlap), the E_p of the oxidative stripping wave is independent of the coverage (in terms of atoms) if the system is electrochemically irreversible and is a function of ln(coverage) if the system is electrochemically reversible. Also, they predicted that E_p depends on NP diameter if the system is irreversible, but does not depend on the NP diameter if it is reversible. We studied the effect of Au coverage on E_p for the 4 nm diameter Au NPs and determined that E_p is linear as a function of ln(Au coverage) as expected for a reversible system. Figure 4.5 shows LSVs of Glass/ITO electrodes coated with different coverages of chemically-synthesized 4 nm average diameter Au NPs by immersion of the electrode into Au NP solution for different amounts of time as indicated. Table 4.1 shows the corresponding data obtained from LSVs and Figure 4.6 shows a plot of peak potential versus ln(Au Coverage), or ln(Q). The linear relationship is indicative of an electrochemically reversible reaction. The charge passed during the oxidation of the Au deposited at -0.2 V, 0.0 V, 0.2 V, 0.4 V, 0.6 V, 0.8 V, and the 4 nm diameter Au NPs in Figure 4.4 was (2.8, 2.9, 2.9, 2.7, 2.7, 2.7, and 3.3)$\times 10^{-4}$ C, respectively, showing a nearly constant coverage of Au atoms. With a constant coverage and a reversible system under conditions of planar diffusion, theory based on diffusion alone predicts that E_p does not shift as a function of NP diameter. Since we clearly show a 200 mV shift for a size
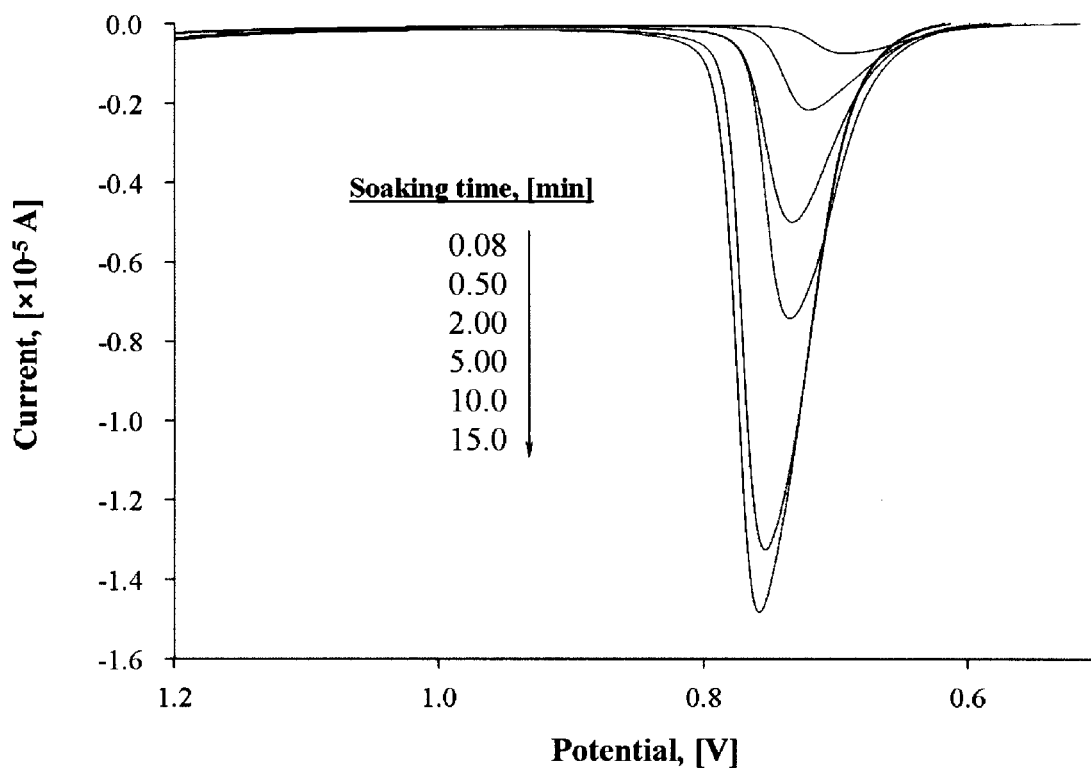
Figure 4.5 LSVs obtained in 10 mM KBr plus 0.1 M HClO₄ solution of Glass/ITO electrodes coated with 4 nm average diameter Au NPs by soaking in an Au NP solution for 0.08, 0.50, 2, 5, 10 and 15 min as indicated.

Soaking time, [min]	Coverage or Charge (Q) in coulombs (C)	ln (Q)	Peak Potential [mV]
0.08	6.235×10^{-5}	- 9.68	692
0.5	16.81×10^{-5}	- 8.69	720
2	35.17×10^{-5}	- 7.95	734
5	49.59×10^{-5}	- 7.61	735
10	86.57×10^{-5}	- 7.05	753
15	98.75×10^{-5}	- 6.92	758

Table 4.1 Peak oxidation potential of 4 nm Au NPs as a function of coverage.
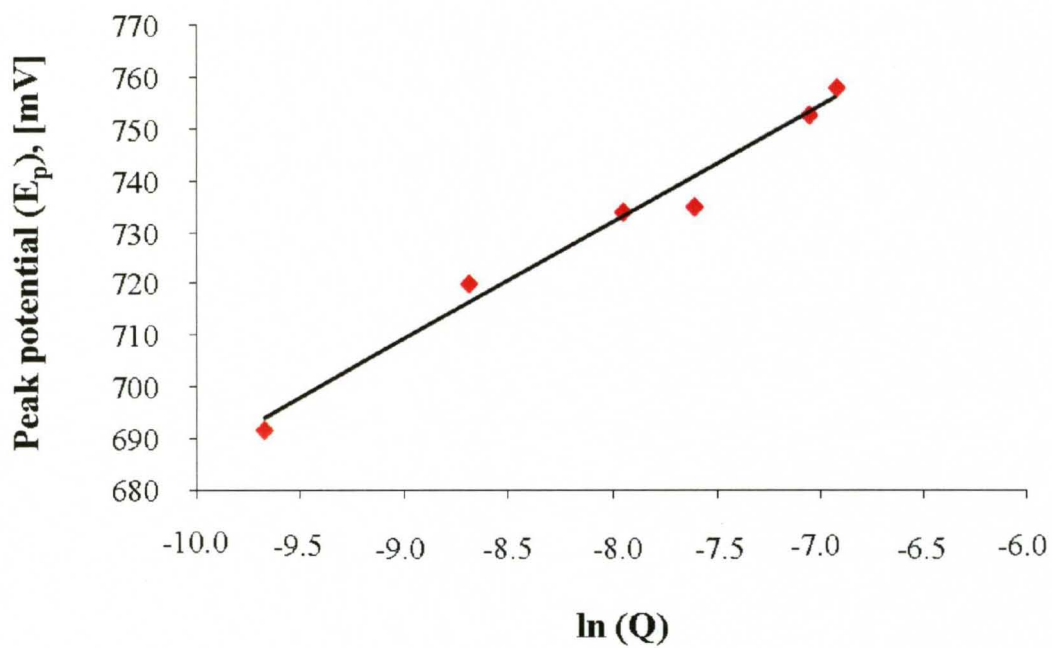
Figure 4.6 Plot of peak oxidation potential (E_p) in mV versus ln (Au Coverage), or ln (Q).

range of 4 nm to 250 nm, we conclude that the shift in E_p is due to a size-dependent shift in the thermodynamic oxidation potential (E^0) of the Au NPs as opposed to an effect of ion diffusion away from the NPs. An approximation of the diffusion layer at the small scan rates used in the LSVs (1.0 mV/s) showed that significant overlap of the diffusion layers exists, where planar diffusion would dominate.

We found that a deposition of $\sim 6 \times 10^{-4}$ C led to the oxidation of $\sim 3 \times 10^{-4}$ C as shown in Figure 4.4. Assuming a 3 e^- reduction of $AuCl_4^-$ during deposition, the oxidation corresponds to 1.5 e^-. The possible oxidation reactions are:

$$Au^0 + 2\ Br^- \rightarrow AuBr_2^- + e^- \qquad E^0_{\ Au(I)/Au(0)} = 0.963\ V\ vs.\ NHE \qquad (Rxn\ 3.3)$$

$$Au^0 + 4\ Br^- \rightarrow AuBr_4^- + 3\ e^- \qquad E^0_{\ Au(III)/Au(0)} = 0.858\ V\ vs.\ NHE \qquad (Rxn\ 3.4)$$
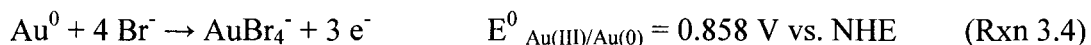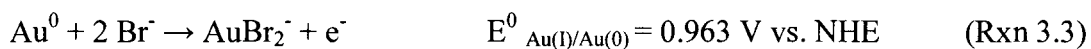
Theoretically to satisfy the 1.5 e^- oxidation process, 75% of the Au oxidation product would be $AuBr_2^-$ and 25% would be $AuBr_4^-$. It is interesting that the $AuBr_2^-$ is favored over the more thermodynamically stable $AuBr_4^-$. A second explanation for half the charge upon oxidation relative to the Au reduction is that not all of the Au oxidized from the surface. SEM images obtained after Au oxidation show essentially complete removal of Au, ruling out this possibility (Figure 4.7).

Table 4.2 displays the size of the electrochemically-deposited Au NPs as a function of deposition potential, as determined by SEM, and the corresponding E_p and charge as determined by LSV (average of at least 3 samples). The size of the Au NPs deposited on Glass/ITO electrodes are all statistically different, except for those deposited
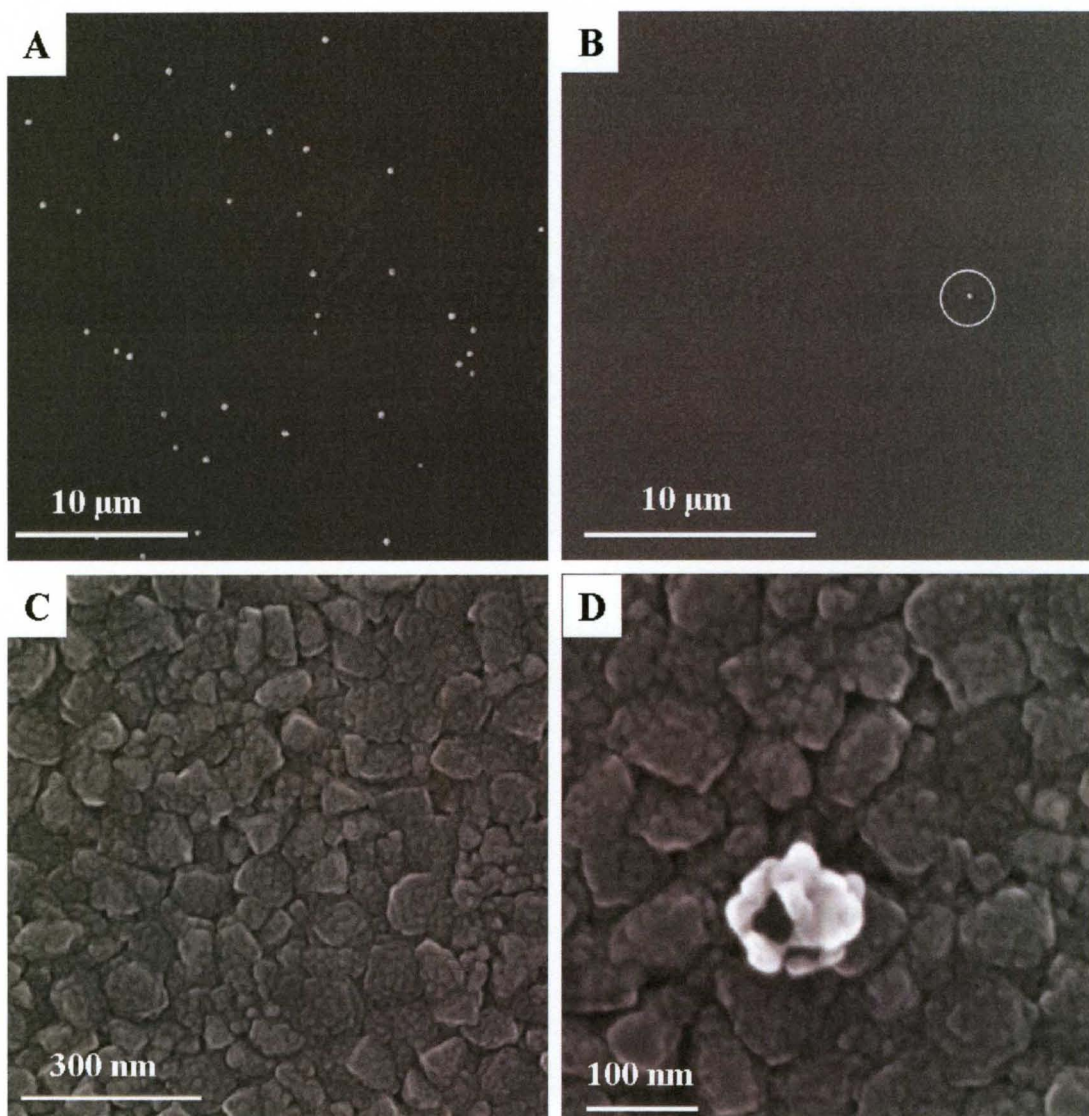
Figure 4.7 SEM images of Glass/ITO/Au NP samples prepared by deposition at 0.8 V A) before electrochemical oxidation and B-D) after electrochemical oxidation. The circle in Frame B shows the area imaged in Frame D.

Deposition potential, [mV]	Diameter, [nm] SEM	Oxidation peak potential E_p, [mV]	Theoretical E_p [mV] 1e$^-$ reaction	Theoretical E_p [mV] 1.5e$^-$ reaction	Charge under the peak ($\times 10^{-4}$ C)
Au Seed	4 (±2)	734 (±1)	714	780	3.45 (±0.12)
-200	8 (±6)	822 (±10)	814	847	2.86 (±0.13)
0	10 (±7)	829 (±8)	834	860	2.90 (±0.20)
200	13 (±7)	842 (±7)	847	875	2.91 (±0.04)
400	23 (±9)	890 (±15)	880	891	2.83 (±0.13)
600	61 (±20)	910 (±14)	900	904	2.85 (±0.13)
800	249 (±53)	913 (±19)	910	911	2.79 (±0.17)

Table 4.2 Statistical size and electrochemical data for all Glass/ITO/Au NP electrodes. The theoretical $E_{p,theor}$ values are based on the Plieth equation.

at -0.2 and 0.0 V. The oxidation potential for Au NPs deposited at -0.2 V and 0.0 V, and at 0.6 V and 0.8 V, are statistically the same with 95% confidence level. Taking into account the experimental conditions of constant coverage and planar diffusion, we believe that the shift in E_p is due to a size-dependent change in E^0 as predicted by Plieth[86] and Henglein.[85] Figure 4.8 shows three theoretical plots (dashed lines) of the difference between the oxidation potential of Au NPs ($E_{p, AuNP}$) and oxidation potential of bulk Au ($E_{p, bulk}$) as a function of nanoparticle radius calculated using the Equation 3.1 developed by Plieth. [86] Note that for calculating the shift in oxidation potential we used the surface stress (γ) of Au in vacuum (1880 erg cm^{-2}).[86] The actual value could be different in electrolyte solution. Also we used E_p of Au NPs deposited at 0.8 V (913 mV) as the bulk value in order to perform theoretical calculations. The three plots in Figure 4.8 correspond to using 1.0, 1.5, and 3.0 as the value for z in equation (3.1). As discussed previously, the oxidation is a combination of a 3 e⁻ and 1 e⁻ process with an average of 1.5 e⁻. The experimentally obtained values of E_p match reasonable well with the 1 e⁻ and 1.5 e⁻ curve, especially for the smaller sized Au NPs (see Table 4.2). The shift in E_p is forced to be zero at the larger sizes and does not match the curve as well. Interestingly, the data for the Au NPs fits the theory of Plieth much better than our previous work on Ag NPs, although the general trend was the same in both reports.[6] The main differences in this work is that we synthesized the Au NPs electrochemically directly on Glass/ITO, except for the 4 nm Au NPs, and the oxidation process involved the formation of a complex anion with ligands ($AuBr_2^-$) versus direct oxidation of the metal with no ligands (Ag^+). It is interesting to note that there is a 88 mV difference in

$$\Delta E = E_p - E_b = -\frac{2\gamma W_m}{zF} \times \frac{1}{r}$$

- • Experiment
- --- 3 e⁻ process
- ---- 1.5 e⁻ process
- --- 1 e⁻ process

E$_{p,\ AuNP}$ - E$_{b,\ Bulk\ Au}$ [V]

Particle Radius, [nm]
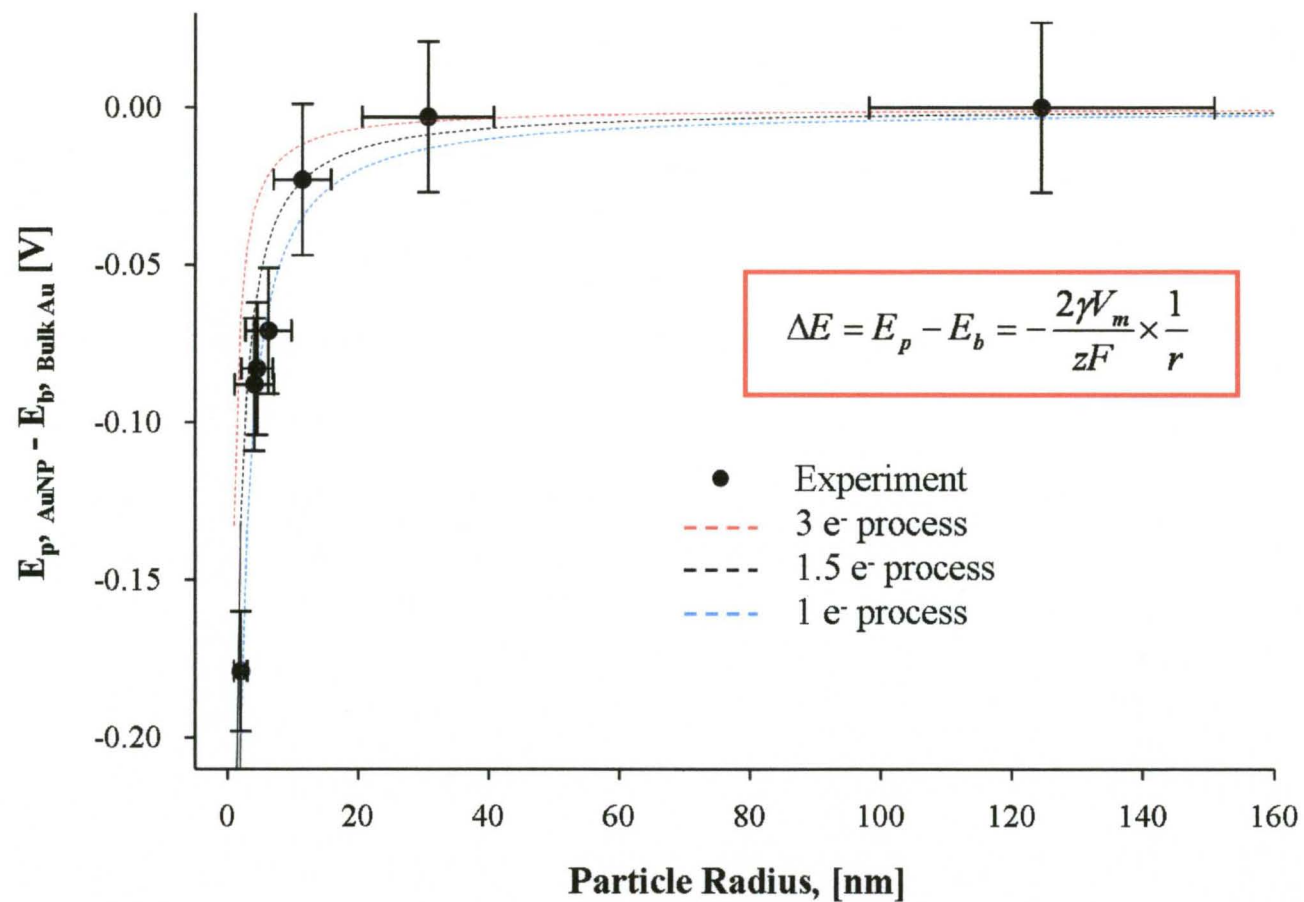
Figure 4.8 Experimentally measured shift in oxidation potential (•) for Au NPs versus bulk Au as a function of radius as compared to theory (---). Blue dashed line (1 electron process), black dashed line (1.5 electron process), and red dashed line (3 electron process).

the oxidation potential of Au NPs with average diameters of 8 nm and 61 nm (53 nm difference) and the same 88 mV difference in oxidation potential of Au NPs with average diameters of 4 nm and 8 nm (4 nm difference). There is clearly a more dramatic property change as the Au NP diameter decreases below 8 nm as predicted by theory.[86]

One potential benefit of different NPs having different oxidation potentials is that LSV could be utilized for size analysis. It might even be used to determine relative populations of different sized NPs in a solution. Different sized NPs having different biological receptors could also potentially serve as electrochemical tags in a bioassay for analyzing multiple analytes. For these applications, it is necessary to be able to measure more than one size NP in the same experiment. Figure 4.9 shows our first attempt to monitor the oxidation of two different sized particles simultaneously from one LSV. In this example, we performed the experiment with the 4 nm chemically-synthesized Au NPs and the 250 nm electrodeposited Au NPs. We used the most drastically different sizes as a proof of concept. First, we deposited the larger Au NPs at 0.8 V and then immersed the electrode into an aqueous solution of the 4 nm Au NPs for 60 min without functionalizing the Glass/ITO with APTES as we did for the 4 nm Au NPs in Figure 4.4. The LSV in Figure 4.9 clearly shows two well-resolved oxidation peaks corresponding to the 4 nm Au NPs (710 mV) and 250 nm Au NPs (918 mV) as labeled. These two different sizes oxidize with a more than 200 mV difference in E_p, making it easy to resolve the two sizes by LSV. This experiment clearly shows that we can distinguish between two different sizes of Au NPs present on an electrode surface at the same time by LSV, which may be important for using this technique to analyze NPs or for using different-sized Au NPs as electrochemical tags for sensing applications.
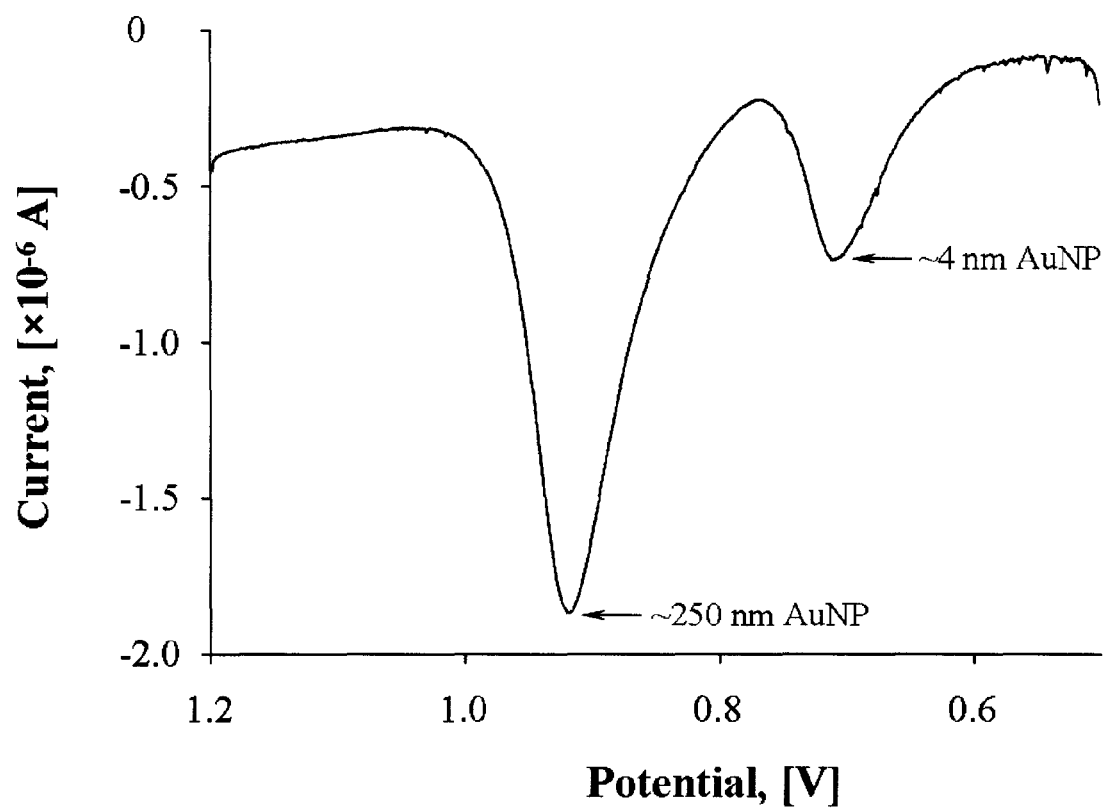
Figure 4.9 Linear sweep voltammogram of a Glass/ITO electrode containing a mixture of 250 nm and 4 nm average diameter Au NPs obtained in 0.01 M KBr plus 0.1 M HClO₄ at 1.0 mV/s.

4.4 CONCLUSIONS

Here we described the direct measurements of E_p for the oxidation of Au NPs as a function of size. Au NPs of different size were directly deposited at glass/ITO using chronocoulomentry at various potentials, which is easy to perform, fast, reproducible, and allows control over size and coverage. The oxidation potential for the Au NPs shifted negative with decreasing nanoparticle size which is consistent with the theory of Plieth,[86] calculations of Henglein,[85] and previously reported experimental data for different metals.[6] Our experimental results show that the oxidation of Au NPs is likely the combination of 1 and 3 electron processes. The oxidation of Au NPs of two different sizes deposited on the electrode surface at the same time shows two well resolved oxidation peaks. We believe that these results will motivate future fundamental and applied studies in the area of electrochemistry of nanomaterials.

CHAPTER V

SIZE-DEPENDENT ALLOYING OF COPPER WITH GOLD NANOPARTICLES

AT UNDERPOTENTIAL DEPOSITION (UPD) POTENTIALS

This Chapter describes the size-dependent alloying of Cu with Au nanoparticles (NPs) at underpotential deposition (UPD) potentials. This is the first observation of the alloying of Cu with Au NPs at UPD potentials. UPD of Cu on Au NPs of 8 ± 6 nm, 61 ± 20 nm, and 249 ± 53 nm directly deposited on the surface of Glass/ITO electrodes, and also on gold film, and on chemically synthesized Au NPs with average diameter of 4 nm which were chemisorbed on Glass/ITO electrode was studied. Stripping voltammetry demonstrated the formation of UPD layer of Cu for all sizes of Au NPs and for Au film. In addition, unusual bulk copper deposition occurred for Au NPs size from 4 to 60 nm diameter. Up to four different Cu oxidation peaks were detected. These peaks attributed to different phases of Cu in Au-Cu alloy nanostructure. The composition of the alloy depends on the Cu deposition time. Alloying of Cu with Au occurs to a lesser extent on larger particles.

5.1 INTRODUCTION

Underpotential deposition (UPD) is well-known phenomenon of deposition of a monolayer or a sub-monolayer of one metal on the surface of another metal at potentials more positive than Nernst potential for bulk deposition. Cu UPD on Au is the most widely studied system in this research area. Most of work has been focused on the Au (111) electrodes. The UPD of Cu on Au (111) occurs in two stages.[113] These two stages were extensively studied experimentally and in theory. The Cu deposition in sulfuric acid starts with random deposition of Cu adatoms and sulfate ions on the electrode surface followed by the formation of ordered phase at 2/3 of a monolayer Cu coverage. Cu adlayer at this stage has a honeycomb $(\sqrt{3}\times\sqrt{3})R30°$ structure in which surface coverage of Cu is 0.67 and with sulfate anions occupying the centers of honeycomb (coverage of anions is 0.33).[114] The second stage corresponds to the formation of full monolayer of Cu with (1×1) structure and sulfate ions adsorbed on top of the copper adlayer.[115] Adsorption of Cu can be affected by the presence of adsorbed anions. It was shown that the honeycomb structure can be transformed to (5×5) structure in the presence of chloride anions.[116] At chloride concentrations below 10^{-5} M a (2×2) structure was observed at potentials below +0.14 V vs SCE and copper coverage of 0.75 was determined. In perchloric acid solution, the situation is similar to low chloride concentration electrolytes. Cu UPD was observed on different crystal faces of Au electrodes. Thus, Au (110) and Au (100) both have (1×1) structure in sulfuric acid media.

While there is massive amount of publications on macro-sized electrodes, there are few reports on UPD of metal on the surface of metal nanoparticles (NPs). Hernandez et. al. used Pb UPD on Au nanoparticles to characterize their shape and relative size.[117] Compton and co-workers demonstrated the absence of UPD of Pb, Cd and Tl on the nanoelectrode arrays composed of silver nanoparticles with diameter less than 50 nm[118,119] as well as on Au NPs with average diameter of 10±5 nm.[120]

While study the UPD on macro scale is important for corrosion and catalysis, nanometer scale materials are interesting due to their size-dependent properties that can be applied in areas of catalysis and sensing.

Here we describe the size-dependent alloying of Cu with Au NPs at UPD potentials. We studied the UPD of copper on gold nanoparticles of 8±6 nm, 61±20 nm and 249±53 nm directly deposited on the surface of Glass/ITO (indium tin oxide) electrode. Also UPD deposition of copper was performed on gold film and chemically synthesized gold nanoparticles (Au NPs) with average diameter of 4 nm which we chemisorbed on Glass/ITO electrode. In contrast to results available in literature, UPD layer of copper was observed by stripping voltammetry for all sizes of gold nanoparticles. In addition, unusual bulk copper deposition was observed for nanoparticle size from 4 to 60 nm. We believe that unusual alloying of these two metals on nanometer scale could be a result of diffusion of copper atoms into the crystal lattice of Au NPs.

106

5.2 EXPERIMENTAL DETAILS

Synthesis of Au NPs. Au nanoparticles of 8, 60 and 250 nm were synthesized by direct electrochemical deposition on Glass/ITO electrode as described in Chapter IV. Briefly, 3 electrode cell was constructed with Glass/ITO as working electrode, Ag/AgCl (3M KCl) as reference electrode and Pt wire as counter electrode. Electrochemical deposition was performed in Chronocoulometry. The potential was stepped from 1.0 V to a final deposition potential -0.2 V, 0.6 V and 0.8 V for an appropriate time until 6×10^{-4} Coulombs (C) of charge passed during deposition. After the desired charge was achieved, the Glass/ITO/Au NPs electrode was removed from the cell. The electrodes were gently rinsed further with water and dried under N_2. The deposition time ranged between 2 and 5 min and the average Au NP diameter was 8, 60 and 250 nm respectively for -0.2 V, 0.6 V and 0.8 V deposition potentials.

Underpotential deposition of Cu on Au NPs. The electrochemical cell consisted of three electrodes with Glass/ITO/Au NP as the working electrode, a Pt wire counter electrode and an Ag/AgCl reference electrode. Cu UPD was deposited at 300 mV from the solution of 0.01 M $Cu(ClO_4)_2$ $\times 6H_2O$ in 0.1 M $HClO_4$ using linear sweep voltammetry (LSV). Working electrode was immersed into the electrolyte solution under potential control at 500 mV and scanned to 300 mV were it was paused for desired period of time (from 1sec to 17 h). Scan rate was 20 mV/s. Then sample was taken out under potential control, gently rinsed with nanopure water and used for oxidation experiments.

Electrochemical Oxidation Measurements. All measurements were performed in three electrode cell with Glass/ITO/Au NP/Cu UPD as the working electrode, a Pt wire

counter electrode and an Ag/AgCl reference electrode. All data were taken in 0.1 M

$HClO_4$ solution at room temperature at a scan rate of 20 mV/s with a potential range from

0 to 1.6 V.

5.3 RESULTS AND DISCUSSION

Figure 5.1 shows our general experimental set-up (see full details in supporting information). In the first step, we perform electrodeposition of Au nanoparticles of 8 ± 6 nm, 61 ± 20 nm and 249 ± 53 nm in diameter onto indium-tim-oxide (ITO)-coated glass electrodes as reported previously.[7] We compared these electrodes to bulk Au films and 4 nm diameter chemically-synthesized Au nanoparticles that were assembled electrostatically onto the glass/ITO electrodes. We refer to these electrodes as glass/ITO/Au$_{8nm}$, glass/ITO/Au$_{60nm}$, glass/ITO/Au$_{250nm}$, glass/ITO/Au$_{4nm}$, and Au films. Next, we deposited Cu at a UPD potential of 0.3 V versus Ag/AgCl for various times in a 0.01 M Cu(ClO$_4$)$_2$ + 0.1 M HClO$_4$ solution. Finally, we monitored Cu UPD stripping by cyclic voltammetry from 0.0 to 1.6 V versus Ag/AgCl at 20 mV/s in a Cu-free 0.1 M HClO$_4$ solution.

Figure 5.2 (A) shows cyclic voltammograms (CVs) of glass/ITO and glass/ITO/Au electrodes measured from 0.5 to -0.5 V in a solution of 0.01 M Cu(ClO$_4$)$_2$ and 0.1 M HClO$_4$. The cathodic peak in the CVs corresponds to Cu^{2+} reduction by the following reaction:

$$Cu^{2+}_{(aq)} + 2e^- \rightarrow Cu^0_{(s)} \qquad \text{(Rxn. 5.1)}$$

The potential for bulk Cu^{2+} reduction follows the order of Au$_{8nm}$ (190 mV) > Au$_{60nm}$ (225 mV) > Au$_{250nm}$ (240 mV) = bare glass/ITO. This shows that the growth of bulk Cu deposition is more energetically favored as the size of the Au NPs decreases. This is due to the well-know phenomenon of nucleation and growth. The growth of bulk Cu is more favorable at small Au nucleation sites. Interestingly, large Au NPs do not catalyze Cu
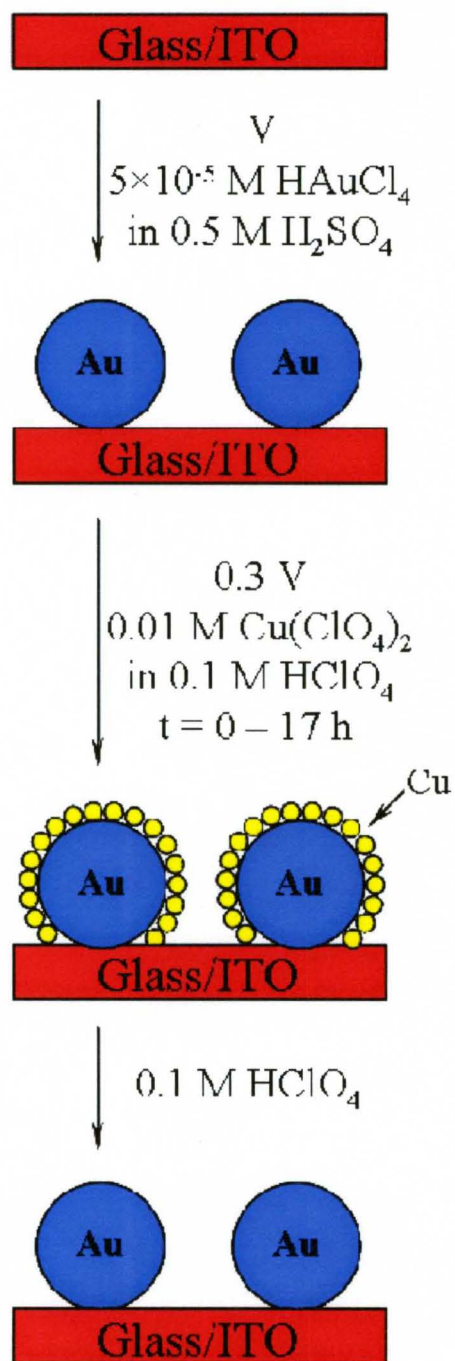
Figure 5.1 General scheme of experiment.
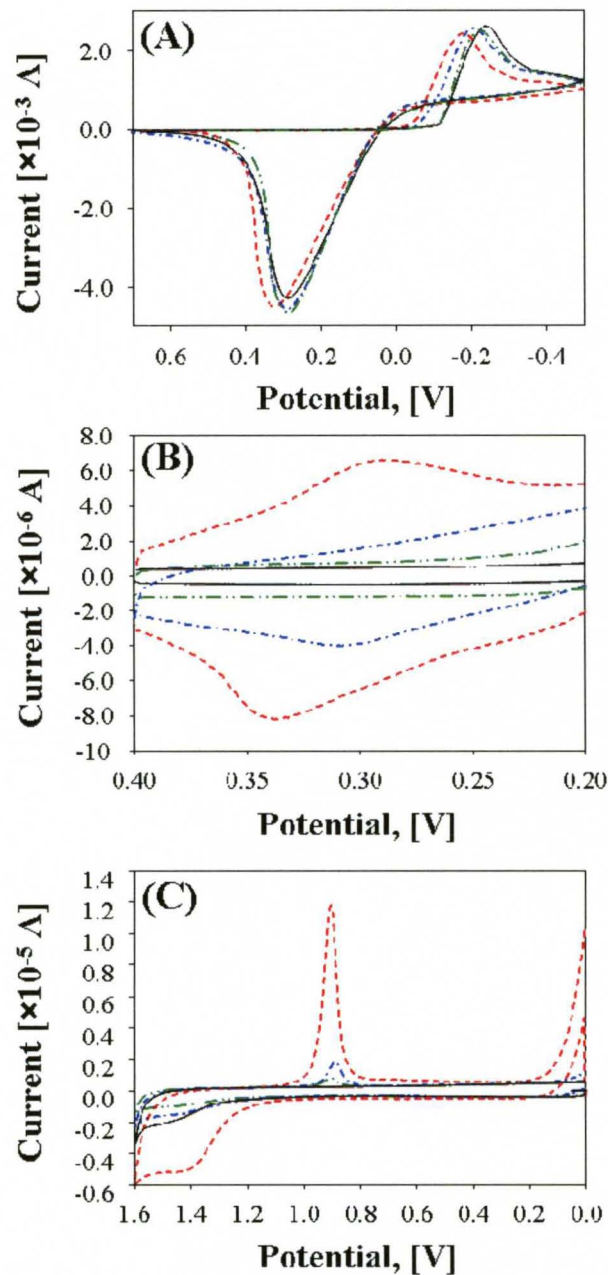
Figure 5.2 (A) CVs of Glass/ITO/Au NPs in 0.01 M Cu(ClO$_4$)$_2$ and 0.1 M HClO$_4$. **(B)** CVs of Glass/ITO/Au NPs in 0.01 M Cu(ClO$_4$)$_2$ and 0.1 M HClO$_4$. Narrow range of potentials. **(C)** CVs of Glass/ITO/Au NPs in 0.1 M HClO$_4$. (---) Au-8 nm, (- · -) Au 60 nm, (- ·· -) Au-250 nm, and (—) bare ITO. Scan rate 20 mV/s.

deposition any better than bulk ITO. The corresponding stripping peak for bulk Cu is at ~300 mV for all sizes.

Figure 5.2 (B) shows CVs of bare glass/ITO and glass/ITO/Au in 0.01 M $Cu(ClO_4)_2$ and 0.1 M $HClO_4$ measured from 0.4 to 0.2 V, focusing on the Cu UPD region. For glass/ITO/Au_{8nm}, the Cu UPD reduction and corresponding oxidation peaks occurred at ~300 mV and ~330 mV, respectively. The peaks are well-pronounced and visible above the background charging current. For glass/ITO/Au_{60nm}, the Cu UPD reduction was not well-pronounced, but the subsequent oxidation was visible at ~310 mV. In the case of glass/ITO/Au_{250nm} and bare glass/ITO electrodes, there was no visible reduction or oxidation peaks for Cu UPD. The Cu UPD peaks are likely absent in the voltammetry for Au_{250nm} and difficult to observe in the Au_{60nm} because of the much lower Au surface area. Since the amount of Au is the same for all electrodes, but the size changes, the surface area increases with decreasing Au NP size.

Figure 5.2 (C) shows the CVs of Glass/ITO Au NPs in 0.1 M $HClO_4$. From these CVs we can quantify the relative Au surface area based on the Au oxide reduction peak that occurs at 0.9 V. This reduction corresponds to the reduction of the surface Au oxided formed at ~1.4 V. The glass/ITO/Au_{8nm} has the biggest reduction peak, indicating that it has high surface area. This reduction peak decreases with increasing size of the Au NPs.

Our initial goal was to determine if the oxidation potential of the Cu UPD layer on Au depended on the size of the Au, since we recently determined that the oxidation potential of Au and Ag nanoparticles depends on the size.[6,7] To study this we performed the experiment in Figure 5.1. At a deposition potential of 300 mV, only a single Cu UPD

layer should form on the Au NPs. The stripping of this UPD layer after deposition for 1 s was difficult to compare between the different sizes because of the low currents associated with the small surface area Au_{60nm} and Au_{250nm} NPs (Figure 5.3). From the limited data, it appeared that there was not a very large dependence on the stripping potential as a function of size. All visible UPD stripping peaks were in the range of 280 – 320 mV. From this experiment we observed an interesting peak at ~1.2 V in the voltammetry for the small 8 nm NPs that led us to believe other forms of Cu deposited onto the small Au NPs.

Figure 5.4 shows CVs of glass/ITO/Au_{8nm} electrodes from 0.0 to 1.6 V using the procedure in Figure 5.1 after Cu UPD deposition at 300 mV for times ranging from 0 sec to 17 h. Instead of just observing 1 stripping peak for Cu UPD oxidation as expected for one layer of Cu on Au, we observed several different oxidation peaks depending on the deposition time, which we attribute to different forms of Cu. After 0 s of deposition time, we only observed the oxidation and reduction of Au at ~1400 mV and 880 mV, respectively. After 1 s, we observed two oxidation peaks attributed to Cu at 300 mV (Cu-1) and 1220 mV (Cu-2). After 1 min, the Cu-1 and Cu-2 peaks increase slightly and shift negative in potential while a new Cu-3 peak appeared at 575 mV. With increasing time, the Cu-1 and Cu-3 peaks remain similar in magnitude but shift negative in potential. For example, the Cu-1 oxidation peak shifted from ~300 mV after 1 sec to 140 mV for 17 h. The Cu-3 oxidation peak appeared at ~575 mV, and shifted negative with an increase in the Cu deposition time until it disappeared at times of 4h and longer. The Cu-2 peak at ~1200 mV increased more dramatically with time and shifted negative to ~1170 mV after 17 h. Another oxidation peak (Cu-4) appeared at ~900 mV for deposition times of 30
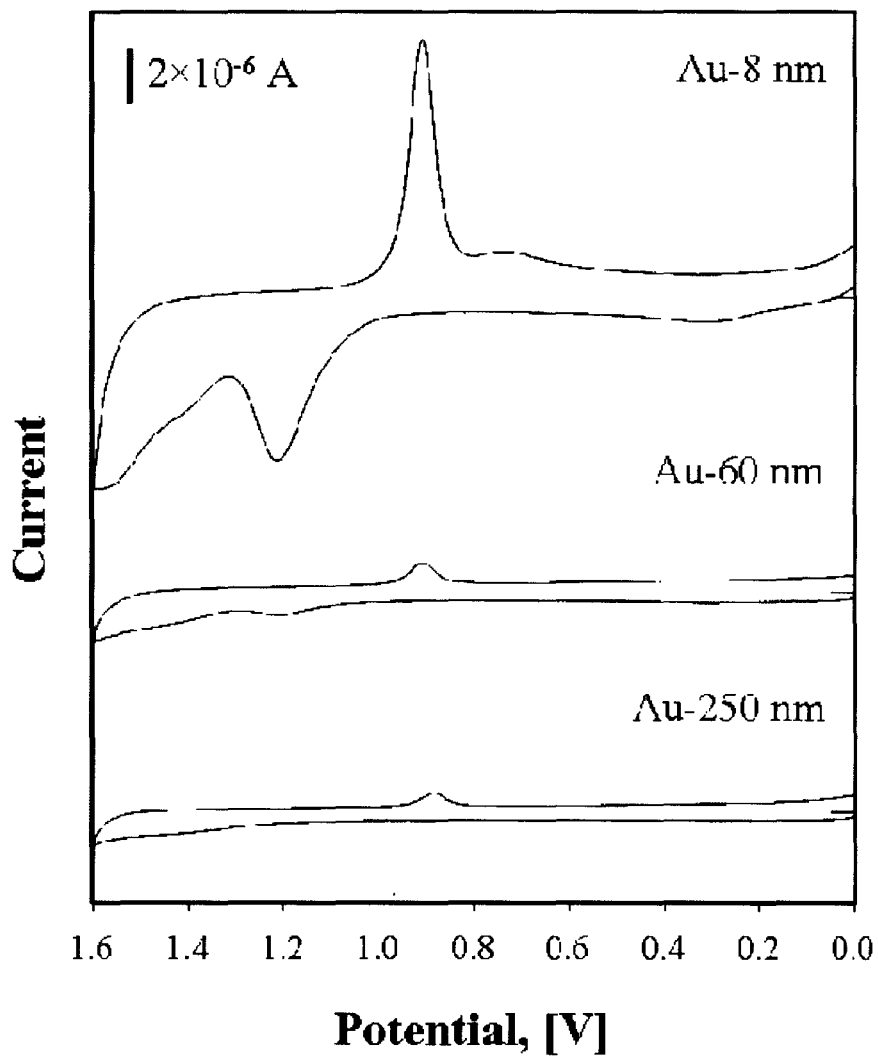
Figure 5.3 CVs of Glass/ITO/Au NPs after 1 sec of Cu UPD deposition performed in 0.1 M HClO₄ for different Au NP sizes as indicated. Cu deposition time was 1 sec. Scan rate was 20 mV/s.
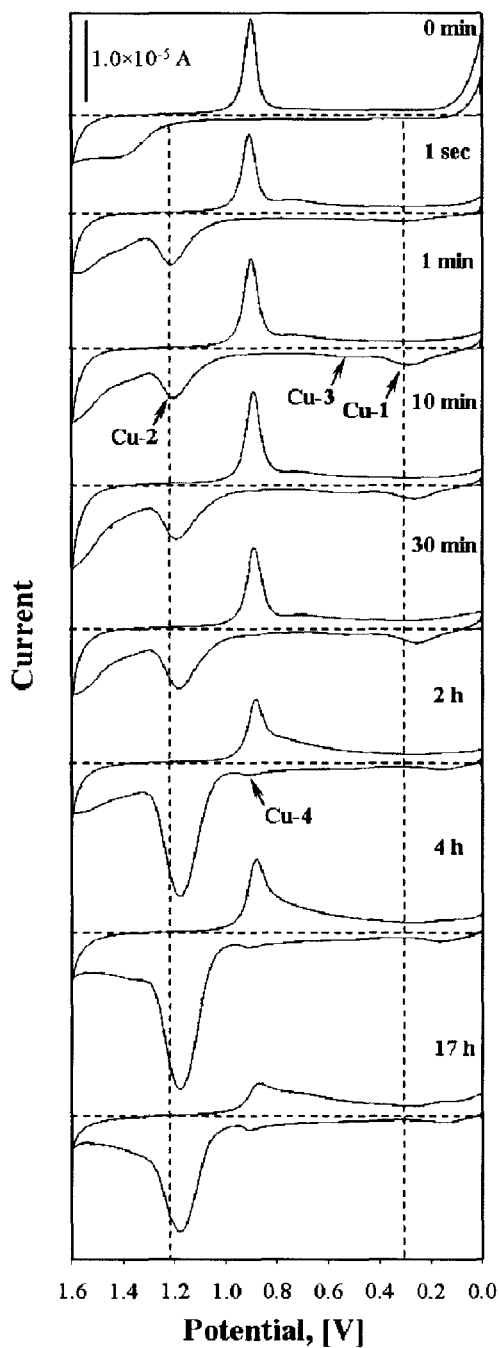
Figure 5.4 . CVs of Glass/ITO/Au-8 nm/Cu in 0.1 M HClO₄ for different Cu

deposition times, as indicated. Scan rate 20 mV/s. horizontal dashed lines point level 0

current. Vertical dashed lines are to easier visualize shift in oxidation potential for Cu-1

and Cu-3.

115

min or longer. The area under the Cu-4 peak increased slightly with an increase in deposition time, but the peak potential remained fairly constant. Control experiments on glass/ITO in the Cu deposition solution and on glass/ITO/Au$_{8nm}$ in Cu-free 0.1 M HClO$_4$ solution did not show any of these peaks in these regions for any deposition time (Figure 5.5). This confirms that these peaks are associated with Cu and the Au NPs and shows that up to 4 forms of Cu can deposit onto these Au NPs at UPD potentials.

Figure 5.6 shows CVs comparing glass/ITO electrodes coated with Au$_{8nm}$, Au$_{60nm}$, and Au$_{250nm}$ after Cu deposition at 300 mV for 30 min. There are similar Cu Cu-1, Cu-2, and Cu-3 stripping peaks for the Au$_{60nm}$ and the Au$_{8nm}$, but we did not observe any Cu stripping peaks for the Au$_{250nm}$. Figure 5.7 and 5.8 shows the voltammetry for all of the Cu deposition times for Au$_{60nm}$ and Au$_{250nm}$, respectively. Cu stripping peaks were present at all times on Au$_{60nm}$, but only appeared on Au$_{250nm}$ after 17 h. To further confirm that the peaks in these CVs were due to Cu, we stripped the Cu by obtaining a linear sweep voltammogram (LSV) from 0.0 to 1.6 V, then removed the sample from solution under potential control at 1.6 V, and then ran another LSV from 0.0 to 1.6 V in a fresh 0.1 M HClO$_4$ solution. The latter LSV (Figure 5.9) resembled bare Au (although smaller in size, see SI for details), indicating that the anodic peaks during the first LSV were due to Cu.

To better understand the dependence of the Cu deposition process on Au size, we plotted the Cu$_{total}$/Au$_{surf}$ ratio and Cu$_{total}$/Au$_{total}$ ratio as a function of Cu deposition time for Au$_{8nm}$, Au$_{60nm}$, and Au$_{250nm}$ NPs on glass/ITO as shown in Figure 5.10. Cu$_{total}$ is the total amount of Cu deposited as determined by integrating all of the Cu stripping peaks and Au$_{surf}$ and Au$_{total}$ are the amount of surface Au and total Au as determined by
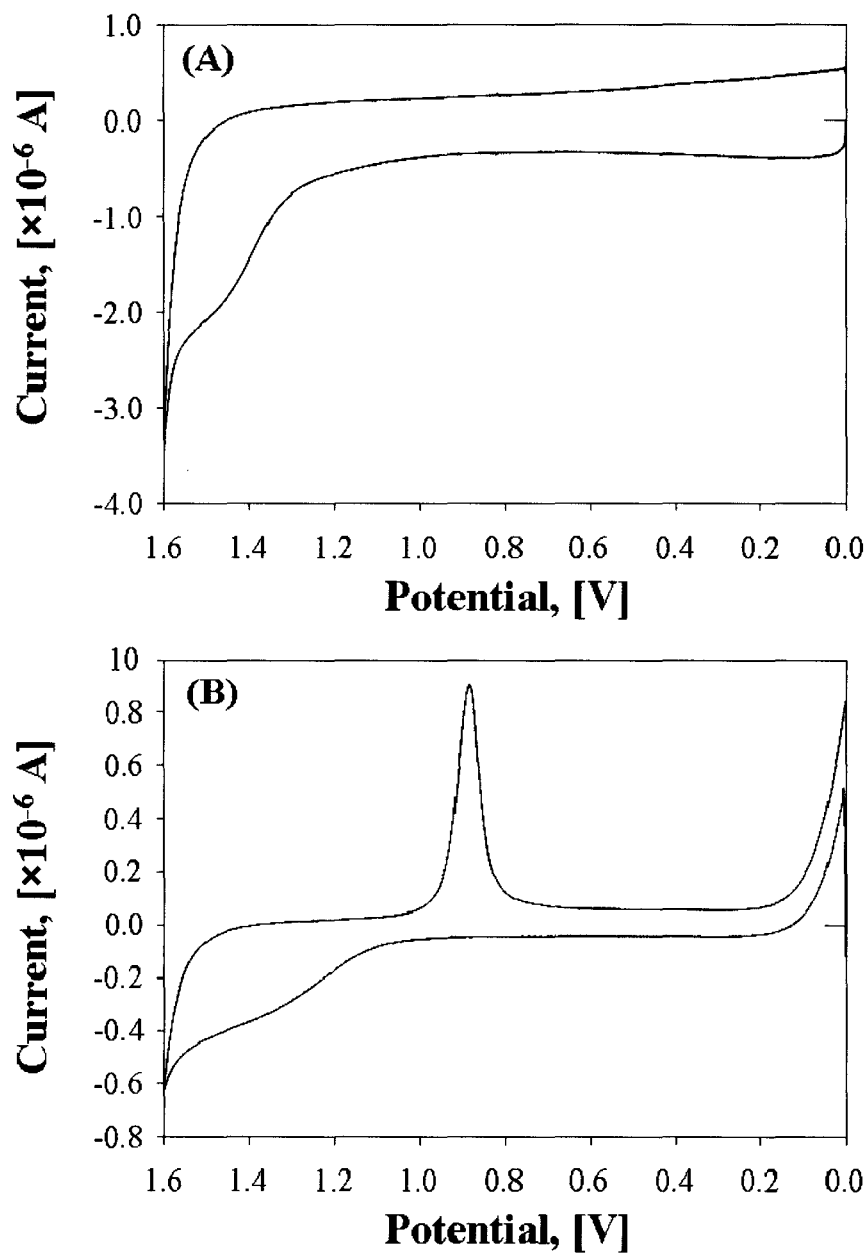
Figure 5.5 (A) CV of Glass/ITO in 0.1 M $HClO_4$ performed after Cu UPD

deposition from 0.01 M $Cu(ClO_4)_2$ for 30 min, indicating the absence of Cu UPD peaks.

(B) CV of Glass/ITO/Au-8nm after holding the sample at 0.3 V for 30 min in solution of

0.1 M $HClO_4$, performed in 0.1 M $HClO_4$ at scan rate of 20 mV/s.
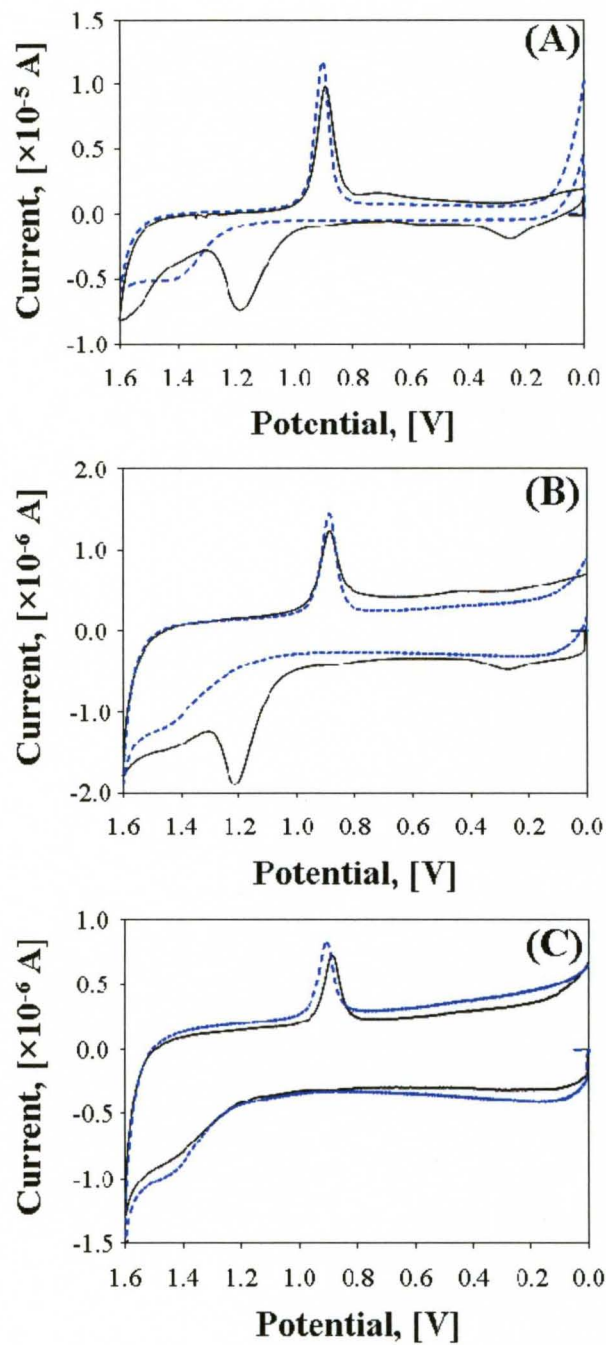
Figure 5.6 . CVs of Glass/ITO/Au NPs/Cu in 0.1 M HClO$_4$ before (dashed blue line) and after Cu deposition for 30 min for (A) Au-8 nm, (B) Au-60 nm, and (C) Au-250 nm.
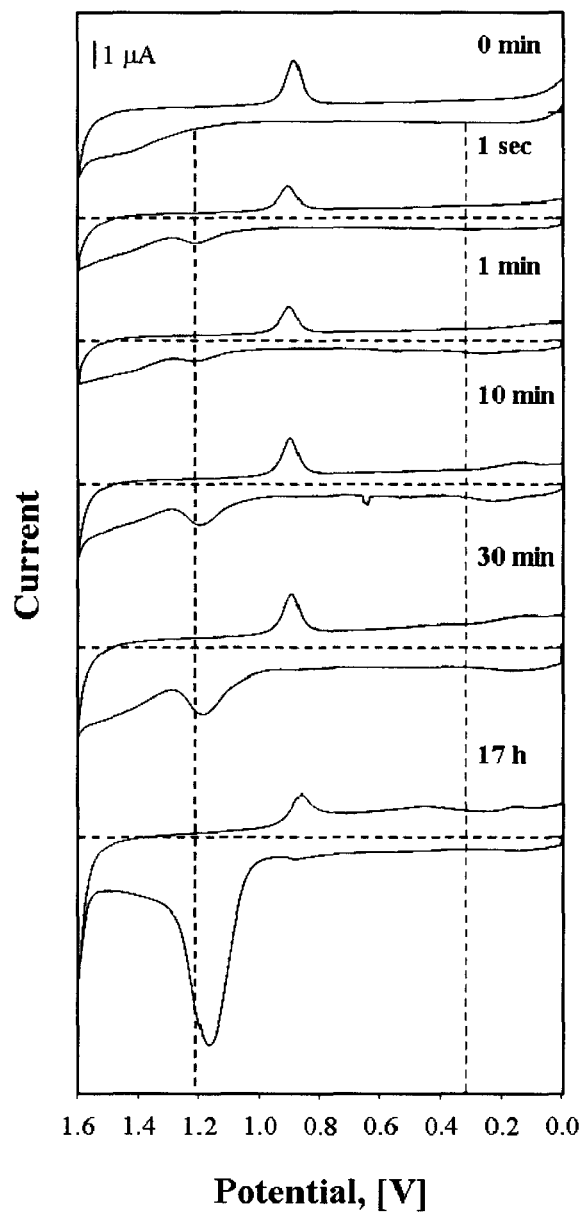
Figure 5.7 CVs of Glass/ITO/Au-60 nm/Cu in 0.1 M HClO$_4$ for different Cu deposition time, as indicated. Scan rate was 20 mV/s. Horizontal dashed lines points level 0 current. Vertical dashed line is to easier visualize shift in oxidation potential for Cu-2 and Cu-1 peaks.
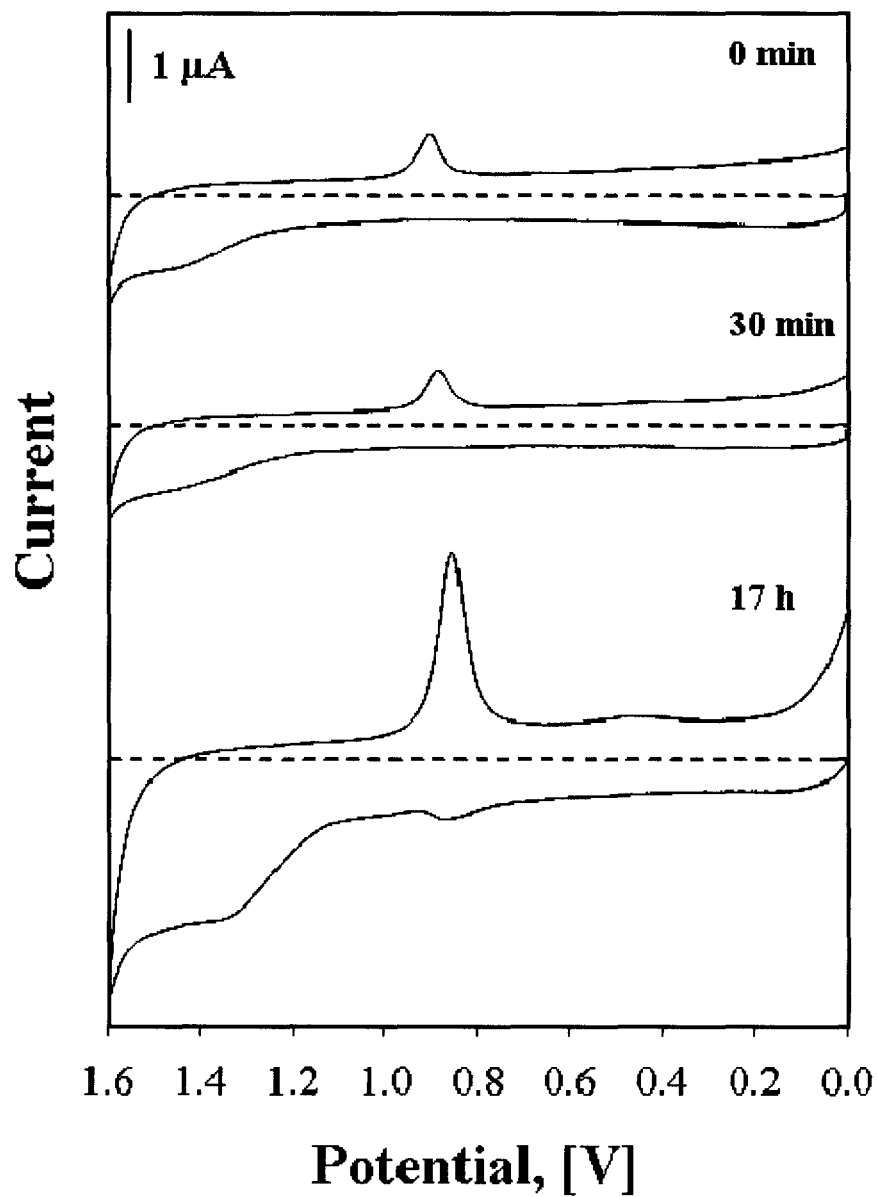
Figure 5.8 CVs of Glass/ITO/Au-250 nm/Cu in 0.1 M HClO₄ for different Cu

deposition time, as indicated. Scan rate is 20 mV/s. Horizontal dashed lines points level

0 current.
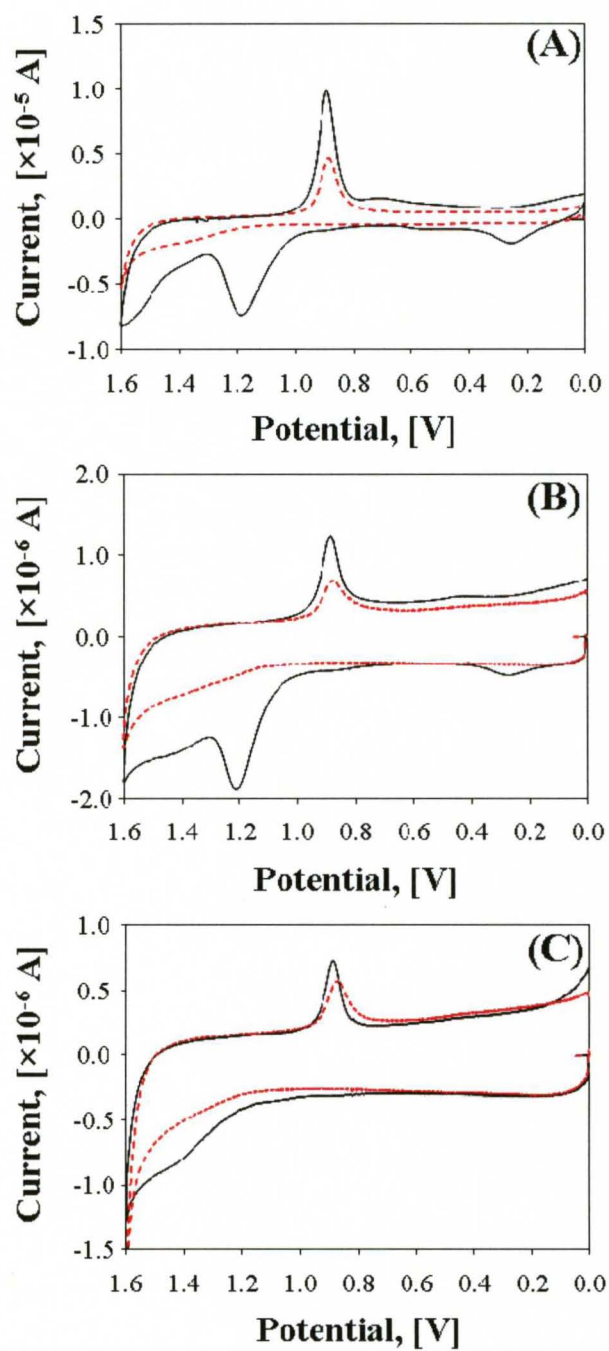
Figure 5.9 . CVs of Glass/ITO/Au NPs after Cu UPD for 30 min (black solid line), and after oxidation of Cu (red dashed line) for (A) Au-8 nm, (B) Au-60 nm, and (C) Au-250 nm performed in 0.1 M HClO$_4$.
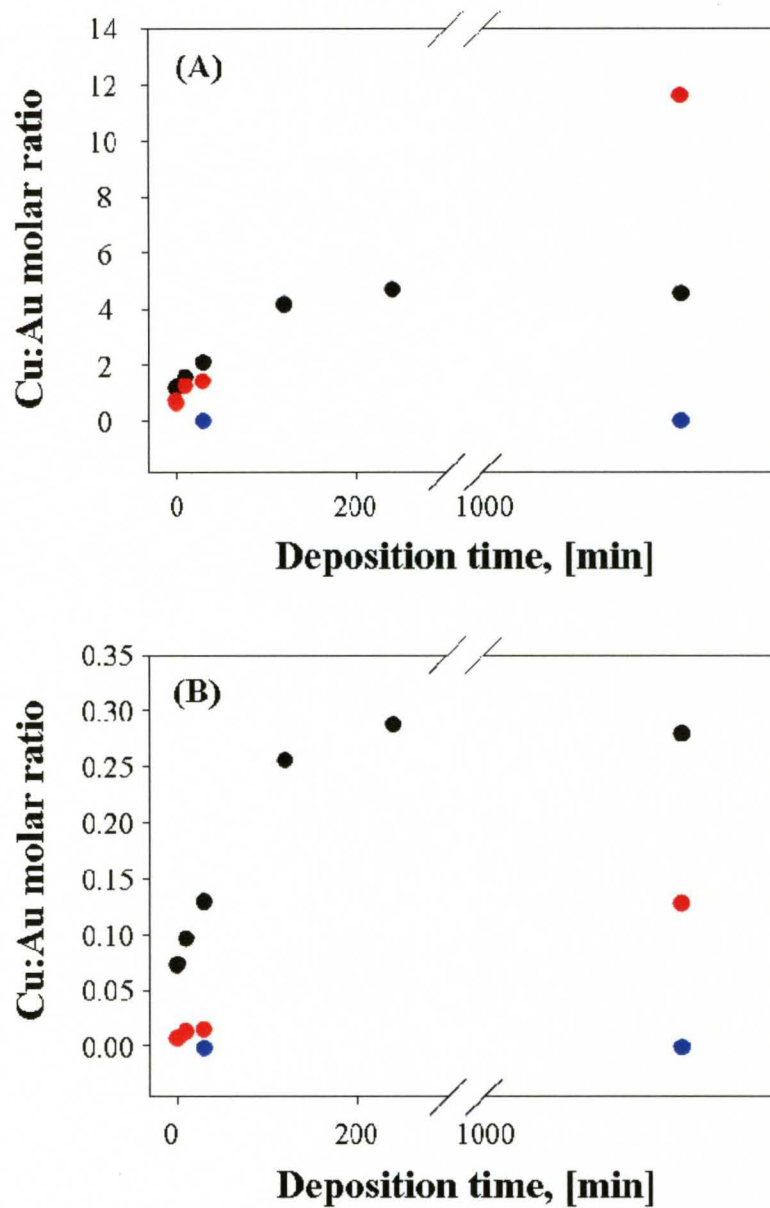
Figure 5.10 . Plots of Cu:Au ratio versus Cu deposition time. Calculated using total amount of Cu oxidized (sum of all 4 peaks) and (A) Au surface (from Au reduction peak) and (B) total Au deposited on electrode surface (6×10^{-4}C). (●) Au-8, (●) Au-60, and Au-250 (●).

integrating the Au oxide reduction peak and monitoring the total charge during Au deposition (6.0×10^{-5} C), respectively. The Cu_{total}/Au_{surf} ratio (Figure 5.10 (A)) follows the order $Au_{60nm} > Au_{8nm} > Au_{250nm}$. The plots are dominated by the Cu-2 stripping peak because it is the largest and increases with increasing deposition time. For short deposition times the Cu_{total}/Au_{surf} is similar for Au_{60nm} and Au_{8nm} but reaches 12:1 and 4:1, respectively after 17 h. The larger value for the Au_{60nm} is due to the smaller surface area of Au_{60nm}. The large ratios (>1) and large oxidation potential (~1200 mV) suggests that this Cu is due to bulk AuCu alloying within the interior of the Au NPs. The 4:1 ratio for Au_{8nm} reaches it maximum after 4 h, while the 12:1 ratio for Au_{60nm} was still increasing even up to 17 h. This shows that the bulk alloying is not limited by the surface Au atoms and that the alloying process occurs much faster for smaller nanoparticles. The value is 0.01 for Au_{250nm} at 17 h, also suggesting that a small amount of bulk alloying is possible even with the larger Au NPs after long deposition times.

The Cu_{total}/Au_{total} (Figure 5.10 (B)) follows the order of $Au_{8nm} > Au_{60nm} > Au_{250nm}$. The Cu-2 stripping peak also dominates this ratio, which represents the maximum amount of AuCu alloying possible at this deposition potential. The bulk alloying on Au_{8nm} occurs the fastest and the ratio reaches a maximum of 30% Cu after 4 h. This value was 15% and 0.02 % for Au_{60nm} and Au_{250nm}, respectively, after 17h, again showing that the rate of alloying is slower on larger Au nanoparticles. It is not clear if the extent of alloying decreases with increasing particle size, however. If the 30% Cu ratio is limited by the amount of Au present, we would expect that bulk alloying on Au_{60nm} and possibly even Au_{250nm} NPs would also eventually result in 30% Cu if we allowed the deposition to proceed even longer than 17 h. This experiment was not conducted. From

our data, we can conclude that the rate of bulk AuCu alloying at UPD potentials increases with decreasing Au NP size, leading to a larger amount of Cu at any given time for the smaller NPs up to 17 h.

These same plots are shown for the Cu-1, Cu-3, and Cu-4 stripping peaks in Figure 5.11 and 5.12. The Cu/Au_{surf} associated for all of these peaks are very similar for both Au_{8nm} and Au_{60nm}. These peaks therefore correspond to surface or near-surface Cu layers since they are related to the number of surface Au atoms. The Cu/Au_{total} for these same three peaks is 4-6 times larger for Au_{8nm} compared to Au_{60nm} since the total Au is the same in both cases, but the number of surface Au atoms are much larger for the Au_{8nm}. This leads to a larger number of Cu atoms bound to the surface of Au and overall larger Cu/Au_{total} for Au_{8nm}. Au_{250nm} does not exhibit these peaks.

Figure 5.13 shows the change in oxidation potential for Cu-1, Cu-2, Cu-3, and Cu-4 stripping peaks as a function of Cu UPD deposition time. The oxidation potential decreases with increasing deposition time in all cases, except for the Cu-4 peak. Figure 5.14 illustrates the Cu UPD deposition process as a function of time for small Au NPs based on the Cu/Au ratios shown in Figure 5.10 and the shift in oxidation potential with time for each peak. Figure 5.14 shows that at short times, there exists an outer traditional Cu UPD layer (Cu-1) and interior CuAu alloy (Cu-2). With later times, Cu continues to diffuse into the interior of the Au NP to form more interior AuCu alloy, which causes this peak to increase with deposition time. Another exterior Cu UPD phase also forms at later times (Cu-3), which could be a higher coverage of the outer Cu UPD layer or a sub-surface Cu layer. As the deposition continues, the Cu-1 oxidation peak shifts negative, showing that it is easier to strip the outer Cu layer. This is because the interior formation

124

of bulk AuCu renders the outside Cu layer less stable, since a Cu UPD layer is stronger on pure Au compared to AuCu. The outer Cu UPD layer becomes weakened further with more bulk alloying, leading to a further shift negative and complete loss of the Cu-3 UPD peak. A new Cu-4 peak appears, which could be a subsurface AuCu alloy different from the bulk AuCu Cu-3 alloy peak.
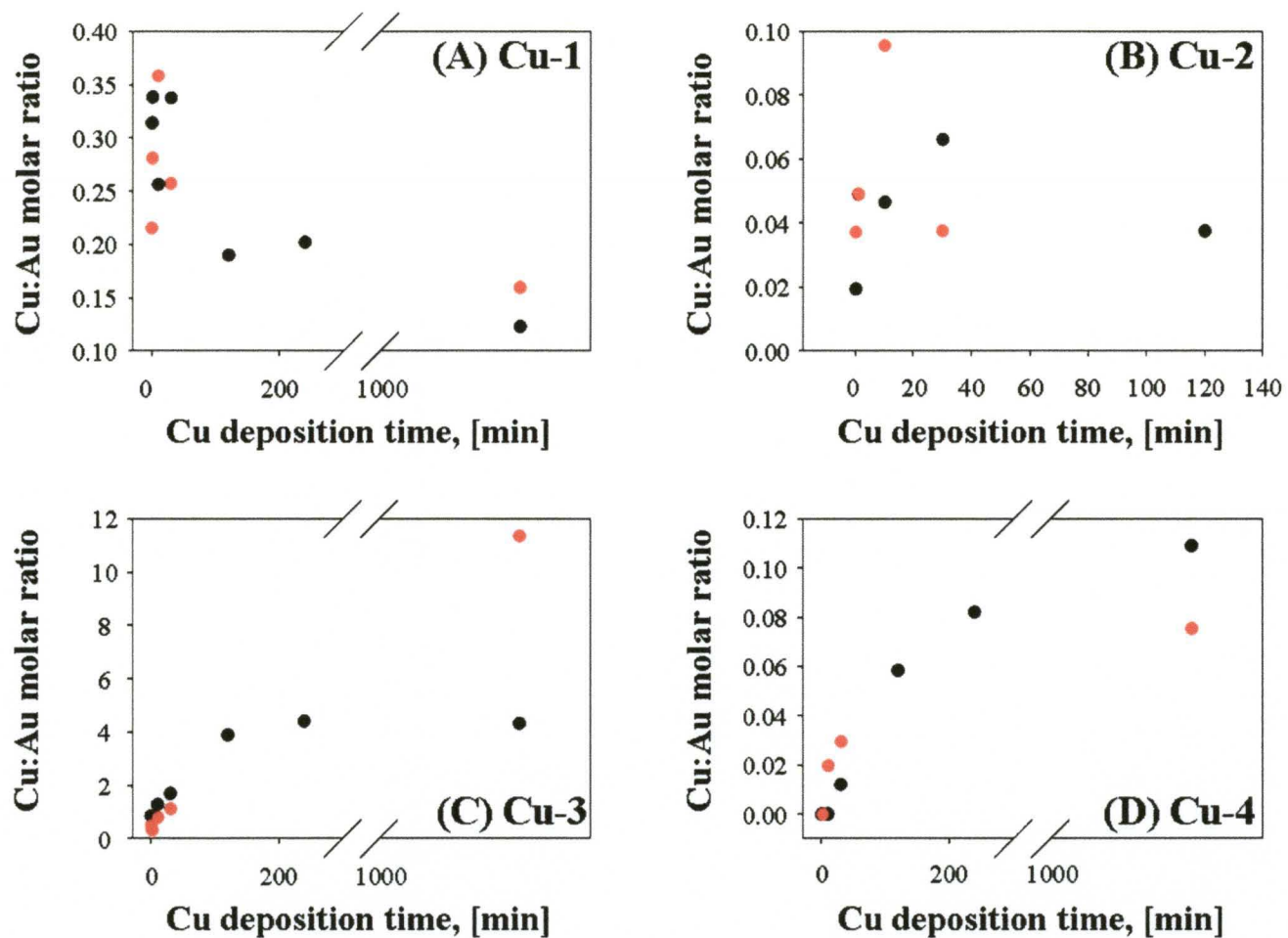
Figure 5.11 Plots of Cu:Au ratio versus Cu deposition time. Calculated using Au surface area obtained from CVs in HClO4. Plots (A), (B), (C) and (D) for Cu-1, Cu-2, Cu-3 and Cu-4 peaks as indicated. (●) Au-8, (●) Au-60.
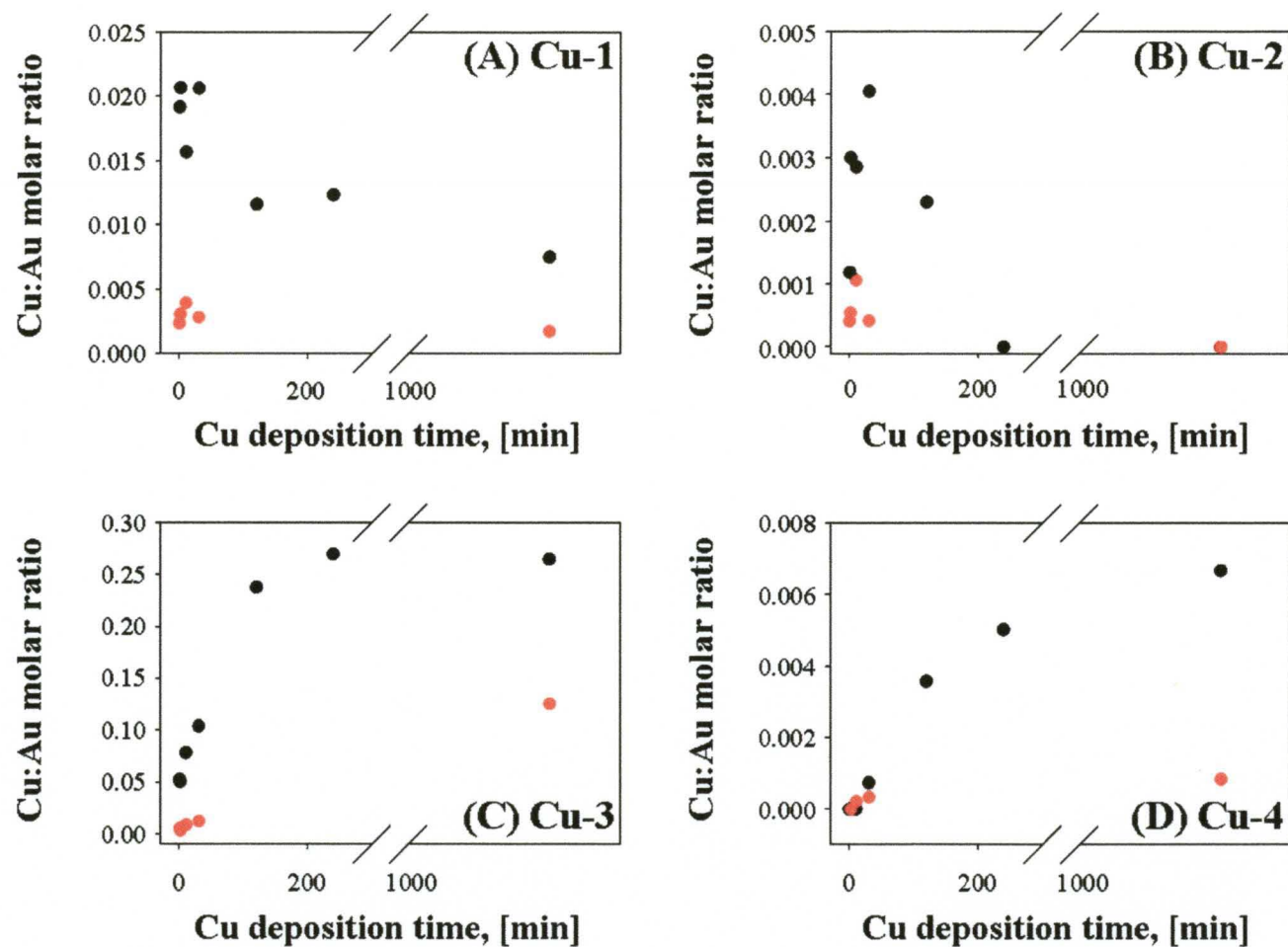
Figure 5.12 Plots of Cu:Au ratio versus Cu deposition time. Calculated using total amount of Au deposited on electrode surface (6×10^{-4}C). Plots (A), (B), (C) and (D) for Cu-1, Cu-2, Cu-3 and Cu-4 peaks as indicated. (●) Au-8, (●) Au-60.
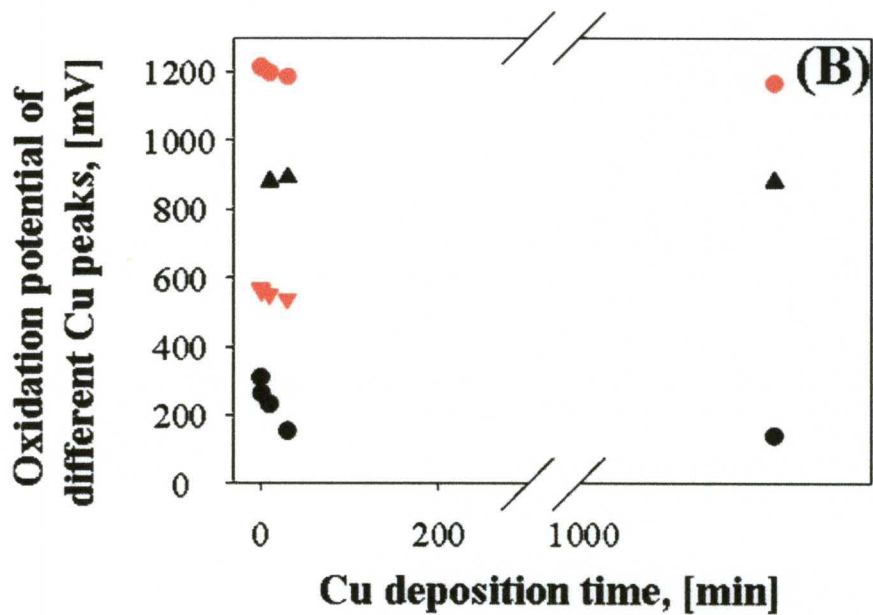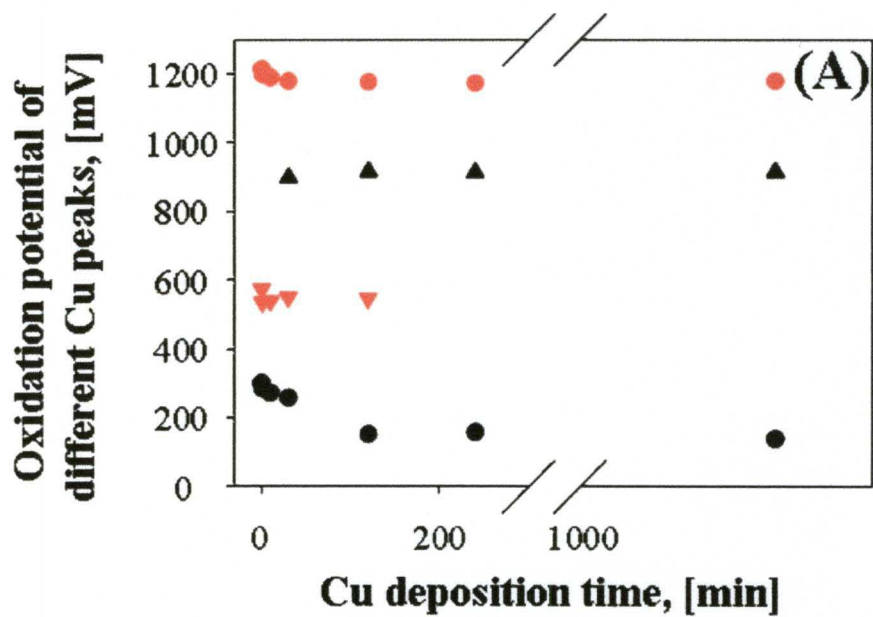
Figure 5.13 Plots of Cu oxidation potential versus Cu deposition time on (A) Au-8 nm NPs and (B) Au-60 nm NPs. Cu-1 (●), Cu-2 (●), Cu-3 (▼) and Cu-4 (▼).
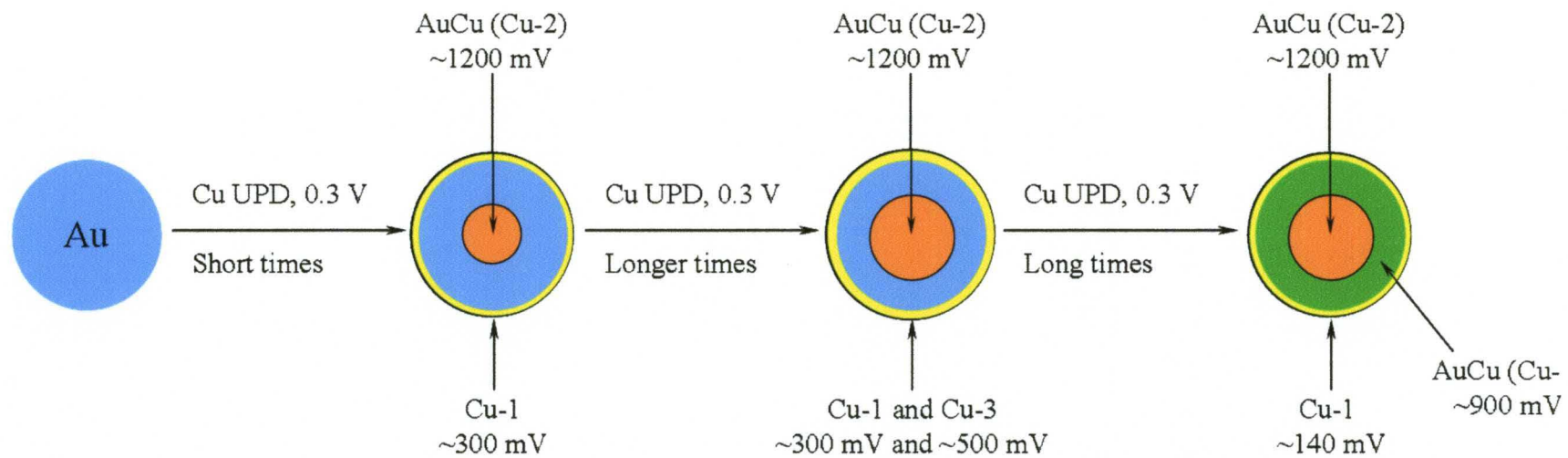
Figure 5.14 Proposed mechanism of alloying Cu with Au NPs.

5.4 CONCLUSIONS

We demonstrated here the underpotential deposition of Cu on Au NPs of different sizes. By using cyclic voltammetry we were able to monitor up to four different oxidation peaks for Cu. For the first time, alloying of Cu with Au NPs of 8 and 60 nm at UPD potentials was demonstrated. This alloying behavior happens with less extent on bigger particles. We believe that the Cu-3 peak is due to the diffusion of Cu into the Au lattice. This effect was observed previously during the chemical synthesis of Au/Cu alloys at high temperature.[121] Diffusion of Cu into the Au lattice did not proceed to the same extend for bigger Au NPs (~250 nm in diameter) and on Au film. Peak at ~1200 nm was not observed for these samples even after 17 h of Cu deposition time. These results can be useful for the electrochemical synthesis of bi-metallic nanostructures with controlled metal/metal composition by simply varying the deposition time.

CHAPTER VI

DEALLOYING OF GOLD FROM GOLD/SILVER CORE/SHELL NANOSTRUCTURES BY ELECTROCHEMICAL CYCLING IN BROMIDE CONTAINING ELECTROLYTE

Here we describe the dealloying of gold from gold/silver core/shell nanostructures by electrochemical cycling in bromide containing electrolyte. Gold/silver core/shell structures were synthesized directly on the surface of a Glass/ITO electrode [ref], and then samples were cycled in electrolyte solution containing 0.01 M KBr and 0.1 M $HClO_4$ for 1 and 10 cycles. Analysis by UV-vis spectroscopy and SEM showed the formation of "bulb"-like structures and porous spherical structures were observed after electrochemical cycling for Au/Ag nanostructures. We determined the amount of gold left on the electrode surface after electrochemical cycling in KBr by electrochemical removal of the Ag shell in H_2SO_4 and electrochemical stripping of the remaining Au in KBr again. These experiments showed that after 1 cycle in KBr there is from 1.5 to 3% of the initial amount of Au left on the electrode surface. After 10 cycles in KBr there is less than 1% of the initial Au left on the surface of Glass/ITO. Results show that we were able to remove gold from gold/silver nanostructures and that the resulting bulb-like or porous shapes are made from silver only. This work represents the first example of forming hollow or porous Ag structures by electrochemical dealloying of Au from Ag. The reverse case is common however.

131

6.1 INTRODUCTION

Bimetallic alloy and core-shell nanoparticles have received a great deal of attention due to the fact that their properties are distinct from those of the corresponding monometallic particles. The synthesis of bimetallic alloys and core-shell nanostructures has been reported in many papers.[122-125] Such structures were characterized using transmission electron microscopy (TEM), SEM, UV-vis spectroscopy, X-ray photoelectron spectroscopy (XPS), and X-ray diffraction (XRD).

Solid metallic nanostructures have been used in a wide range of applications that take advantage of their high surface-to-volume ratio. Recently, a lot of attention has been paid to the synthesis of nanoporous metals for various applications such as catalysis[126] and sensing.[127] Nanoporous structures can be formed by chemical etching or electrolytic dealloying. In the case of chemical etching, one element is selectively etched out of the alloy in a suitable solution. For example, nitric acid is typically used to dealloy Ag from Au-Ag alloys.[128] During the electrolytic dealloying, the electrode potential is applied to the sample in order to electrochemically remove usually the less noble metal from the alloy, leaving the more noble metal on the surface of the electrode. Electrochemical dealloying can be performed on any system where a large difference between the electrochemical oxidation potentials of the elements in the alloy exists. Dealloyed structures can be coarsened at elevated temperatures[129] or room temperature depending on the applied voltage[130] and nature of the electrolyte.[128]

This chapter describes the first example of electrochemical dealloying Au from an Au-Ag core-shell nanostructure grown directly on an electrode surface. The findings of

this chapter will show that we were not able to synthesize a perfect Ag shell on an Au core. Interestingly, the experiments showed that we are able to dealloy a more noble metal (in this case Au) from the alloy structure by using an appropriate complexing agent (Br⁻). The dealloying process led to the formation of porous nanostructures, similar to those described in literature, but for the less noble metal, Ag in this case.

6.2 EXPERIMENTAL DETAILS

The experimental procedure consists of 4 main steps (Figure 6.1): 1) growth of Au nanostructures directly on the Glass/ITO electrode, 2) growth of an Ag shell with various thickness on top of Au, 3) removal of Au from the Au/Ag nanostructure by electrochemical cycling and 4) characterization of nanostructures before and after electrochemical experiments by UV-vis spectroscopy, SEM, and linear sweep voltammetry in order to determine the composition of the final structure.

Growth of Au/Ag core/shell nanostructures. Glass/ITO electrodes were cleaned and functionalized with MPTMS as described in Chapter II. Then samples were placed in Au seed solution for 20 min and after that in Au growth solution for 1h (See Chapter II for details). Then Glass/ITO/MPTMS/Au NP samples were rinsed with water, dried under N_2 and placed into Ag growth solution at pH 10.6 for 30 min. This step was repeated up to 5 times to produce thicker Ag shells. Glass/ITO/MPTMS/Au-core/Ag-shell samples were rinsed with nanopure water, dried under nitrogen and characterized by UV-vis, SEM and electrochemical methods.

Characterization. UV-vis spectroscopy was used to monitor the growth of Au and Ag on the electrode surface by observing the localized surface plasmon band before and after electrochemical experiments. SEM was used to determine the morphology of the Au/Ag nanostructures before and after electrochemical treatment. Cyclic voltammetry was used in order to remove Au from the Au/Ag nanostructures, and LSV was used in order to determine the amount of Au left on the electrode surface after removal. See Chapter II for description of techniques.
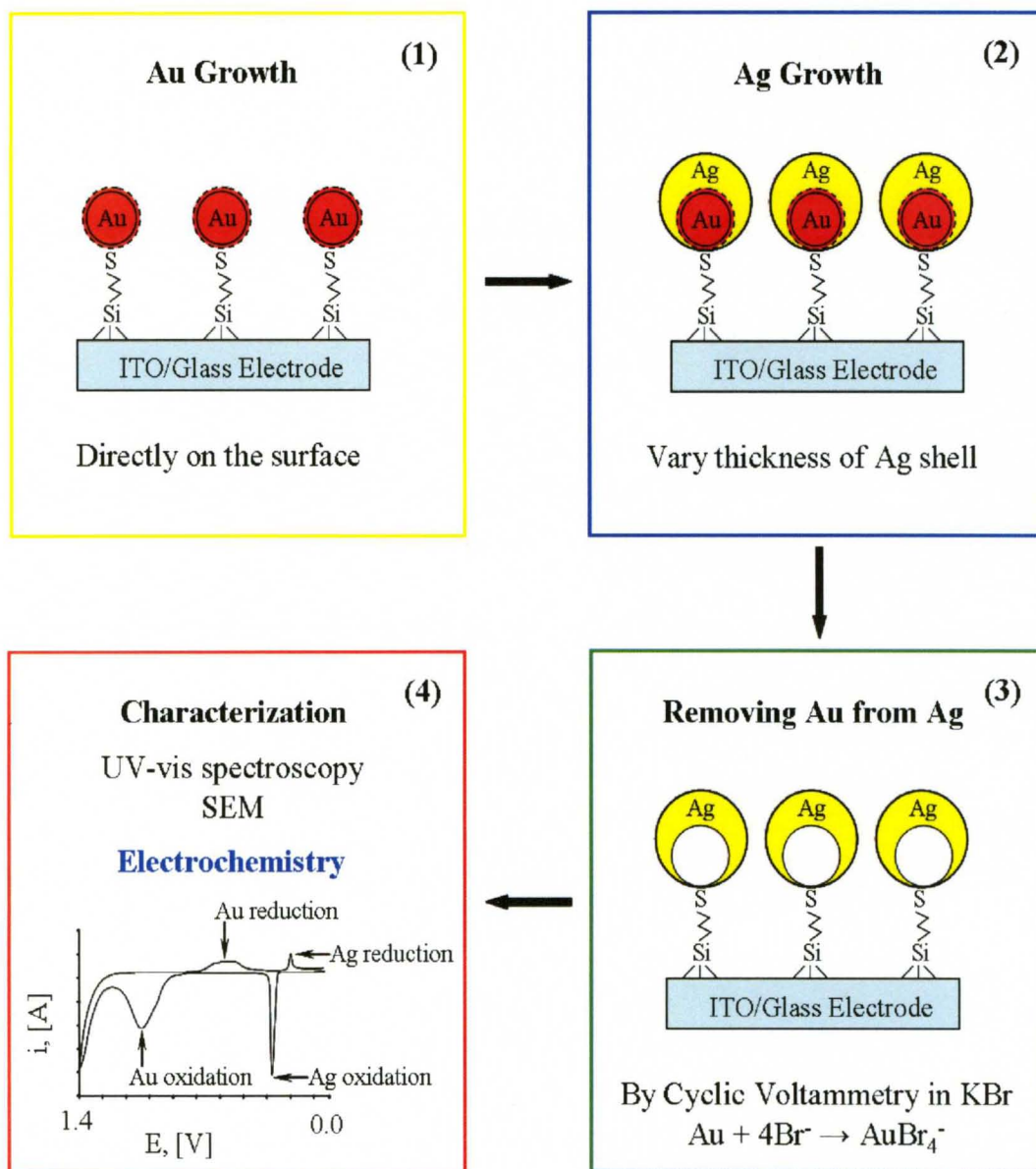
Figure 6.1 Experimental steps.

6.3 RESULTS AND DISCUSSION

The first step in the experimental procedure was to synthesize Au nanostructures directly on the Glass/ITO/MPTMS electrodes by a seed-mediated growth procedure.[131] We characterized the final Au structures by LSV, UV-vis and SEM. Figure 6.2 (A) shows the characteristic LSV of Glass/ITO/MPTMS/Au NPs from 0 V to 1.8 V performed in 0.01 M KBr and 0.1 M $HClO_4$ electrolyte solution at a scan rate of 5 mV/s. The peak at ~970 mV is due to the oxidation of gold and formation of $AuBr_4^-$, according to the Reaction 3.4. The UV-vis spectrum of the electrode before electrochemistry is shown on Figure 6.2 (B) (black line). The UV-vis spectrum has a characteristic absorption band for gold at ~550 nm. The average absorbance was 0.20 ±0.05. After the oxidation reaction the absorbance dropped to 0.04 and the peak shifted to ~560 nm (Figure 6.2 (B) red line). According to the UV-vis data there is a small amount of gold remained on the electrode surface after the oxidation of Au. The size of Au nanostructures was determined by SEM. SEM data shows that the majority of the nanoparticles on the electrode surface are spherical with average diameter of 88 ±20 nm and coverage of 20 particles per $1\mu m^2$. There are some short nanorods and platelets present on the electrode surface but their amount is insignificant (9 and 6 % respectively). Also SEM images were taken after the oxidation reaction was performed. The average size of Au NPs after the oxidation reaction was 44±15 nm with coverage of 5 particles per $1\mu m^2$. A typical SEM image before and after electrochemical oxidation is shown in Figure 6.3 (A) and (B) respectively.
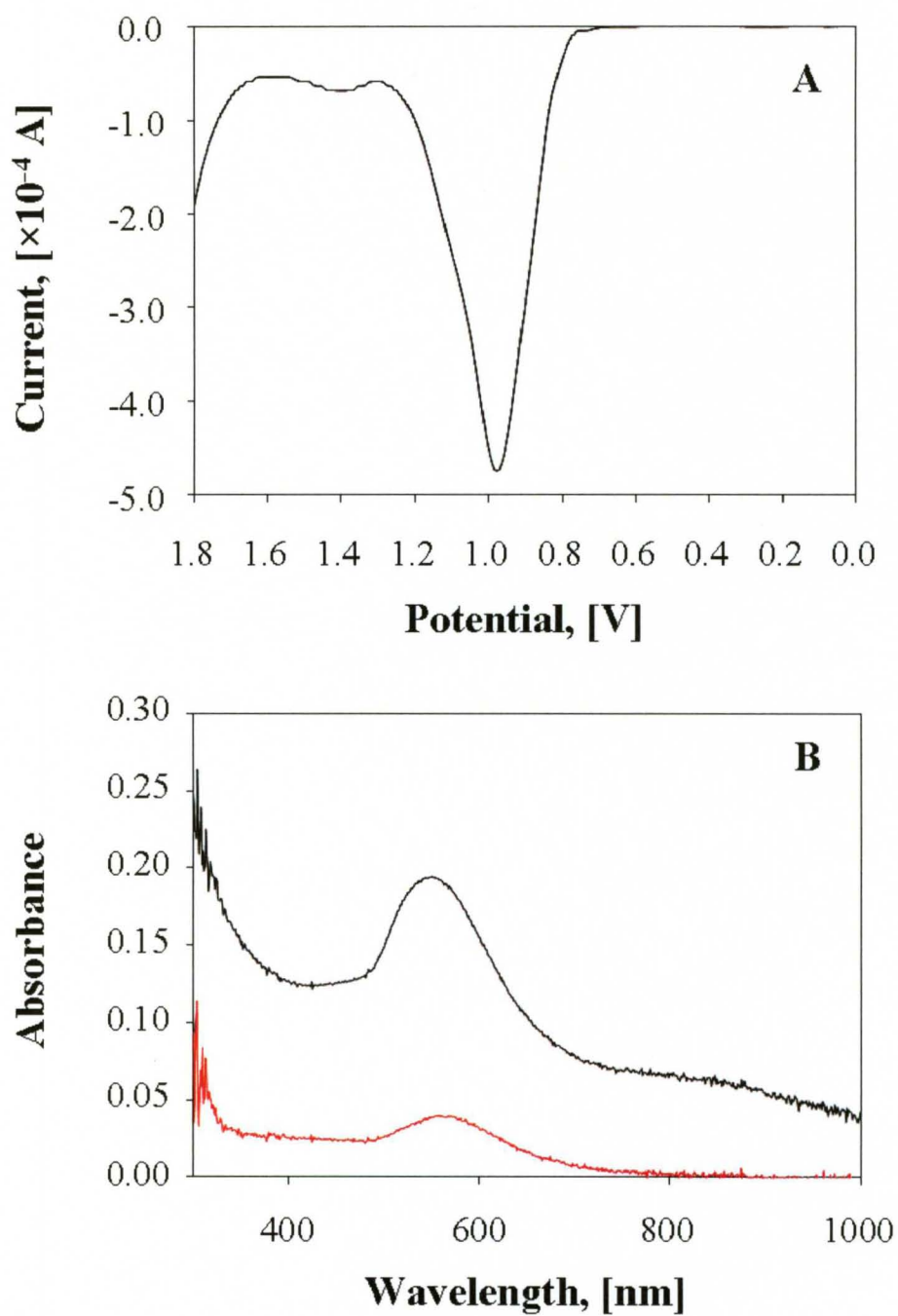
Figure 6.2 (A) LSV of Glass/ITO/MPTMS/Au NPs in 0.01 M KBr and 0.1 M

HClO$_4$. Scan rate 5 mV/s. (B) UV-vis spectrum of Glass/ITO/MPTMS/Au NPs before

(black) and after (red) electrochemical oxidation.

137
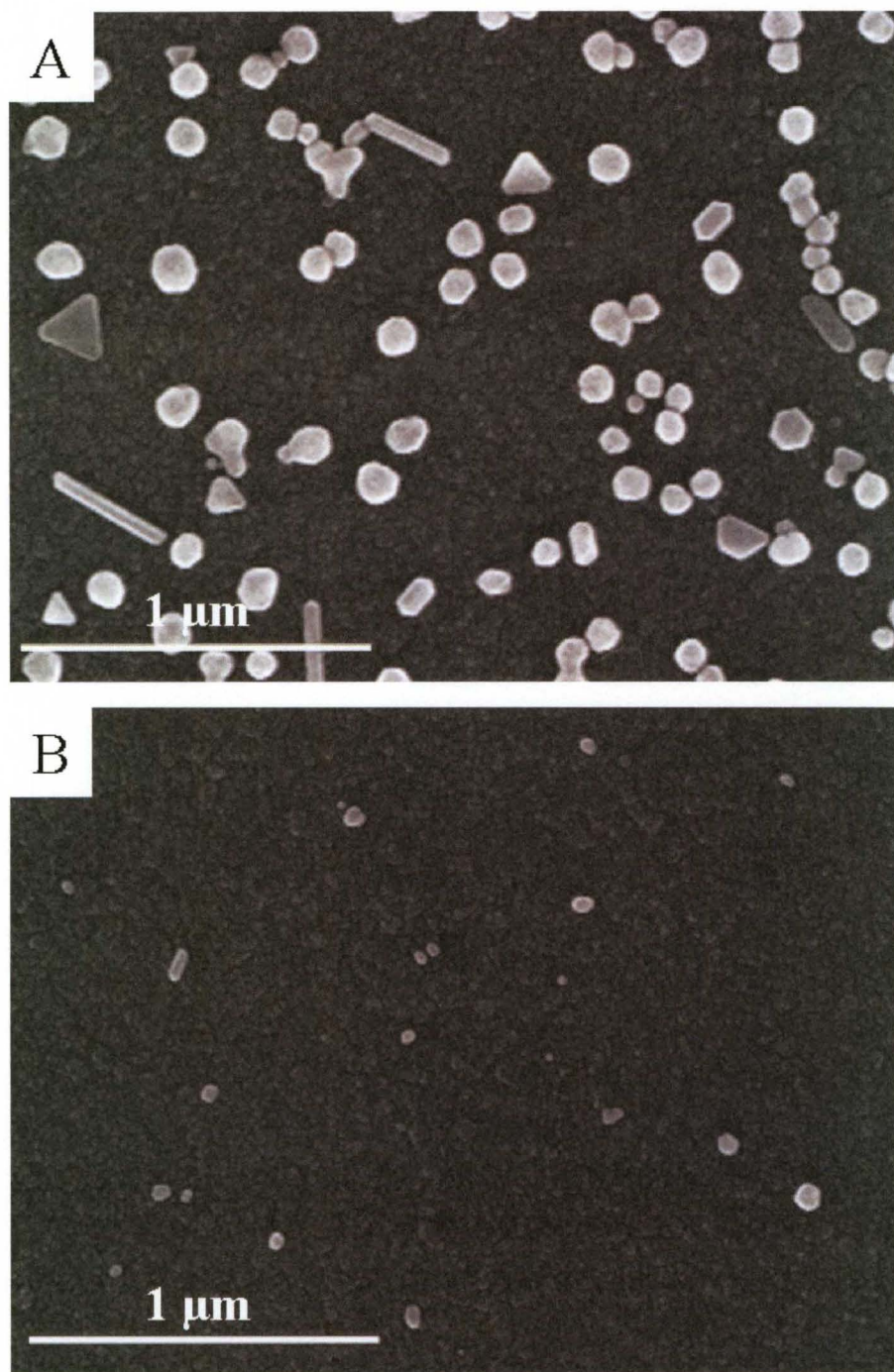
Figure 6.3 SEMs of Glass/ITO/MPTMS/Au NPs before (A) and after (B)

electrochemical oxidation in KBr.

Au-core/Ag-shell nanostructures were synthesized with various Ag-shell thicknesses and characterized electrochemically. The idea of the project was to electrochemically characterize the core-shell metal nanostructures. When we monitor the oxidation reaction on Au-core/Ag-shell nanoparticles in KBr containing electrolyte solution, Ag should form AgBr, according to the following reaction:

$$Ag^0 + Br^- \rightarrow AgBr_{(s)} + e^- \qquad E^0 = 0.07 \text{ V vs NHE} \qquad \text{(Rxn. 6.1)}$$
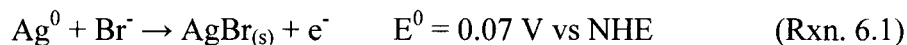
AgBr that forms during the reaction is insoluble and remains on the electrode surface. In the case when Ag forms a perfect shell, Au oxidation and formation of $AuBr_4^-$ will not be possible because of the protecting layer of AgBr on top of it (Figure 6.4 (A)). In the case where defects exist in the Ag-shell, or when a full shell of Ag does not exist on top of the Au NP, it will be possible to oxidize Au to $AuBr_4^-$, which is soluble in water and will leave the electrode surface while Ag remains on the electrode in the form of AgBr. Since Au in our case is a core, after the oxidation reaction occurs, we hypothesized that Ag would remain on the electrode surface in the form of a hollow Ag-shell (Figure 6.4 (B)). AgBr can be easily re-reduced to Ag^0 by performing the scan in the direction of negative potentials.

We grew an Ag-shell on top of the Au NPs using the overgrowth approach.[132] The thickness of the Ag-shell was varied by the number of Ag growths performed. We made Glass/ITO/MPTMS/Au-core/Ag-shell samples with 1, 3 and 5 Ag growths. The growth of Ag on top of Au was monitored by UV-vis spectroscopy. Figure 6.5 shows UV-vis spectra of Glass/ITO/MPTMS/Au NPs (red) and Glass/ITO/MPTMS/Au-core/Ag-shell up to 5 Ag growths. Au by itself showed an absorbance maximum at ~550
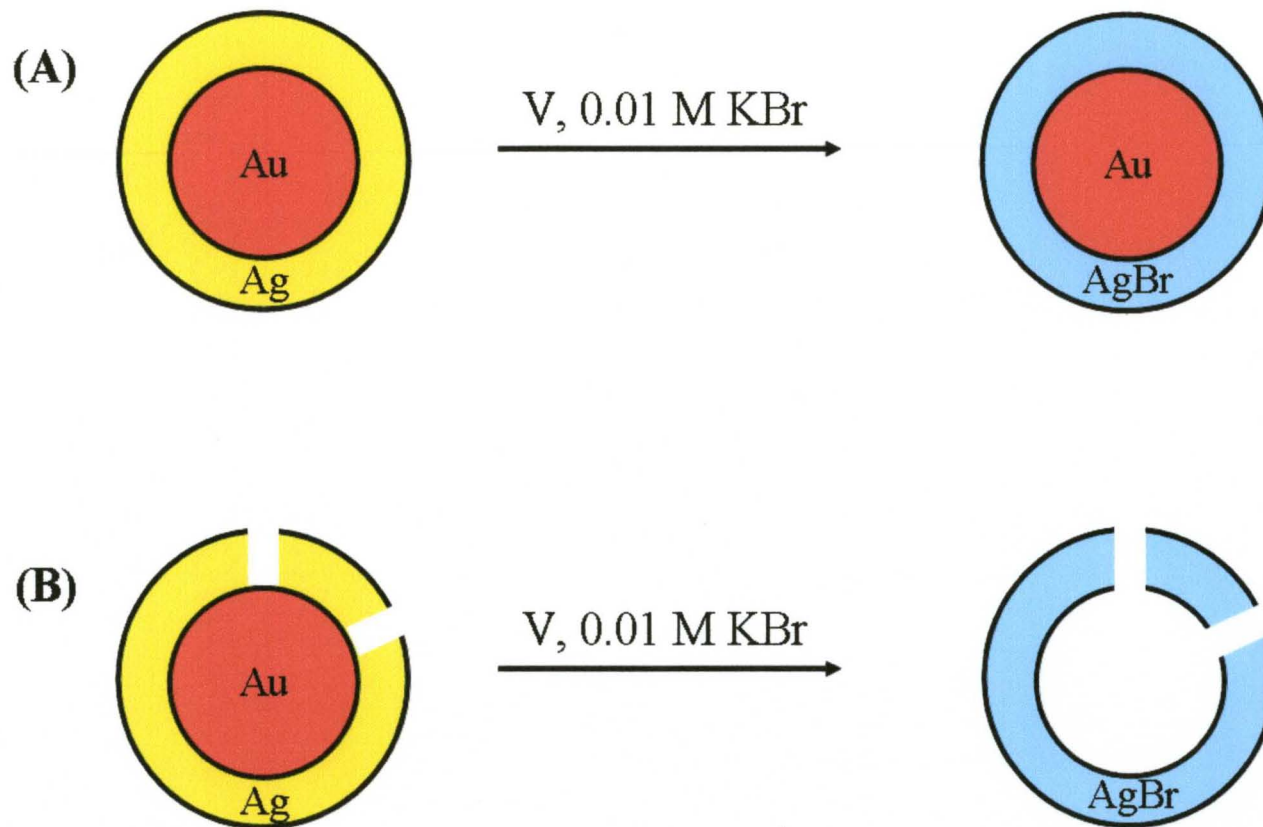
Figure 6.4 Possible result of electrochemical oxidation of Au-core/Ag-shell nanostructures. (A) Perfect Ag-shell leads to formation of insoluble AgBr shell, while gold stays intact. (B) Ag-shell has defects and it is possible to oxidize Au leaving AgBr-shell on the surface.
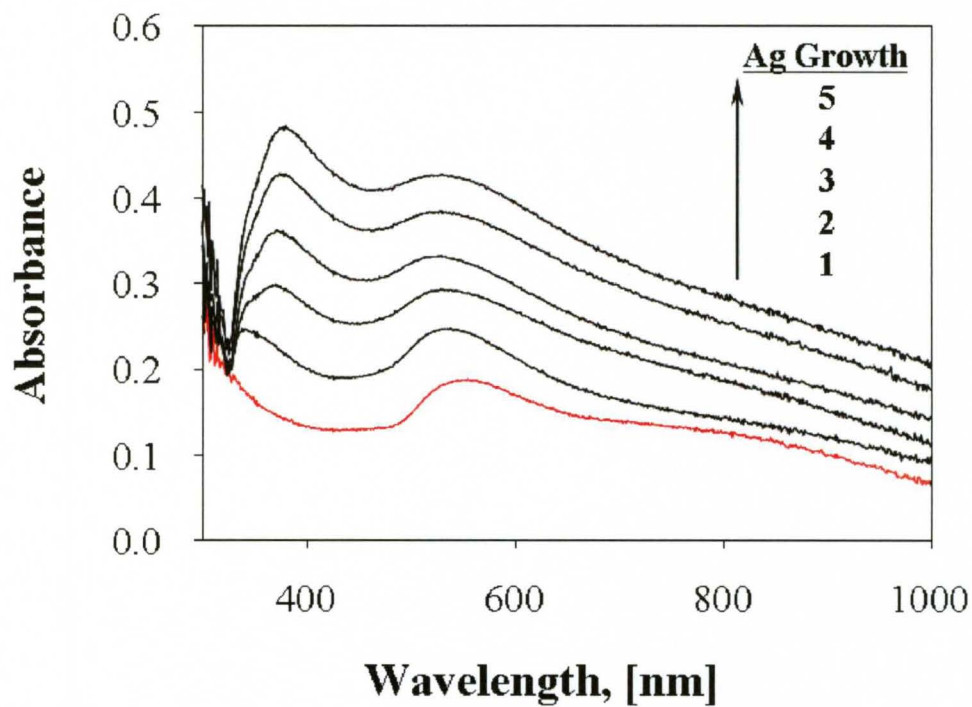
Figure 6.5 UV-vis spectra of Glass/ITO/MPTMS/Au NPs (red) and Glass/ITO/MPTMS/Au-core/Ag-shell (black) up to 5 Ag growths.

nm. When 1 Ag growth was performed on the same sample, the characteristic Ag absorption band appeared at ~340 nm, while the Au peak shifted to red (~532 nm). With every consecutive Ag growth the peak wavelength for Ag shifted to more positive values and reached 378 nm after 5 growths. The Au peak wavelength shifted slightly to more negative with the increase of Ag content on the surface and reached 525 nm after 5 growths. The shift in Au confirms deposition of Ag onto Au. The intensity of both peaks increased with each Ag growth, indicating the increased amount of metal (in this case Ag) on the surface. Figure 6.6 shows typical SEM images of Glass/ITO/MPTMS/Au-core/Ag-shell nanostructures with different Ag-shell thicknesses. Similar to the Au NPs, Au-core/Ag-shell nanostructures were mostly spherical with some short nanorods and plates also present on the surface. Average sizes of the Au-core/Ag-shell structures were 129 ± 59, 128 ± 48, and 143 ± 48 nm for Ag growth 1, 3 and 5 respectively. After synthesis and characterization by UV-vis and SEM, we obtained LSVs or CVs in 0.01 M KBr and 0.1 M $HClO_4$ electrolyte solution in order to examine them. LSVs of Glass/ITO/MPTMS/Au-core/Ag-shell with different shell thickness are shown in Figure 6.7. The peak at ~140 mV on Figure 6.7 (A) is due to oxidation of Ag to form AgBr on the electrode surface. With an increase in the amount of Ag on the electrode surface (Figure 6.7 (B) and (C)), this peak shifts to more positive potentials and increases in current. Second peak at ~820 mV is due to the oxidation of Au to form $AuBr_4^-$. This peak has the same oxidation potential (~820 mV) and similar area (1×10^{-3} C) regardless of the amount of Ag on the electrode surface. We believe that the Ag is not forming a perfect shell on top of the Au NPs and therefore it is possible to oxidize Au electrochemically and remove it from the Au/Ag nanostructures. We characterized the

142
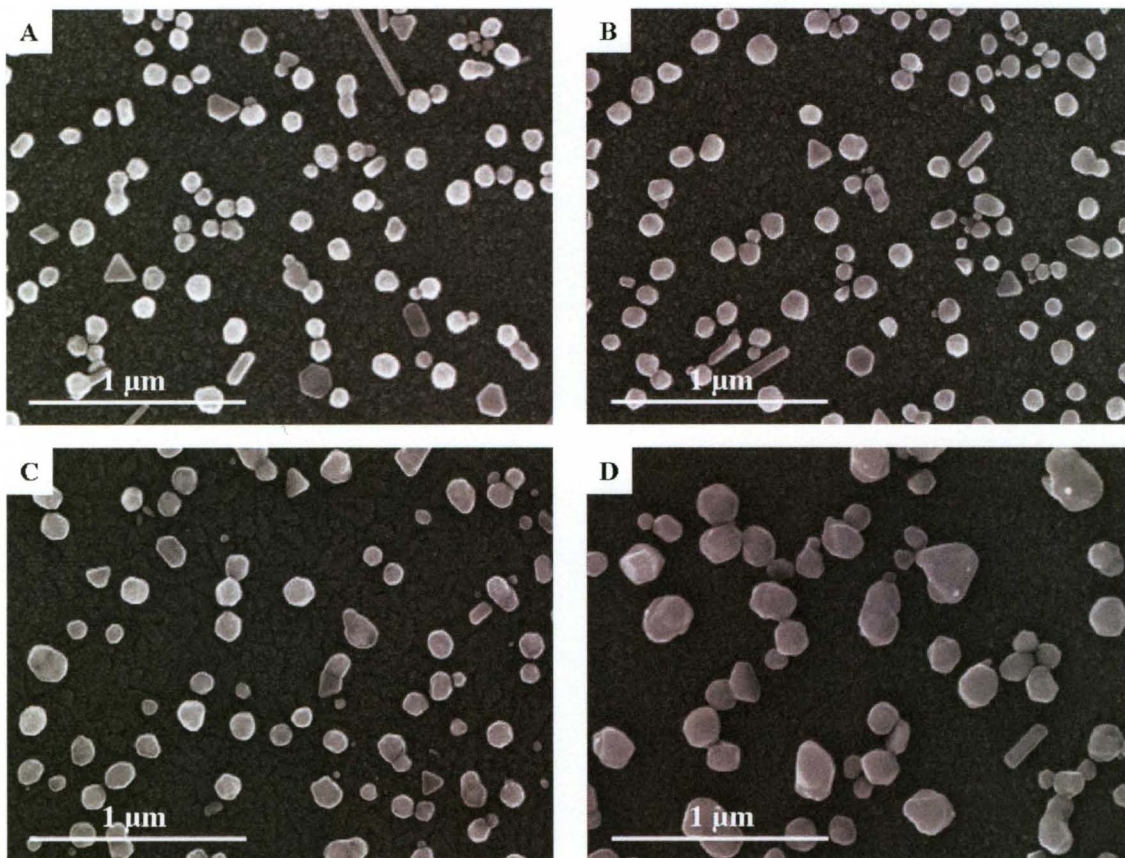
Figure 6.6 SEMs of Glass/ITO/MPTMS/ with (A) Au growth only, (B) Au growth and 1 Ag growth, (C) Au growth and 3 Ag growths, and (D) Au growth and 5 Ag growths.
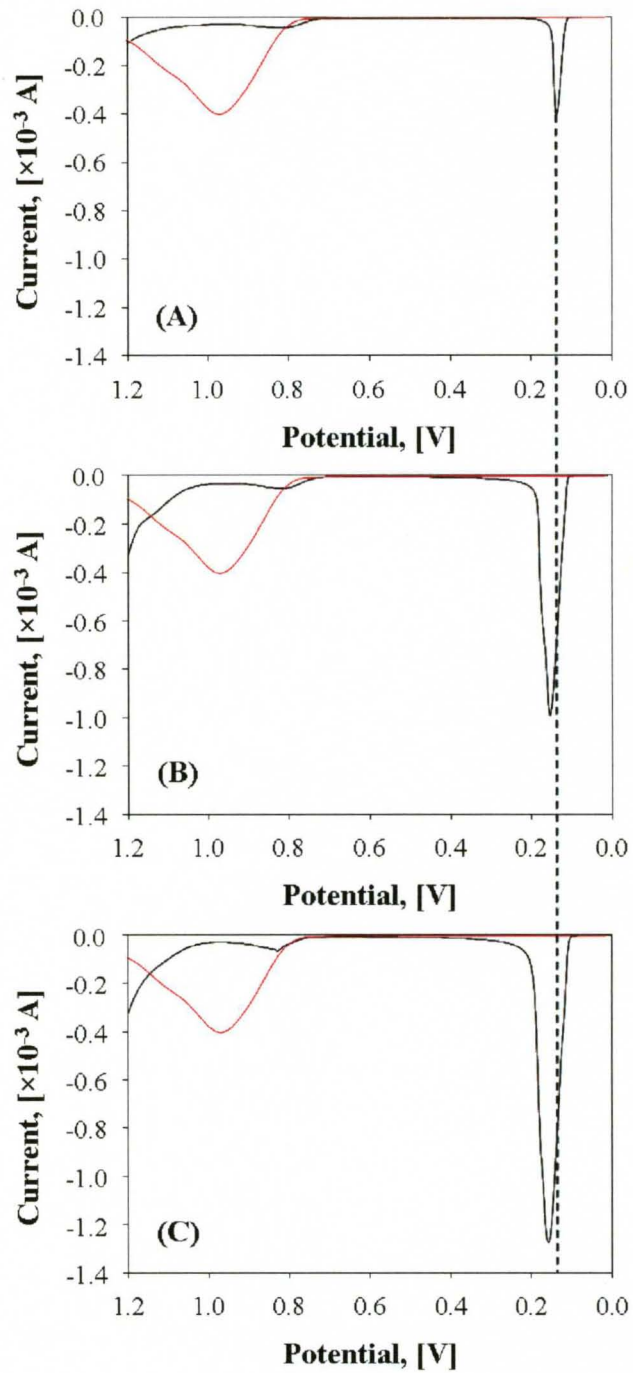
Figure 6.7 LSVs of Glass/ITO/MPTMS/Au-core/Ag-shell nanostructures (black line) with 1 Ag growth (A), 3 Ag growths (B), and 5 Ag growths (C) in 0.01 M KBr and 0.1 M HClO₄, in comparison with Glass/ITO/MPTMS/Au NPs (red line)Scan rate 5 mV/s.

144

samples by UV-vis spectroscopy before and after performing the electrochemical experiments. Figure 6.8 shows the UV-vis spectra of Glass/ITO/MPTMS/Au-core/Ag-shell before and after oxidation in KBr. For Ag growth 1, the Ag absorption peak is not visible and the absorbance increased in the region of 300-350 nm. The Au absorption band disappeared and an additional band at ~650 nm appeared. The shift in absorption band toward higher wavelengths is an indicator of the presence of hollow nanostructures.[133] For 3 and 5 Ag growths, the absorption band for Ag shifted a little to the negative wavelengths (~330 and ~350 nm respectively for 3 and 5 Ag growths) and increased significantly in absorbance. Similar to Ag 1 growth, a peak at ~ 750 nm appeared, indicating the presence of hollow structures on the electrode surface. Figure 6.9 shows SEM images of Glass/ITO/MPTMS/Au-core/Ag-shell before (A, B, and C) and after (D, E, and F) electrochemical oxidation in KBr. After oxidation particles appear almost perfectly spherical and bigger in size, compared to the sample before the electrochemical reaction was performed. In addition, all particles appear much brighter after the oxidation, compared to before. We refer to these particles as "bulbs" because of their large size, hollow interior, and bright appearance. For 5 Ag growths very large bright "bulb" nanoparticles exist at the same time with much smaller particles on the electrode surface for resons not fully understood at this time. The sizes of the "bulb" particles were 177±76, 190±77, and 233±88 nm for 1, 3 and 5 Ag growth, respectfully. We believe that the increase in size is due to the formation of AgBr during the oxidation reaction. The size of the new structures ("bulbs") for 5 Ag growths was determined without taking into account the smaller particles that varied in size from 25 to 90 nm.
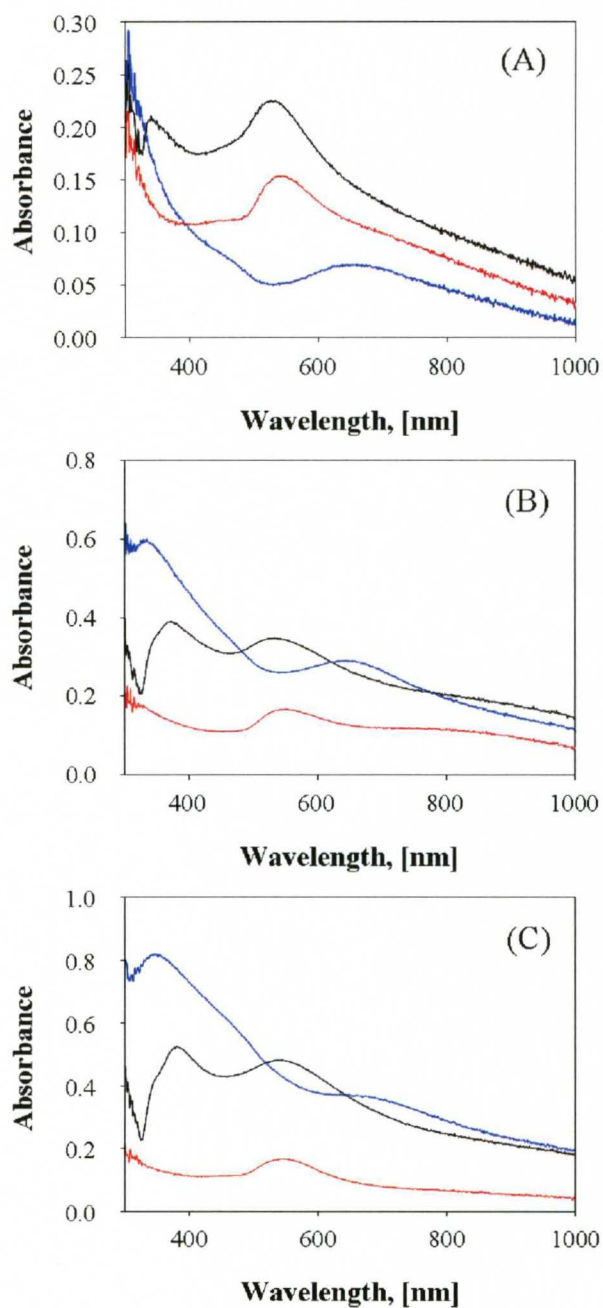
Figure 6.8 UV-vis spectra of Glass/ITO/MPTMS/Au-core/Ag-shell nanostructures with (A) 1 Ag growth, (B) 3 Ag growths, and (C) 5 Ag growths before (black) and after (blue) oxidation in 0.01 M KBr, in comparison with Glass/ITO/MPTMS/Au NPs (red line).
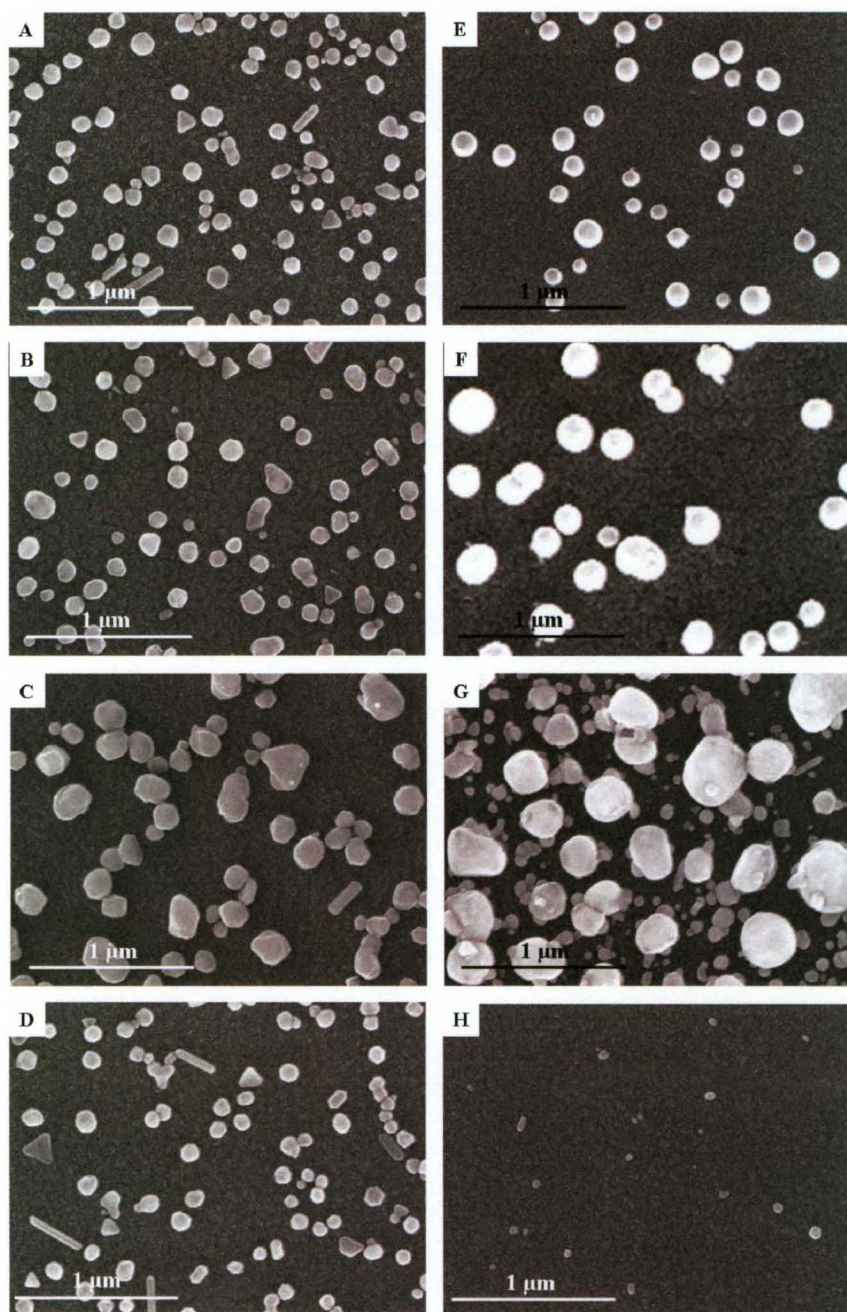
Figure 6.9 SEM images of Glass/ITO/MPTMS/Au-core/Ag-shell (A, B, and C for 1, 3 and 5 Ag growths respectively) and Glass/ITO/MPTMS/Au NPs (D) before oxidation, and after (E, F, and G for 1, 3, and 5 Ag growths respectively and H for Au only) oxidation in 0.01 M KBr.

During the imaging with SEM, obtaining high magnification (zoom-in) pictures led to the "bulb" NPs, showing that they are less stable than non-hollow spherical particles. Figure 6.10 shows "bulb" particles melted by the SEM beam at different stages of melting.

In view of the fact that Au-core/Ag-shell NPs undergo morphological changes during the oxidation reaction, we decided to extend this work and perform 1 and 10 electrochemical cycles on the samples. In this case Au-core/Ag-shell structures went through both oxidation and reduction in 0.01 M KBr solution. Typical electrochemical cycle in 0.01 M KBr for Glass/ITO/MPTMS/Au-core/Ag-shell is shown in Figure 6.11. The peak at ~150 mV is due to the oxidation of Ag^0 and formation of AgBr and the second peak on the forward scan (at ~820 mV) is due to the oxidation of Au^0 to $AuBr_4^-$ or $AuBr_2^-$. On the reverse scan the reduction of Au^I or Au^{III} still in the vicinity of the electrode surface occurs at ~460 mV. Reduction of AgBr to Ag^0 occurred at ~20 mV. While the areas of the peaks for Ag oxidation and reduction increased with increase of amount of Ag on the electrode surface, the Au oxidation and reduction peaks remained relatively constant. The UV-vis absorption spectra before and after 1 cycle in KBr for different amount of Ag growth are shown in Figure 6.12. For 1 Ag growth, the Ag peak shifted to more negative wavelengths and the Au peak significantly decreased in intensity. For 3 Ag growths, the Ag peak absorbance increased and λ_{max} blue shifted. The Au peak was not well pronounced in the spectra; most likely it is buried under the Ag peak. In the case of 5 Ag growths, the absorbance of the Ag peak increased and broadened while the Au peak was not visible. There was no peak at ~650 nm as in the
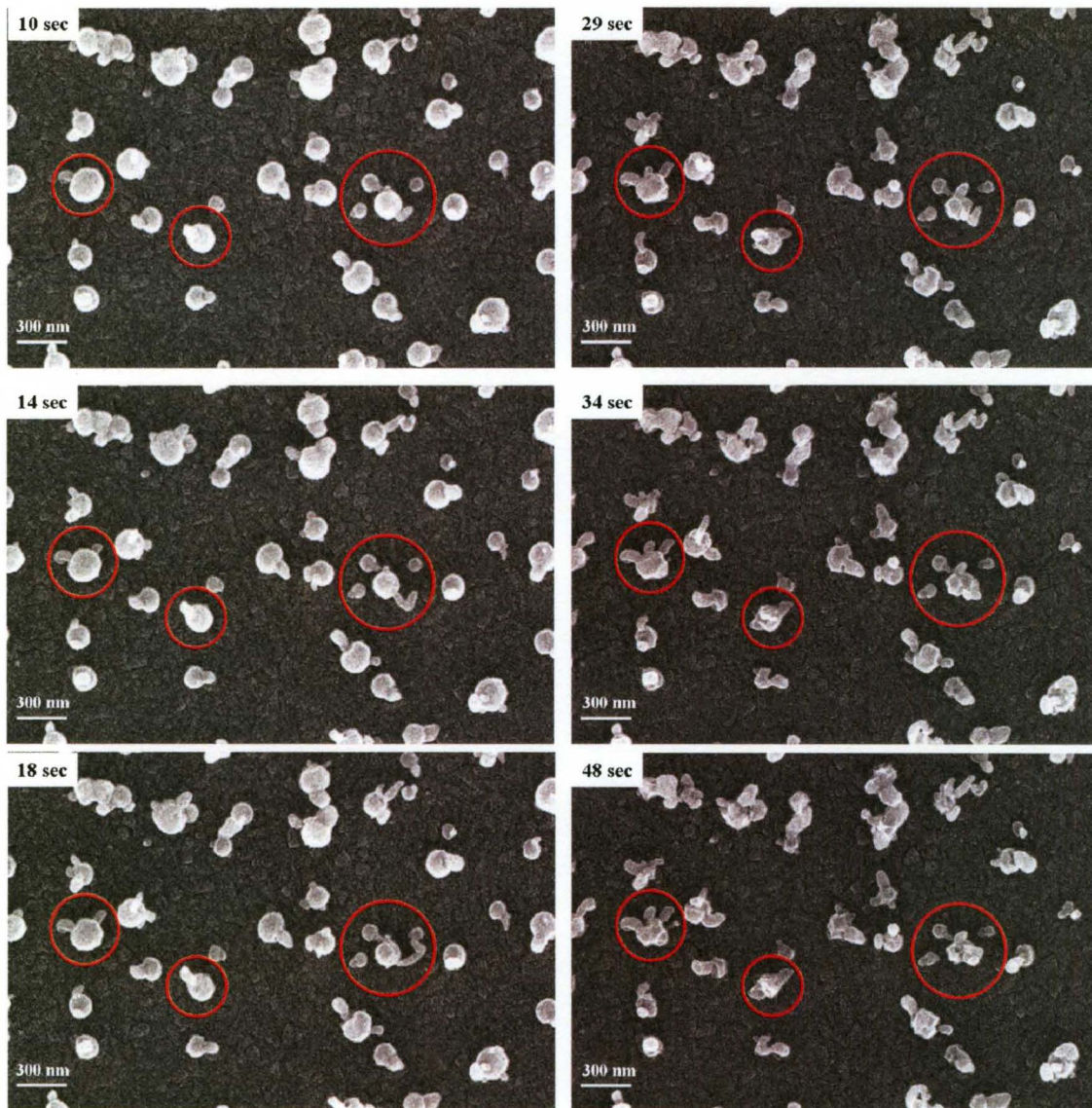
Figure 6.10 SEM image of the Glass/ITO/MPTMS/Au-core/Ag-shell after the oxidation in 0.01 M KBr, melted by the SEM beam for different beam exposure time, as indicated.
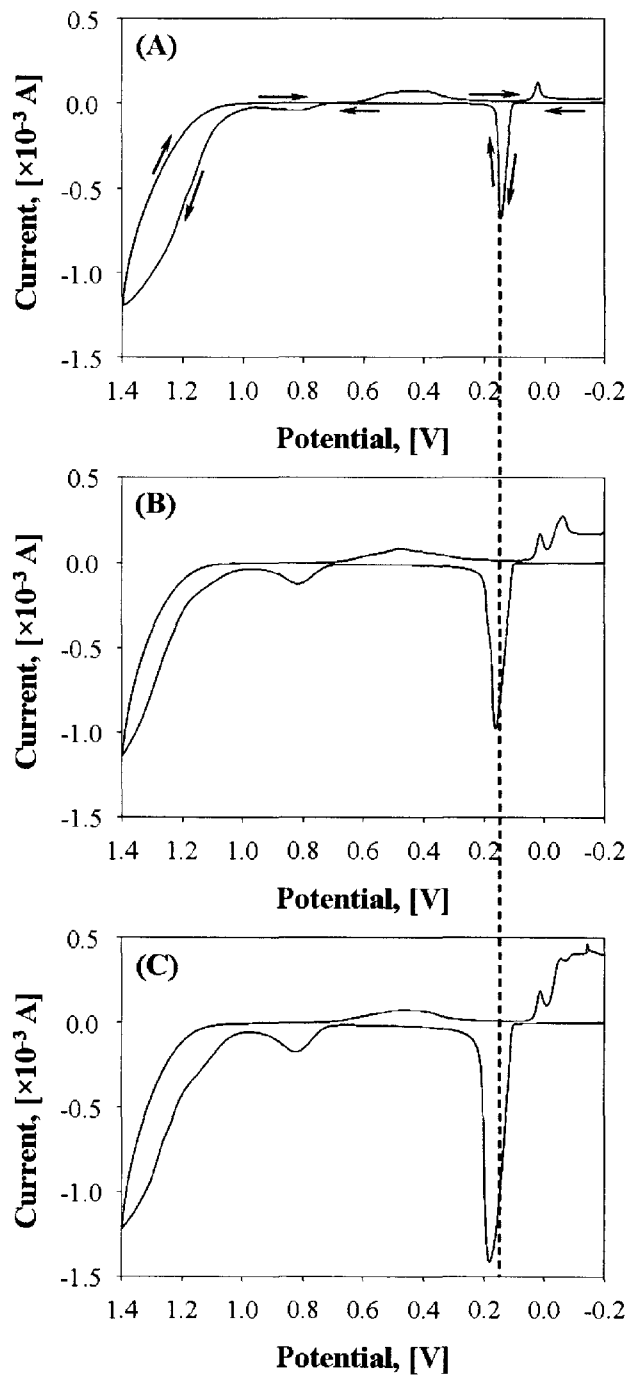
Figure 6.11 CVs of Glass/ITO/MPTMS/Au-core/Ag-shell recorded in 0.01 M

KBr and 0.1 M HClO4 solution. Scan rate 5 mV/s. (A) 1 Ag growth, (B) 3 Ag growths,

and (C) 5 Ag growths. Arrows indicate direction of the cycle.

150
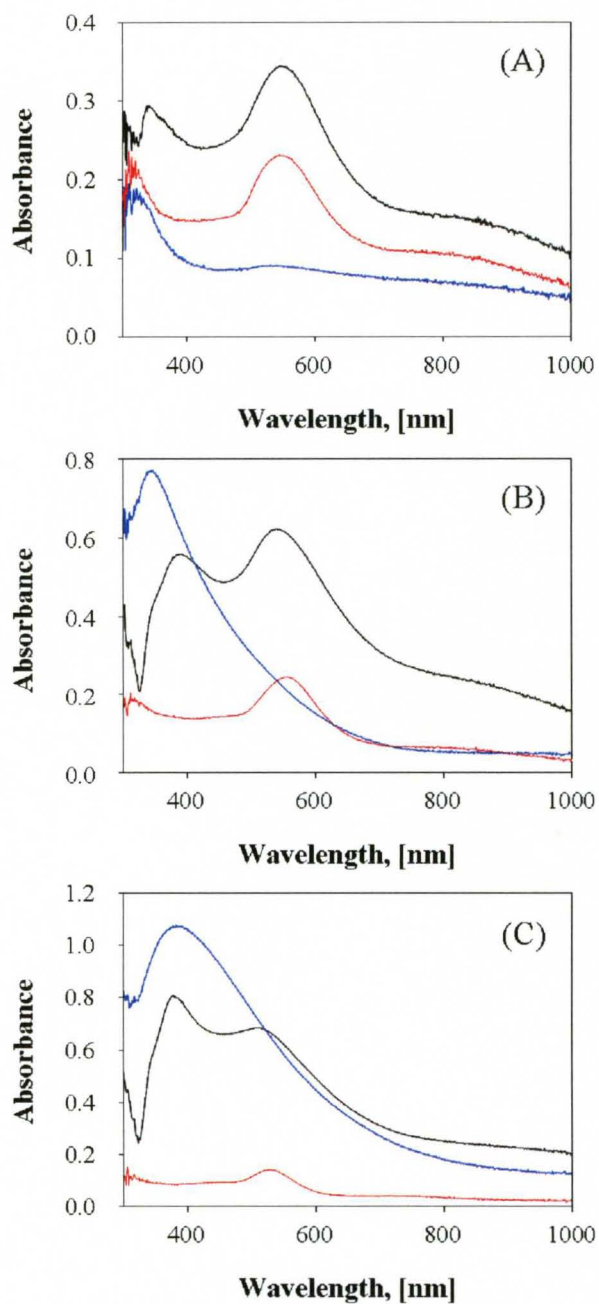
Figure 6.12 UV-vis spectra of Glass/ITO/MPTMS/Au-core/Ag-shell nanostructures with (A) 1 Ag growth, (B) 3 Ag growths, and (C) 5 Ag growths before (black) and after (blue) 1 cycle in 0.01 M KBr, in comparison with Glass/ITO/MPTMS/Au NPs (red line).

case of samples that underwent the oxidation reaction only (Figure 6.8). Figure 6.13 shows the SEM images of Glass/ITO/MPTMS/Au-core/Ag-shell after 1 cycle in 0.01 M KBr solution. The samples that underwent a full cycle appeared similar to those only treated by the oxidation reaction only. The formation of "bulbs" occurred in all three cases (1, 3 and 5 Ag growths). In addition to "bulbs", islands of much smaller particles from 30 to 60 nm were observed on all samples. The sizes of "bulb" particles were 128±30, 170±61, and 199±64 nm for 1, 3 and 5 Ag growths respectively. Among the regular spherical particles, there were some interesting structures like an "open shell" (Figure 6.13 (D)) and porous nanostructures (Figure 6.13 (E)).

Figure 6.14 displays the 1st, 5th, and 10th cycle of CVs recorded on Glass/ITO/MPTMS/Au-core/Ag-shell samples. The Ag oxidation peak decreases approximately 3 times in size with the 2nd cycle and remains relatively constant with every other cycle. The Au oxidation and reduction peaks are visible only during the 1st cycle, demonstrating the absence of Au on the electrode surface after the 1st cycle was performed. UV-vis spectra before and after the 10 cycles are shown in Figure 6.15 and they are very similar to those obtained after 1 electrochemical cycle. SEM images after 10 cycles demonstrated the formation of "bulbs" and some irregular structures for 1 Ag growth. In the case of 3 and 5 Ag growths the "bulbs" transformed into spherical porous structures and some porous networks. The size of the porous spherical particles was similar to size of the "bulb" particles. Some very small particles were observed on the electrode surface as well. SEM images of Glass/ITO/MPTMS/Au-core/Ag-shell nanostructures after 10 electrochemical cycles in 0.01 M KBr and 0.1 M $HClO_4$ are
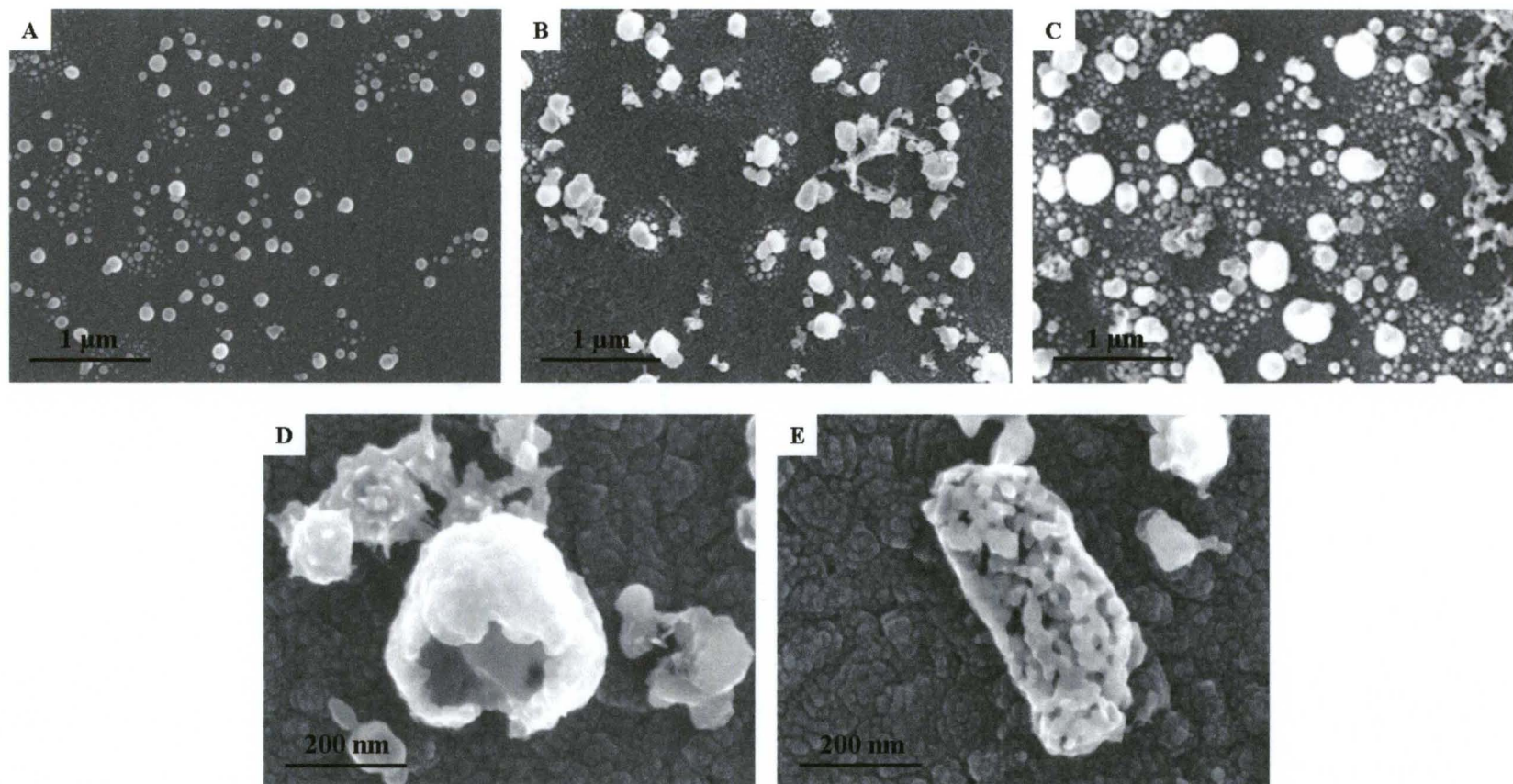
Figure 6.13 SEM images of Glass/ITO/MPTMS/Au-core/Ag-shell structures after 1 cycle in 0.01 M KBr. (A) 1 Ag growth, (B) 3 Ag growths, and (C) 5 Ag growths. Figures (D) and (E) are expanded images of structures found on the surface of 3 and 5 Ag growth samples respectively.
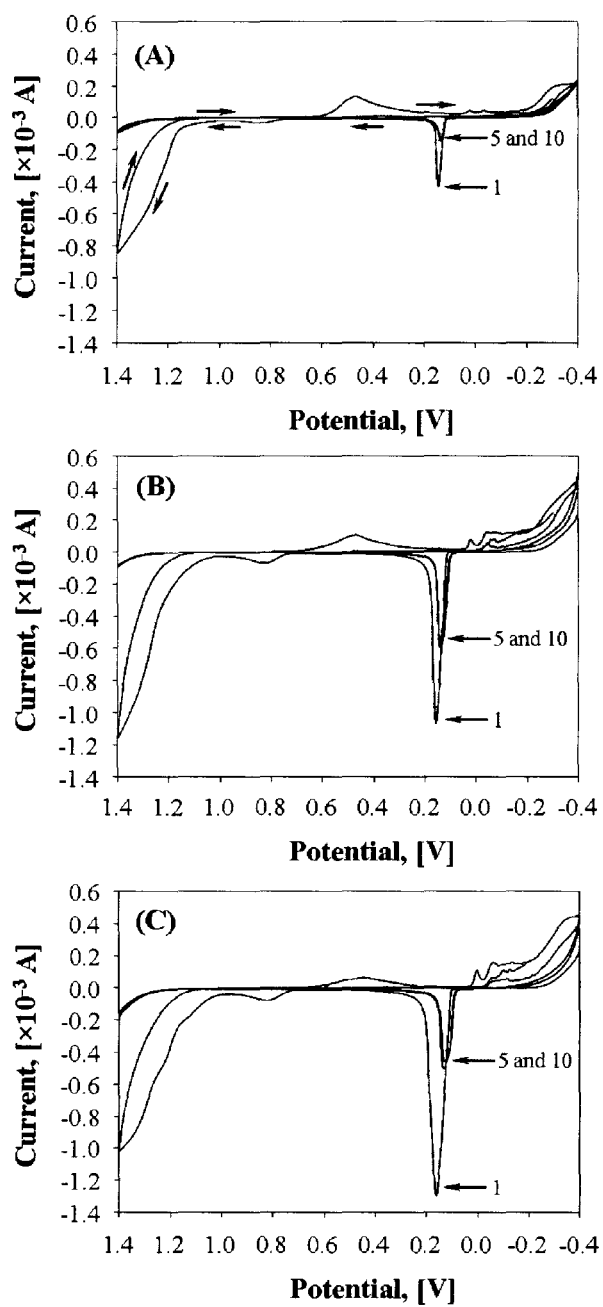
Figure 6.14 CVs of Glass/ITO/MPTMS/Au-core/Ag-shell recorded in 0.01 M

KBr and 0.1 M $HClO_4$ solution. Scan rate 5 mV/s. (A) 1 Ag growth, (B) 3 Ag growths,

and (C) 5 Ag growths. Arrows indicate the direction of the cycle. Cycle 1, 5 and 10 are

shown.
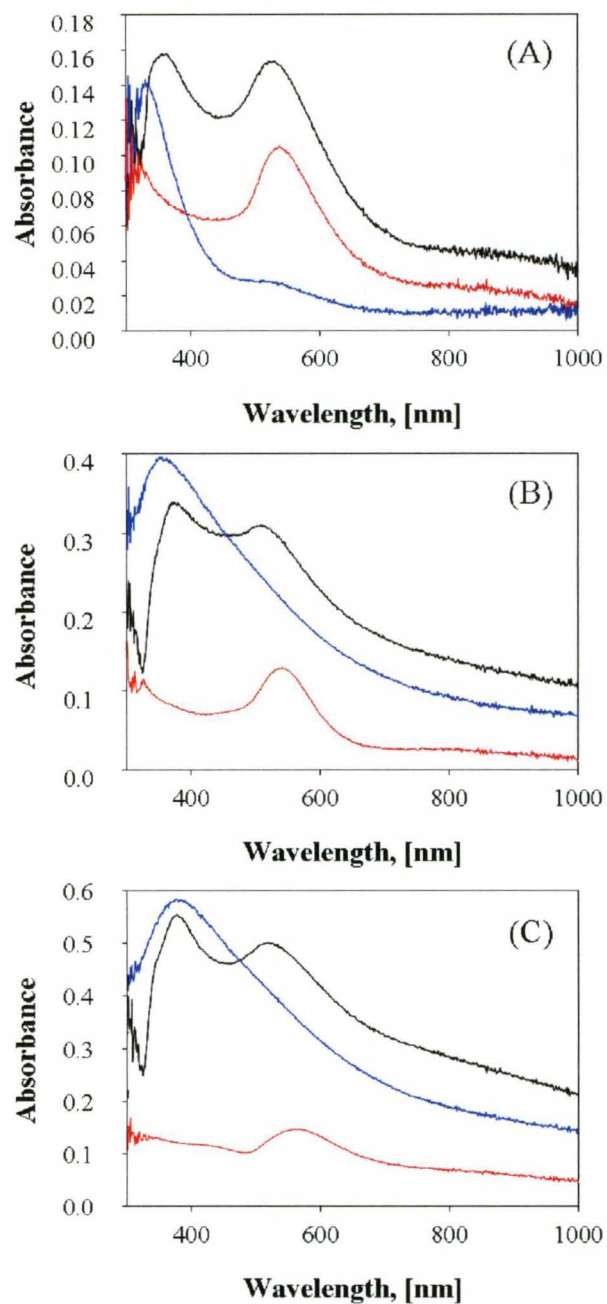
Figure 6.15 UV-vis spectra of Glass/ITO/MPTMS/Au-core/Ag-shell with (A) 1 Ag growth, (B) 3 Ag growths, and (C) 5 Ag growths before (black) and after (blue) 10 cycles in 0.01 M KBr, in comparison with Glass/ITO/MPTMS/Au NPs (red line).

shown in Figure 6.16. The sizes of the final porous structures and "bulbs" after 10 cycles were 123±22, 186±58, and 247±98 nm for 1, 3 and 5 Ag growth respectively.

The formation of nanoporous, sponge-like structures during dealloying on macroscale (usually bulk alloys or films) has been described in literature.[97,134,135] The dealloying process starts with dissolution of one element from the alloy surface, leaving behind the second element. There are many systems studied in this area, such as Au-Ag,[128,129,136,137] Cu-Au,[138] and Cu-Pt,[93] etc. In all cases, the less noble metal was dissolved while the more noble element remained on the surface. This is almost always the case, especially in examples of AuAg alloys. In our case, we removed the more noble metal (Au) from the AuAg alloy and performed the experiment on nanometer-scale objects, making the system unique. Corcoran et. al. reported the formation of porous Au by dealloying Ag from Ag-Au bulk alloy samples in halide containing electrolytes.[97] According to the author, applying a certain overvoltage to the electrode in halide containing electrolyte (0.1 M K(halide) and 0.1 M $HClO_4$) led to the formation of nanoporous Au structures. There was no evidence presented that the remaining element on the surface was Au. We performed a series of experiments in order to determine the amount of Au left on the electrode surface after the oxidation reaction was performed as shown on Figure 6.17 to confirm that we dealloyed Au from the Ag. First, we obtained a CV of a Glass/ITO/MPTMS/Au-core/Ag-shell electrode in 0.01 M KBr and 0.1 M $HClO_4$ for 1 or 10 cycles. Then we performed the oxidation of Ag from the same sample in 0.5 M H_2SO_4. In the latter case Ag^0 will form Ag^+ and dissolve from the electrode surface into the solution. This step was necessary in order to rule out the possibility that the Ag-shell was blocking the oxidation of Au in KBr solution. By removing the Ag in
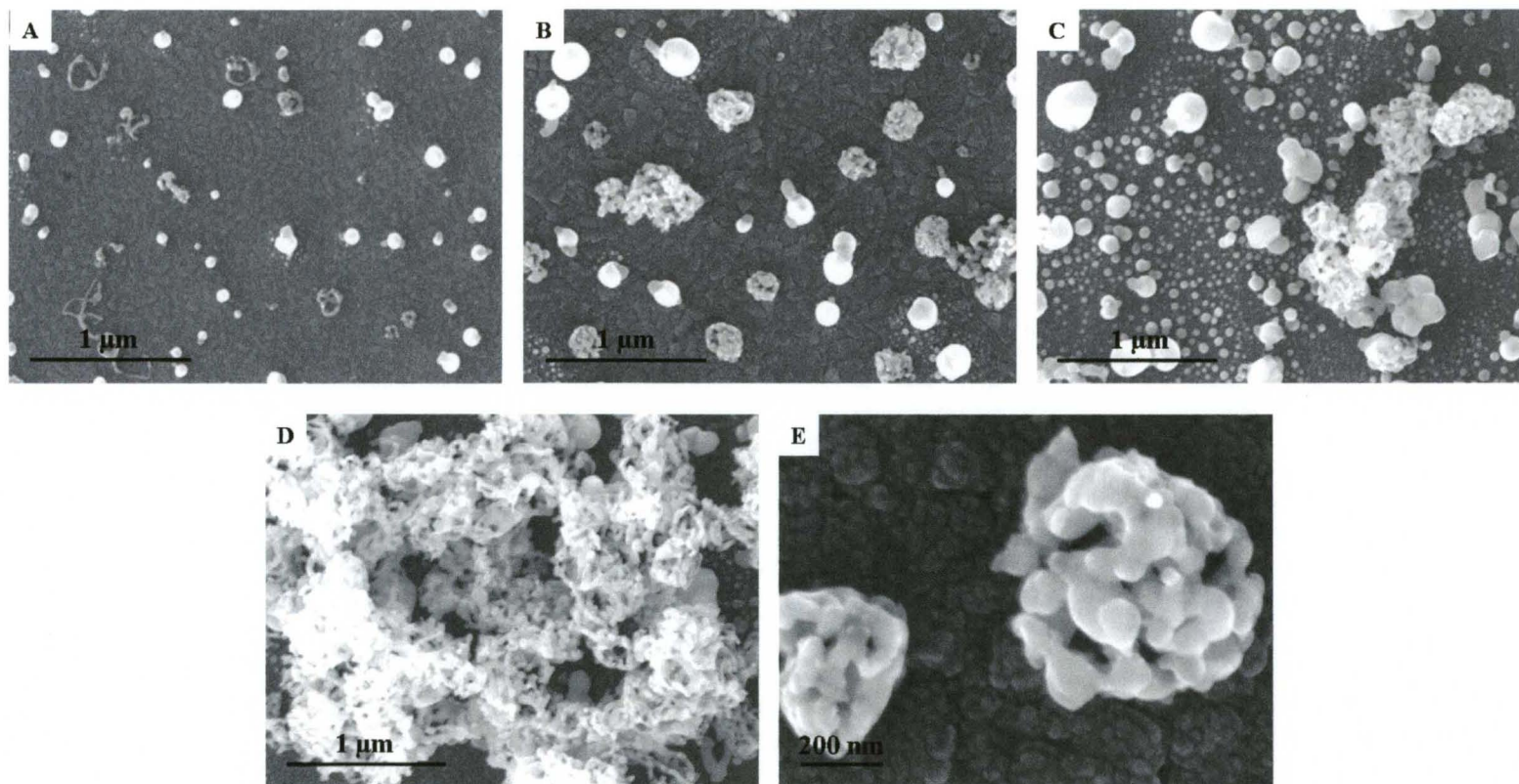
Figure 6.16 SEM images of Glass/ITO/MPTMS/Au-core/Ag-shell structures after 10 cycles in 0.01 M KBr. (A) 1 Ag growth, (B) 3 Ag growths, and (C) 5 Ag growths. Figure (D) represents a nanoporous network (sample with 5 Ag growths). (E) zoom-in on the porous spherical nanostructure.

(1) CV of ITO/Au/Ag core-shell in KBr 1 or 10 cycles

To oxidize/dealloy Au

(2) LSV of ITO/Au/Ag core-shell in H₂SO₄

To oxidize Ag

(3) LSV of ITO/Au/Ag core-shell in KBr

To oxidize leftover Au
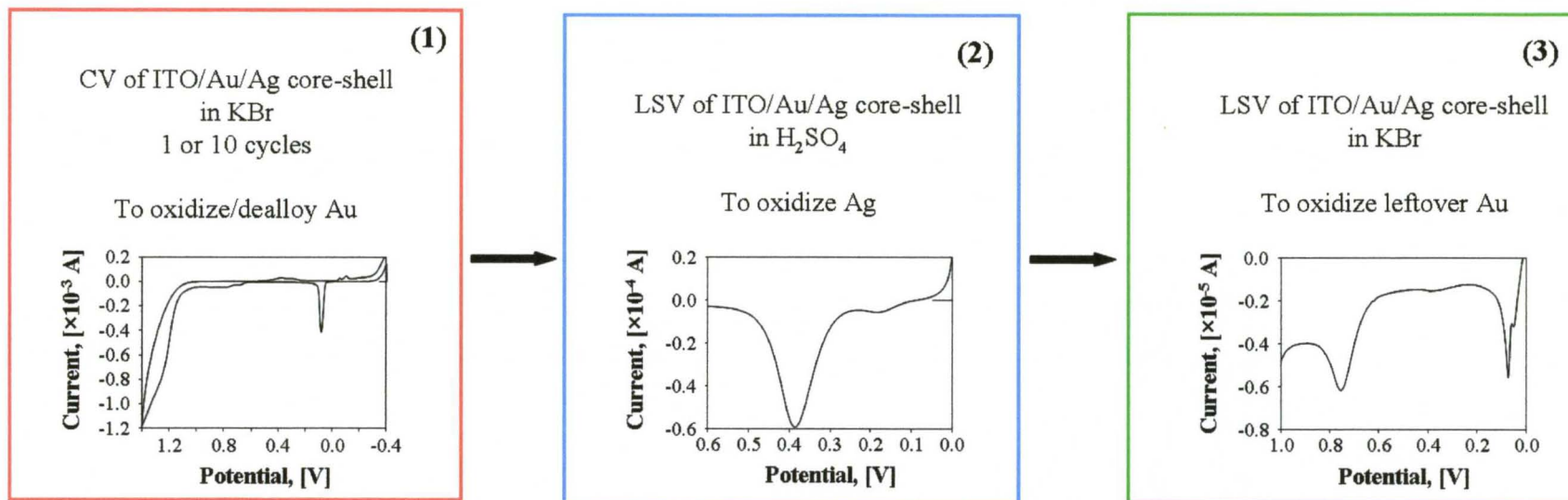
Figure 6.17 Experimental steps performed to determine the amount of Au on the electrode surface after electrochemical cycling in 0.01 M KBr and 0.1 M HClO₄ solution.

H$_2$SO$_4$ we should allow access to only remaining Au on the electrode surface. In the last step, we obtain a VS of the same sample in 0.01 M KBr and 0.1 M HClO$_4$ again, in order to determine if there is any Au (and how much).

Figures 6.18 and 6.19 show CVs of Glass/ITO/MPTMS/Au/Ag NPs in (A) 0.01 M KBr and 0.1 M HClO$_4$, (B) 0.5 M H$_2$SO$_4$, and (C) 0.01 M KBr and 0.1 M HClO$_4$. Numbers 1, 3 and 5 correspond to the number of Ag growths performed on the sample. Figures 5.17 and 5.18 (B) show that after 1 and 10 cycles in KBr media, we can oxidize Ag in H$_2$SO$_4$. It proves that the "bulbs" and porous structures formed after the electrochemical cycling contain Ag. The Ag oxidation peak in H$_2$SO$_4$ increases with an increase in the number of Ag growths performed on the sample. After 10 cycles, the amount of Ag determined by LSV was smaller than that after 1 cycle, showing that some Ag is lost during the cycling in KBr. As described above, to determine the amount of Au left on the surface we performed an additional sweep in KBr electrolyte after removing Ag. During this step, we compared the remaining amount of Au to the initial amount present on the sample, also determined by LSV of the original Au sample only. From the CVs shown in Figures 6.17 and 6.18 (C) we determined that samples cycled once in step (1) and processed through the rest of the route as described before had 1 to 3 % of original amount of Au left on the surface, independent of the amount of Ag overgrowths. The amount of Au left on the electrode surface after 10 cycles in KBr varied from 0.03 to 0.05 % and was also independent of the number of Ag growths. These results show that the "bulbs", porous structures, and networks formed on the electrode surface during the electrochemical cycling in KBr solution are made from Ag, not Au. This is likely the case in the Corcoran study, since the conditions are very similar.
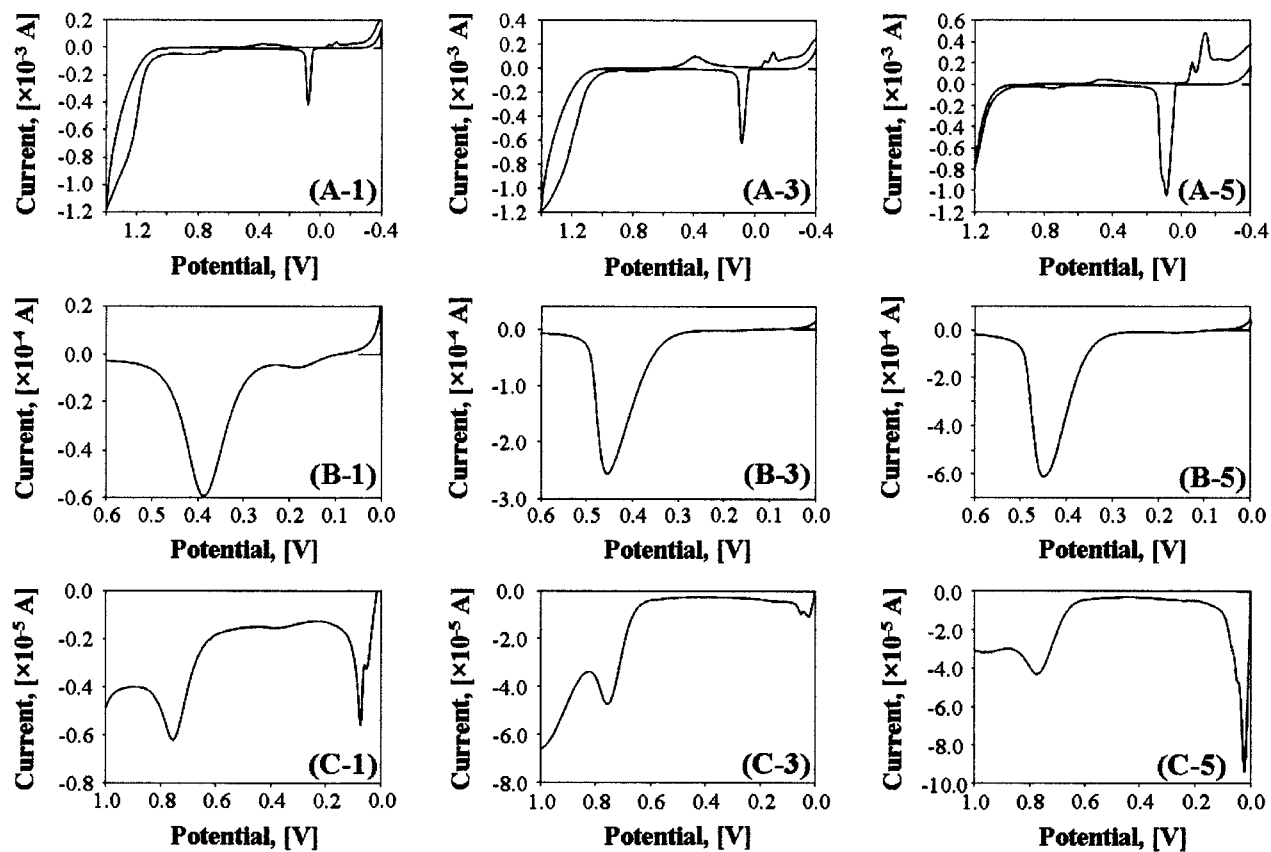
Figure 6.18 CVs and LSVs of Glass/ITO/MPTMS/Au-core/Ag-shell recorded in (A) 0.01 M KBr and 0.1 M HClO₄ (1 cycle),

(B) 0.5 M H₂SO₄, and (C) 0.01 M KBr and 0.1 M HClO₄ (second run). Numbers 1, 3 and 5 correspond to number of Ag growths on

the sample. Scan rate 5 mV/s.
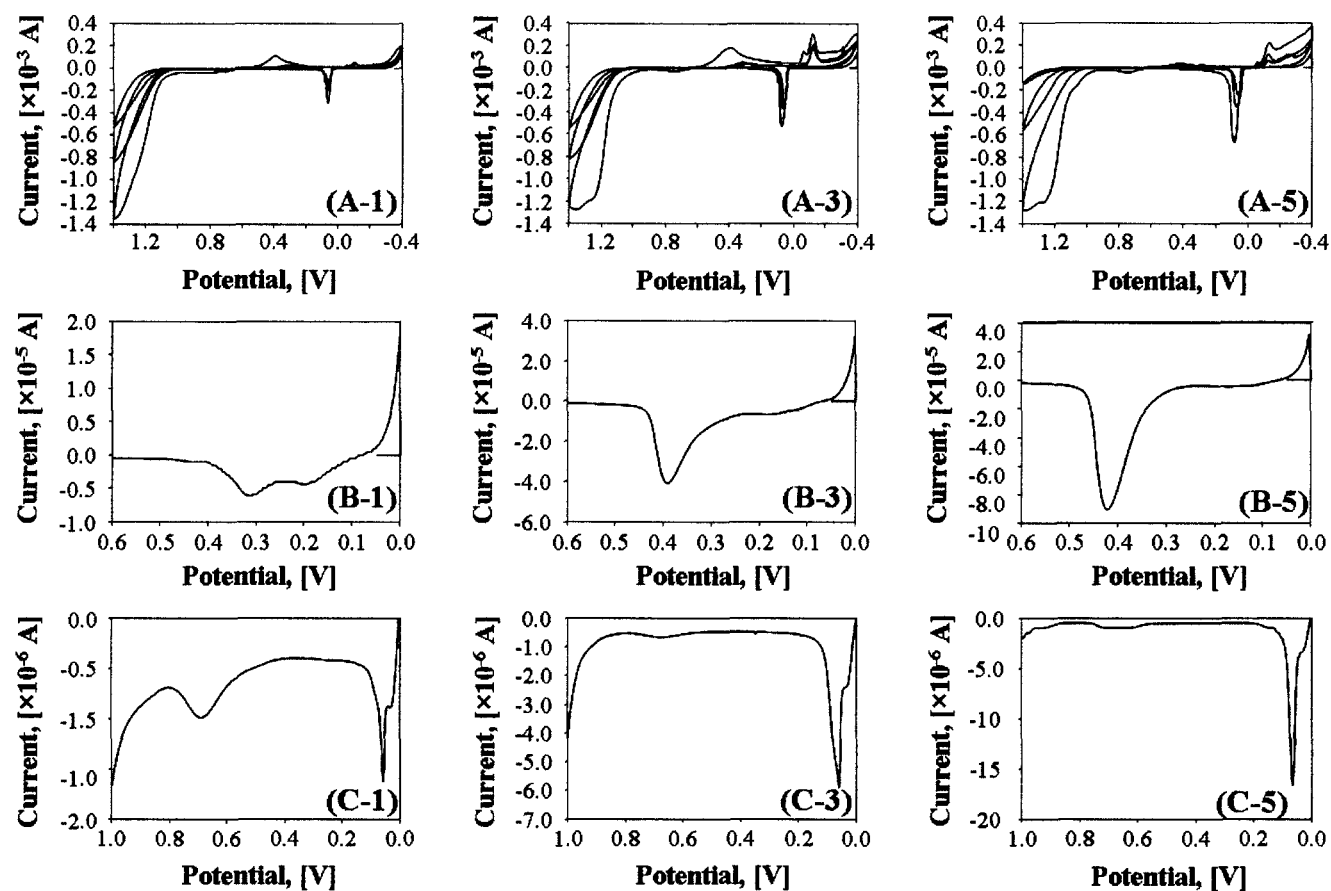
Figure 6.19 CVs and LSVs of Glass/ITO/MPTMS/Au-core/Ag-shell recorded in (A) 0.01 M KBr and 0.1 M HClO₄ (10 cycles), (B) 0.5 M H₂SO₄, and (C) 0.01 M KBr and 0.1 M HClO₄ (second run). Numbers 1, 3 and 5 correspond to number of Ag growths on the sample. Scan rate 5 mV/s

To verify if Au has any role on formation of porous Ag nanostructures via dealloying, we carried out similar experiments on pure Ag nanostructures chemically synthesized on Glass/ITO surface. We performed Ag overgrowth on Ag nanostructures as we did in the case of Ag overgrowth on Au and kept the same number of overgrowth layers 1, 3, and 5. Figure 5.20 shows UV-vis spectra and SEM images of Glass/ITO/MPTMS/Ag NPs. UV-vis spectra represent Ag nanostructures with sequential growth of Ag on top of them. With an increase in the number of overgrowth cycles the intensity of the Ag plasmon band increases. The SEM images show typical Ag nanostructures formed after 1 (A), 3 (B), and 5 (C) Ag growths on the ITO surfaces. The majority of the nanostructures were spherical nanoparticles with average sizes of 52±16, 126±38, and 142±75 nm for 1, 3, and 5 growths respectively. Other shapes appeared sporadically, including rods, triangles, and hexagons. As in the case of Au/Ag overgrowth, these structures were smooth.

These Ag nanostructures were further used in electrochemical experiments. Similar to the Au/Ag core-shell structures, samples were cycled once or 10 times in 0.01 M KBr and 0.1 M $HClO_4$. Figure 6.21 and 6.22 shows CVs and UV-vis spectra before and after electrochemical oxidation for 1 and 10 cycles, respectively. Frame (A) of Figure 6.21 shows the oxidation peak of Ag at ~140 mV. Frames (B) and (C) show that with an increase of the amount of Ag on the electrode surface, the oxidation peak for Ag increased and shifted slightly to more positive potentials. Ag reduction peak shifted to more negative with increase of amount of Ag on the electrode surface. The CVs in Figure 6.22 show the 1st, 5th and 10th cycles of a Glass/ITO/MPTMS/Ag NP electrode in 0.01 M KBr solution. The Ag peak area decreased drastically on the 2nd cycle (~5 times)
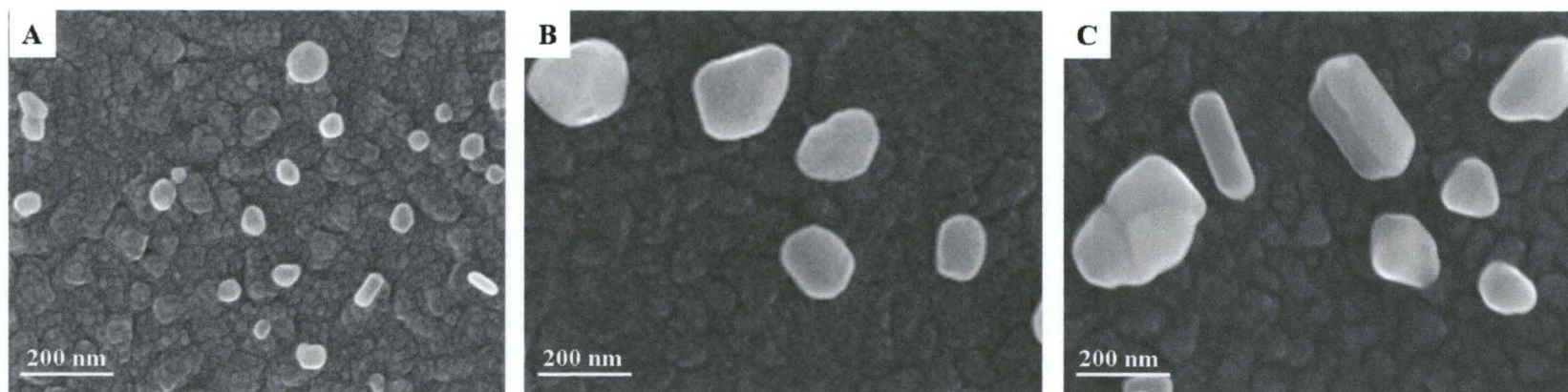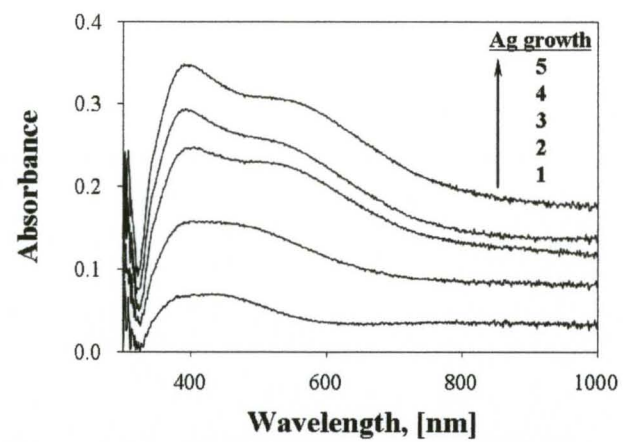
Figure 6.20 UV-vis spectra of Glass/ITO/MPTMS/Ag NPs overgrowth (up to 5 Ag growths) and SEM images of Glass/ITO/Ag NPs with (A) 1 Ag growth, (B) 3 Ag growths, and (C) 5 Ag growths.
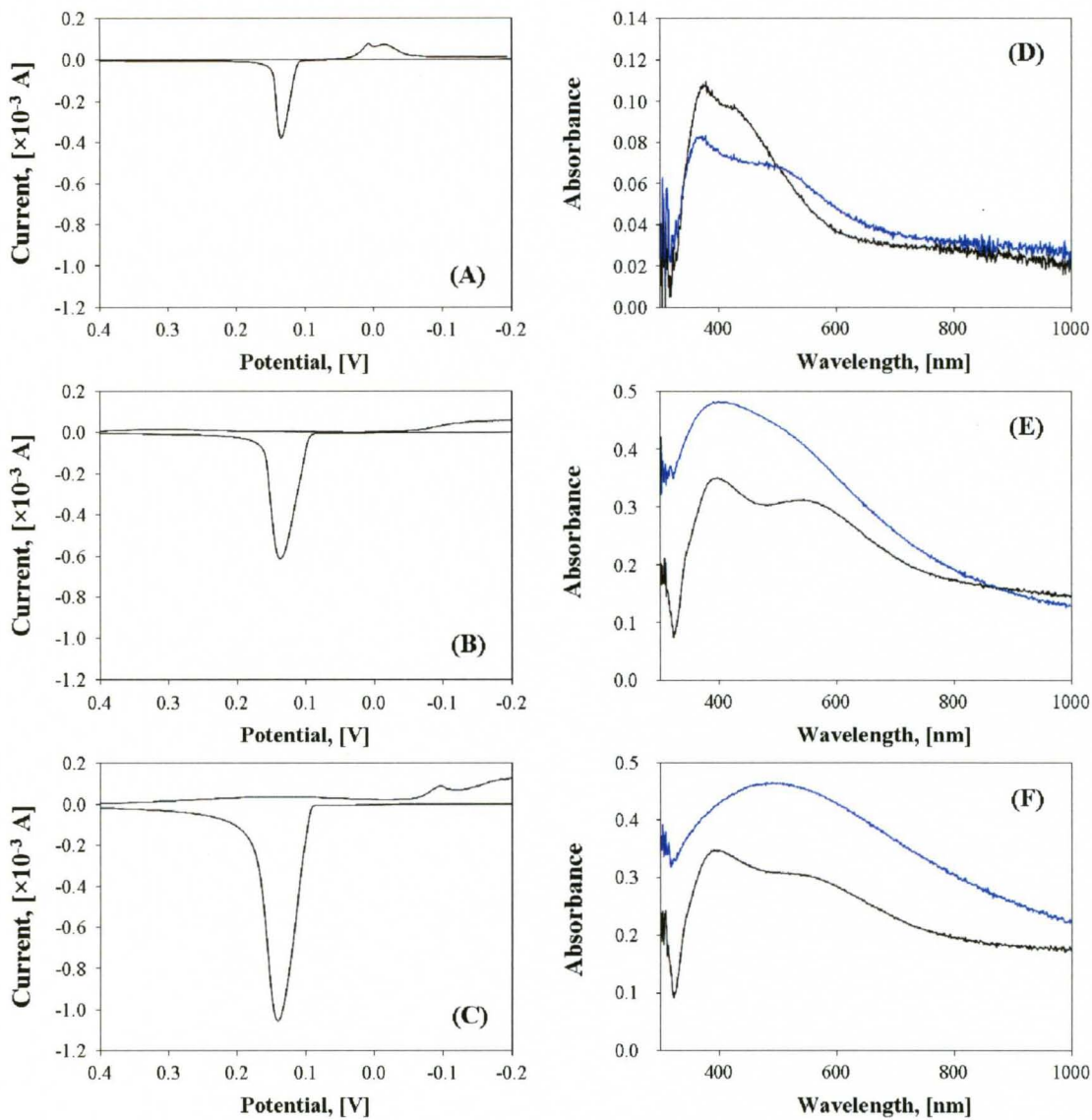
Figure 6.21 CVs of Glass/ITO/MPTMS/Ag NPs in 0.01 M KBr and 0.1 M HClO$_4$, 1 cycle for (A) 1 Ag growth, (B) 3 Ag growths, and (C) 5 Ag growths. Frames (D), (E), and (F) show corresponding UV-vis spectra for 1, 3 and 5 growths, respectively.
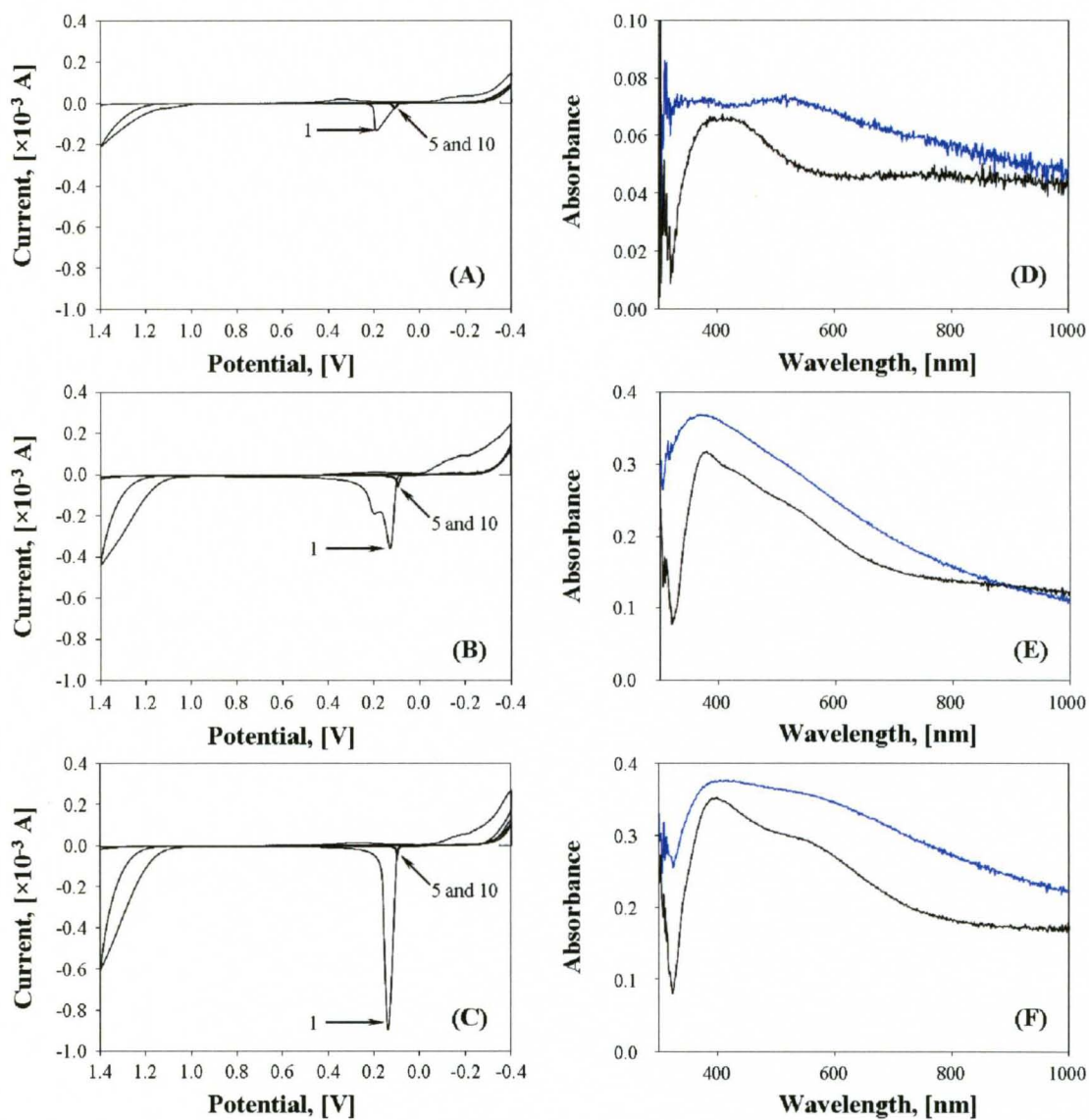
Figure 6.22 CVs of Glass/ITO/MPTMS/Ag NPs in 0.01 M KBr and 0.1 M HClO₄, 10 cycles for (A) 1 Ag growth, (B) 3 Ag growths, and (C) 5 Ag growths. Frames (D), (E), and (F) show corresponding UV-vis spectra for 1, 3 and 5 growths, respectively.

compared to 1st one, and continued to decrease until the 5th cycle, where it stabilized. Frames (D), (E) and (F) show UV-vis spectra of corresponding samples. The intensity of the spectra increased throughout the entire wavelength range. The peaks became broader and shifted towards higher wavelengths, which points out to either formation of hollow nanostructures[133] or aggregation of them on the electrode surface.

To verify morphological changes we obtained SEM images after the electrochemical oxidation for 1 and 10 cycles in KBr solution. Typical SEM images after electrochemical oxidation of Ag in KBr are shown in Figure 6.23. Frames (A), (B), (C) display nanostructures obtained after 1 cycle in KBr with 1, 3, and 5 Ag growths, respectively. Average diameters were 83±33, 195±112, and 279±136 nm for 1, 3 and 5 Ag growths respectively. Frames (D), (E) and (F) show images after 10 cycles in KBr. Average diameters in this case were 131±53, 209±102, and 278±133 nm for 1, 3 and 5 Ag growths respectively. Similar to Au/Ag core-shell nanostructures, the formation of "bulbs" were observed for all conditions of pure Ag samples. Porous structures were rarely seen on the surface, regardless of the number of growths and cycles.
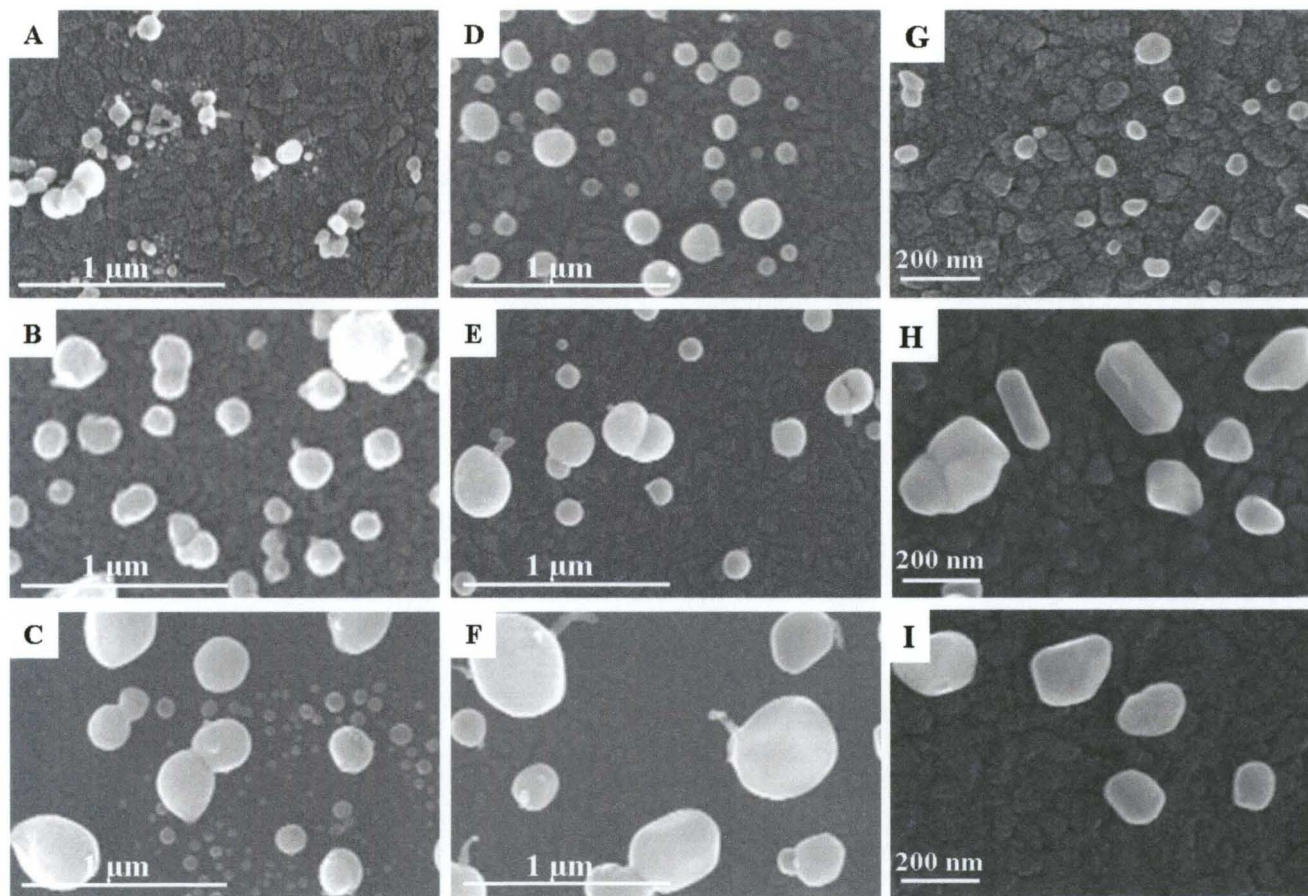
Figure 6.23 SEM images of Glass/ITO/MPTMS/Ag NPs after electrochemical oxidation in KBr solution for 1 cycle, frames (A), (B), and (C) with 1, 3 and 5 Ag growths respectively. And after 10 cycles, frames (D), (E), and (F) with 1, 3, and 5 Ag growths respectively. Figures G, H, and I shows Glass/ITO/MPTMS/Ag NPs with 1, 3 and 5 Ag growths, respectively.

6.4 CONCLUSIONS

Here we successfully synthesized Ag and Au/Ag nanostructures directly on ITO surface with controlled size. Then we effectively dealloyed Au from Au/Ag nanostructures by oxidation in bromide containing electrolyte. The composition analysis based on LSV showed that there is less than 3% of Au on the electrode surface, indicating successful dealloying of Au from Ag. During the dealloying process we formed interesting porous and hollow bulb structures of Ag by electrochemical oxidation of pure Ag or Au/Ag in Br⁻. Pure Ag forms bulbs, Au/Ag structures forms bulbs or porous structures depending on number of electrochemical cycles. Table 6.1 shows change in diameter of nanostructures after 1 and 10 electrochemical cycles in comparison with original size of nanostructures. 1 cycle in bromide media led to formation of bulbs for both pure Ag and Au/Ag nanostructures. 10 electrochemical cycles led to formation of bulbs for pure Ag sample and mixture of bulbs and porous structures for Au/Ag nanostructures. These hollow or porous Ag nanostructures could find use in various applications such as catalysis, sensing or drug delivery.

(A)

Au/Ag # of Ag growths	Diameter [nm]	Diameter after 1 cycle [nm]	Diameter after 10 cycles [nm]
1	129±59	128±30	213±22
3	128±48	120±61 (132 %)	186±58 (145 %)
5	143±48	199±64 (139 %)	247±98 (172 %)

(B)

Pure Ag # of Ag growths	Diameter [nm]	Diameter after 1 cycle [nm]	Diameter after 10 cycles [nm]
1	52±16	83±33 (160 %)	131±53 (151 %)
3	126±38	195±112 (112 %)	209±102 (167 %)
5	142±75	279±136 (196 %)	278±133 (195 %)

Table 6.1 Diameter of the particles before and after electrochemical cycling for (A) Au-core/Ag-shell structures and (B) for pure Ag nanostructures.

CHAPTER VII

ELECTROCHEMICAL AND OPTICAL CHARACTERIZATION OF BIMETALLIC (Ag)Au AND (Au)Ag NANOPARTICLES PREPARED BY SEED MEDIATED GROWTH METHOD

Here we describe the electrochemical characterization of Au/Ag alloy nanoparticles (NPs). The goal of the experiments was to distinguish between the two methods of synthesis by Linear Sweep Voltammetry (LSV). Au/Ag NPs were synthesized by a seed mediated growth method. Two routes of synthesis were used: 1) Ag ions were reduced onto preformed Au NP seeds and 2) Au ions were reduced onto preformed Ag NP seeds. The solution molar ratio of 1:1 (Au:Ag) was studied in both cases. The electrochemical composition analysis was used to determine the Au:Ag ratio and atomic arrangement at different stages of the synthesis. In the case of $(Au_{4nm})Ag$, heating solution for 24 h led to disappearance of Ag oxidation peak, while in the case of the $(Ag_{8nm})Au$ NPs showed the presence of Ag oxidation peak even after 24 h. This indicates the different atomic arrangement in Au/Ag alloy NP for two different synthesis methods. In the first case, Ag is stabilized by Au and therefore is not accessible for oxidation. In the latter case Ag is on the surface of the Au NPs, which makes it possible to oxidize. Quenching the alloy solution in an ice bath provided the study of alloy composition and atomic arrangement at earlier (first 5 min) stages of synthesis.

170

7.1 INTRODUCTION

Bimetallic nanoparticles exhibit unique optical, magnetic and catalytic properties different not only from the bulk metals, but also from corresponding monometallic nanoparticles.[122,139-141] This provides another method to tune their properties besides size and shape manipulation. Two main groups of bimetallic colloids exist, alloys and core-shell colloids. Au-Ag alloy nanoparticles can be prepared by number of methods. The most common one is the co-reduction of metal salts in the presence of stabilizing agent.[123,142] Another well established method is to reduce metal salt (Au or Ag) on preformed colloid of a different metal.[122,125] Au-Ag alloy nanostructures were used for SERS demonstrating that Ag atoms provide SERS-active sites on a Au surface at a wavelength where Au itself is not active.[143] Au-Ag alloy NPs are also good materials for tuning the localized Surface Plasmon Resonance (SPR) by varying the composition of the alloy. It was also shown that Au-Ag alloy NPs are better as a catalyst for CO oxidation compared to pure Ag or pure Au NPs.[144] There are many publications focused on the synthesis of bimetallic nanostructures. Most of them characterize the final product by optical methods and High Resolution TEM (HRTEM) technique. There is little known about the electrochemistry of these bimetallic NPs.

Here we describe preliminary results on synthesis of AuAg bimetallic NPs by seed-mediated growth and their electrochemical and optical characterization at different stages of the synthesis procedure. We used two different ways of synthesis of AuAg bimetallic NPs and two different temperature protocols in order to determine if the electrochemistry of the Au and Ag are sensitive to these differences.

7.2 EXPERIMENTAL

Figure 7.1 shows the general experimental route used in this study. The main steps involve the synthesis of Au-Ag alloy NPs in solution, characterization of the colloidal solution by UV-vis spectroscopy, assembly of the alloy NPs on an electrode surface, and characterization by LSV and UV-vis on the electrode.

Synthesis of AuAg NPs. AuAg NPs were synthesized by seed mediated growth method at high temperatures, similar to the procedure used for the synthesis of different size Ag NPs described in Chapter III. In this case Ag or Au metal ions were reduced in the presence of citrate (act as a reducing and capping agent at the same time) and at high temperatures over preformed Au or Ag colloidal NPs. Figure 7.2 shows a schematic of the synthesis procedure. In route one, a 0.01 M $AgNO_3$ solution was brought to boil and then a 40 m L of 4 nm diameter Au Seed NPs (2.5×10^{-4} M in Au) (described in Chapter II) were added simultaneously with a 1% citrate solution. The mixture was allowed to boil for desired period of time (1 min to 24 h), with vigorous stirring. The solution was then cooled down to room temperature before UV-vis and electrochemical analysis. The resulting NP alloy will be further referred as (Au_{4nm})Ag since Au was used as the seed. In route 2, 0.01 M $AuCl_4^-$ was reduced onto preformed 8 nm diameter Ag Seed NPs (see Chapter II) using the same approach as in route one. The resulting colloid NPs will be further referred as (Ag_{8nm})Au since Ag NPs were the seed.

Attachment of alloy NPs to the electrode surface. The alloy NPs were chemisorbed onto Glass/ITO electrodes functionalized with APTES according to the
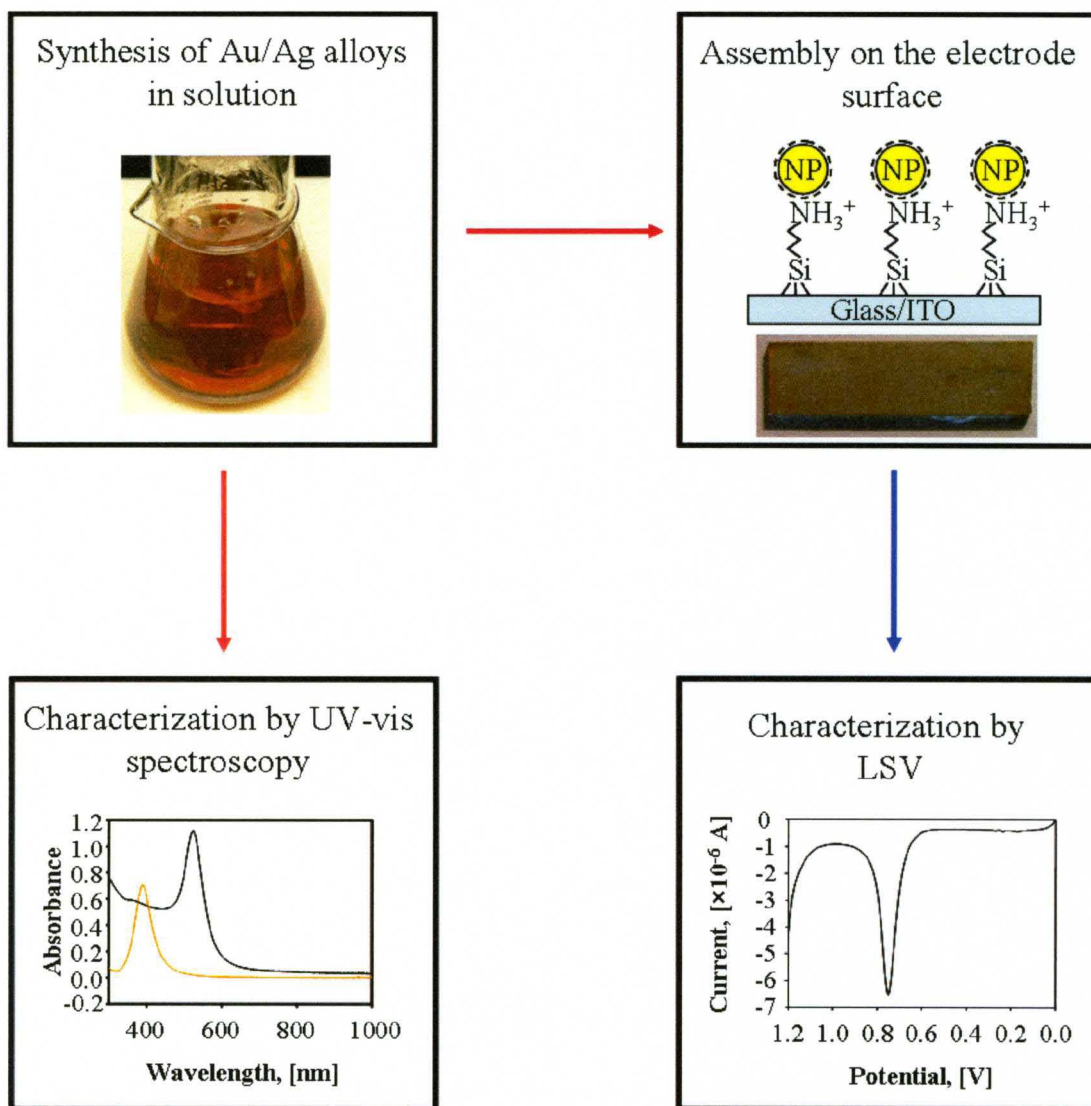
Figure 7.1 Experimental steps.
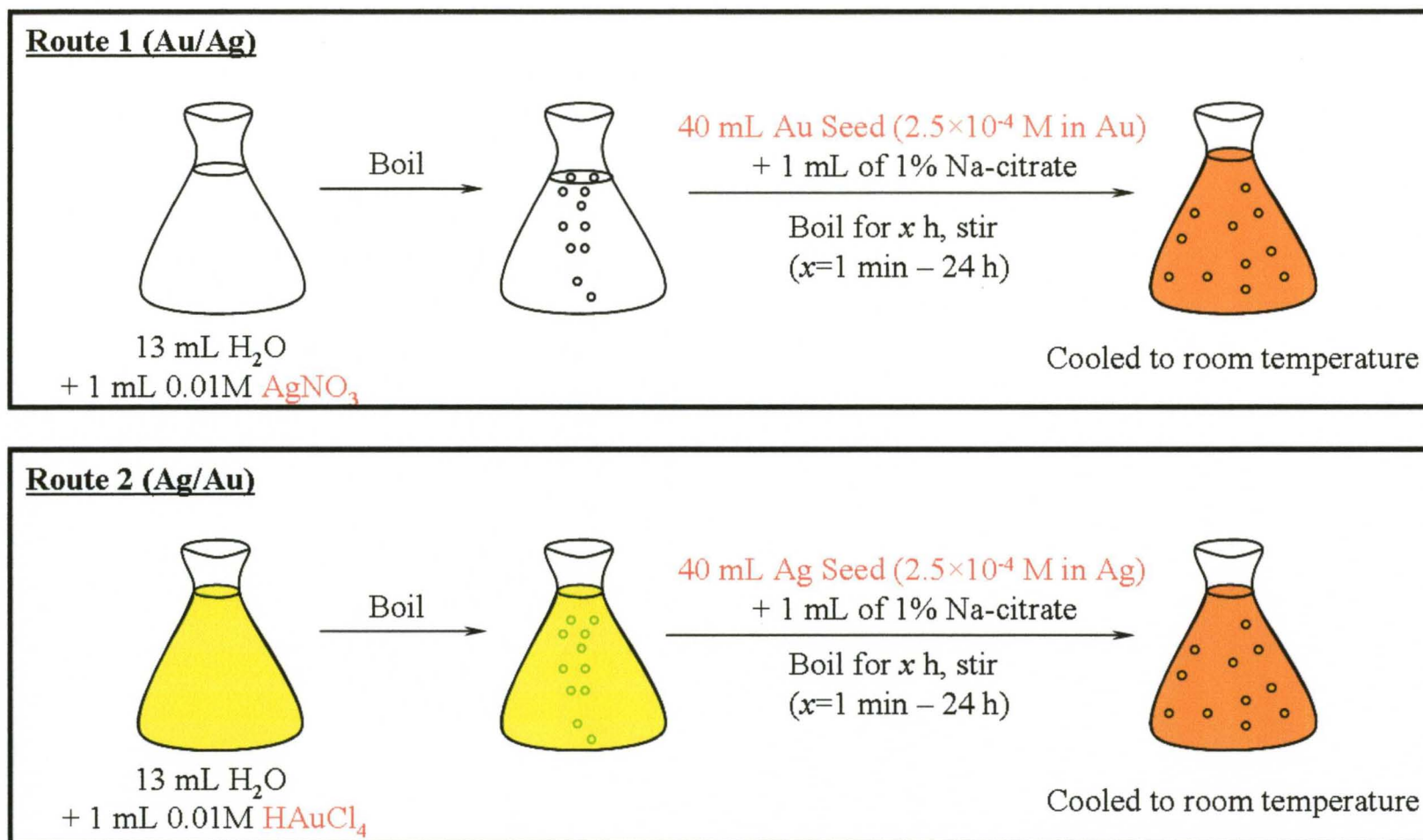
Figure 7.2 Schematic of (Au$_{4nm}$)Ag and (Ag$_{8nm}$)Au alloy synthesis by seed mediated growth method.

procedure described in Chapter II. The soaking time was kept constant at 20 min for all samples.

Characterization of alloy NPs. AuAg NP solutions were characterized by UV-vis spectroscopy. The composition of the alloy nanoparticles were determined by LSV. Electrochemical characterization involved two consequent oxidation steps: 1) The LSV was performed in 0.5 M H_2SO_4 from 0 to 1.0 V at 5 mV/sec in order to determine the oxidation potential and the amount of Ag present and 2) the LSV was obtained in 0.01 M KBr and 0.1 M $HClO_4$ electrolyte solution from 0 to 1.2 V to determine the oxidation potential and the amount of Au.

7.3 RESULTS AND DISCUSSION

Figure 7.3 (A) shows the photographs of $(Au_{4nm})Ag$ alloy NPs colloidal solutions synthesized with a 1:1 Au:Ag molar ratio. The photographs were taken at different times following the addition of Au seed. The 0 min time represents $AgNO_3$ solution only, which is colorless. 1 min to 24 h represents the time of boiling the solution after addition of Au Seed NPs and 1% citrate solution. Immediately after the addition of Au Seed NPs, the solution turned red, similar to the Au Seed color shown in Figure 7.3 (B)). With increasing heating time, the color of solution changed from red to red-orange and at 60 min became orange. Heating for 24 h led to a color change from orange to brown. Figure 7.3 (B) shows the color of Ag Seed and Au Seed for comparison. We obtained UV-vis spectra of (Au)Ag colloidal solutions after each heating time as well as a monometallic Au and Ag NPs (Figure 7.3 (C)). Only one LSPR band was detected for each alloy. After 1 min of heating time the wavelength of the peak did not change, compared to Au Seed NPs (510 nm), while the intensity of the peak increased. With further increase in heating time the peak intensity was increased and the wavelength shifted to more negative values, such as 490 and 465 nm, for 15 min and 30 min, respectively. The absorption spectra for 30, 45 and 60 min heating times were identical. The peak was broadened and blue-shifted relative to that at 15 min. Further heating for 24 h led to an increase in the intensity and formation of one single peak at 458 nm. Heating the solution for longer time (up to 29 h) did not change the peak intensity or wavelength further, indicating that all Ag ions in solution were reduced. A single LSPR peak and the fact that this peak is located in between pure Au NPs (510 nm) and pure Ag
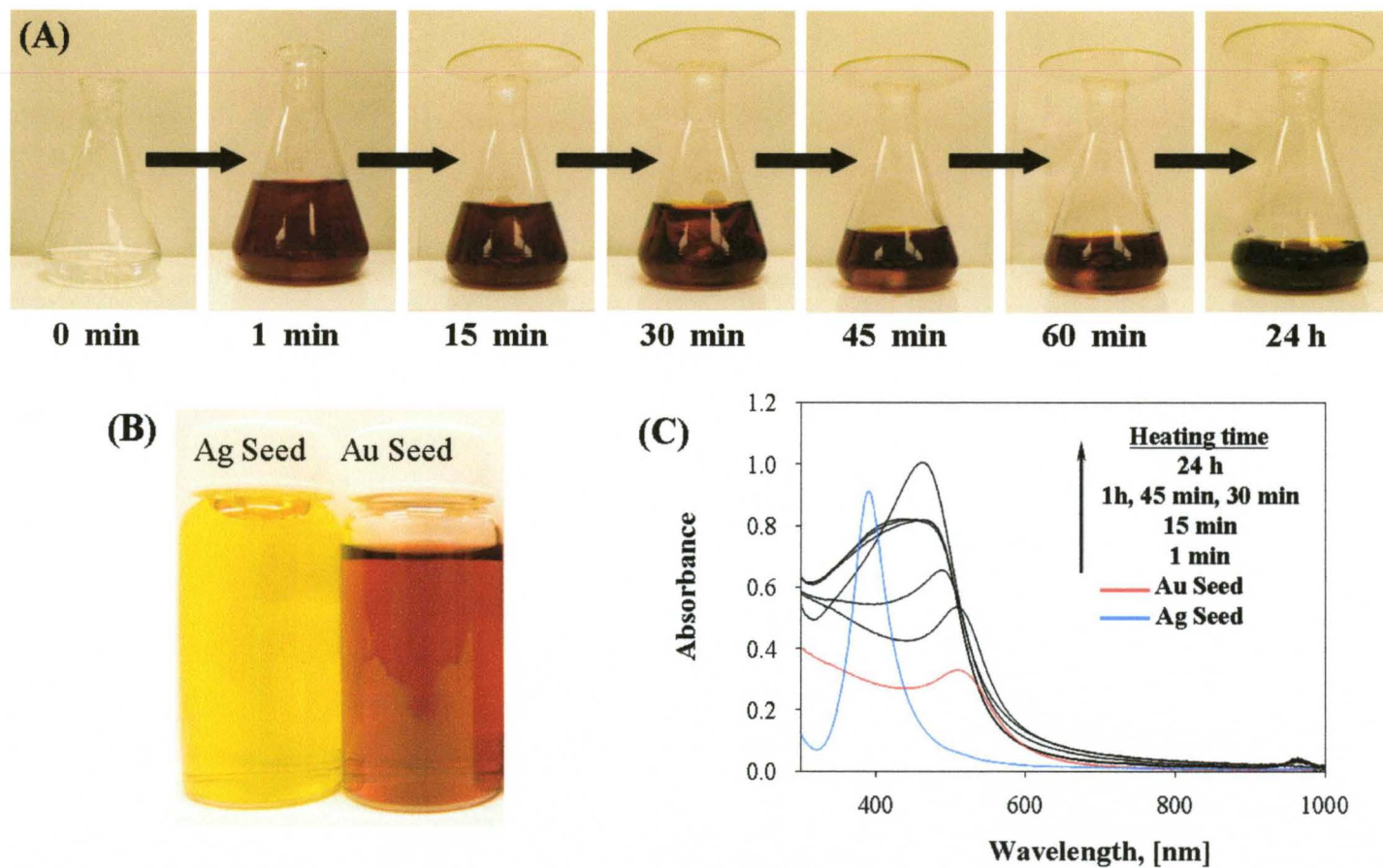
Figure 7.3 (A) photographs of (Au)Ag NPs solutions at different heating times. (B) Photographs of monometallic Ag Seed and Au Seed NPs. (C) UV-vis spectra of (Au)Ag NPs solutions at different heating times, and Au Seed and Ag Seed NPs for comparison.

NPs (390nm) indicates that the synthesized particles were alloys rather than core-shell or a mixture of monometallic Au and Ag NPs. Table 7.1 shows the change in peak wavelength (λ_{max}) with heating time, in comparison with pure Ag NP seed and Au NP seed solutions.

We characterized these alloy NPs electrochemically by LSV. Figure 7.4 shows the LSVs of Glass/ITO/APTES/(Au)Ag NPs for different heating time. Column (A) shows the oxidation of Ag from (Au_{4nm})Ag NPs in 0.5 M H_2SO_4 while column (B) shows the oxidation of Au from the (Au_{8nm})Ag NPs in 0.01 M KBr and 0.1 M $HClO_4$ solution obtained afterwards. The electrochemical data is presented in Table 7.2. The peak for Ag oxidation is 329 mV for 1min of heating time and shifts slightly to more positive values with an increase in heating time. The shift in the oxidation potential for Ag could be due to two reasons: an increase in Ag coverage or diffusion of Ag into the Au lattice, which makes it harder to oxidize. The Ag coverage increased with an increase in heating time up to 30 min, and remained similar for 30, 45 and 60 min of heating time, which is consistent with our UV-vis data. Interestingly, we did not observe an oxidation peak for Ag for the (Au_{8nm})Ag alloy NPs prepared by heating 24 h. We believe that the long heating time results in diffusion of Ag atoms into the Au lattice, which makes it difficult to oxidize. The diffusion of Ag into the Au NP and increase of Au at the surface is consistent with the LSPR band shifting positive and sharpening after 24 h. The Au oxidation potential and coverage remained approximately the same, except for the 24 h heating time. The reduction in Au could be due to a lower overall coverage of NPs on the surface or stabilization of Au. Converting coulombs into the number of moles showed that after 1 min of heating alloy, Au:Ag ratio was approximately 9:1 and reaches

178

Heating time	λ_{max}
1 min	510
15 min	490
30 min	~465
45 min	~465
60 min	~465
24 h	458
Ag Seed	390
Au Seed	510

Table 7.1 UV-vis data for (Au_{4nm})Ag NPs.

179
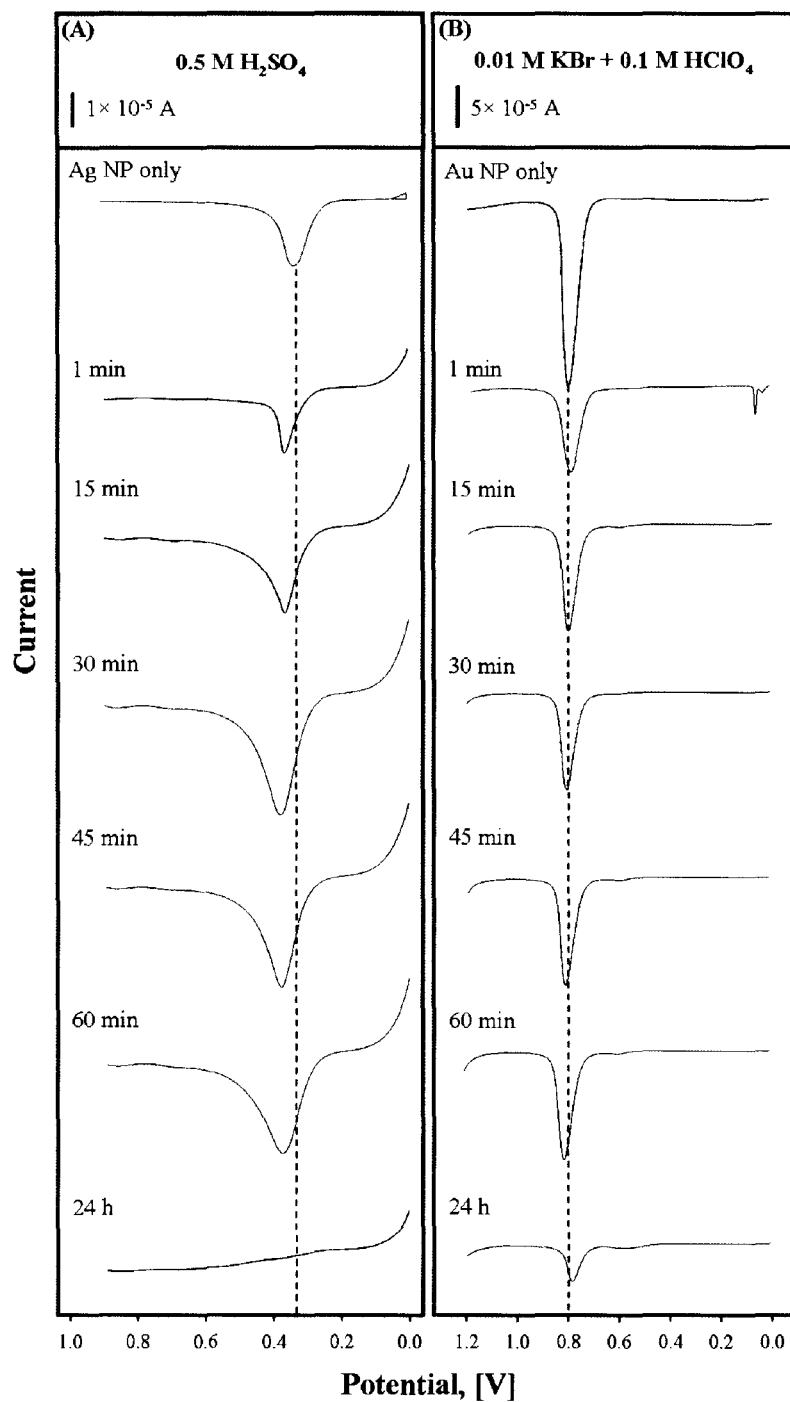
Figure 7.4 LSVs of Glass/ITO/APTES/(Au)Ag NPs performed in (A) 0.5 M
H_2SO_4 and (B) in 0.01 M KBr and 0.1 M $HClO_4$ for different heating times as indicated.
Scan rate 5 mV/s.

Heating time	E_p Ag, [mV]	A_p Ag, [×10^{-4} C]	E_p Au, [mV]	A_p Au, [×10^{-4} C]	Au:Ag ratio
1 min	329 ± 51	1.3 ± 0.5	809 ± 2	17 ± 1.9	8.7
15 min	370 ± 1	2.6 ± 0.1	806 ± 1	9.8 ± 1.3	2.5
30 min	378 ± 3	4.0 ± 0.1	808 ± 3	12 ± 3.9	2.0
45 min	379 ± 3	3.7 ± 0.2	804 ± 4	9.9 ± 1.4	1.8
60 min	388 ± 14	3.3 ± 0.9	808 ± 2	7.7 ± 3.4	1.6
24 h	-	-	779 ± 4	5.5 ± 0.6	-

Table 7.2 Summary of electrochemical data for oxidation of (Au$_{4nm}$)Ag alloy NPs attached to Glass/ITO/APTES electrodes.

2:1 after 60 min of heating.

Figure 7.5 (A) and (B) represents the photographs of $(Ag_{8nm})Au$ 1:1 molar ratio colloidal solutions at different stages of the synthesis. The colors of the solutions were different from those obtained for the $(Au_{4nm})Ag$ synthesis. The initially yellow solution (the color of $HAuCl_4$ solution, not shown), became plum immediately after $AgNO_3$ addition. Continued heating changed the color from plum to pink (15 min), dark pink (30 min), pink-reddish (45 min), red (60 min), and yellow-brown (24 h). UV-vis spectra of the solutions are shown in Figure 7.5 (C). As in the case of $(Au_{4nm})Ag$ alloy NPs, only one LSPR peak was observed. The wavelength of the peak was shifted from 532 nm for 1 min heating time to 486 nm for 24 h heating time. Table 7.3 shows the summary of UV-vis data.

Note, that since the standard reduction potential of $AuCl_4^-/Au^0$ is higher than that of Ag^+/Ag^0, Ag NPs can undergo galvanic exchange with Au ions according to the following reaction[133]:

$$3\ Ag_{(s)} + AuCl_4^- \rightarrow Au_{(s)} + 3\ Ag^+_{(aq)} + 4\ Cl^- \qquad (Rxn\ 7.1)$$

The alloy composition and oxidation potentials were determined by LSV. Figure 7.6 shows LSVs of Glass/ITO/APTES/(Ag)Au NPs for different heating times and Table 7.4 represents the summary of the electrochemical data. While the coverage of Ag stays approximately constant for all heating times, the oxidation potential shifts positive with an increase in heating time (except for 24 h of heating). The shift to more positive potentials is due to the formation of the $(Ag_{8nm})Au$ alloy and possibility that Au is forming an outer shell, which prevents Ag from oxidation. The amount of Au on the
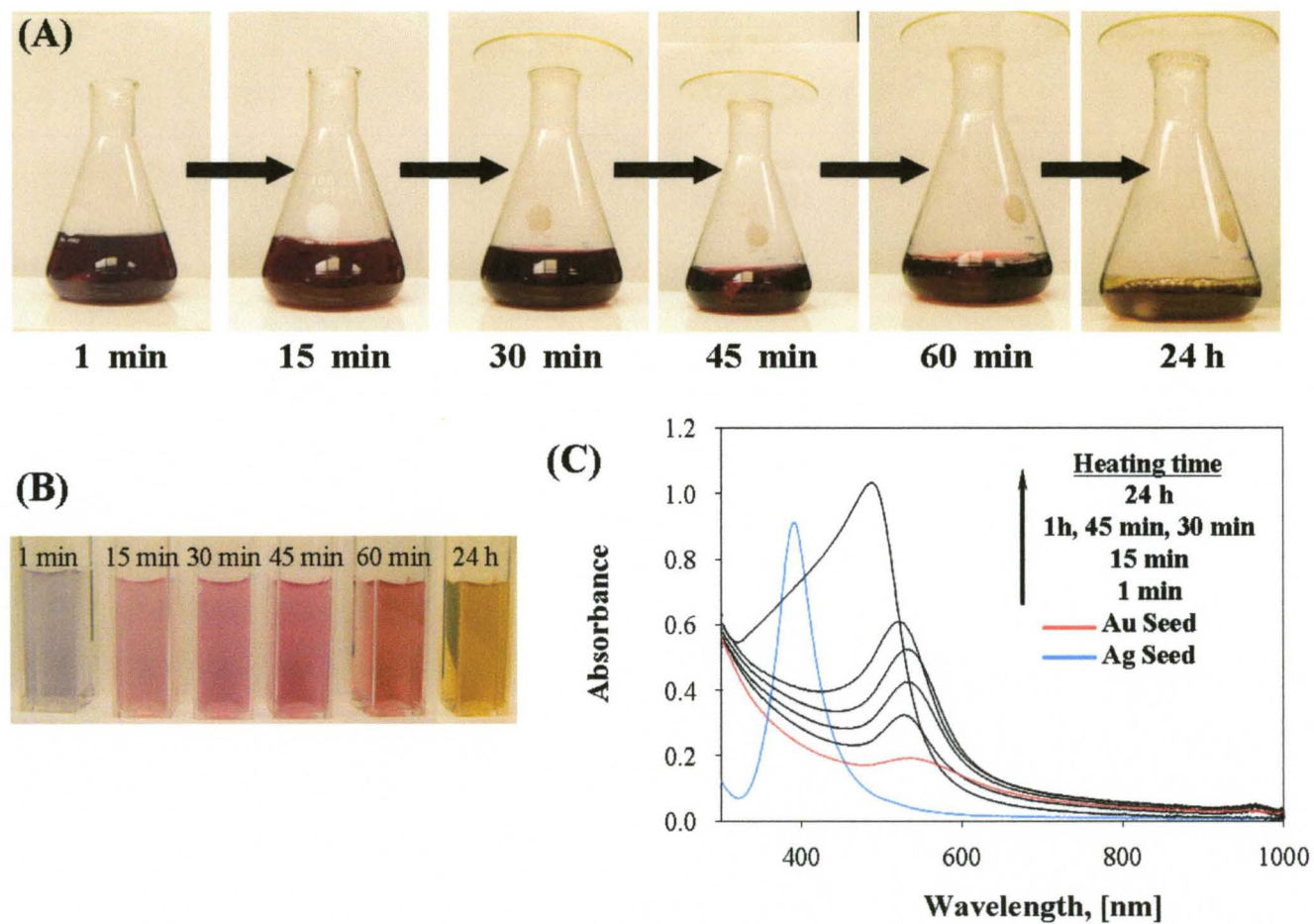
Figure 7.5 (A) and (B) photographs of $(Ag_{8nm})Au$ NPs solutions at different heating times. (C) UV-vis spectra of $(Ag_{8nm})Au$ NPs solutions at different heating times, and Au Seed and Ag Seed NPs for comparison.

Heating time	λ_{max}
1 min	532
15 min	527
30 min	532
45 min	532
60 min	521
24 h	486
Ag Seed	390
Au Seed	515

Table 7.3 UV-vis data for (Ag_{8nm})Au NPs.
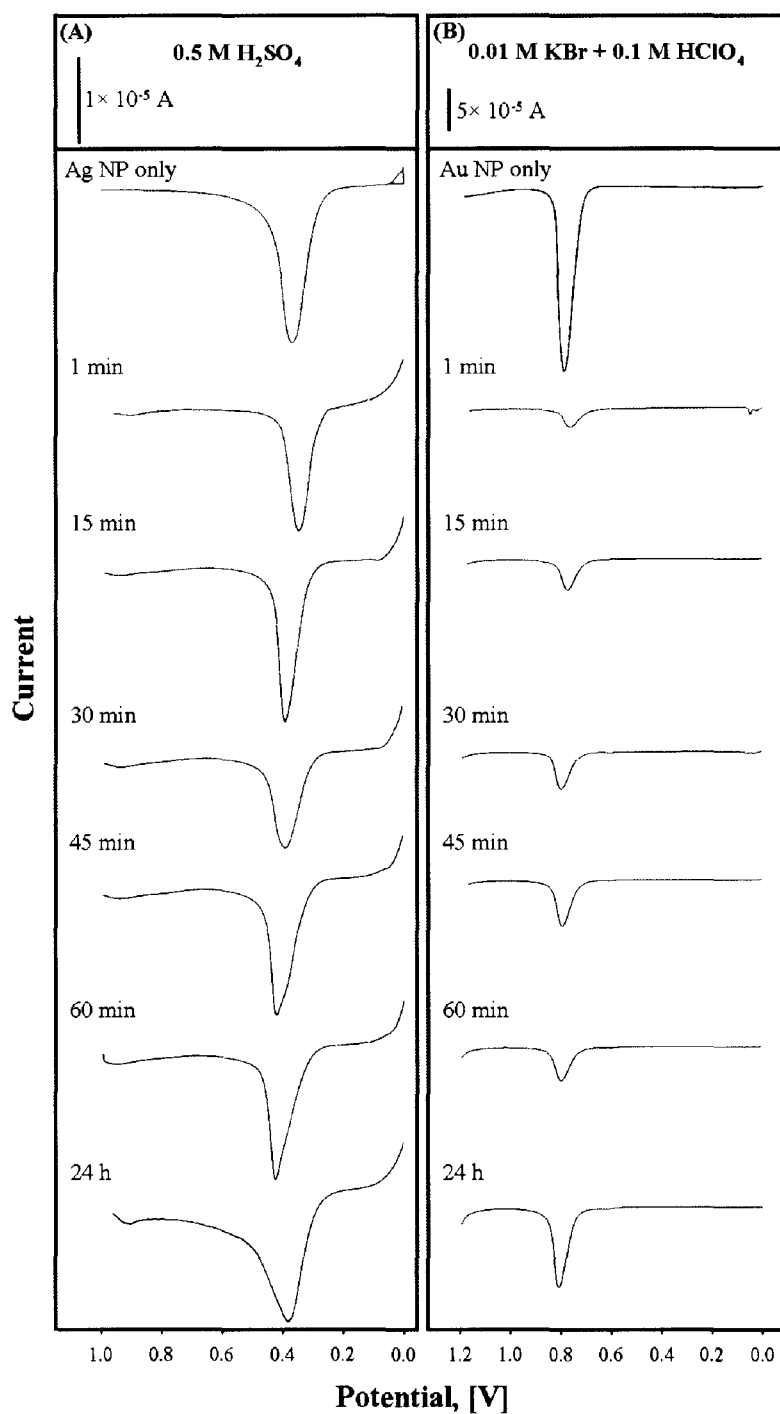
Figure 7.6 LSVs of Glass/ITO/APTES/(Ag)Au NPs performed in (A) 0.5 M

H₂SO₄ and (B) in 0.01 M KBr and 0.1 M HClO₄ for different heating times as indicated.

Scan rate 5 mV/s.

185

Heating time	E_p Ag, [mV]	A_p Ag, [×10⁻⁴ C]	E_p Au, [mV]	A_p Au, [×10⁻⁴ C]	Au:Ag ratio
1 min	378 ± 10	1.5 ± 0.2	802 ± 7	2.4 ± 0.2	1.0
15 min	399 ± 3	1.9 ± 0.4	801 ± 4	3.1 ± 0.6	1.1
30 min	401 ± 5	1.3 ± 0.2	803 ± 4	3.5 ± 0.7	1.8
45 min	429 ± 2	2.1 ± 0.3	807 ± 6	5.1 ± 1.2	1.6
60 min	430 ± 3	1.9 ± 0.3	797 ± 6	3.3 ± 1.1	1.2
24 h	406 ± 18	1.4 ± 0.9	813 ± 2	7.7 ± 1.1	3.6

Table 7.4 Summary of electrochemical data for oxidation of (Ag)Au alloy NPs attached to Glass/ITO/APTES electrodes.

186

sample increases with increase in heating time (except for 60 min of heating), indicating that more $AuCl_4^-$ was reduced on the Ag template with time. The Ag:Au ratio for 1 min heating time was 1:1 and reached 4:1 after heating the solution for 24.

We also performed the synthesis of $(Au_{4nm})Ag$ NPs as described previously, but after desired time, the solutions were quenched in an ice bath. It took about 3 min to cool it down. The ice bath should force the reaction to slow down and eventually stop, allowing us to study the composition of the alloy at earlier stages. The colloidal solution of $(Au_{4nm})Ag$ NPs was then divided in two parts. The first was analyzed immediately, and second part left to stir at room temperature overnight (~19 h). We studied synthesis times of 1.3, and 5 min. The reasoning behind these experiments is the drastic color change during the first few minutes of the synthesis, after addition of Au NPs Seed to the boiling Ag salt solution and change in the color of synthesized alloy with time at room temperature.

We studied synthesis times of 1, 3 and 5 min. Figure 7.7 (A) shows the UV-vis spectra of $(Au_{4nm})Ag$ colloidal solutions after 1 (red), 3 (blue) and 5 (green) min of heating time in comparison with the monometallic Au seed NPs (black). The LSPR band increased in intensity and shifted to more negative wavelengths with an increase in the heating time, which is consistent with the described above results for $(Au_{4nm})Ag$ NPs. The peak absorption wavelength shifted from 510 nm for Au Seed NPs to 508, 503, and 498 nm for 1, 3 and 5 min of heating time respectively. The LSVs of Glass/ITO/APTES/$(Au_{4nm})Ag$ NPs are shown in Figure 7.7 (B). As expected, with an increase in heating time, the Ag oxidation peak increased, indicating that more Ag was reduced onto the Au NPs during the synthesis. The Au oxidation peak remained the same
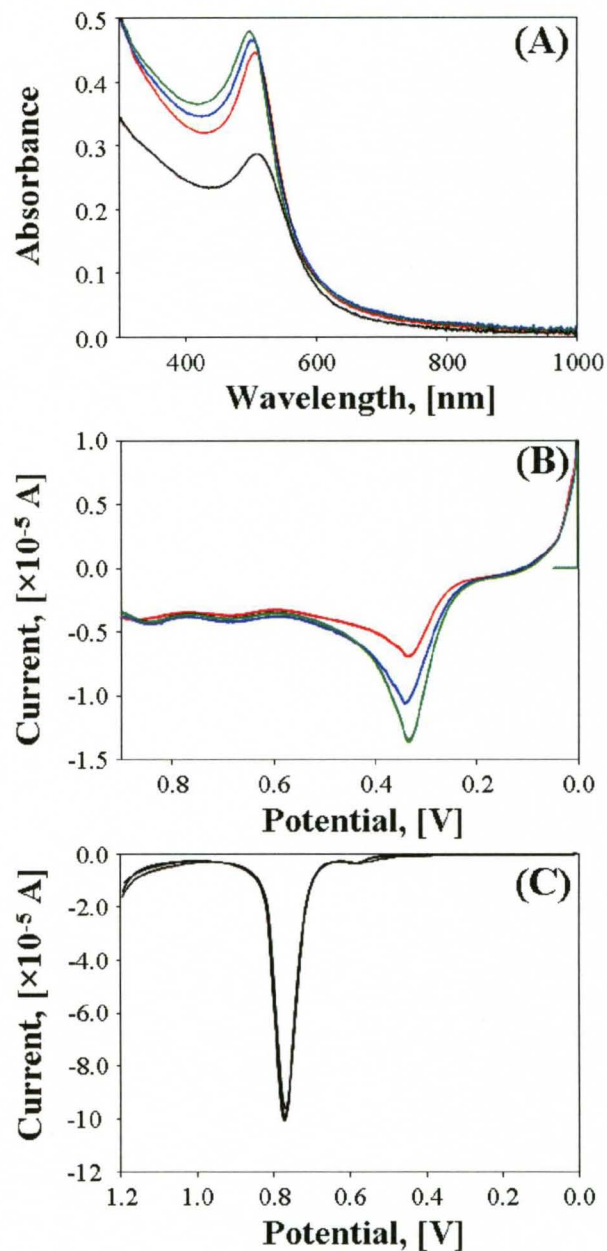
Figure 7.7 (A) UV-vis of (Au)Ag colloidal solution taken after 1 (red), 3 (blue), and 5 (green) minutes of heating time, compared to Au Seed NPs (black). LSVs of Glass/ITO/APTES/(Au)Ag NPs in (B) 0.5 M H_2SO_4 and (C) 0.01 M KBr and 0.1 M $HClO_4$, 1 (red), 3 (blue), and 5 (green) minutes of heating time. Scan rate 5 mV/s.

regardless of the heating time (Figure 7.7 (C)). Summary of the electrochemical oxidation experiments are in Table 7.5. According to electrochemical data, the Au:Ag ratio was 6:1, 4:1 and 3:1 for 1, 3 and 5 min of heating time respectively.

UV-vis spectra and electrochemical data of $(Au_{4nm})Ag$ NP solutions that were left to stir overnight at room temperature showed that the reduction of Ag occurs without heat being applied. Despite the length of heating time before putting the sample in the ice bath, all three alloys (1, 3 and 5 min), demonstrated identical LSPR spectra after 19 h stirring at room temperature (Figure 7.8 (A)). The electrochemical analysis is in good agreement with the UV-vis data. Figure 7.8 (B) shows LSVs of Glass/ITO/APTES/$(Au_{4nm})Ag$ NPs after stirring for 19 h and Table 7.4 summarizes the LSV data. From the LSV experiments we can observe that the amount of Ag and Au is highly reproducible for all samples. Interestingly, the conversion of the coverage from Coulombs into moles, showed that we have a little bit more silver on the surface than Au. The Ag:Au ratios were 1.5:1, 1.4:1 and 1.8:1 for 1, 3 and 5 min of heating respectfully. The reason is not understood at this point since we should have a 1:1 Ag:Au ratio if the reaction went to completion.

Heating time	E_p Ag, [mV]	A_p Ag, [$\times 10^{-4}$ C]	E_p Au, [mV]	A_p Au, [$\times 10^{-3}$ C]	Au:Ag ratio
1	321 ± 11	1.5 ± 0.2	770 ± 1	1.3 ± 0.1	5.8
3	337 ± 5	2.2 ± 0.2	772 ± 7	1.3 ± 0.2	3.9
5	333 ± 1	2.9 ± 0.1	774 ± 3	1.4 ± 0.1	3.2

190

Table 7.5 Summary of electrochemical data for oxidation of (Au)Ag NPs synthesized by heating the solution for 1, 3 and 5 min and placing it into the ice bath.
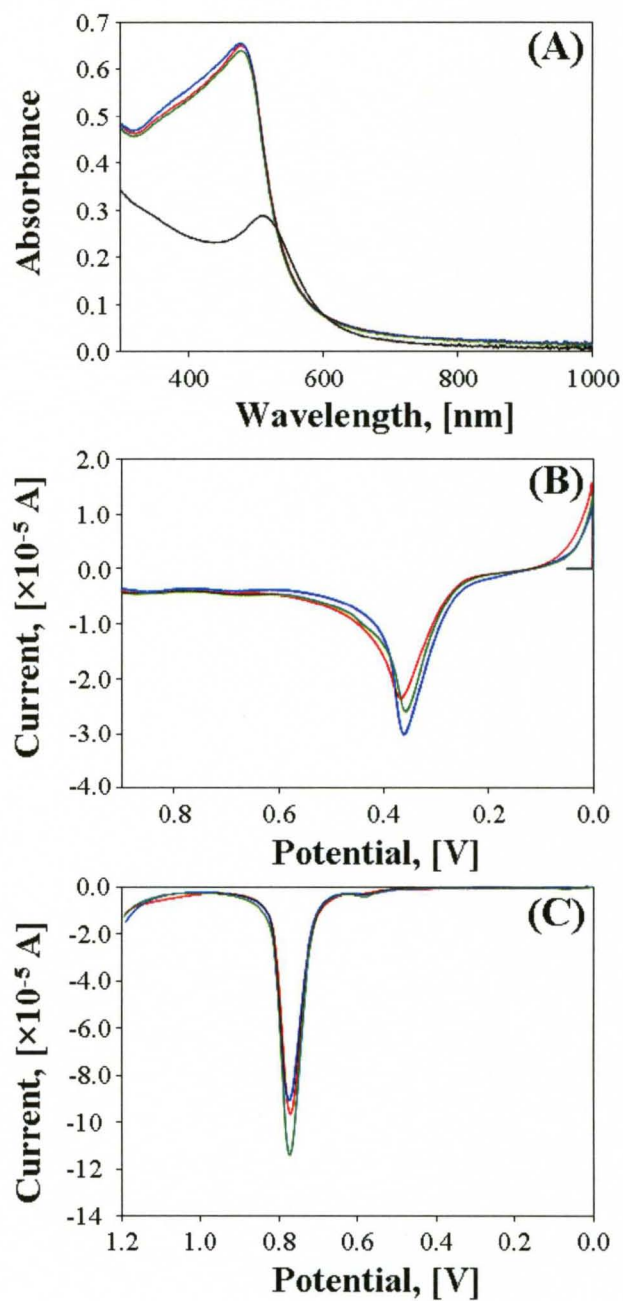
Figure 7.8 (A) UV-vis of (Au)Ag colloidal solution taken after 1 (red), 3 (blue),

and 5 (green) minutes of heating time and stirring for 19 h, compared to Au Seed NPs

(black). LSVs of Glass/ITO/APTES/(Au)Ag NPs in (B) 0.5 M H_2SO_4 and (C) 0.01 M

KBr and 0.1 M $HClO_4$, 1 (red), 3 (blue), and 5 (green) minutes of heating time. Scan rate

5 mV/s.

191

Heating time	E_p Ag, [mV]	A_p Ag, [$\times 10^{-4}$ C]	E_p Au, [mV]	A_p Au, [$\times 10^{-3}$ C]	Au:Ag ratio
1	341 ± 26	5.4 ± 0.3	766 ± 4	1.2 ± 0.1	1.5
3	357 ± 6	5.8 ± 0.1	769 ± 3	1.2 ± 0.1	1.4
5	354 ± 8	4.7 ± 0.9	773 ± 3	1.3 ± 0.1	1.8

Table 7.6 Summary of electrochemical data for oxidation of (Au)Ag NPs synthesized by heating the solution for 1, 3 and 5 min, placing it into the ice bath and stirring for 19 h at room temperature.

7.4 CONCLUSIONS

The optical properties and composition of bimetallic Au-Ag NPs was studied at different stages of the synthesis procedure. Alloy NPs were synthesized by seed-mediated growth at high temperatures and samples were analyzed after desired periods of heating time with UV-vis spectroscopy and LSV. The solution molar ratio of 1:1 (Au:Ag) was studied. Both (Au$_{4nm}$)Ag and (Ag$_{8nm}$)Au NPs are alloy nanoparticles according to the UV-vis data. The electrochemical composition analysis was used to determine the Au:Ag ratio and atomic arrangement at different stages of the synthesis. In the case of (Au$_{4nm}$)Ag, heating solution for 24 h led to disappearance of Ag oxidation peak, which indicates that heating for 24 h stabilizes Ag, probably by diffusion of Ag atoms into the Au NP lattice. In the case when alloys were heated from 1 to 5 min and then quenched in an ice bath, Ag oxidation was observed for all three times, which indicated that Ag reduced on the surface of the Au and remains there even after 19 h of vigorous stirring. LSV results for the heating of the (Ag$_{8nm}$)Au NPs showed the presence of Ag oxidation peak even after 24 h. These results shows that LSV can be used to determine composition of the alloy NPs and atomic arrangement.

CHAPTER VIII

ELECTROCHEMICAL CHARACTERIZATION OF GOLD AND SILVER NANOPARTICLES ELECTROSTATICALLY ATTACHED TO THE POLYMER FILMS USING LAYER-BY-LAYER PROCEDURE

This Chapter describes the electrooxidation of the metal nanoparticle (NP)/polymer films constructed using layer-by-layer (LBL) assembly technique. LBL-assembled Au and Ag NP multilayer films were studied by UV-vis spectroscopy, scanning electron microscopy (SEM) and linear sweep voltammetry (LSV). SEM images show that the nature of the metal NP influences the morphology of the films. Ag NPs tend to aggregate and form large clusters during assembly, while films of Au NPs, are more continuous and porous. For films metal NP/polymer films charge increased with increase in the number of layers, suggesting that all of the metal is electroactive. For films with non-conductive spacers (PSS/PDDA), charge for Ag and Au oxidation decreased with increase in the number of polymer bilayers. After deposition of 1, 3 or 5 polymer bilayers, percent of Ag oxidized changes from 15 to 1.5, to 0.8, respectively. In the case of Au, percent of Au oxidized drops from 24 to 5, to 0 for 1, 3 and 5 polymer bilayers, respectively.

194

8.1 INTRODUCTION

Assembled films of metal nanostructures are useful in electrochemical sensing devices for several reasons.[15] Multilayers of conductive NPs give rise to porous, high surface area electrodes, where the metal nanoparticles can be assembled through cross-linking elements via specific and selective interactions with electrode surfaces.[145,146] Mono- or multilayer arrays of conductive NPs assembled on electrode surfaces may be considered as assemblies of nanoelectrodes of controllable active areas.[16] One of the most common ways to fabricate nanostructured multilayer films is through layer-by-layer (LBL) electrostatic attachment. There are several reports on the morphology, optical and electrochemical properties of metal nanoparticle – polymer LBL films.[101,147] The assembly is usually electrostatic in nature, involving negatively-charged metal nanoparticles and positively-charged polymers. Srinivasan et. al. reported the formation of multilayer Au NP films using poly(allylamine hydrochloride) and showed that with an increase in the number of assembled layers, the particles tend to agglomerate and form large aggregates.[147] Chirea et. al. fabricated polyelectrolyte/Au NP multilayer films using poly(L-lysine) and characterized the films electrochemically using $[Fe(CN)_6]^{3-/4-}$ and $[Ru(NH_3)_6]^{3+/2+}$.[100] It was shown that the permeability of these ions depends strongly on the charge of the last layer deposited and on the charge of the Au NPs. Crespilho et. al. studied charge transport and the incorporation of redox mediators in LBL films containing dendrimer-encapsulated Au NPs[101] and considered electron hopping as a charge transport mechanism between the Au NPs and polymers in the LBL film.

195

Here we describe the electrochemical characterization of multilayer films constructed from Au and Ag NPs using positively and negatively charged polymers as building blocks. The metal NPs films were characterized by LSV. The goal of this research was to study the charge transport through multilayers composed of polyelectrolytes and NPs, and through polyelectrolyte layers to metal NPs. The electron transfer through polymer films is not studied well. There is no information about oxidation of metal nanoparticles through the film. Others have studied the electron transport to redox molecules, such as ferrocene, but not for metal NP oxidation. It is important to study electrochemistry of such systems to control permeability of multilayers, for applications such as stripping analysis voltametry for chemical and biosensors, and catalysis.

8.2 EXPERIMENTAL SECTION

Fabrication of metal NP/polymer multilayer films. The LBL procedure is described in detail in Chapter II. Shortly, the Glass/ITO electrodes were cleaned and dried under N_2. Then, the electrodes were functionalized with aminopropyltriethoxy silane (APTES), which provides positively charged $-NH_3^+$ groups on the surface. Negatively-charged, citrate-stabilized Au (3-5 nm diameter) or Ag (8-12 nm diameter) NPs were then attached to the Glass/ITO/APTES by soaking in the NP solution for a desired period of time (20 min to 1 h). This is the 1st layer. In order to construct multilayer films, the Glass/ITO/APTES/Metal (Me) NP electrode was immersed into a positively-charged polymer solution (Poly(diallyldimethylammonium chloride - PDDA) for 20 min, then to the solution of Me NPs again and so on, until a desired number of bilayers (MeNP/PDDA) are deposited. Multilayer polymer films were constructed using the same strategy, but instead of using metal NPs, negatively-charged polymer (Poly(styrenesulfonate) - PSS) was used.

Characterization. Metal NP/polymer films were characterized by UV-vis spectroscopy, SEM and LSV. Details of these techniques are provided in Chapter II.

8.3 RESULTS AND DISCUSSION

Figure 8.1 (A) shows UV-vis absorption spectra of Glass/ITO/(APTES/Ag)/(PDDA/Ag)$_x$, where x = 0-9, and the number of Ag layers is x+1. There is single LSPR band at 399 nm for 1 layer (x = 0) and the peak shifts positive with an increase in the number of layers (Figure 8.1 (B) inset), most likely due to the aggregation of nanoparticles and formation of bigger structures. The intensity of the LSPR peak increases linearly with an increase in the number of layers (Figure 8.1 (B)). This shows a similar amount of Ag deposited in each layer. These multilayer films were characterized electrochemically by obtaining a LSV in 0.5 M H_2SO_4. In this solution, the Ag oxidizes from Ag^0 to Ag^+. Figure 8.1 (C) represents typical LSVs of Glass/ITO/(APTES/Ag)/(PDDA/Ag)$_x$ multilayer films. With an increase in the number of layers, the coverage increases linearly and the peak potential shifts to more positive values (Figure 8.1 (D)). The increase in current with increasing layers shows that Ag NPs are electroactive. The positive shift in potential is due to an increase in the coverage of Ag NPs on the electrode surface and due to the aggregation of the particles and formation of big agglomerates.

Figure 8.2 shows UV-vis absorption spectra and LSVs for Glass/ITO/(APTES/Au)/(PDDA/Au)$_x$ multilayer electrodes. Similar to the case of Ag, the LSPR intensity increased linearly with an increase in the number of layers. The wavelength of the LSPR peak shifted drastically from 520 nm to 560 nm for 1 and 3 layers, respectfully. With a further increase in the number of layers, the peak wavelength increased linearly up to 405 nm at 10 layers. LSVs recorded in 0.5 M H_2SO_4 showed
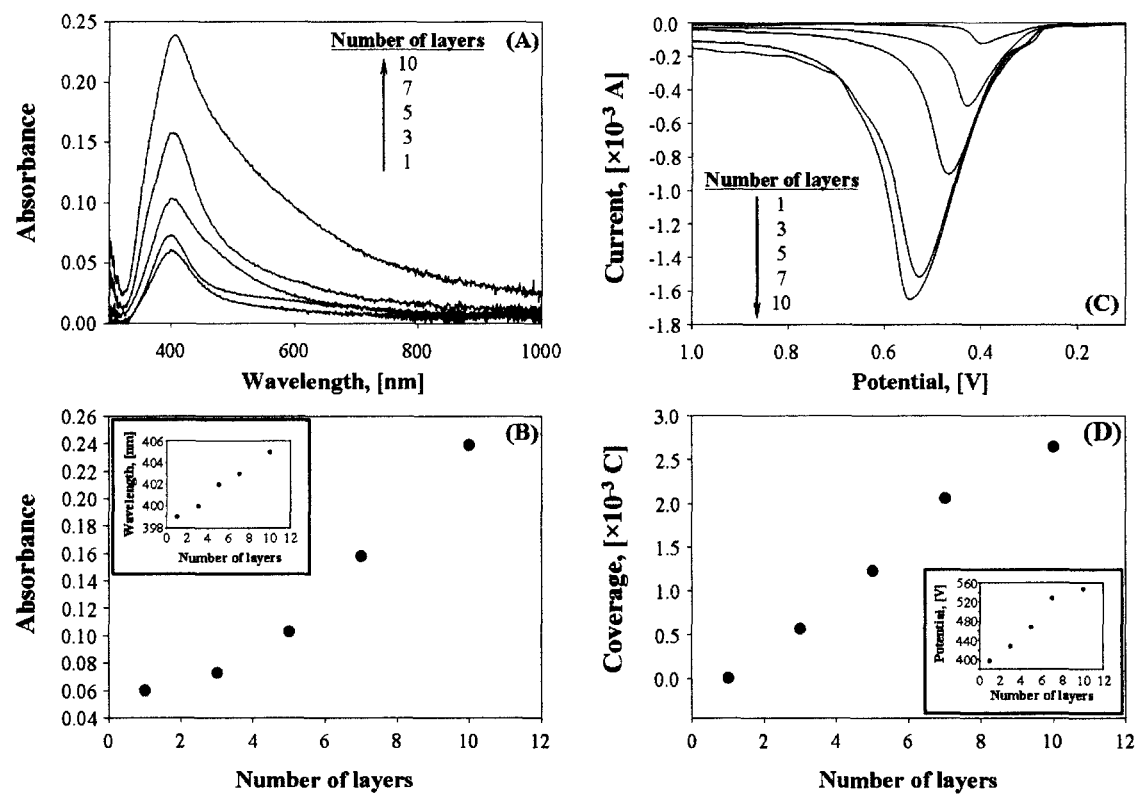
Figure 8.1 (A) UV-vis absorption spectra for Glass/ITO/(APTES/Ag)/(PDDA/Ag)$_x$ multilayer films, (B) plot of absorbance as a function of number of layers. Inset: plot of wavelength versus number of layers. (C) Corresponding LSVs, recorded in 0.5 M H$_2$SO$_4$, scan rate 100 mV/s. (D) Plot of peak coverage versus number of layers. Inset: oxidation peak potential as a function of number of layers.
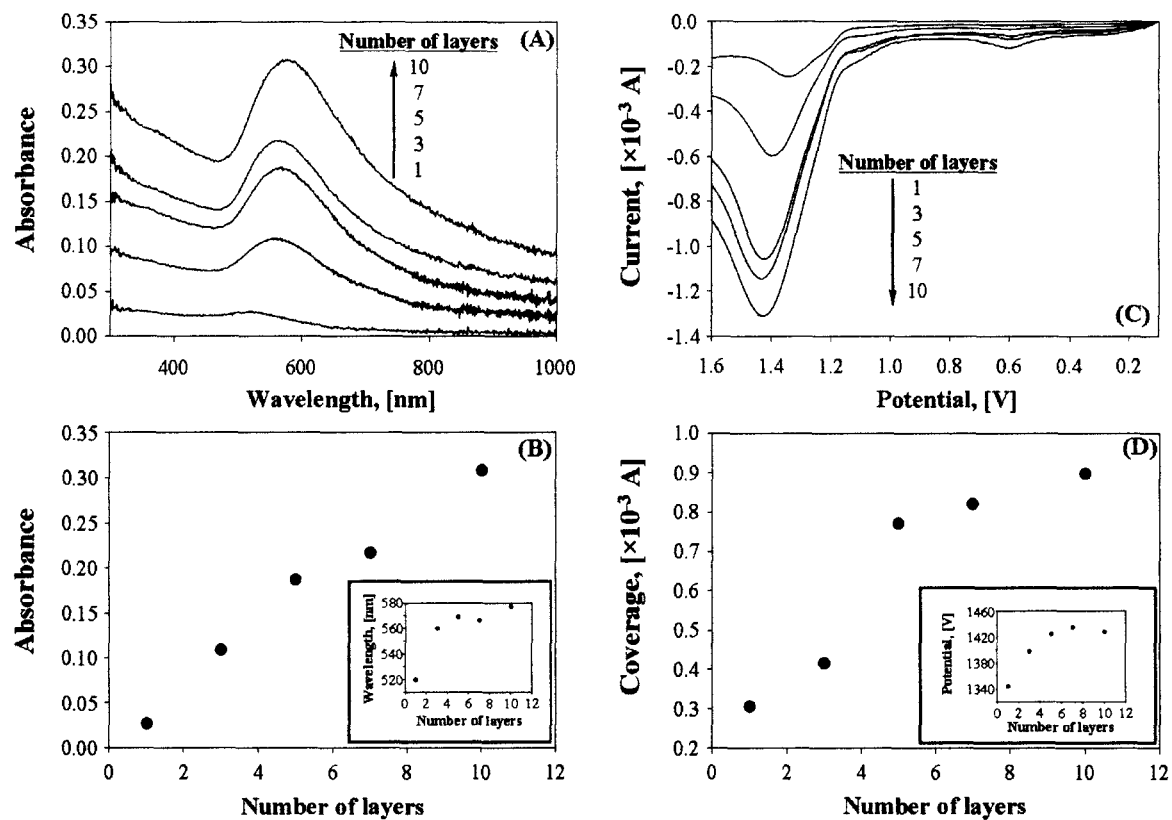
Figure 8.2 (A) UV-vis absorption spectra for Glass/ITO/(APTES/Au)/(PDDA/Au)ₓ multilayer films, (B) plot of

absorbance as a function of number of layers. Inset: plot of wavelength versus number of layers. (C) Corresponding LSVs, recorded in

0.5 M H₂SO₄, scan rate 100 mV/s. (D) Plot of peak coverage versus number of layers. Inset: oxidation peak potential as a function of

number of layers.

an increase in peak current with an increase in the number of layers. The peak at ~1300 mV in the LSV corresponds to Au oxide formation. The peak oxidation potential shifted positive with an increase in the number of layers and remained constant after 7 layers.

Multilayer in a non-uniform fashion Au and Ag metal NPs/polymer films were also characterized by Scanning Electron Microscopy (SEM). Figure 8.3 shows SEM images for Ag NPs (left column) and Au NPs (right column) deposited using the LBL method with PDDA for different numbers of layers as indicated. We observed a remarkable difference in the structure of the two films constructed from the different metals. In the case of Ag, an increase in the number of deposition layers led to the formation of large looking particles, which we attribute to the formation of aggregates of the ~8 nm Ag NPs attached to the film. In the case of Au NPs, the initial coverage (1st layer) is more dense and uniform compared to the film of Ag NPs, and with an increase in the number of layers, the Au formed a more continuous porous film. Figure 8.4 shows the proposed growth of these films.

Electron transfer to the Ag and Au NPs through the polymer films was studied next. We were interested in understanding electron transport through the polymer to the electrode during metal oxidation. Several aspects have to be understood to fully describe the process, including how long will electron transfer occur during metal oxidation and how the distance from electrode affects oxidation potential and current. These are important questions when using metal NPs in stripping analysis. The multilayer metal/polymer films contained negatively and positively charged polymers, PSS and PDDA, respectfully were fabricated. Note that PSS is not a conductive polymer. After the polymer film was constructed, a single layer of Au or Ag NPs was assembled on top

201
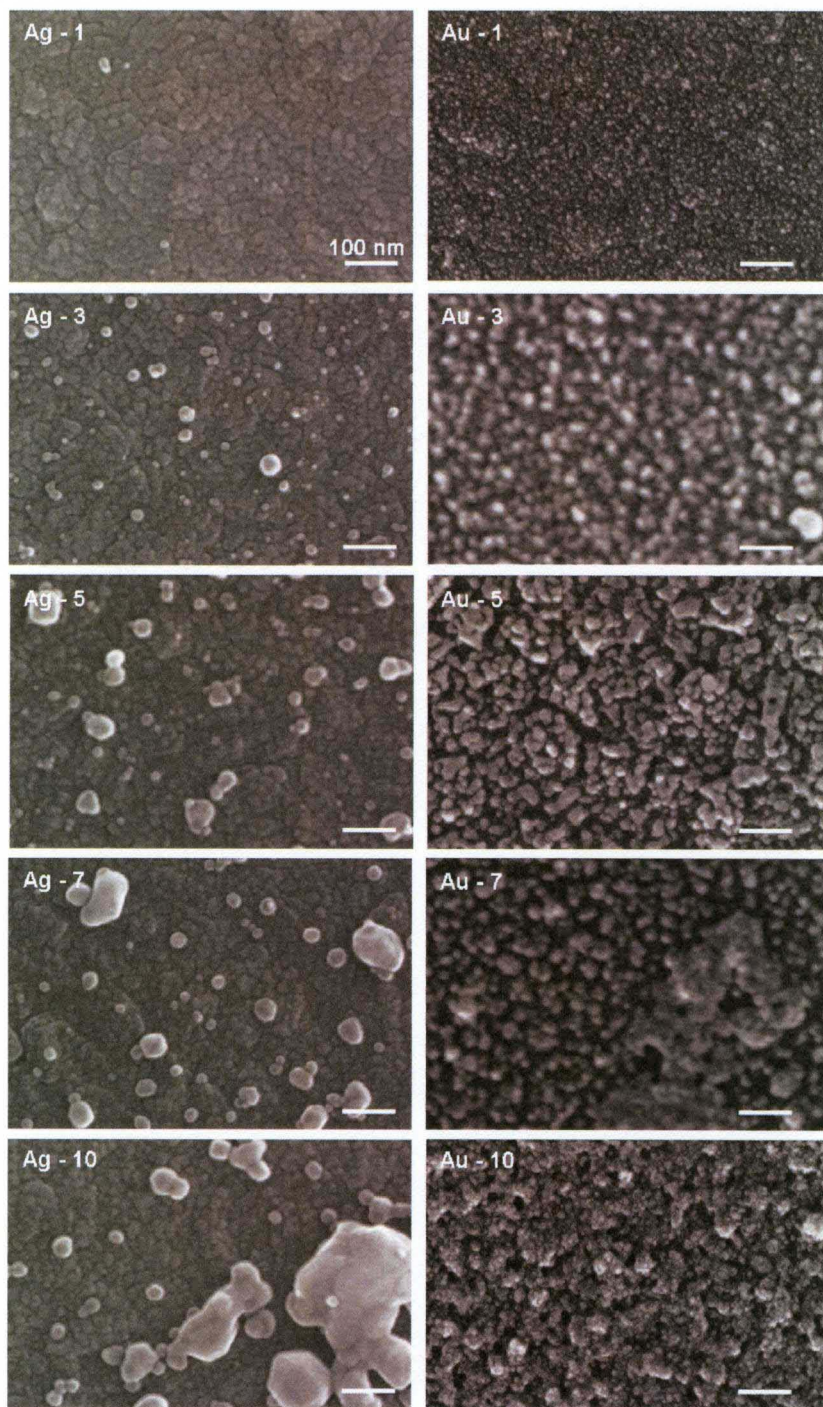
Figure 8.3 SEM images of Glass/ITO/APTES/(Ag or Au NP/PDDA)$_x$ fabricated with 1, 3, 5, 7, and 10 bilayers as indicated.

(A)
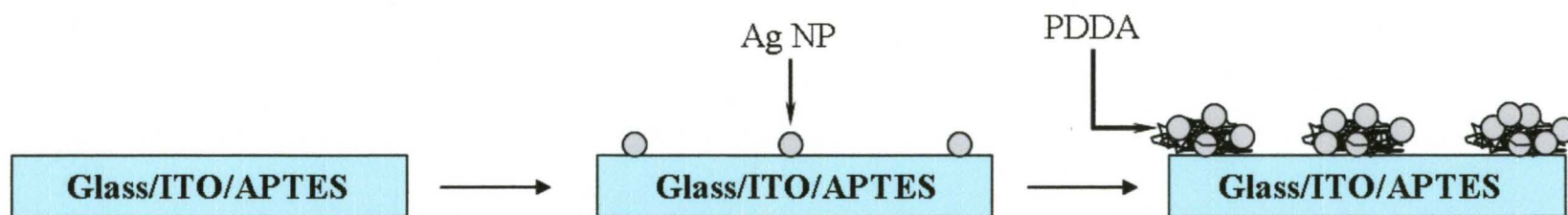
(B)
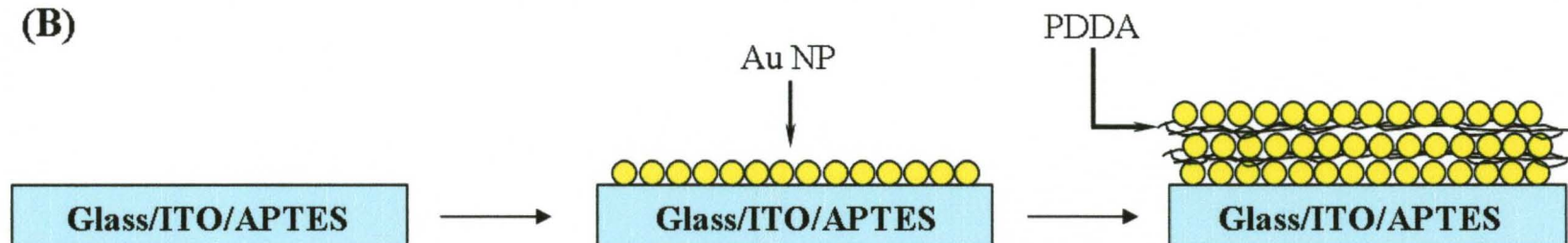
Figure 8.4 Proposed growth of Ag (A) and Au (B) multilayer films.

of the film. Number of (PSS/PDDA) bilayers varied from 1 to 5 as shown in Figure 8.5. Figure 8.6 (A) Shows UV-vis spectra of Glass/ITO/(PSS/PDDA)$_x$/Ag NPs. The LSPR band for Ag shifted to more positive with an increase in the number of polymer layers while the peak absorbance remained at the same level, showing approximately equal Ag in all cases. The LSVs (Figure 8.6 (B)) showed that one bilayer of polymer limits the electron transfer from electrode to the Ag NPs significantly. The peak area for 1 bilayer was ~7 times smaller than the original Ag peak for oxidation of Ag on APTES. With an increase in the number of polymer layers, the amount of Ag oxidized decreased further, but did not reach zero, even after 5 polymer bilayer were deposited (Figure 8.6 (C)). Values of percent Ag oxidized are shown in Figure 8.6 (D).

Similar experiments for Au NPs were obtained. Figure 8.7 shows the UV-vis and LSVs of Glass/ITO/(PSS/PDDA)$_x$/Au NPs. Interestingly, the optical properties of these films were significantly different from those obtained for Ag NPs. The Intensity of the LSPR peak increased with an increasing number of polymer layers. This is difficult to understand assuming the Au NPs can only attach to the outer PDDA layer. The results suggest that Au can intercalate into the polymer film to some degree. The LSVs showed that with an increase in the number of polymer layers, the amount of Au oxidized was ~4 times less after depositing 1 layer of PSS/PDDA, and completely inhibited after 5 layers of PSS/PDDA.

Ag$^+$, Au^{III}Br$_4^-$, Au^{I}Br$_2^-$

Me NP (Au or Ag)

n e$^-$

$\begin{bmatrix} \text{PSS} \\ \text{PDDA} \end{bmatrix}_x$

APTES

ITO
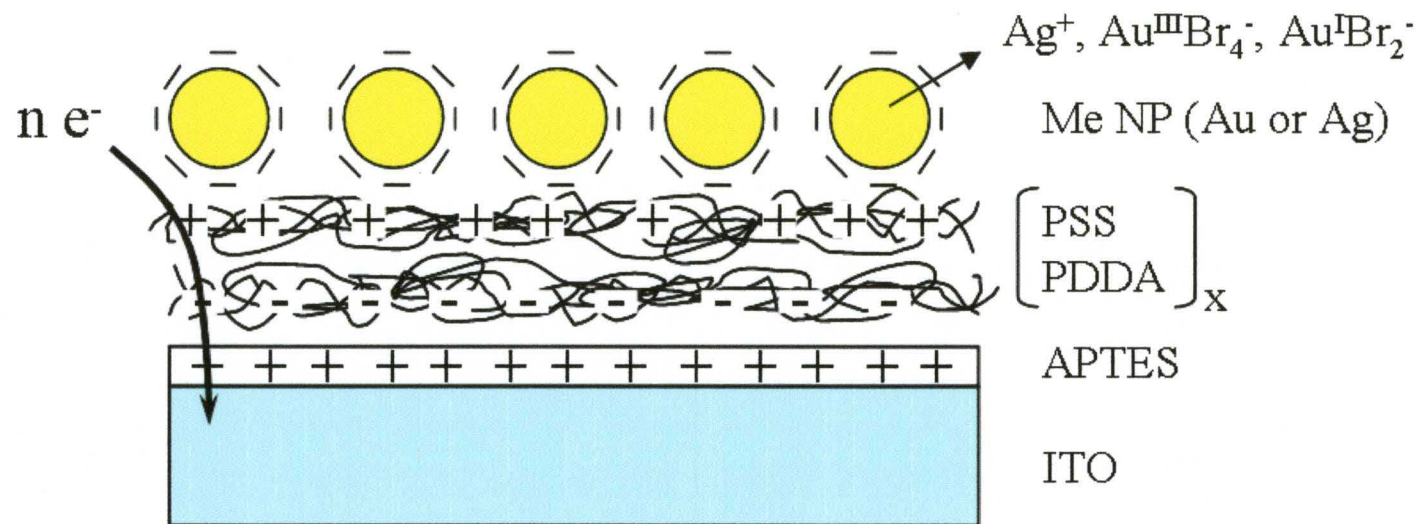
Figure 8.5 Electron transfer from metal NP to the electrode surface through polymer film.
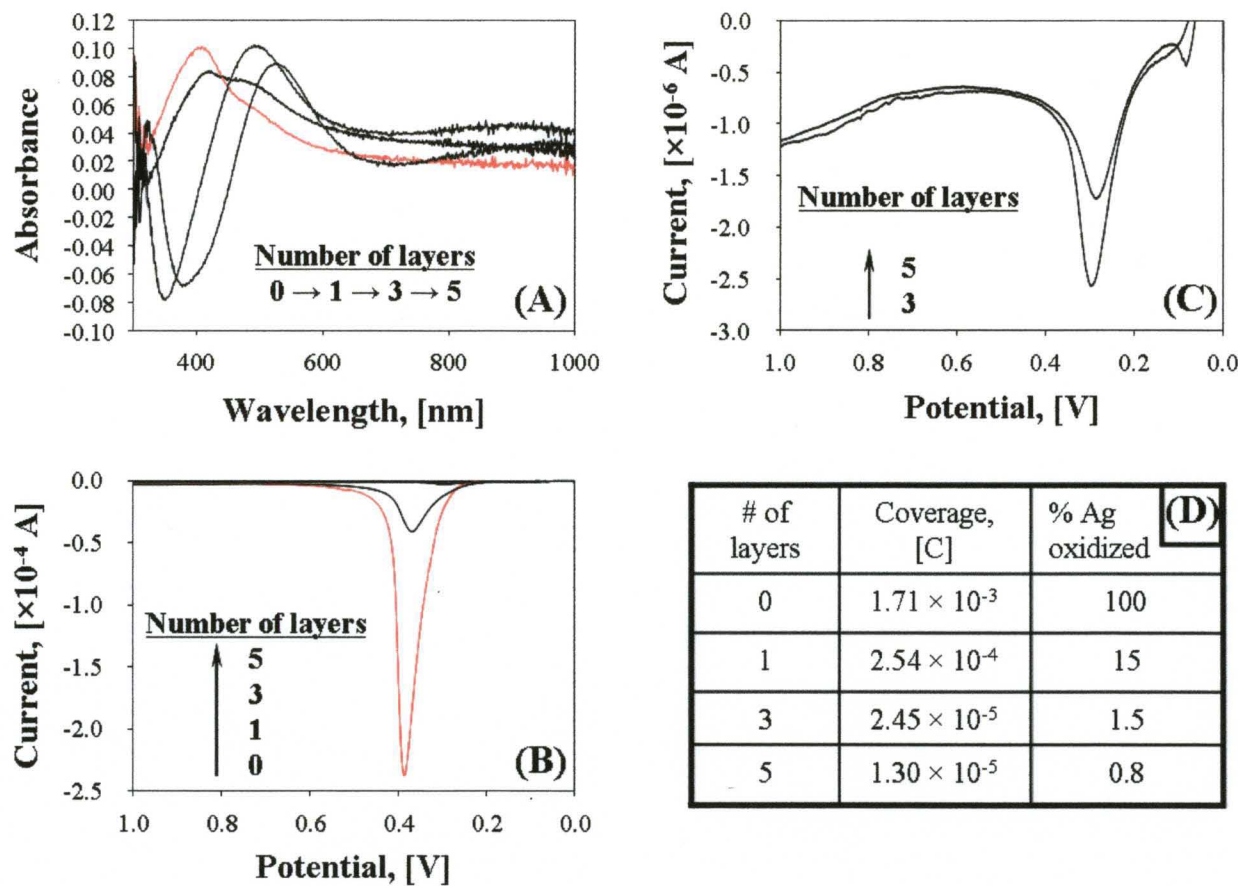
Figure 8.6 (A) UV-vis spectra of Glass/ITO/APTES/(PSS/PDDA)$_x$/Ag NPs for different number of polymer layers, as

indicted. (B) Corresponding LSVs obtained in 0.5 M H$_2$SO$_4$, scan rate 5 mV/s. (C) Zoom in on LSVs for 3 and 5 polymer layers. (D)

Summary of LSV results
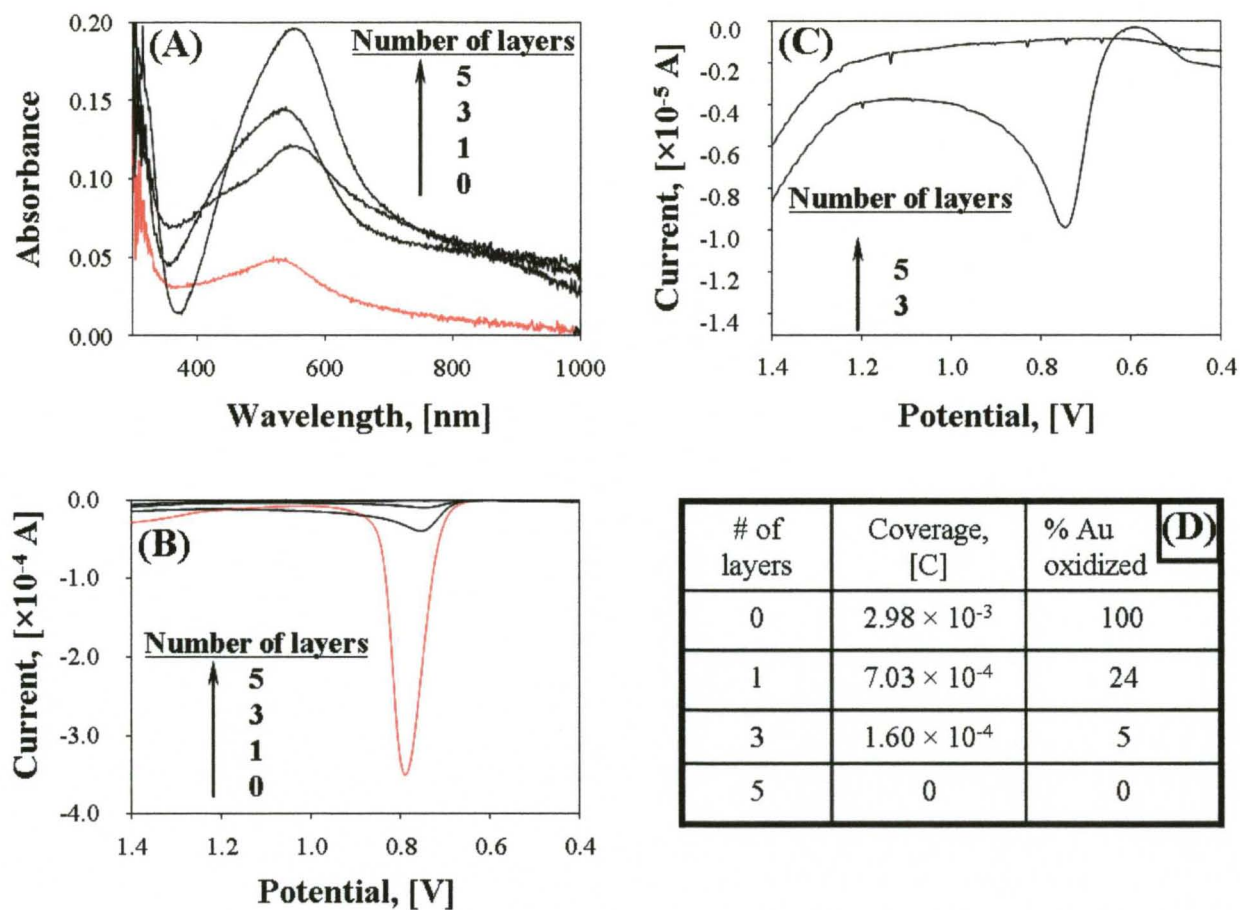
Figure 8.7 (A) UV-vis spectra of Glass/ITO/APTES/(PSS/PDDA)$_x$/Au NPs for different number of polymer layers, as indicted. (B) Corresponding LSVs obtained in 0.01 M KBr and 0.1 M HClO$_4$, scan rate 5 mV/s. (C) Zoom in on LSVs for 3 and 5 polymer layers. (D) Summary of LSV results.

8.4 CONCLUSIONS

Here we described the fabrication of metal NPs/polymer multilayer films by electrostatic attachment of Au and Ag NPs through positively-charged PDDA. These films were characterized by UV-vis spectroscopy, SEM and LSV. The LSPR peak increased with an increase in the number of Me NPs/PDDA layers due to an increase in the metal coverage on the electrode surface for both metals. The peak wavelength shifted to more positive values due to the aggregation of metal NPs. LSV analysis showed a similar behavior; an increase in the number of bilayers led to an increase in peak current, and positive shift in peak oxidation potential. This showed that most of the metal NPs in the film were in electronic communication with the electrode likely through electron hopping. SEM analysis showed that the morphology of the film is drastically different, depending on the metal deposited. While the experimental conditions were kept constant and only the nature of the metal NPs varied (and size varied), the final structures were extremely different. Films of Ag NPs consisted of large aggregated structures on the electrode surface while films of Au NPs were uniform and porous. Experiments on the electron transfer through the polymer film to the metal NPs demonstrated that it depends on the nature of the NPs as well. After deposition of 5 layers of polymer, we did not observe oxidation peak for gold (electron transfer fully blocked), while Ag oxidation peak was lower compared to 1 layer, but still observable. This occurred even though Au NPs appeared to intercolate into thicker multilayer polymer films. After deposition of 1, 3 or 5 polymer bilayers, percent of Ag oxidized

changes from 15 to 1.5, to 0.8, respectively. In the case of Au, percent of Au oxidized

drops from 24 to 5, to 0 for 1, 3 and 5 polymer bilayers, respectively.

This is a preliminary data and there are several unanswered questions regarding

the difference in morphologies of the films as well as the optical and electrochemical

properties.

CHAPTER IX

SUMMARY, CONCLUSIONS AND FUTURE DIRECTIONS

This dissertation focused on the stability of metal nanoparticles and nanostructures toward oxidation and the electrochemical characterization of metal NPs as a function of size and composition.

We demonstrated in Chapters III and IV the effect of size of metal NPs on their oxidation potential. Two different metal NPs were studied, Ag and Au. Ag NPs were synthesized by seed mediated growth, and their diameter varied from 8 to 50 nm. The oxidation of Ag NPs was performed by linear sweep voltammetry in sulfuric acid media. The main conclusions from the research on Ag NPs are:

- The oxidation potential for Ag shifts negative with a decrease in the average Ag NP diameter.

- The shift in oxidation potential is due to a size-dependent shift in the standard electrode potential for the Ag^+/Ag^0 redox couple.

- Constant potential experiments show the fast dissolution rates for small particles and slow dissolution rates for larger particles.

- This was the first direct measurement of size-dependent stripping of metal NPs by linear sweep voltametry.

- The shift in oxidation potential with size follows the general trend predicted by theory.

Au NPs of different size were electrochemically deposited directly onto a Glass/ITO electrode surface. The stability toward oxidation of these particles was studied by linear sweep voltammetry in bromide containing electrolyte. The main conclusions from the project on Au NPs are:

- Au NPs with different size (from 8 to 250 nm diameter) can be synthesized electrochemically by reduction of an Au salt at varied deposition potentials, but there is a constant coverage in terms of total Au atoms.

- The shift in oxidation potential with size (from 4 to 250 nm diameter) followed the theoretical predictions of Plieth much better compared to Ag NPs.

- On the basis of the charge during Au deposition versus the charge during oxidation, the oxidation process appears to be a mixture of 1 and 3 e^- processes.

- The oxidation of Au NPs of two different sizes deposited on the same electrode surface showed two well resolved oxidation peaks that correlated to the two sizes.

Cu UPD was carried out on Au NPs of different size as discussed in Chapter V. The work on copper UPD on Au NPs led to the following conclusions:

- It is possible to deposit a UPD layer of Cu on Au NPs with different size.

- During Cu deposition at UPD potentials, Cu underwent bulk-alloying with Au.

- The composition of the alloy depends on the deposition time.

- LSVs show several oxidation peaks for Cu, corresponding to different Cu-Au alloy formations.

- Alloying of Cu with Au occurs to a lesser extent on larger particles.

- This is the first example of AuCu alloying at UPD potentials.

Electrochemical characterization of Au/Ag core-shell structures was also performed. Au/Ag core-shell nanostructures were synthesized by seed-mediated growth procedure directly on the electrode surface. These structures were then characterized by UV-vis spectroscopy and LSV. The conclusions of this work are:

- Dealloying of Au from the Au/Ag alloy structures is possible by cyclic voltammetry in bromide containing electrolyte.

- While Au gets dissolved, Ag remains on the electrode surface.

- The morphology of the structures remaining after electrochemical cycling in bromide is different from the morphology of the original Au/Ag core-shell nanostructures. Interesting hollow Ag bulb structures form on the surface.

- Pure Ag nanostructures also undergo the bulb formation during cycling in bromide media.

- This is the first description of dealloying Au from Ag and formation of hollow Ag nanostructures by electrochemical cycling in bromide.

Au/Ag alloy NPs were synthesized by a high temperature seed-mediated growth method. Two different synthesis routs were applied: Au seed–Ag salt and Ag seed–Au salt. In both cases, the molar ratio of 1:1 (Au:Ag) was studied. UV-vis and electrochemical measurements obtained at different stages of synthesis and different heating times led to the following conclusions:

- Both synthesis methods led to the formation of alloy (not core-shell) NPs according to UV-vis data.

- The composition and atomic arrangement of the alloy strongly depends on the heating time.

- LSV can be used to determine atomic arrangements in alloy NPs.

Multilayer metal NP/polymer films were fabricated and analyzed electrochemically. The conclusions of this project are:

- With an increase in the number of metal/polymer layers, the intensity of the peak (by UV-vis) increased while the wavelength was red–shifted for both Au and Ag NPs.

- The charge passed during oxidation of metal NPs, determined by LSV, increased with an increase in the number of layers showing that the NPs are in electronic communication with the electrode.

- The morphology of the films depended on the metal used during assembly.

- Polymer films (PSS/PDDA) assembled before the metal NPs limit or block electron transfer from the electrode to the metal NPs during metal oxidation. 5 layers completely inhibit Au oxidation, while some Ag still oxidized at 5 layers.

FUTURE DIRECTIONS

Future projects could include a study of the electrochemical oxidation of metal nanoparticles with sizes below 4 nm. In that size regime the shift in the oxidation peak potential should be more dramatic compared to the bigger sizes, according to Plieth (see Figure 1.1 Chapter I). There are methods to synthesize smaller clusters of Au NPs as small as Au_{25}, which is composed of 25 Au atoms and has size below 1.0 nm diameter. The experimental procedure would be similar to our project on Au NPs but with smaller clusters. These experiments would require removal of the passivating thiol layer.

Based on the results from Chapter VI, I would like to continue work on the shape evolution of metal nanostructures during electrochemical cycling. I would synthesize different shaped Au nanostructures using different methods, then deposit them on an ITO electrode surface, and test their shape evolution during electrochemical oxidation. After synthesis and deposition of various shaped Au nanostructures, I would perform electrochemical experiments using cyclic voltammetry and observe the topographic images on the substrate before and after the oxidation/reduction reaction occurred. I would expect that the method of synthesis, the deposition procedure, the nature of the electrolyte, and the number of electrochemical cycles would affect the shape evolution of the Au nanostructures. I would perform experiments on the substrates prepared by different methods and then electrochemically cycle them in different electrolyte solutions for different numbers of cycles. I would expect that the shape change would be more significant with an increase in the number of electrochemical cycles. I would monitor the shape evolution of the Au nanostructures in-situ using EC-AFM (Electrochemical Atomic

Force Microscopy). First of all, I would obtain a topographic image of the electrode surface modified with gold nanostructures using tapping mode AFM. Then I would perform cyclic voltammetry using the AFM fluid cell which provides flow capability and allows insertion of the reference and counter electrodes. Samples would be the working electrode. An advantage of this set-up is that I can image exactly the same area of the electrode surface before, during, and after the electrochemical reaction. From these experiments, I would learn about the shape evolution of the gold nanostructures as a function of the number of cycles. Also, I would study the effect of electrolyte solution and the effect of different methods of synthesis and deposition on the shape evolution of gold nanostructures. This study would provide important information on stability of the nanoparticles towards electrochemical oxidation.

Au NPs have been found to be useful for the catalysis of NO oxidation and reduction.[148] Nitric oxide is a free radical signal molecule involved in many physiological functions and pathological changes in the nervous system, immune system, epithelial system, smooth muscles, and other tissues. The ability to measure NO in real time will advance the understanding of physiological and pathological processes. Due to the importance of NO in biology, there is an increasing interest in the development of methods for detecting this compound. Typical NO detection methods,[149] including chemiluminescence and colorimetry, provide indirect NO detection and cannot be used *in vitro* for localized, real-time sensing. Electrochemical detection may allow the direct measurement of NO concentration and is inexpensive, sensitive, and relatively non destructive to biological surroundings.

To accomplish this, I would synthesize different shapes of gold nanoparticles and then test them as catalysts. NO will be produced by adding $NaNO_2$ in acidic buffer solution according to the disproportionation reaction as reported by Yomathan et al.:[150]

$$3HONO \rightarrow H^+ + NO_3^- + 2NO + H_2O \qquad \text{(Rxn. 8.1)}$$
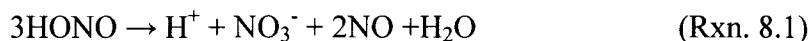
Cyclic voltammograms of gold nanostructures should not show any faradaic current in Na_2HPO_4–citric acid buffer solution (pH 2.2).[151] But after adding $NaNO_2$ into the buffer solution, an anodic peak at ~ +0.9V should appear indicating the oxidation of NO on the nanoparticles, which we can express by the following reaction:[152]

$$NO + H_2O \rightarrow HNO_2 + H^+ + e^- \qquad \text{(Rxn. 8.2)}$$
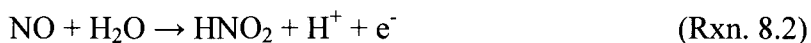
To prove the catalytic effect of gold nanoparticles, I would perform blank voltammetric measurements for $NaHPO_4$ – citric acid buffer solution (pH 2.2) containing $NaNO_2$ on bare ITO electrodes and cyclic voltammogramms of buffer solution at modified electrodes before adding $NaNO_2$. I would expect not to get any electrocatalytic response toward NO oxidation on bare ITO. To determine the dependence of catalytic activity of Au NPs on their shape, I would measure the catalytic current as a function of nanoparticle shape. Since the average size of each shape of gold nanoparticles should be different, I would have to normalize the catalytic current to the number of gold atoms/cm^2 on the surface and number of surface gold atoms on particles for a proper comparison. Using Au reduction peak, I would calculate the active surface area of the Au on the electrode surface and normalize the catalytic current as a function of shape.

Keeping in mind that the reactivity of nanoparticles depends on the amount of corners and edges,[37] I would expect to get the highest catalytic current for triangles, stars, and branched structures in comparison with spheres, cubes, and nanorods. To examine the stability of as-prepared electrodes I would measure the electrochemical response of the gold nanoparticles in Na_2HPO_4-citric acid buffer solution (pH 2.2) containing $NaNO_2$ by multiple cyclic voltammetric scans. If the response to NO does not show noticeable change after a number of successive cyclic voltammetric scans, it would indicate the stability of these electrodes.

I would also examine the effect of electrocatalysis on the shape and size of Au NPs during and after its catalytic function. I would use EC-AFM for in-situ examination of shape stability of gold nanostructures during and after the catalytic reaction. If, during the catalytic reaction, Au NPs change their shape due to dissolution of atoms from the corners and edges, I would expect deformation of the original shapes closer to a spherical shape. This drastic shape change would likely result in a reduction in the catalytic activity because the most active surface atoms which are located on the corners and edges would be dissolved. I would expect a higher rate of shape change for the particles that would have more active sites (edges and corners) such as branched structures, nanoflowers, nanostars.

The main requirement for this part of the research is to deposit uniform nanostructures on the electrode surface. If different shapes are present on the same sample, I would not be able to examine the catalytic activity as a function of shape since all shapes are present.

Also I would perform amperometric measurements to determine the detection limit for NO sensing on the nanoparticles of different shapes. Typical chronoamperometric experiments will be done in Na_2HPO_4-citric acid buffer solution on ITO modified with different shapes of gold nanoparticles during successive addition of $NaNO_2$. The catalytic current should increase with the addition of nitrite. According to these chronoamperometric measurements, the plots of the catalytic current versus the nitrite concentration would be drawn and the relationship between catalytic current and nitrite concentration would be found. This study would give information about the catalytic properties of gold nanoparticles of different shapes. I would determine catalytic activity as a function of shape, perform in-situ monitoring of the shape change during and after their catalytic function, and determine the detection limit for NO.

In addition, I would like to continue my study on Au-Ag alloy nanostructures by varying the molar ratio of metals and temperature to complete that project. For the multilayer metal NPs-polymer films, I would like to study in more detail the electron transfer from the electrode to NPs through the polymer film. To achieve that goal, I would have to learn elipsommetry techniques in order to determine the thickness of the polymer film. This would give information on how far from the electrode surface the electrons can travel in order to oxidize metal NPs, which could be different from electron transfer to a redox molecule like ferrocene.

These studies can be useful for the next step in nanoresearch – fabrication of nanodevices. In this case, these electrodes could be useful as sensors and provide fundamental information about catalytic systems.

REFERENCES

(1)   Jain, P. K.; Huang, X.; El-Sayed, I. H.; El-Sayed, M. A. *Acc. Chem. Res.* **2008**, *41*, 1578-1586.

(2)   Mulvaney, P. *Langmuir* **1996**, *12*, 788-800.

(3)   Chen, D. H.; Hsieh, C. H. *J. Chem. Mater.* **2002**, *12*, 2412.

(4)   Shemer, G.; Markovich, G. *J. Phys. Chem. B* **2002**, *106*, 9195.

(5)   Ristau, R.; Tiruvalam, R.; Clasen, P. L.; Gorskowski, E. P.; Harmer, M. P.; Kiely, C. J.; Hussain, I.; Brust, M. *Gold Bull.* **2009**, *42*, 133-143.

(6)   Ivanova, O. S.; Zamborini, F. P. *J. Am. Chem. Soc.* **2010**, *132*, 70-72.

(7)   Ivanova, O. S.; Zamborini, F. P. *Anal. Chem.* **2010**, *82*, 5844-5850.

(8)   Sardar, R.; Funston, A. M.; Mulvaney, P.; Murray, R. W. *Langmuir* **2009**, *25*, 13840-13851.

(9)   Grzelczak, M.; Perez-Juste, J.; Mulvaney., P.; Liz-Marzan, L. M. *Chem. Soc. Rev.* **2008**, *37*, 1783-1791.

(10)   Friedrich, K. A.; Henglein, F.; Stimming, U.; Unkauf, W. *Electrochimica Acta* **2000**, *45*, 3283.

(11)   Friedrich, K. A.; Henglein, F.; Stimming, U.; Unkauf, W. *Electrochimica Acta* **2001**, *47*, 689.

(12)   Park, S.; Tong, Y. Y.; Wieckowski, A.; Weaver, M. J. *Electrochem. Commun.* **2001**, *3*, 509.

(13)   Park, S.; Wasileski, S. A.; Weaver, M. J. *J. Phys. Chem. B* **2001**, *105*, 9719.

(14)   Spiro, M.; De Jesus, D. *Langmuir* **2000**, *16*, 2464-2468.

(15)   Hernandez-Santos, D.; Gonzalez-Garcia, M. B.; Garcia, A. C. *Electroanalysis* **2002**, *14*, 1225.

(16)   Cheng, W.; Dong, S.; Wang, E. *Anal. Chem.* **2002**, *74*, 3599.

(17)   Ibanez, F. J.; Growrishetty, U.; Crain, M. M.; Walsh, K. M.; Zamborini, F. P. *Anal. Chem.* **2006**, *78*, 753-761.

(18)   Ibanez, F. J.; Zamborini, F. P. *Langmuir* **2006**, *22*, 9789-9796.

(19)   Ibanez, F. J.; Zamborini, F. P. *J. Am. Chem. Soc.* **2008**, *130*, 622-633.

(20)   Storholf, J. J.; Elghanian, R.; Miucic, R. C.; Mirkin, C. A.; Letsinger, R. L. *J. Am. Chem. Soc* **1998**, *120*, 1959.

(21)   Taton, T. A.; Mirkin, A. A.; Letsinger, R. L. *Science* **2000**, *289*, 1757.

(22)   Zehbe, I.; Hacker, G. W.; Su, H. C.; Hauser-Kronberger, C.; Hainfeld, J. F.; Tubbs, R. *Am. J. Pathol.* **1997**, *150*, 1553.

(23)   Narayanan, R.; El-Sayed, M. A. *Langmuir* **2005**, *21*, 2027-2033.

(24)   Gopidas, K. R.; Whitesell, J. K.; Fox, M. A. *Nano Lett.* **2003**, *3*, 1757-1760.

(25) Kogan, V.; Aizenshtat, Z.; Popovitz-Biro, R.; Neumann, R. *Org. Lett.* **2002**, *4*, 3529-3532.

(26) Li, Y.; Boone, E.; El-Sayed, M. A. *Langmuir* **2002**, *18*, 4921-4925.

(27) Li, Y.; El-Sayed, M. A. *J. Phys. Chem. B* **2001**, *105*, 8938-8943.

(28) Li, Y.; Hong, X. M.; Collard, D. M. *Org. Lett.* **2000**, *2*, 2385-2388.

(29) Na, Y.; Park, S.; Hans, B.; Han, H.; Ko, S.; Chang, S. *J. Am. Chem. Soc.* **2004**, *126*.

(30) Narayanan, R.; El-Sayed, M. A. *J. Am. Chem. Soc.* **2003**, *125*, 8340-8347.

(31) Narayanan, R.; El-Sayed, M. A. *J. Phys. Chem. B* **2004**, *108*, 8572-8580.

(32) Narayanan, R.; El-Sayed, M. A. *J. Phys. Chem. B* **2004**, *108*, 5726-5733.

(33) Yeung, L. K.; Crooks, R. M. *Nano Lett.* **2001**, *1*, 14-17.

(34) Li, Y.; Petroski, J.; El-Sayed, M. A. *J. Phys. Chem. B* **2000**, *104*, 10956-10959.

(35) Narayanan, R.; El-Sayed, M. A. *J. Phys. Chem. B* **2003**, *107*, 12416-12424.

(36) Narayanan, R.; El-Sayed, M. A. *Nano Lett.* **2004**, *4*, 1343-1348.

(37) Narayanan, R.; El-Sayed, M. A. *J. Am. Chem. Soc.* **2004**, *126*, 7194-7195.

(38) Yoo, J.; Hathcock, D.; El-Sayed, M. A. *J. Phys. Chem. A* **2002**, *106*, 2049-2054.

(39) Claus, P.; Hotmeister, H. *J. Phys. Chem. B* **1999**, *103*, 2766-2775.

(40) Moore, J. T.; Corn, J. D.; Chu, D.; Jiang, R.; Boxall, D. L.; Kenik, E. A.; Lekehart, C. M. *Chem. Mater.* **2003**, *15*, 3320-3325.

(41) Anderson, M. L.; Stroud, R. M.; Rolison, D. R. *Nano Lett* **2002**, *2*, 235-240.

(42) Sidorov, S. N.; Volkov, V.; Davankov, V. A.; Tsyurupa, M. P.; Valetsky, P. M.; Bronstein, L. M.; Karlinsey, R.; Zwanziger, J. W.; Matveeva, V. G.; Sulman, E. M.; Lakina, N. V.; Wilder, E. A.; Spontak, R. J. *J. Am. Chem. Soc.* **2001**, *123*, 10502-10510.

(43) Liu, F.-K. *J. Chromatogr. A* **2009**, *1216*, 9034-9047.

(44) Eustis, S.; El-Sayed, M. A. *Chem. Soc. Rev.* **2006**, *35*, 209-217.

(45) Love, S. A.; Marquis, B. J.; Haynes, C. L. *Appl. Spectrosc.* **2008**, *62*, 346-362.

(46) Uechi, I.; Yamada, S. *Anal. Bioanal. Chem.* **2008**, *391*, 2411-2421.

(47) Feldheim, D. L.; Keating, C. D. *Chem. Soc. Rev.* **1998**, *27*, 1-12.

(48) Boisselier, E.; Astruc, D. *Chem. Soc. Rev.* **2009**, *38*, 1759-1782.

(49) Park, K.; Lee, S.; Kang, E.; Kwon, I. C. *Adv. Funct. Mater.* **2009**, *19*, 1553-1566.

(50) Sonvico, F.; Dubernet, C.; Colombo, P.; Couvreur, P. *Curr. Pharm. Design* **2005**, *11*, 2091-2105.

(51) Jain, P. K.; El-Sayed, I. H.; El-Sayed, M. A. *Nano today* **2007**, *2*, 18-29.

(52) Murphy, C. J.; Gole, A. M.; Stone, J. W.; Sisco, P. N.; Alkilany, A. M.; Goldsmith, E. C.; Baxter, S. C. *Acc. Chem. Res.* **2008**, *41*, 1721-1730.

(53) Rosi, N. L.; Mirkin, C. A. *Chem. Rev.* **2005**, *105*, 1547-1562.

(54) Tong, L.; Wei, Q.; Wei, A.; Cheng, J.-X. *Photochem. Photobiol.* **2009**, *85*, 21-32.

221

(55)   Castaneda, M. T.; Alegret, A.; Merkoci, A. *Electroanalysis* **2007**, *19*, 743-753.

(56)   Guo, S.; Wang, E. *Anal. Chim. Acta* **2007**, *598*, 181-192.

(57)   Katz, E.; Willner, I. *Angew. Chem. Int. Ed.* **2004**, *43*, 6042-6108.

(58)   Katz, E.; Willner, I.; Wang, J. *Electroanalysis* **2004**, *16*, 19-44.

(59)   Luo, X.; Morrin, A.; Killard, A. J.; Smyth, M. R. *Electroanalysis* **2006**, *18*, 319-326.

(60)   Riskin, M.; Tel-Vered, R.; Bourenko, T.; Granot, E.; Willner, I. *J. Am. Chem. Soc.* **2008**, *130*, 9726-9733.

(61)   Wang, J. *Analyst* **2005**, *130*, 421-426.

(62)   Guerin, S.; Hayden, B. E.; Pletcher, D.; Rendall, M. E.; Suchsland, J.-P. *J. Comb. Chem.* **2006**, *8*, 679-686.

(63)   Hayden, B. E.; Pletcher, D.; Rendall, M. E.; Suchsland, J.-P. *J. Phys. Chem. C* **2007**, *111*, 17044-17051.

(64)   Li, Y.; Cox, J. T.; Zhang, B. *J. Am. Chem. Soc.* **2010**, *132*, 30-47-3054.

(65)   Welch, C. M.; Compton, R. G. *Anal. Bioanal. Chem.* **2006**, *384*, 601-619.

(66)   Hicks, J. F.; Zamborini, F. P.; Murray, R. W. *J. Phys. Chem. B* **2002**, *106*, 7751-7757.

(67)   Hicks, J. F.; Zamborini, F. P.; Osisek, A. J.; Murray, R. W. *J. Am. Chem. Soc.* **2001**, *123*, 7048-7053.

(68)   Lee, D.; Donkers, R. L.; Wang, G.; Harper, A. S.; Murray, R. W. *J. Am. Chem. Soc.* **2004**, *126*, 6193-6199.

(69)   Menard, L. D.; Gao, S.-P.; Xu, H.; Twesten, R. D.; Harper, A. S.; Song, Y.; Wang, G.; Douglas, A. D.; Yang, J. C.; Frenkel, A. I.; Nuzzo, R. G.; Murray, R. W. *J. Phys. Chem. B* **2006**, *110*, 12874-12883.

(70)   Miles, D. T.; Murray, R. W. *Anal. Chem* **2003**, *75*, 1251-1257.

(71)   Murray, R. W. *Chem. Rev.* **2008**, *108*, 2688-2720.

(72)   Zamborini, F. P.; Hicks, J. F.; Murray, R. W. *J. Am. Chem. Soc.* **2000**, *122*, 4514.

(73)   Del Popolo, M.; Leiva, E.; Klein, H.; Meier, J.; Stimming, U.; Mariscal, M.; Schmickler, W. *Appl. Phys. Lett.* **2002**, *81*, 2635.

(74)   Kolb, D. M.; Engelmann, G. E.; Ziegler, J. C. *Angew. Chem. Int. Ed.* **2000**, *39*, 1123-1125.

(75)   Ng, K. H.; Liu, H.; Penner, R. M. *Langmuir* **2000**, *16*, 4016-4023.

(76)   Redmond, P. L.; Hallock, A. J.; Brus. L. E. *Nanolett.* **2005**, *5*, 131-135.

(77)   Lee, T. M.-H.; Li, L.-L.; Hsing, I.-M. *Langmuir* **2003**, *19*, 4338-4343.

(78)   Pumera, M.; Castaneda, M. T.; Pividori, M. I.; Eritja, R.; Merkoci, A.; Alegret, S. *Langmuir* **2005**, *21*, 9625-9629.

(79)   Ambrosi, A.; Castaneda, M. T.; Killard, A. J.; Smyth, M. R.; Alegret, S.; Merkoci, A. *Anal. Chem.* **2007**, *79*, 5232-5240.

(80)   Escosura-Muniz, A.; Maltez-da Costa, M.; Merkoci, A. *Biosens. Bioelectron.* **2009**, *24*, 2475-2482.

(81)   Tang, L.; Han, B.; Persson, K.; Friesen, C.; He, T.; Sieradzki, K.; Ceder, G. *J. Am. Chem. Soc.* **2009**, *132*, 596-600.

(82)   Del Popolo, M. G.; Leiva, E. P.; Mariscal, M.; Schmickler, W. *Nanotechnology* **2003**, *14*, 1009-1013.

(83)   Maupai, S.; Dakkouri, A. S.; Schmuki, P. *Surf. Sci.* **2005**, *597*, 20-25.

(84)   Nielinger, M.; Baltruschat, H. *Chem. Phys. Chem.* **2003**, *4*, 1022-1024.

(85)   Henglein, A. *J. Phys. Chem.* **1993**, *97*, 5457-5471.

(86)   Plieth, W. J. *J. Phys. Chem.* **1982**, *86*, 3166.

(87)   Ward Jones, S. E.; Campbell, F. W.; Baron, R.; Xiao, L.; Compton, R. G. *J. Phys. Chem. C* **2008**, *112*, 17820.

(88)   Ward Jones, S. E.; Chevallier, F. G.; Paddon, C. A.; Compton, R. G. *Anal. Chem.* **2007**, *79*, 4110.

(89)   Ward Jones, S. E.; Chevallier, F. G.; Paddon, C. A.; Compton, R. G. *Anal. Chem.* **2007**, *79*, 4110-4119.

(90)   Ward Jones, S. E.; Toghill, K. E.; Zheng, S. H.; Morin, S.; Compton, R. G. *J. Phys. Chem.C* **2009**, *113*, 2846.

(91)   Lu, D.-l.; Tanaka, K.-i. *Phys. Rev. B* **1997**, *55*, 13865-13868.

(92)   Lu, D.-l.; Tanaka, K.-i. *Surf. Sci.* **1998**, *409*, 283-289.

(93)   Dutta, I.; Carpenter, M. K.; Balogh, M. P.; Ziegelbauer, J. M.; Moylan, T. E.; Atwan, M. H.; Irish, N. P. *J. Phys. Chem. C* **2010**, *114*, 16309-16320.

(94)   Wang, X.; Qi, Z.; Zhao, C.; Wang, W.; Zhang, Z. *J. Phys. Chem. C* **2009**, *113*, 13139-13150.

(95)   Ji, C.; Searson, P. C. *J. Phys. Chem. B* **2003**, *107*, 4494-4499.

(96)   Snyder, J.; Livi, K.; Erlebacher, J. *J. Electrochem. Soc.* **2008**, *155*, C464-C473.

(97)   Dursun, A.; Pugh, D. V.; Corcoran, S. G. *J. Electrochem. Soc.* **2003**, *150*, B355-B360.

(98)   Yeh, F.-H.; Tai, C.-C.; Huang, J.-F.; Sun, I.-W. *J. Phys. Chem. B* **2006**, *110*, 5215-5222.

(99)   Supriya, L.; Claus, R. O. *Chem. Mater.* **2005**, *17*, 4325-4334.

(100)   Chirea, M.; Garcia-Morales, V.; Manzanares, J. A.; Pereira, C.; Gulaboski, R.; Silva, F. *J. Phys. Chem. B* **2005**, *109*, 21808-21817.

(101)   Crespilho, F. N.; Zucolotto, V.; Brett, C. M. A.; Oliveira, O. N.; Nart, F. C. *J. Phys. Chem. B* **2006**, *110*, 17478-17483.

(102)   Jana, N. R.; Gearheart, L.; Murphy, C. J. *J. Phys. Chem. B* **2001**, *105*, 4065-4067.

(103)   Block, B. P. *Inorg. Syn.* **1953**, *4*, 14-17.

(104)   Meier, J.; Friederich, K. A.; Stimming, U. *Faraday Discuss.* **2002**, *121*, 365-372.

(105)   Pyatenko, A.; Yamaguchi, M.; Suzuki, M. *J. Phys. Chem. C* **2007**, *111*, 7910-7917.

(106)   Henglein, A. *J. Phys. Chem. B* **1999**, *103*, 9533-9539.

(107)   Zamborini, F. P.; Crooks, R. M. *Langmuir* **1998**, *14*, 3279-3286.

(108)   Martin, H.; Carro, P.; Creus, A. H.; Gonzalez, S.; Salvarezza, R. C.; Arvia, A. J. *Langmuir* **1997**, *13*, 100-110.

(109)   Guo, S.; Wang, L.; Wang, E. *Chem. Commun.* **2007**, 3163-3165.

(110)   Lu, D.-L.; Okawa, Y.; Suzuki, K.; Tanaka, K.-i. *Surf. Sci.* **1995**, *325*, 397-405.

(111)   Fransaer, J. L.; Penner, R. M. *J. Phys. Chem. B* **1999**, *103*, 7643-7653.

(112)   Penner, R. M. *J. Phys. Chem. B* **2001**, *105*, 8672-8678.

223

(113) Vasiljevic, N.; Viyannalage, L. T.; Dimitrov, N.; Sieradzki, K. *J. Electroanal. Chem.* **2008**, *613*, 118-124.

(114) Toney, M. F.; Howard, J. N.; Richer, J.; Borges, G. L.; Gordon, J. G.; Melroy, O. R.; Yee, D.; Sorensen, L. B. *Phys. Rev. Lett.* **1995**, *75*, 4472-4475.

(115) Holzle, M. H.; Zwing, V.; Kolb, D. M. *Electrochim. Acta* **1995**, *40*, 1237-1247.

(116) Hotlos, J.; Magnussen, O. M.; Behm, R. J. *Surf. Sci.* **1995**, *335*, 129-144.

(117) Hernandez, J.; Solla-Gullon, J.; Herrere, E.; Aldaz, A.; Feliu, J. M. *J. Phys, Chem. C* **2007**, *111*, 14078-14083.

(118) Campbell, F. W.; Compton, R. G. *Int. J. Electrochem. Sci.* **2010**, *5*, 407-413.

(119) Campbell, F. W.; Zhou, Y.-G.; Compton, R. G. *New J. Chem.* **2010**, *34*, 187-189.

(120) Batchelor-McAuley, C.; Wildgoose, G. G.; Compton, R. G. *New J. Chem.* **2008**, *32*, 941-946.

(121) Chen, W.; Yu, R.; Li, L.; Wang, A.; Peng, Q.; Li, Y. *Angew. Chem. Int. Ed.* **2010**, *49*, 2917-2921.

(122) Freeman, R. G.; Hommer, M. B.; Grabar, K. C.; Jackson, M. A.; Natan, M. J. *J. Phys. Chem.* **1996**, *100*, 718.

(123) Link, S.; Wang, Z. L.; El-Sayed, M. A. *J. Phys. Chem. B* **1999**, *103*, 3529.

(124) Mulvaney, P.; Giersig, M.; Henglein, A. *J. Phys. Chem.* **1993**, *97*, 1.

(125) Srnova-Sloufova, I.; Lednicky, F.; Gemperle, A.; Gemperlova, J. *Langmuir* **2000**, *16*, 9928.

(126) Ding, Y.; Chen, M.; Erlebacher, J. *J. Am. Chem. Soc.* **2004**, *126*, 6876-6877.

(127) Bonroy, K.; Friedt, J.-M.; Frederix, F.; Laureyn, W.; Langerock, S.; Campitelli, A.; Sara, M.; Borghs, G.; Goddeeris, B.; Declerck, P. *Anal. Chem.* **2004**, *76*, 4299-4306.

(128) Forty, A. J.; Durkin, P. *Philos. Mag. A* **1980**, *42*, 295.

(129) Li, R.; Sieradzki, K. *Phys. Rev. Lett.* **1992**, *68*, 1168.

(130) Corcoran, S. G.; Weisler, D. G.; Sieradzki, K. *Mater. Res. Soc. Symp. Proc.* **1997**, *451*, 93.

(131) Murphy, C. J.; Sau, T. K.; Gole, A. M.; Orendorff, C. J.; Gao, J.; Gou, L.; Hunyadi, S. E.; Li, T. *J. Phys. Chem. B* **2005**, *109*, 13857-13870.

(132) Slawinski, G. W.; Zamborini, F. P. *Langmuir* **2007**, *23*, 10357-10365.

(133) Sun, Y.; Mayers, B.; Xia, Y. *Adv. Mater.* **2003**, *15*, 641-646.

(134) Dong, H.; Cao, X. *J. Phys. Chem. C* **2009**, *113*, 603-609.

(135) Jia, F.; Yu, C.; Deng, K.; Zhang, L. *J. Phys. Chem. C* **2007**, *111*, 8424-8431.

(136) Sieradzki, K. *J. Electrochem. Soc.* **1993**, *140*, 2868.

(137) Sieradzki, K.; Corderman, R. R.; Shukla, K.; Newman, R. C. *Philos. Mag. A* **1989**, *59*, 713.

(138) Moffat, T. P.; Fan, F.-R. F.; Bard, A. J. *J. Electrochem. Soc.* **1991**, *138*, 3224.

(139) Liz-Marzan, L. M.; Philipse, A. P. *J. Phys. Chem.* **1995**, *99*, 15120.

(140) Michaelis, M.; Henglein, A.; Mulvaney, P. *J. Phys. Chem.* **1994**, *98*, 6212.

(141) Turkevich, J.; Kim, G. *Science* **1970**, *169*, 873.
(142) Mallin, M. P.; Murphy, C. J. *Nano Lett.* **2002**, *2*, 1235.
(143) Loo, B. H.; Furtak, T. E. *Chem. Phys. Lett.* **1980**, *71*, 68-71.
(144) Liu, J. H.; Wang, A. Q.; Chi, Y. S.; Lin, H. P.; Mou, C. Y. *J. Phys. Chem. B* **2005**, *109*, 40.
(145) Shipway, A. N.; Willner, I. *Chem. Commun.* **2001**, 2035.
(146) Shipway, A. N.; Willner, I.; Lahav, M. *Adv. Mater.* **2000**, *12*, 993.
(147) Zhang, F. X.; Srinivasan, M. P. *J. Colloid Interface Sci.* **2008**, *319*, 450-456.
(148) Sculz, J.; Roucoux, A. *Chem. Eur. J* **2000**, *6*, 618.
(149) Nagano, T. *Luminescence* **1999**, *14*, 283-290.
(150) Yomathan, J. N.; Wood, K. S.; Meyer, T. J. *Inorg. Chem.* **1992**, *31*, 3280-3285.
(151) Zhang, J.; Oyama, M. *Anal. Chim. Acta* **2005**, *540*, 299-306.
(152) Vooys, A. C. A. d.; Beltramo, G. L.; Riet, B. v.; Veen, J. A. R. v.; Koper, M. T. M. *Electrochimica Acta* **2004**, *49*, 1307–1314.

225

APPENDIX

AMERICAN CHEMICAL SOCIETY LICENSE
TERMS AND CONDITIONS

Dec 09, 2010

This is a License Agreement between Olga S Ivanova ("You") and American Chemical Society ("American Chemical Society") provided by Copyright Clearance Center ("CCC"). The license consists of your order details, the terms and conditions provided by American Chemical Society, and the payment terms and conditions.

All payments must be made in full to CCC. For payment instructions, please see information listed at the bottom of this form.

License Number

2552690564831

License Date

Nov 19, 2010

Licensed content publisher

American Chemical Society

Licensed content publication

Journal of the American Chemical Society

Licensed content title

Size-Dependent Electrochemical Oxidation of Silver Nanoparticles

Licensed content author

Olga S. Ivanova et al.

Licensed content date

Jan 1, 2010

Volume number

132

Issue number

1

Type of Use

Thesis/Dissertation

Requestor type

Not specified

Format

Print and Electronic

Portion

Table/Figure/Micrograph

Number of Table/Figure/Micrographs

23

Author of this ACS article

Yes

Order reference number

Title of the thesis / dissertation

Size-Dependent Electrochemical Stability of Metal Nanostructures

Expected completion date

Dec 2010

Estimated size(pages)

200

Billing Type

Invoice

Billing Address

2011 Alta ave apt #9

Louisville, KY 40205

United States

Customer reference info

Total

0.00 USD

Terms and Conditions

Thesis/Dissertation

ACS / RIGHTSLINK TERMS & CONDITIONS
THESIS/DISSERTATION

INTRODUCTION
The publisher for this copyrighted material is the American Chemical Society. By
clicking "accept" in connection with completing this licensing transaction, you agree that
the following terms and conditions apply to this transaction (along with the Billing and
Payment terms and conditions established by Copyright Clearance Center, Inc. ("CCC"),
at the time that you opened your Rightslink account and that are available at any time at
<http://myaccount.copyright.com>).

LIMITED LICENSE

Publisher hereby grants to you a non-exclusive license to use this material. Licenses are
for one-time use only with a maximum distribution equal to the number that you
identified in the licensing process; any form of republication must be completed within
60 days from the date hereof (although copies prepared before then may be distributed
thereafter).

GEOGRAPHIC RIGHTS: SCOPE
Licenses may be exercised anywhere in the world.

RESERVATION OF RIGHTS

Publisher reserves all rights not specifically granted in the combination of (i) the license details provided by you and accepted in the course of this licensing transaction, (ii) these terms and conditions and (iii) CCC's Billing and Payment terms and conditions.

PORTION RIGHTS STATEMENT: DISCLAIMER

If you seek to reuse a portion from an ACS publication, it is your responsibility to examine each portion as published to determine whether a credit to, or copyright notice of, a third party owner was published adjacent to the item. You may only obtain permission via Rightslink to use material owned by ACS. Permission to use any material published in an ACS publication, journal, or article which is reprinted with permission of a third party must be obtained from the third party owner. ACS disclaims any responsibility for any use you make of items owned by third parties without their permission.

REVOCATION
The American Chemical Society reserves the right to revoke a license for any reason, including but not limited to advertising and promotional uses of ACS content, third party usage, and incorrect figure source attribution.

LICENSE CONTINGENT ON PAYMENT

While you may exercise the rights licensed immediately upon issuance of the license at the end of the licensing process for the transaction, provided that you have disclosed complete and accurate details of your proposed use, no license is finally effective unless and until full payment is received from you (by CCC) as provided in CCC's Billing and Payment terms and conditions. If full payment is not received on a timely basis, then any license preliminarily granted shall be deemed automatically revoked and shall be void as if never granted. Further, in the event that you breach any of these terms and conditions or any of CCC's Billing and Payment terms and conditions, the license is automatically revoked and shall be void as if never granted. Use of materials as described in a revoked license, as well as any use of the materials beyond the scope of an unrevoked license, may constitute copyright infringement and publisher reserves the right to take any and all action to protect its copyright in the materials.

COPYRIGHT NOTICE: DISCLAIMER

You must include the following copyright and permission notice in connection with any reproduction of the licensed material: "Reprinted ("Adapted" or "in part") with permission from REFERENCE CITATION. Copyright YEAR American Chemical Society."

229

WARRANTIES: NONE
Publisher makes no representations or warranties with respect to the licensed material.

INDEMNITY
You hereby indemnify and agree to hold harmless publisher and CCC, and their respective officers, directors, employees and agents, from and against any and all claims arising out of your use of the licensed material other than as specifically authorized pursuant to this license.

NO TRANSFER OF LICENSE

This license is personal to you or your publisher and may not be sublicensed, assigned, or transferred by you to any other person without publisher's written permission.

NO AMENDMENT EXCEPT IN WRITING

This license may not be amended except in a writing signed by both parties (or, in the case of publisher, by CCC on publisher's behalf).

OBJECTION TO CONTRARY TERMS

Publisher hereby objects to any terms contained in any purchase order, acknowledgment, check endorsement or other writing prepared by you, which terms are inconsistent with these terms and conditions or CCC's Billing and Payment terms and conditions. These terms and conditions, together with CCC's Billing and Payment terms and conditions (which are incorporated herein), comprise the entire agreement between you and publisher (and CCC) concerning this licensing transaction. In the event of any conflict between your obligations established by these terms and conditions and those established by CCC's Billing and Payment terms and conditions, these terms and conditions shall control.

JURISDICTION
This license transaction shall be governed by and construed in accordance with the laws of the District of Columbia. You hereby agree to submit to the jurisdiction of the courts located in the District of Columbia for purposes of resolving any disputes that may arise in connection with this licensing transaction.

THESES/DISSERTATION TERMS

Publishing implications of electronic publication of theses and dissertation material
Students and their mentors should be aware that posting of theses and dissertation material on the Web prior to submission of material from that thesis or dissertation to an ACS journal may affect publication in that journal. Whether Web posting is considered prior publication may be evaluated on a case-by-case basis by the journal's editor. If an ACS journal editor considers Web posting to be "prior publication", the paper will not be accepted for publication in that journal. If you intend to submit your unpublished paper

230

to ACS for publication, check with the appropriate editor prior to posting your manuscript electronically.

If your paper has already been published by ACS and you want to include the text or portions of the text in your thesis/dissertation in **print or microfilm formats**, please print the ACS copyright credit line on the first page of your article: "Reproduced (or 'Reproduced in part') with permission from [FULL REFERENCE CITATION.] Copyright [YEAR] American Chemical Society." Include appropriate information.

Submission to a Dissertation Distributor: If you plan to submit your thesis to UMI or to another dissertation distributor, you should not include the unpublished ACS paper in your thesis if the thesis will be disseminated electronically, until ACS has published your paper. After publication of the paper by ACS, you may release the entire thesis (**not the individual ACS article by itself**) for electronic dissemination through the distributor; ACS's copyright credit line should be printed on the first page of the ACS paper.

Use on an Intranet: The inclusion of your ACS unpublished or published manuscript is permitted in your thesis in print and microfilm formats. If ACS has published your paper you may include the manuscript in your thesis on an intranet that is not publicly available. Your ACS article cannot be posted electronically on a publicly available medium (i.e. one that is not password protected), such as but not limited to, electronic archives, Internet, library server, etc. The only material from your paper that can be posted on a public electronic medium is the article abstract, figures, and tables, and you may link to the article's DOI or post the article's author-directed URL link provided by ACS. This paragraph does not pertain to the dissertation distributor paragraph above.

Other conditions:

v1.1

Gratis licenses (referencing $0 in the Total field) are free. Please retain this printable license for your reference. No payment is required.

If you would like to pay for this license now, please remit this license along with your payment made payable to "COPYRIGHT CLEARANCE CENTER" otherwise you will be invoiced within 48 hours of the license date. Payment should be in the form of a check or money order referencing your account number and this invoice number RLNK10887107.

Once you receive your invoice for this order, you may pay your invoice by credit card. Please follow instructions provided at that time.

Make Payment To:

Copyright Clearance Center

Dept 001

P.O. Box 843006

Boston, MA 02284-3006

If you find copyrighted material related to this license will not be used and wish to cancel, please contact us referencing this license number 2552690564831 and noting the reason for cancellation.

Questions? customercare@copyright.com or +1-877-622-5543 (toll free in the US) or +1-978-646-2777.

AMERICAN CHEMICAL SOCIETY LICENSE
TERMS AND CONDITIONS

Dec 09, 2010

This is a License Agreement between Olga S Ivanova ("You") and American Chemical Society ("American Chemical Society") provided by Copyright Clearance Center ("CCC"). The license consists of your order details, the terms and conditions provided by American Chemical Society, and the payment terms and conditions.

All payments must be made in full to CCC. For payment instructions, please see information listed at the bottom of this form.

License Number

2552690715330

License Date

Nov 19, 2010

Licensed content publisher

American Chemical Society

Licensed content publication

Analytical Chemistry

Licensed content title

Electrochemical Size Discrimination of Gold Nanoparticles Attached to Glass/Indium–Tin-Oxide Electrodes by Oxidation in Bromide-Containing Electrolyte

Licensed content author

Olga S. Ivanova et al.

Licensed content date

Jul 1, 2010

Volume number

82

Issue number

13

Type of Use

Thesis/Dissertation

Requestor type

Not specified

Format

Print and Electronic

Portion

Table/Figure/Micrograph

Number of Table/Figure/Micrographs

11

Author of this ACS article

Yes

Order reference number

Title of the thesis / dissertation

Size-Dependent Electrochemical Stability of Metal Nanostructures

Expected completion date

Dec 2010

Estimated size(pages)

200

Billing Type

Invoice

Billing Address

2011 Alta ave apt #9

Louisville, KY 40205

United States

Customer reference info

Total

0.00 USD

Terms and Conditions

Thesis/Dissertation

ACS / RIGHTSLINK TERMS & CONDITIONS

THESIS/DISSERTATION

INTRODUCTION
The publisher for this copyrighted material is the American Chemical Society. By clicking "accept" in connection with completing this licensing transaction, you agree that the following terms and conditions apply to this transaction (along with the Billing and Payment terms and conditions established by Copyright Clearance Center, Inc. ("CCC"), at the time that you opened your Rightslink account and that are available at any time at <http://myaccount.copyright.com>).

LIMITED LICENSE

Publisher hereby grants to you a non-exclusive license to use this material. Licenses are for one-time use only with a maximum distribution equal to the number that you identified in the licensing process; any form of republication must be completed within 60 days from the date hereof (although copies prepared before then may be distributed thereafter).

GEOGRAPHIC RIGHTS: SCOPE

Licenses may be exercised anywhere in the world.

RESERVATION OF RIGHTS

Publisher reserves all rights not specifically granted in the combination of (i) the license details provided by you and accepted in the course of this licensing transaction, (ii) these terms and conditions and (iii) CCC's Billing and Payment terms and conditions.

PORTION RIGHTS STATEMENT: DISCLAIMER

If you seek to reuse a portion from an ACS publication, it is your responsibility to examine each portion as published to determine whether a credit to, or copyright notice of, a third party owner was published adjacent to the item. You may only obtain permission via Rightslink to use material owned by ACS. Permission to use any material published in an ACS publication, journal, or article which is reprinted with permission of a third party must be obtained from the third party owner. ACS disclaims any responsibility for any use you make of items owned by third parties without their permission.

REVOCATION
The American Chemical Society reserves the right to revoke a license for any reason, including but not limited to advertising and promotional uses of ACS content, third party usage, and incorrect figure source attribution.

LICENSE CONTINGENT ON PAYMENT

While you may exercise the rights licensed immediately upon issuance of the license at the end of the licensing process for the transaction, provided that you have disclosed complete and accurate details of your proposed use, no license is finally effective unless and until full payment is received from you (by CCC) as provided in CCC's Billing and Payment terms and conditions. If full payment is not received on a timely basis, then any license preliminarily granted shall be deemed automatically revoked and shall be void as if never granted. Further, in the event that you breach any of these terms and conditions or any of CCC's Billing and Payment terms and conditions, the license is automatically revoked and shall be void as if never granted. Use of materials as described in a revoked license, as well as any use of the materials beyond the scope of an unrevoked license, may constitute copyright infringement and publisher reserves the right to take any and all action to protect its copyright in the materials.

COPYRIGHT NOTICE: DISCLAIMER

You must include the following copyright and permission notice in connection with any reproduction of the licensed material: "Reprinted ("Adapted" or "in part") with permission from REFERENCE CITATION. Copyright YEAR American Chemical Society."

236

WARRANTIES: NONE

Publisher makes no representations or warranties with respect to the licensed material.

INDEMNITY
You hereby indemnify and agree to hold harmless publisher and CCC, and their respective officers, directors, employees and agents, from and against any and all claims arising out of your use of the licensed material other than as specifically authorized pursuant to this license.

NO TRANSFER OF LICENSE

This license is personal to you or your publisher and may not be sublicensed, assigned, or transferred by you to any other person without publisher's written permission.

NO AMENDMENT EXCEPT IN WRITING

This license may not be amended except in a writing signed by both parties (or, in the case of publisher, by CCC on publisher's behalf).

OBJECTION TO CONTRARY TERMS

Publisher hereby objects to any terms contained in any purchase order, acknowledgment, check endorsement or other writing prepared by you, which terms are inconsistent with these terms and conditions or CCC's Billing and Payment terms and conditions. These terms and conditions, together with CCC's Billing and Payment terms and conditions (which are incorporated herein), comprise the entire agreement between you and publisher (and CCC) concerning this licensing transaction. In the event of any conflict between your obligations established by these terms and conditions and those established by CCC's Billing and Payment terms and conditions, these terms and conditions shall control.

JURISDICTION
This license transaction shall be governed by and construed in accordance with the laws of the District of Columbia. You hereby agree to submit to the jurisdiction of the courts located in the District of Columbia   for purposes of resolving any disputes that may arise in connection with this licensing transaction.

THESES/DISSERTATION TERMS

Publishing implications of electronic publication of theses and dissertation material
Students and their mentors should be aware that posting of theses and dissertation material on the Web prior to submission of material from that thesis or dissertation to an ACS journal may affect publication in that journal. Whether Web posting is considered prior publication may be evaluated on a case-by-case basis by the journal's editor. If an ACS journal editor considers Web posting to be "prior publication", the paper will not be

237

accepted for publication in that journal. If you intend to submit your unpublished paper to ACS for publication, check with the appropriate editor prior to posting your manuscript electronically.

If your paper has already been published by ACS and you want to include the text or portions of the text in your thesis/dissertation in **print or microfilm formats**, please print the ACS copyright credit line on the first page of your article: "Reproduced (or 'Reproduced in part') with permission from [FULL REFERENCE CITATION.] Copyright [YEAR] American Chemical Society." Include appropriate information.

Submission to a Dissertation Distributor: If you plan to submit your thesis to UMI or to another dissertation distributor, you should not include the unpublished ACS paper in your thesis if the thesis will be disseminated electronically, until ACS has published your paper. After publication of the paper by ACS, you may release the entire thesis (**not the individual ACS article by itself**) for electronic dissemination through the distributor; ACS's copyright credit line should be printed on the first page of the ACS paper.

Use on an Intranet: The inclusion of your ACS unpublished or published manuscript is permitted in your thesis in print and microfilm formats. If ACS has published your paper you may include the manuscript in your thesis on an intranet that is not publicly available. Your ACS article cannot be posted electronically on a publicly available medium (i.e. one that is not password protected), such as but not limited to, electronic archives, Internet, library server, etc. The only material from your paper that can be posted on a public electronic medium is the article abstract, figures, and tables, and you may link to the article's DOI or post the article's author-directed URL link provided by ACS. This paragraph does not pertain to the dissertation distributor paragraph above.

Other conditions:

v1.1

Gratis licenses (referencing $0 in the Total field) are free. Please retain this printable license for your reference. No payment is required.

If you would like to pay for this license now, please remit this license along with your payment made payable to "COPYRIGHT CLEARANCE CENTER" otherwise you will be invoiced within 48 hours of the license date. Payment should be in the form of a check or money order referencing your account number and this invoice number RLNK10887109.

Once you receive your invoice for this order, you may pay your invoice by credit card. Please follow instructions provided at that time.

Make Payment To:

Copyright Clearance Center

Dept 001

P.O. Box 843006

Boston, MA 02284-3006

If you find copyrighted material related to this license will not be used and wish to cancel, please contact us referencing this license number 2552690715330 and noting the reason for cancellation.

Questions? <u>customercare@copyright.com</u> or +1-877-622-5543 (toll free in the US) or +1-978-646-2777.

CURRICULUM VITAE

Olga S. Ivanova

Department of Chemistry
University of Louisville
Louisville, KY 40292
Telephone: (502) 852-5982
Mobile: (502) 821-9480
E-mail:
osivan01@louisville.edu
1.olga.s.ivanova@gmail.com

Objective

Doctoral and postdoctoral research in Analytical Chemistry, Materials Chemistry, or Nanoscience.

Education

2008 – 2010	**University of Louisville, Louisville KY** Ph.D. in Chemistry, expected December 2010 Department of Chemistry, college of Arts and Sciences Mentor: Dr. Francis P. Zamborini Dissertation title: "Size-Dependent Electrochemical Stability of Metal Nanostructures"
2005 – 2008	**University of Louisville, Louisville KY** M.S. in Chemistry, December 2008 Department of Chemistry, college of Arts and Sciences Mentor: Dr. Francis P. Zamborini
1998 – 2004	**Perm State University, Perm, Russia** M.S. in Chemistry, July 2004

Department of Chemistry
Mentor: Prof. Anatoly B. Shein
Thesis: "Influence of Anions and Cations on Anodic
Dissolution of Iron Group Metal Silicides in Acidic
Media".

Research Experience

2005 – Present   **Department of Chemistry, University of Louisville,
                        Louisville KY**
                        Research assistant
                        Research on the:
                        - Size-controlled synthesis of metal nanostructures.
                        - Studied electrochemical and optical properties and
                        morphology of metal nanostructures as a function of size.
                        - Studied effect of nanoparticle size on underpotential
                        deposition (UPD).
                        - Studied electrochemical oxidation of Au/Ag alloy
                        nanoparticles.
                        - Studied the electrochemical behavior of metal
                        nanoparticles – polymer multilayer films.

2001 – 2004   **Department of Chemistry, Perm State University,
                        Perm, Russia**
                        Research assistant
                        Research on anodic dissolution (corrosion) of metal
                        silicides in acidic media.

Instrumentation

Electrochemical methods: Voltammetry,
                             Chronoamperometry,
                             Chronocoulometry

Surface techniques: Atomic Force Microscopy (AFM)
                             Scanning Electron Microscopy (SEM)

Optical techniques: Ultraviolet visible spectroscopy (UV-vis)

Publications

1. Olga S. Ivanova, Francis P. Zamborini; "**Electrochemical Size Discrimination of Gold Nanoparticles Attached to Glass/Indium-Tin-Oxide Electrodes by Oxidation in Bromide-Containing Electrolyte**". *Anal. Chem.* **2010**, *82* (13), 5844-5850.

2. Olga S. Ivanova, Francis P. Zamborini; "**Size – Dependent Electrochemical Oxidation of Silver Nanoparticles**". *J. Am. Chem. Soc.* **2010**, *132* (1), 70-72.

3. Shein A.B., Ivanova O.S., Minkh R.N.; "**The Effect of Anions on the Anodic Dissolution of Nickel Silicide in Sulfate Electrolytes**". *Protection of Metals* **2008**, *44* (1), 32-38.

Presentations

1 – Olga S. Ivanova and Francis P. Zamborini; "Electrochemical Properties of Metal Nanoparticles" Gordon Research Conference on Electrochemistry in Ventura, CA (January 2007) – Poster

2 – Olga S. Ivanova and Francis P. Zamborini; "Electrochemical Properties of Metal Nanoparticles" 39th Central Regional Meeting of the American Chemical Society in Covington, KY (May 2007) - Poster

3 – Olga S. Ivanova and Francis P. Zamborini; "Electrochemical Properties of Metal Nanoparticles" KY NanoMat in Louisville, KY (April 2008) – Poster

4 – Olga S. Ivanova and Francis P. Zamborini; "Electrochemical Oxidation of Gold Nanoparticles as a Function of Size" Gordon Research Conference on Electrochemistry in Ventura, CA (January 2010) - Poster

5 – Olga S. Ivanova and Francis P. Zamborini; Electrochemical Oxidation of Gold Nanoparticles as a Function of Size" Electrochemistry Mini Symposium and Student Poster Session sponsored by the Cleveland section of the Electrochemical Society and the Yeager Center for Electrochemical Sciences at Case Western Reserve University in Cleveland, Ohio (May 2010). - Poster

Teaching Experience

University of Louisville, Louisville, KY

2005 – 2008   Graduate teaching assistant
                     Taught basic concepts and principles of general, organic
                     and physical chemistry.

                     Courses taught:

                     201 – General chemistry I-S
                     202 – General chemistry II-S
                     207 – Intro to Chem. Analysis I-SL
                     208 – Intro to Chem. Analysis II-SL
                     343 – Organic Chemistry Lab I
                     470 – Physical Chemistry Lab – WR

2007 – 2010   Undergraduate and Graduate research mentor
                     - Taught laboratory techniques such as Voltammetry,
                     Chronocoulometry and UV-Vis.
                     - Explain important concepts of electrochemical oxidation
                     of metals.
                     - Taught chemical synthesis of metal nanostructures of
                     different size.

                     Undegraduate students:

                     Davin Spaulding
                     Vy Tran

                     Graduate students:

                     Lina Abdelmoti
                     Rafael Masitas
                     Tulashi Luitel

Service Activities
- Judging at the 3rd Annual Kentuckiana   2006
  Undergraduate Research Symposium in Louisville, KY

Languages:

English (fluent), Russian (native).

Awards

Poster presentation, 3rd prize winner. KY NanoMat   2008

Professional Affiliations

American Chemical Society   2007 – current

References

Dr. Francis P. Zamborini
Department of Chemistry
University of Louisville
2320 South Brook Street
Louisville, KY 40292
Phone: (502) 852 6550
E-mail: f.zamborini@louisville.edu

Dr. Richard P. Baldwin
Department of Chemistry
University of Louisville
2320 South Brook Street
Louisville, KY 40292
Phone: (502) 852-5892
E-mail: rick.baldwin@louisville.edu

Dr. Aleeta M. Powe
Assistant Professor
Department of Chemistry
University of Louisville
Louisville, KY 40292
Phone: (502) 852-5969
Email: aleeta.powe@louisville.edu

Dr. Mehdi. M. Yazdanpanah
CEO-Founder
NaugaNeedles,
11509 Commonwealth Dr., Suite #2
Louisville, KY, 40299
www.nauganeedles.com
Cell: (502) 807-1199
Office: (502) 619-5156
E-mail: mehdi@nauganeedles.com

Prof. Shein Anatoly B.
Dean of Department of Chemistry
Head of the Division of Physical Chemistry
Perm State University
Bukireva Str., 15 Perm, Russia 614990
Phone: 7(342) 239-6349
E-mail: ashein@psu.ru
        Anatoly173@yandex.ru